A Pilot-Aided, Time-Domain Doppler Estimator, Tracker and Compensator for Doubly Dispersive Underwater Acoustic Channels Dominated by Wave Motion

by

Ali M. Bassam

Submitted in partial fulfillment of the

requirements for the degree of Doctor of Philosphy

at

Dalhousie University

Halifax, Nova Scotia

December 2020

Dedication

To my beloved mother, father and grandparents. To my friends and family. Rest in peace, grandma. You'll always be in my heart.

Table of Contents

List of Figures

Abstract

In this thesis, a time-domain Doppler estimator, tracker, and compensator using shift-orthogonal OFDM pilot sequences are designed based on the theory presented and tested using simulations and real-life experiments. OFDM signals are assumed and used throughout the dissertation, and a shift-orthogonal OFDM pilot sequence is designed. The UWA channel is analyzed and a simplified theoretical model is presented that holds under achievable conditions.

The Doppler estimator is then developed, which uses an approach reminiscent of existing differential demodulation techniques. The estimator is developed with the flexibility of handling any Mach number provided the designer has the liberty of adjusting the signal's bandwidth, carrier frequency, or preamble size. The CRLB for the estimator is derived. The Doppler estimator performance is compared against existing estimators in literature and is shown to outperform most existing estimators in terms of MSE, with the added features of Doppler tracking and low computational complexity. The Mach number estimates also have a closed-form expression.

A Doppler tracker is developed that reduces the size of the Mach number estimates' array while simultaneously tracking significant changes in the Mach number. A novel and practical Doppler compensator based on the proposed estimator is developed, which compensates the Doppler effect in two stages. The first stage involves resampling, which takes in the estimates at the tracker output and applies a form of time-varying resampling which we call block-by-block resampling. The second stage involves estimating the residual Doppler shift with the proposed Doppler estimator, followed by eliminating the residual shift via a simple phase rotation. The proposed tracker and compensator subsystem is shown to outperform most existing compensators in terms of MSE, while also being more computationally efficient.

Each element of the proposed receiver subsystem is tested in simulations and the results are shown to agree with theory. Finally the full receiver subsystem is tested in real undersea experiments at various ranges, bandwidths and power levels, and the subsystem is shown to yield minimal residual errors when tracking and compensating the Mach number.

List of Abbreviations and Symbols Used

$\hat{a}_i$	sample mean of $\hat{a}_i[n]$
A	signal amplitude at the receiver
B_{coh}	channel's coherence bandwidth, $:= 1/T_m$
B_{d}	Doppler spread of the UWA channel across the time interval of interest (in Hz)
c	speed of sound in UWA channels
d	transmission range
$\bar{f}_{\text{d}}$	frequency shift (in bins) of the Doppler power spectrum for the UWA channel across the entire duration of transmission
f_c	carrier frequency
$\bar{f}_{\text{d}}$	common Doppler shift of the UWA channel across the total transmission time (in bins)
I	downsampling factor of the Doppler tracker
M	number of pilots in a preamble
N	number of samples of the discrete-time sequence
N_b	number of received signal blocks
N_p	number of propagation paths
N_{pre}	number of preamble repetitions,$:= N/M$
N_u	upsampling factor of the transmit filter

P	number of channel paths
P_A	acoustic power
R	distance from transmitter to a point in a UWA channel
s_{d}	rms Doppler spread of the UWA channel across the total transmission time (in bins)
t	observation time
T	symbol duration of an N-point signal
T_{coh}	channel's coherence time, $:= 1/B_{\mathrm{d}}$
T_g	guard interval
T_{m}	multipath (or delay) spread
T_s	sampling period
T'	total duration of the transmitted signal, $:= T + T_g$
W	channel bandwidth
$a(f)$	absorption coefficient
$\hat{a}_i[n]$	Mach number estimator output; also discrete-time representation of $\hat{a}_i(t)$
$\hat{a}_i^I[n]$	Mach number estimates at the output of the tracker
$a_i(t)$	Mach number for the ith received preamble or block
$\hat{a}_i(t)$	estimate for $a_i(t)$
$A(l, f)$	path loss
$A(R)$	cross-sectional area modelling the spreading geometry

$B_M[k]$	DFT of $b_M[n]$ with frequency index k (sometimes written as $B[k]$)
$B_N[k]$	DFT of $b_N[n]$ with frequency index k
$b_M[n]$	M-point shift-orthogonal pilot sequence
$b_M^{\mathrm{p}}(t)$	bandpass shift-orthogonal pilot sequence of size M
$b_N[n]$	N-point extension of $b_M[n]$
$b(t)$	transmitted lowpass shift-orthogonal pilot signal
$b_p(t)$	transmitted bandpass shift-orthogonal pilot signal
$\lvert\mathcal{C}_p\rvert$	random variable of $\lvert c_p\rvert$
$c(t,\tau)$	bandpass impulse response of the channel
$c_p(t)$	pth path's bandpass attenuation factor of the underwater acoustic channel
$C(t,f)$	Fourier transform of $c(t,\tau)$
$C_p(t,f)$	attenuation factor for path p
$d_i(t)$	residual resampling factor of the ith received block
E[$\cdot$]	expected value
$f(z_i(t)\lvert a_i(t))$	joint PDF of lowpass, downsampled noise given the true Mach number value.
$g(t)$	transmit interpolation filter
$h_i^I[\ell]$	FIR filter modelling the tracker
$h(t,\tau)$	lowpass impulse response of the channel
$H(t,f)$	Fourier transform, or frequency response, of $h(t,\tau)$

$h_p(t)$	pth path's lowpass attenuation factor of the underwater acoustic channel
$I(R)$	acoustic power intensity at point R
$\mathcal{I}(a_i)$	Fisher information
$L(a_i\|z_i)$	likelihood function of $z_i[n]$
$L(R, f)$	total path loss
$L_a(R, f)$	absorption loss in dB
$L_s(R)$	spreading loss evaluated in dB
$M_p(t)$	channel tap's multiplicative noise
$N(f)$	Fourier tranform of $n(t)$
$\tilde{N}(f)$	Fourier transform of $\tilde{n}(t)$
$n(t)$	bandpass noise signal
$\tilde{n}(t)$	lowpass noise signal
$r(t)$	received bandpass signal
$R(f)$	Fourier transform of $r(t)$
$R_h(t_1, t_2, \tau_1, \tau_2)$	autocorrelation function of $h(t, \tau)$
$R_h(\tau)$	delay power spectrum of $h(t, \tau)$
$R_H(t_1, t_2, f_1, f_2)$	autocorrelation function of $H(t, f)$
$R_b[n]$	autocorrelation function of $b_M[n]$
$R_{bb}[n]$	cross-correlation function of $b_M[n]$ with $b_N[n]$
$S_H(\nu)$	channel's Doppler power spectrum

$s(t)$	transmitted bandpass signal
$S(f)$	Fourier transform of $s(t)$
$T(z_i(t)\|a_i(t))$	point estimate or statistic, $:= \hat{a}_i(t)$
$X(f)$	Fourier transform of $x(t)$
$X[k]$	DFT of $x(t)$
$x(t)$	transmitted lowpass signal
$Y(f)$	Fourier tranform of $y(t)$
$y(t)$	received lowpass signal
$Z(f)$	Fourier transform of $z(t)$
$Z(t)$	random process representing the filtered lowpass noise
$z(t)$	filtered lowpass noise signal
$\delta_i(t)$	residual Doppler shift
$\hat{\delta}_i(t)$	estimate of $\delta_i(t)$
$\hat{\delta}_i[n]$	discrete-time representation of $\hat{\delta}_i(t)$
$\hat{\delta}_i$	sample mean of $\hat{\delta}_i[n]$
$\hat{\Delta}_i[n]$	phase estimator output
$\widehat{\Delta f}_i[n]$	common Doppler shift estimator output
Δt	time interval over which a UWA channel is analyzed
Γ_p	total reflection coefficient for path p
$\theta_p(t)$	phase offset of the pth path at the baseband, $:= -2\pi f_c \tau_p(t)$
κ	path loss exponent which models spreading loss

$\mu_i[n]$	autocorrelation output sample, $:= y_i[n]y_i^*[n-M]$
ν	Doppler frequency
σ_i	variance of $z_i[n]$
τ	fixed propagation delay (or path delay)
$\tau(t)$	time-varying propagation delay (or path delay)
$\tau_p(t)$	pth path's time-varying propagation delay (or path delay)
AWGN	additive white Gaussian noise
CAF	cross-ambiguity function
CIR	channel impulse response
CFO	carrier frequency offset
CP	cyclic prefix
CRLB	Cramer-Rao lower bound
DFE	decision-feedback equalizer
DFT	discrete Fourier transform
ESD	energy spectral density
FD	frequency domain
FFT	fast Fourier transform
ICI	intercarrier interference
IDFT	inverse discrete Fourier transform
i.i.d.	independent and identically distributed
ISI	intersymbol interference

LTV	linear time-variant
MA	moving average
MSE	mean-square error
MVUE	minimum-variance unbiased estimator
OFDM	orthogonal frequency-division multiplexing
PAPR	peak-to-average power ratio
PDF	probability density function
PL	power level
PLL	phase-locked loop
PSD	power spectral density
PSK	phase-shift keying
QAM	quadrature amplitude modulation
QPSK	quadrature phase-shift keying
RLS	recursive least squares
SNR	signal-to-noise ratio
TD	time domain
WSS	wide-sense stationary
WSSUS	wide-sense stationary uncorrelated scattering

Acknowledgements

Thank you to all the people who have supported me throughout my research. Special thanks to Dr. Christian Schlegel and Dr. Mae Seto for providing their knowledge, wisdom and feedback, without which this dissertation wouldn't be possible. My thanks also goes to Dr. Dmitry Truhachev and Acoubit for providing the necessary equipment, help and support in all the sea trials and tests, as well as my colleague Murwan Bashir for his invaluable participation in these trials. Without all of them this work would not have come to fruition.

Chapter 1

Introduction

1.1 Motivation

The underwater acoustic (UWA) channel ranks among the most difficult and unforgiving for wireless communications with multiple challenges. The major challenges include attenuation with transmitted frequency, time-varying multipath propagation and low speed of sound. Unlike other communications channels where the attenuation is either constant or time-dependent, the attenuation affecting propagating signals in UWA channels are both time- and frequency-dependent. Multipath is governed by sound reflection off the surface and seabed as well as objects in mid-water column. Sound refraction is another multipath source that is due to the spatial variability of the local sound speed. This is governed by Snell's law. Multipath effects delay the signal differently along each propagation path, thereby dispersing the propagating signal in time (time dispersion). This results in intersymbol interference (ISI). This also results in delay spread, which appears in the channel's delay power spectrum.

The third challenge, the low sound speed, which creates Doppler effects, is the focus of this thesis. As the acoustic wave propagation speed in water is 5 orders of magnitude less than the speed of light in air, the impact from Doppler effects are more significant for UWA propagation than electromagnetic wave propagation in air. In multipath environments, Doppler frequencies are different for each path, which results in Doppler spread; this effect disperses the frequency content of the signal (frequency dispersion). For multicarrier modulation, this results in intercarrier interference (ICI). Thus the UWA channels of interest here are doubly dispersive (where time dispersion

is due to multipath effects and frequency dispersion is due to Doppler effects).

In total, the three Doppler effects that persist in UWA channels are (i) Doppler shift common to all paths, which manifests as carrier frequency offset (CFO) in the received signal; (ii) spectral narrowing/broadening, which results in frequency dispersion appearing in the frequency spectrum, as well as Doppler spread, which appears in the Doppler power spectrum; and (iii) time dilation/compression, which is a manifestation of the Doppler effect in time; this causes the received samples to drift, thereby causing channel taps to migrate in time.

Doppler effects are a consequence of relative motion between transmitter and receiver — either by gravity waves, deliberate motion or another mechanism. This manifests in Doppler shifts and Doppler spreading. There are two main sources of Doppler shifts in UWA channels. The first is a deliberate (underway) relative transmitter and receiver platform velocity. The second is wave motion in the medium, specifically motion of gravity waves. Gravity waves occur underwater or on the air-water interface when the medium density changes. Gravity wave motion gives rise to different Doppler shifts on individual propagation paths, which in turn, further gives rise to Doppler spread or dispersion. The underwater channel coherence time, T_{coh} (the larger, the better), is a statistical measure of the time duration over which the channel impulse response, CIR, is unchanged or stationary. A channel that has Doppler effects (i.e. transmitter and receiver in relative motion) will have a small T_{coh} since the channel is constantly changing.

Fast fading is notable changes in signal strength between transmitter and receiver given small (fraction of a wavelength) changes in the range between them. This occurs in a channel whose T_{coh} is less than the duration of the propagating signal. The Doppler effect is one of the main causes of fast fading, and results in the channel's low T_{coh}. Other causes of fast fading are localized objects which results in signal scattering or diffraction.

Due to multipath propagation, UWA channels are frequency selective. Frequency selectivity occurs when the channel's delay spread (time between first and last multipath return) exceeds the duration of the propagating signal. This gives rise to rapid oscillations in the frequency response of the channel making it difficult to receive an uncorrupted signal.

Left uncompensated, Doppler effects make it difficult, if not impossible, to recover and extract information from the originally transmitted signal — especially relevant for UWA communications and data transmission. Towards that, Doppler estimation, tracking and compensation are active research areas in UWA communications. Therefore, it is not unexpected that solutions have been proposed to address Doppler effects though they are not without their limitations.

This treatise focuses on a proposed receiver processor which includes a novel Doppler estimator, tracker and compensator designed for large Doppler effects like those in channels where the transmitter and receiver have an underway relative velocity (e.g. submarines, autonomous underwater vehicles (AUV) or marine mammals). The novel receiver processor was validated by simulations and at-sea tests with Doppler effects induced by waves. Simulations were also performed at Mach numbers representative of transmitters and receivers with relative underway velocity. Future work will address the at-sea validation of high Mach number cases using underwater modems integrated on an underway autonomous underwater vehicle (AUV) and deployed over-the-side transmitter-receiver modems.

1.2 Approach

The orthogonal frequency-division multiplexing (OFDM) modulation scheme is resilient to frequency selectivity as it transmits a signal over multiple subcarriers. In the frequency domain, this means the channel's frequency response is divided into smaller subchannels, where each subchannel uniquely corresponds to a subcarrier. If

the subchannel is small enough from taking a large-enough number of subcarriers, the frequency response appears flat in the domain of the subchannel which is desirable.

After the time-of-arrival (TOA) estimates of acoustic signals, Doppler estimation and compensation make up the first stage of the receiver processing in UWA channels since understanding the channel time variations is necessary prior to channel estimation (as quantified through the CIR). For the thesis work, pilots (a-priori known signals) are used to estimate and track the channel dynamics as measured through the CIR.

Doppler estimation and compensation are thus crucial for proper channel estimation, and due to the rapid time variations in UWA channels, are more critical than in, say, radio frequency channels. Doppler estimation and compensation in UWA channels have been extensively studied and many approaches have been proposed. Approaches that are relevant and contribute to the thesis will be presented.

The proposed Doppler estimator distinguishes itself from other estimators with its built-in Doppler tracking and flexibility to handle any Mach number (ratio of relative transmitter and receiver velocity relative to the local sound velocity) effects provided the designer has the liberty to adapt the signal's bandwidth, carrier frequency, or preamble size. It is acknowledged that this is not always possible as the application / customer may constrain the transmitted signal to specific bandwidths or carrier frequencies in which case only the preamble size can be adjusted. Generally, there is no merit to constrain the preamble so this is (usually) available for the designer to optimize. The proposed estimator and tracker will have greater utility when software-defined sonar becomes more widespread. A measure of the proposed estimator's performance, the mean-square error (MSE), shows it outperforms most other estimators while maintaining low computational complexity regardless of the size of the Mach number. Once Doppler estimation is achieved, compensation becomes possible.

However, prior to compensation for the proposed estimator, a Doppler tracking stage is inserted between the estimation-compensation chain to reduce the computational load on the compensator while also tracking Mach number changes. Unlike other estimators found in literature, the receiver yields estimates and tracks one sample at a time. This is computationally expensive and slow, and is difficult to execute on an embedded platform, like an autonomous underwater vehicle (AUV), with its limited on-board processing. As well, computationally less-expensive receiver processing of active sonar returns is of great value in real-time missions to track mobile targets like submarines or marine mammals where timely compensation makes a difference in the possible actions a ship could pursue. As an example, for a 5-second transmission of a 20-kHz bandwidth signal, there are 100,000 samples to work through.

The Doppler effect is then compensated in two stages. The first stage involves resampling, which takes in the estimates at the tracker output and applies a time-varying resampling technique, referred to as block-by-block resampling. The second stage estimates the residual Doppler shift based on the output of the proposed estimator. The residual shift is then mitigated via a simple phase rotation. The proposed tracker and compensator subsystem outperform most existing compensators as measured by the MSE, while also being more computationally efficient.

Performance tests of the full receiver were in the form of simulations and real undersea trials. After confirming performance with simulations, the full receiver subsystem was first tested in short-range sea trials, followed by a series of medium- and long-range sea trials at different ranges, bandwidths and power levels.

Specifically, the research in this thesis addresses the quasi-stationary case of relative motion between the transmitter and receiver induced by waves. This is a milestone towards developing, testing and validating the proposed receiver processing for large Doppler effects.

1.3 Contributions

This work builds on the M.A.Sc. thesis completed by the author in 2015. It provides both theoretical and practical insights and contributions to UWA communications in particular, and digital signal processing (DSP) in general. Specifically, it presents novel methods and simulations founded on well-known assumptions and theories in UWA communications. The main novel contribution is the theoretical framework and simulation of the Doppler estimator, tracker and compensator, as well as a body of at-sea UWA channel measurements, applicable to many underwater applications.

The estimator, tracker and compensator were tested and validated with synthetic and real UWA channels. The results show that all three have performance acceptable to practical underwater receivers. Specifically, the residual Doppler shift at the subsystem output is shown to be consistently small relative to subcarrier spacings and bandwidth. The channel tap migrations observed in the CIR due to Doppler effects were also successfully eliminated.

The result is a fully functional UWA receiver processor which accurately estimates and eliminates channel Doppler effects when the Mach number is assumed to vary in time within each received block. This means the receiver is applicable to a wide array of channels. The limiting assumption made about the channel is that the channel taps are assumed to be slowly varying within the received block, though it is found that this assumption becomes an accurate reflection of reality for short signal durations, as will be seen later. This work contributed to Acoubit Communications Inc.'s understanding of Doppler effects in UWA channels, and consequently, Acoubit adopted the proposed estimator. It is not yet possible for Acoubit to adopt the proposed tracker and compensator as the work for this was not completed until after Dalhousie University's collaboration with Acoubit. It is expected that this work will benefit them and other parties in the future. The results clearly show that the

estimator, tracker and compensator work well for the quasi-stationary case of relative motion due to waves, which creates the relative motion between the transmitter and receiver. Future work will study UWA channels with high Doppler effects like those experienced by autonomous underwater vehicles (AUV) operations.

Below are the contributions of the thesis in the proposed receiver processor:

1. The proposed estimator is inherently capable of tracking the Doppler variations in the channel.
2. The estimator has a necessary condition to ensure its validity regardless of the size of the Mach number, provided the signal's bandwidth, carrier frequency, or preamble size can be adjusted.
3. The MSE of the proposed estimator outperforms most other estimators while maintaining low computational complexity and regardless of the Mach number size. This holds true for the proposed compensator as well.
4. The proposed tracker can track the Doppler variations without the need to use the entire set of Mach number estimates. This smaller set of estimates reduces the computational load on the compensator.
5. The resampler is driven by a variable resampling factor that depends on the tracker output to eliminate the Doppler variations. The proposed resampling technique is a form of time-varying resampling.
6. The proposed estimator has the added ability to estimate the residual Doppler shift. It can therefore be used as a second-stage Doppler compensator as well.

1.4 Thesis Outline

An outline of the thesis progression is shown in Fig. 1.1. It shows the order and rationale for the steps taken in the research. Essentially, the Doppler estimator was developed first followed by the compensator. Insight into the novel compensator

suggested the heavy computation load for Mach number tracking could be better addressed through down sampling. Then, with all components developed and their nominal performance validated in simulation, at-sea trials were undertaken.

Chapter 2 provides relevant background for the research. To start, it introduces shift-orthogonal pilot sequences and their properties, followed by an overview of multipath fading channels, and introduces the WSSUS channel model used. It proves the validity of the WSSUS assumption for UWA channels and shows how the assumption can be realized under achievable conditions. The chapter then briefly delves into the physics of UWA channels and the different losses encountered in transmission through such channels. The outcome is an impulse response model for UWA channels. It presents a thorough analysis of Doppler effects during transmission in UWA channels, which gives rise to a received signal model for the transmission chain. Chapter 2 provides meaningful background for the literature review in Chapter 3.

Chapter 3 presents a state-of-the-art literature review of Doppler estimators and compensators. This includes the approaches taken by the UWA community and identified shortcomings against the present requirement for estimation, tracking and compensation of large Doppler effects and implementation on mobile transmitter/receiver platforms. This shaped the approach for the receiver processor to be developed in this thesis and set the stage for Chapters 4, 5 and 6 — the contributions from this thesis.

Chapter 4 provides a rigorous derivation of the proposed Doppler estimator. The chapter also includes a derivation for the Cramer-Rao Lower Bound (CRLB) used to assess the proposed estimator's performance. Then, the performance of the estimator in simulation is presented to show that it met the requirements. The chapter ends with an analysis that compares the proposed estimator against the relevant existing ones introduced in Chapter 3. With the estimator defined, it was possible to move forward with the Doppler compensator.

Chapter 5 derives the proposed Doppler compensator with resampling as a first-stage Doppler compensator. The chapter then goes into detail on the second stage of compensation, namely residual Doppler compensation, where the use of the proposed Doppler estimator is motivated as a valid way to estimate the residual Doppler shift. A Doppler tracking approach which reduces the size of the Mach number estimates, while simultaneously tracking the variations of the Mach number, is also presented.

Chapter 6 describes the at-sea validation of the novel estimator, tracker and compensator. It describes the work-up (short-range) sea trials conducted, detailing the trials matrix, apparatus, procedure, and results. The long-range deep-water trials conducted are then comprehensively analyzed. The at-sea measurements confirm expected behaviours of UWA channels and thus the measurements are shown to be valid. The results validate the proposed receiver and provide new insights into Doppler effect mitigations.

Chapter 7 presents conclusions from the overall thesis as well as future work that could build on the work presented.

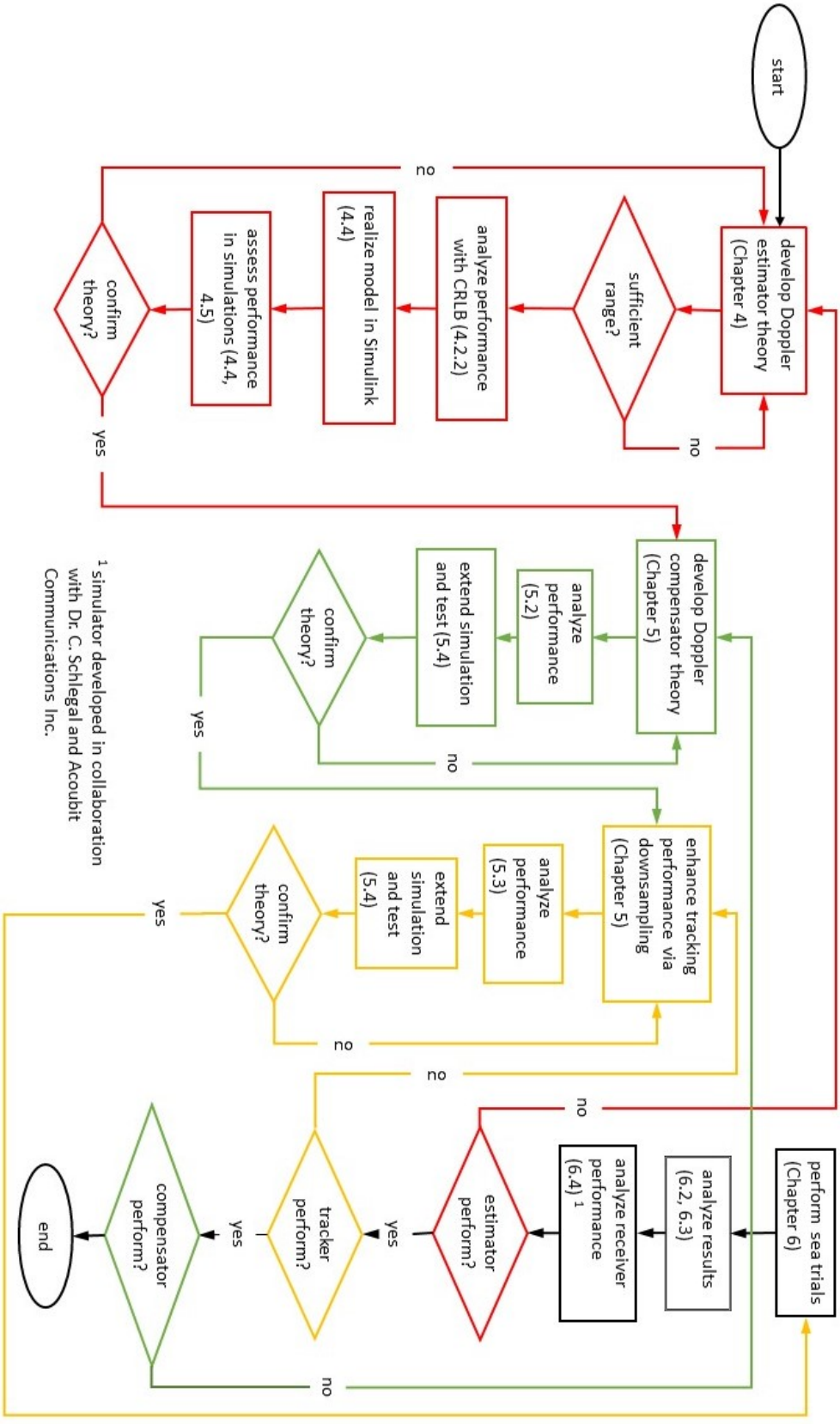

Figure 1.1: Outline of research activities and mapping to thesis chapters. Section numbers are indicated in brackets.

Chapter 2

Background on the UWA Channel

2.1 Introduction

UWA channels are described as linear time-variant (LTV) multipath channels. Multipath propagation is a condition that results in signals reaching a receiver by multiple (two or more) paths. Let the time a signal is observed (received) at the receiver be t and the time for that signal to propagate from the transmitter to the receiver be τ. A time-variant channel (or system) is a channel whose output response changes every time a signal is transmitted. In other words, the impulse response depends on both the time of observation, t, as well as the time the signal is transmitted, $t - \tau$.

In multipath channels, transmitted signals are reflected and scattered, arriving at the receiver along multiple paths. When these paths have similar delays, they add either constructively or destructively, giving rise to fading. When these paths have very different delays, they appear as signal echoes. Due to the relative speed between the transmitter and receiver / scattering object, the channel changes with time. If it is known how the channel modifies the signal, then it is possible to recover the original transmitted signal. Therefore, channel estimation at the receiver is needed, however the dynamic effects of the channel must be removed first via Doppler compensation.

In Chapter 6, the (LTV) UWA channel is assumed to be wide-sense stationary with uncorrelated scattering (WSSUS). A wide-sense stationary channel is a channel whose second-order moments are stationary. The uncorrelated scattering assumption refers to the assumption that the channel scatterers at delay τ are uncorrelated with the scatterers at a different delay τ'. A direct consequence of the WSSUS assumption

is that it allows for the characterization of the UWA channel in terms of scattering functions like delay power profile and Doppler power spectrum.

This chapter presents the background for the thesis work. It starts by introducing OFDM modulation and describing the shift-orthogonal pilot structure for estimation. This is followed by a brief overview of multipath channels as well as a detailed description of the WSSUS model. The UWA channel is then analyzed in detail, including UWA channel physics and signal propagation in UWA channels. Finally, a brief overview of the Cramer-Rao lower bound (CRLB) is presented, which sets the stage for analyzing the performance of the estimator in the next chapter.

2.2 OFDM Theory

Orthogonal Frequency-Division Multiplexing (OFDM) modulation is a specific implementation of multi-carrier modulation. It represents frequency-division signaling with narrowly-spaced as well as mutually orthogonal carriers known as subcarriers. Although the OFDM subcarriers overlap in frequency, they are orthogonal, and their required spectrum is hence narrower compared to conventional frequency-division multiplexing (FDM).

In OFDM modulation, expensive bandpass filters to isolate the carriers are not required as in the case of FDM, but it is prone to crosstalk (the coupling of one carrier into others) in fast fading channels or when timing errors occur [28, p. 696]. The main advantage of OFDM signals is that they can be modulated / demodulated with the fast Fourier transform (FFT). This means that OFDM signals can be generated at the transmitter and processed at the receiver with relatively low complexity compared to other modulation schemes. In fact, the FFT implementation allows one to equalize frequency-selective channels via simple matrix multiplication in the frequency domain. This is the main reason as to why new and emerging signaling standards are adopting OFDM modulation or a variation thereof.

OFDM suffers from two main disadvantages. First, the time variations of the channel may cause frequency shifts in the signal's spectrum that would destroy the orthogonality of the subcarriers, thereby causing inter-carrier interference (ICI). Second, OFDM signals have high peak-to-average power ratio (PAPR) due to the noise-like statistics of the time-domain signal. This however is usually not an issue, since amplifiers nowadays are advanced enough to bypass this problem in one way or another. For example, in 5G cellular standards, both the uplink and downlink signaling formats use an OFDM variant specifically designed to reduce the peak-to-average power ratio, which in turn enables the use of cheaper amplifiers in handsets.

For PSK constellations, symbols are transmitted at equal energies. Thus for PSK the ideal PAPR (where other effects such as filtering are ignored) is 1 on the baseband and 2 on the passband. When PSK mapping is used for N-point OFDM signals, the ideal PAPR becomes N on the baseband and $2N$ on the passband. QAM constellations generally have higher PAPR than PSK, and it can be shown that when large frames are transmitted, the single-carrier PAPR converges to the value $3(\sqrt{C}-1)/(\sqrt{C}+1)$, where C is the modulation order [42]. It then follows that PSK is a better mapping scheme than QAM if one wants to transmit OFDM at lower PAPR. Furthermore, in channels such as UWA channels, the BER of the communicaton system is a major concern. Since BPSK and QPSK have the best bit error rate performance when compared to higher-order PSK mappings, and because QPSK offers twice the bit rate of BPSK, QPSK-OFDM is used throughout this work.

OFDM works as follows: in baseband, the total bandwidth W is divided into N subcarriers, so that each subcarrier has frequency f_k given by

$$f_k = k(W/N) \tag{2.1}$$

where $k \in [0, N-1]$. The spacing between subcarriers is given by

$$\Delta f = f_{k+1} - f_k. \tag{2.2}$$

The symbol rate is hence

$$r = 1/T = \Delta f = W/N \tag{2.3}$$

where T is the symbol duration. Here $W = 1/T_s$ where T_s is the single-carrier symbol time, which by the Nyquist-Shannon sampling theorem is equal to the sample time. Thus $T = NT_s$, and $f_k = k/T$.

OFDM modulation thus generates N mutually orthogonal signals, i.e. the inner product of any two OFDM signals with different subcarriers is 0:

$$\int_0^T e^{j2\pi f_l t} e^{-j2\pi f_m t} dt = 0 \quad \text{where } l \neq m$$

The orthogonality of the modulated subcarriers means that N symbols can be transmitted and decoded independently under ideal transmission conditions. That is, instead of serially transmitting N symbols at the sample rate $r_s = 1/T_s = N/T = W$ (as in a time-domain system), each of the N symbols can be transmitted over its corresponding subcarrier frequencyf_k in parallel at the symbol rate of $r = r_s/N$.

The complex lowpass signal generated at the output of an analog OFDM transmitter is thus given by

$$x(t) = \frac{1}{\sqrt{N}} \sum_{k=0}^{N-1} X[k] e^{j2\pi f_k t} = \frac{1}{\sqrt{N}} \sum_{k=0}^{N-1} X[k] e^{j2\pi kt/T}, \qquad 0 \leq t \leq T \tag{2.4}$$

where $X[k]$ is the kth constellation point (PSK QAM, etc.), and the constant $1/\sqrt{N}$ normalizes the expression. Generally, the constellation points, and by extension

OFDM blocks, vary with time, i.e. they are given by $X_k(t)$ instead of $X[k]$, but the notation $X[k]$ was chosen for simplicity without substantial loss of generality. Although the OFDM signal is time-limited, it is also approximately band-limited, since $X[k]$ is approximately zero outside $k \in [0, N-1]$. Using the fact that $f_k = k/T = k(W/N)$ and sampling $x(t)$ at times $t = nT_s$ yields the discrete-time samples

$$x[n] = \frac{1}{\sqrt{N}} \sum_{k=0}^{N-1} X[k] e^{j2\pi k(W/N)nT_s}$$

Since $T_s = 1/W$, $x[n]$ becomes

$$x[n] = \frac{1}{\sqrt{N}} \sum_{k=0}^{N-1} X[k] e^{j2\pi kn/N}, \qquad 0 \leq n \leq N-1 \tag{2.5}$$

which is the complex lowpass discrete-time sequence.

One can observe that $x[n]$ is related to $X[k]$ via the inverse discrete Fourier transform, i.e., $x[n] = \text{IDFT}\{X[k]\}$ (see Eq. (C.4)). Therefore, rather than working with an analog transmitter, a digital transmitter can be used where, after generating $X[k]$ via PSK, QAM, etc., the transmitter performs an IDFT on the sequence, followed by an interpolation filter. The IDFT can be implemented with an IFFT processor. This makes OFDM systems more efficient computationally and economically.

The interpolation filter is used to oversample the discrete-time sequence. A strictly bandlimiting interpolation filter uses $\text{sinc}(x) = \sin(\pi x)/(\pi x)$, as known from the Nyquist-Shannon sampling theorem:

$$x(t) = \sum_{n=0}^{N-1} x[n] \text{sinc}(W(t - n/W)).$$

However, the sinc pulse has significant pre- and post-cursors and can easily generate intersymbol interference (ISI) unless guard intervals are used. It is also difficult to accurately generate due to its infinite duration in time and its brickwall nature

in frequency. Furthermore, the step response of the sinc filter experiences the Gibbs phenomenon, which gives rise to ringing artifacts (undesired oscillations) and possibly clipping due to the overshoots and undershoots of these oscillations. Thus sinc filters are not used much in practice. A filter $g(t)$ like a root-raised-cosine filter with a small-enough roll-off factor, or other appropriate low-pass transmit filters, is used to avoid excessive temporal sidelobes. Thus

$$x(t) = \sum_{n=0}^{N-1} x[n]g(t - nT_s) = \sum_{n=0}^{N-1} x[n]g(t - nT/N) \tag{2.6}$$

After interpolation the lowpass signal can be upconverted to a real, bandpass signal. The bandpass OFDM signal $s(t)$ is generated from the complex equivalent lowpass signal $x(t)$ as

$$s(t) = \mathrm{Re}\{x(t)e^{j2\pi f_c t}\} = x_i(t)\cos 2\pi f_c t - x_q(t)\sin 2\pi f_c t \tag{2.7}$$

where the real and imaginary components, $x_i(t)$ and $x_q(t)$, are the in-phase and quadrature components of $x(t)$ respectively and f_c is the carrier frequency of the upconverter. After transmitting the signal through the channel, the received signal is downconverted first before passing through the root-raised-cosine filter at the receiver.

Assume that signals are transmitted on the baseband. Let the signal received be $y(t)$ and the AWGN be $n(t)$. $y(t)$ passes through the receive filter $g^*(-t)$, the filter matched to $g(t)$, where it is sampled. In AWGN channels, the matched filtering process results in the following expression for the received symbols:

$$y(t) = \sum_{n=0}^{N-1} x[n]q(t - nT/N) + z(t) \tag{2.8}$$

where $q(t) = g(t) * g^*(-t)$ and $z(t) = n(t) * g^*(-t)$. $q(t)$ satisfies the Nyquist ISI

criterion. That is,

$$q(nT) = \begin{cases} 1, & \text{if } n = 0, \\ 0, & \text{if } n \neq 0. \end{cases}$$

This ensures no ISI at the receiver. Therefore $y(t) = x(t) + z(t)$ and the sample values $y[n]$ obtained at the receiver are given as

$$y[n] = x[n] + z[n]$$

The FFT of $y[n]$ can now be directly computed to retrieve $X[k]$.

For multipath channels, inter-carrier interference (ICI) also needs to be eliminated. This is accomplished by appending a cyclic prefix (CP), which is a copy of the last L samples of $x[n]$, to the beginning of $x[n]$. This is done digitally prior to interpolation and transmission. In slow fading channels, given that the CP duration exceeds the duration of the channel's impulse response (CIR), this allows the receiver to interpret the linear convolution of $x(t)$ with the CIR as a circular convolution. This is the main advantage of the CP. As a result, the received signal can be directly passed to an FFT processor, after which a channel equalizer can be used to extract the constellation points $X[k]$ from the received signal. In fast fading channels, Doppler compensation is required first before FFT processing and channel estimation, which in turn requires Doppler estimation.

To estimate the channel and its dynamics (Doppler and channel estimation) a training sequence is transmitted prior to data transmission, which can be a repetition of pilot bursts (also called preambles). In this case, adding a CP is not necessary because a pilot preamble is repeated N_{pre} times, where N_{pre} is the number of preambles. The duration of each burst should be equal or exceed the CIR duration in order to avoid ISI in channel estimates.

Assume transmission occurs in the baseband over slow fading channels, and let the impulse response of the lowpass slow fading channel be $h(t)$ (time variations are very small). Then

$$y(t) = h(t) * x(t) + n(t) \tag{2.9}$$

After filtering, downsampling and CP removal (in case of non-repeated or data transmissions), the received sequence is given by

$$y[n] = h[n] * x[n] + z[n] \tag{2.10}$$

where $h[n]$ is the discrete-time equivalent of $h(t)$ that results from the downsampling process. $h[n]$ can be modelled with a tapped delay line model. If CP was added, the length of the received sequence becomes N after CP removal. Furthermore, the linear convolution becomes equivalent to circular convolution. By the circular convolution theorem (Eq.(C.9)):

$$Y[k] = H[k]X[k] + Z[k] \quad \text{where } 0 \leq k \leq N-1.$$

Here $H[k] = DFT\{h[n]\}$.

To compensate for the channel distortion and recover $X[k]$, in general, an equalizer or filter is required whose frequency response is the reciprocal of the channel's frequency response $H[k]$. Typically this filter is introduced at the output of the FFT, which effectively results in scaling the values $\{Y[k]\}$ by $H[k]$. Therefore the output of the filter, disregarding noise, equals $X[k]$ and is free of channel frequency gain distortion. With noise, the filter outputs will be noisy estimates of $X[k]$, which are noisy constellation points of the transmitted signals. Now the data signal can be demapped back into the discrete-time information sequence $x[n]$. This allows retrieving the data.

Again, if transmission is performed on fast fading channels, Doppler compensation is required prior to the receiver processing discussed above.

2.3 Shift-Orthogonal Pilot Sequences

When the transmitter is in relative motion with the receiver there is a need to estimate the impact of the channel's time variations on the transmitted signal due to Doppler shifts and spreading. Many approaches have been studied for channel and Doppler estimation applied to narrowband wireless communication systems. Usually, it is assumed that some part of the transmitted signal is known at the receiver. The transmitter can provide a training sequence or periodic pilot symbols, known to the receiver, and used for channel estimation. It should be noted that the discrete-time and discrete-frequency shifts in this work are circular shifts.

A particular piloting comb structure [1] is discussed which guarantees the orthogonality of the transmitted pilots and data, so that the pilot bins are well-defined and do not interfere with the data bins. Start with a random M-periodic sequence of QPSK symbols. This is the frequency-domain (FD) pilot sequence $\{B_M[k]\}$ where $k \in [0, M-1]$ and $|B_M[k]| = 1$. Such a pilot sequence is given by:

$$B_M[k] = \sum_{m=0}^{M-1} a_m \delta[k-m] \tag{2.11}$$

where $\{a_m\}$ are complex random coeffcients of magnitude 1. Note that $B_M[m] = a_m$. The energy (or power) spectrum is shown in Fig. 2.1 for the case of $M = 64$ pilots.

The IDFT gives the time-domain (TD) pilots as

$$b_M[n] = \frac{1}{\sqrt{M}} \sum_{m=0}^{M-1} a_m e^{j2\pi mn/M} \tag{2.12}$$

(see Eq.(C.4) and Eq.(C.7)) where $n \in [0, M-1]$. It can be shown after some

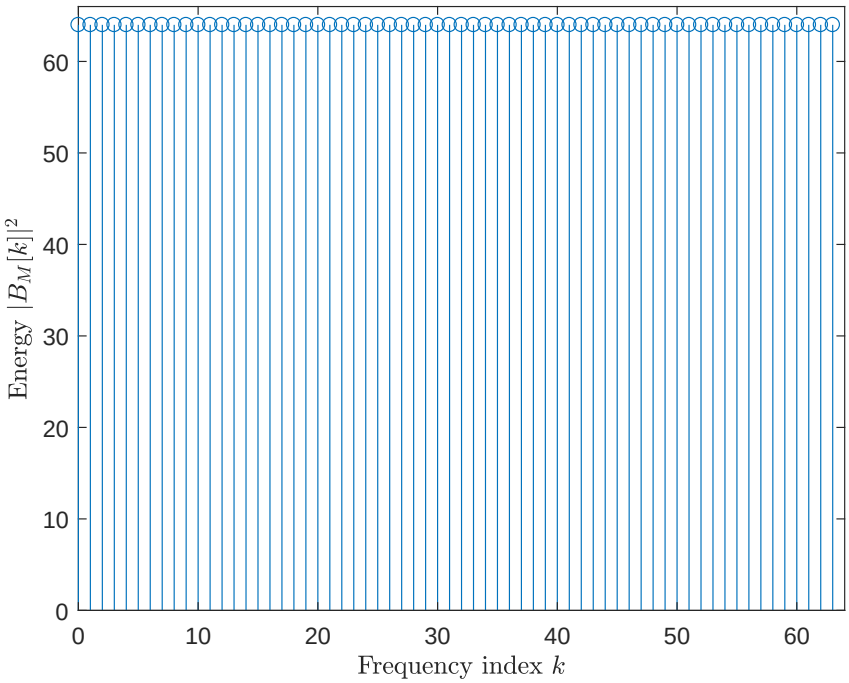

Figure 2.1: Energy spectrum of $B_M[k]$, where $M = 64$.

simplification that this M-point sequence has the property

$$\frac{1}{M}\sum_{n=0}^{M-1} b_M[n]b_M^*[n-n'] = \begin{cases} 1, & n' = 0, \\ 0, & 0 < n' \leq M-1. \end{cases} \tag{2.13}$$

Therefore

$$\frac{1}{M}\sum_{n=0}^{M-1} b_M[n]b_M^*[n-n'] = \delta[n'] \tag{2.14}$$

Fig. 2.2 shows the magnitude of $b_M[n]$. Repeating $b_M[n]$ N_{pre} times yields the N-point TD pilots $b_N[n]$ given by

$$b_N[n] = \sum_{r=0}^{N_{\text{pre}}-1} b_M[n - rM] \tag{2.15}$$

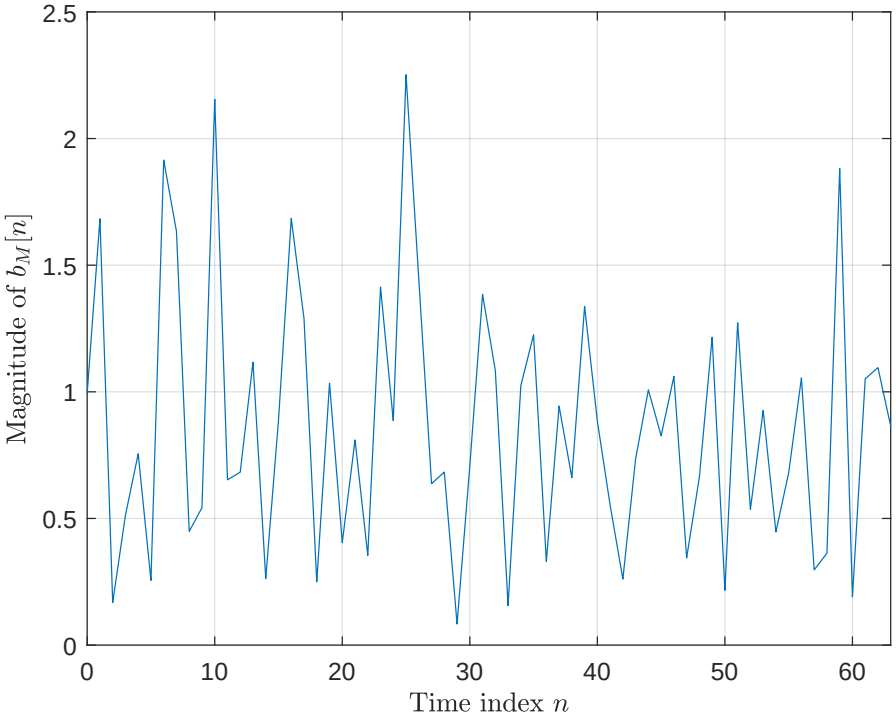

Figure 2.2: Plot of the TD sequence $|b_M[n]|$, where $M = 64$.

where $N = N_{\text{pre}}M$ and $n \in [0, N-1]$. Here we redefined $b_M[n]$ to be

$$b_M[n] = \begin{cases} \frac{1}{\sqrt{M}} \sum_{m=0}^{M-1} a_m e^{j2\pi mn/M}, & \text{if } 0 \leq n \leq M-1, \\ 0, & \text{if } n \geq M. \end{cases} \tag{2.16}$$

M is conveniently chosen as a power of two; for most of the applications here, $M = 64$. Fig. 2.3 shows both the magnitude of the TD sequence and the energy spectrum of $b_N[n]$, where $M = 64$ and the number of preamble repetitions is $N_{\text{pre}} = 16$. The effect of TD repetitions in the FD pilots is clear; repeating the TD sequence N_{pre} times results in interpolating the FD sequence with an upsampling rate of N_{pre} by padding $N_{\text{pre}} - 1$ zeros after every FD sample.

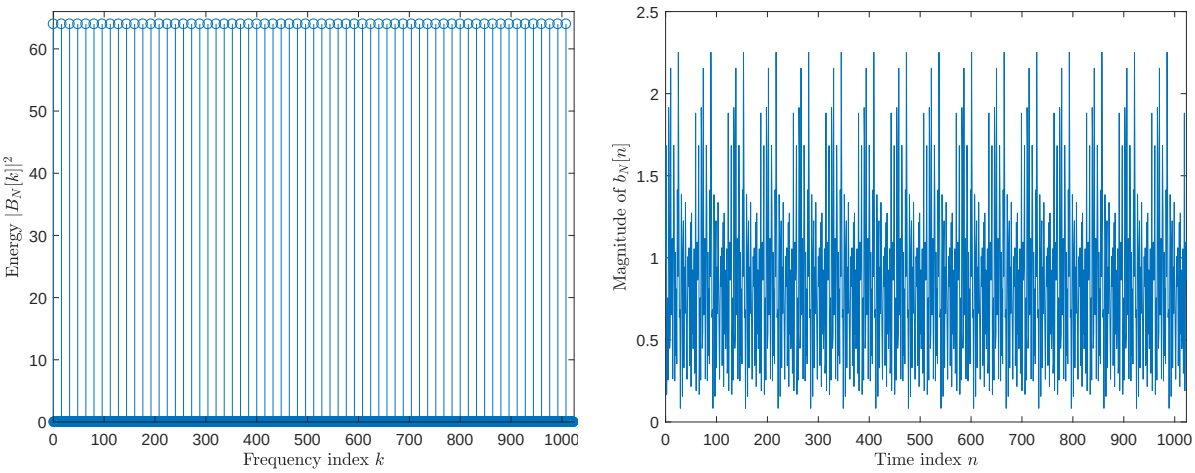

Figure 2.3: Energy spectrum and the corresponding TD signal plot of $b_N[n]$, where $M = 64$ and $N_{\text{pre}} = 16$.

2.3.1 Transmission

The sequence $b_N[n]$ is then passed through a root-raised cosine transmit filter of sampling period of T_s. The next part of the analysis can be in either discrete- or continuous-time. The continuous-time approach is developed next.

Using the Nyquist-Shannon sampling theorem the continuous-time equivalent of $b_N[n]$ can be written as:

$$b(t) = \frac{1}{\sqrt{M}} \sum_{m=0}^{M-1} a_m e^{j2\pi f_m t} \tag{2.17}$$

where $f_m = mN_{\text{pre}}/T$ is the m-th subcarrier frequency in the baseband, and $T = NT_s$ where $t \in [0, T]$. In terms of the transmit filter $p(t)$, $b(t)$ is given by:

$$b(t) = \sum_{n=0}^{N-1} b_N[n] p(t - nT_s). \tag{2.18}$$

Mathematically, the two expressions for $b(t)$ are shown to be the same as if a sinc filter is applied.

This is the end of the transmission chain. The correlation properties of the selected pilot structure are presented in the next section.

2.3.2 Autocorrelation Properties

The circular cross-correlation of two N-point discrete-time signals f and g is defined as

$$R_{fg}[n] = f[n] \star g[n] = \sum_{l=0}^{N-1} f^*[l-n]g[l]. \tag{2.19}$$

(the shift $l-n$ is assumed circular and is modulo N, which is a circular shift with window of size N). When $f = g$, the result is the autocorrelation of f, given by $R_f[n]$. Note mathematically, the circular cross-correlation and circular convolution are related as follows:

$$f[n] \star g[n] = f^*[-n] \circledast g[n]. \tag{2.20}$$

Using DFT properties (Eq.(C.8)), the DFT of the cross-correlation function is:

$$R_{fg}[k] = F^*[k]G[k]. \tag{2.21}$$

When $f = g$, the result is $R_f[k] = |F[k]|^2$. The autocorrelation of $b_M[n]$ can be computed from Eq.(2.19) using the definition in Eq.(2.12). Alternatively, using DFT properties, use Eq.(2.21) and Eq.(2.11). Using the second approach:

$$R_b[k] = \frac{1}{M} \sum_{m=0}^{M-1} \sum_{m'=0}^{M-1} a_m a_m^* \delta[k-m]\delta[k-m']. \tag{2.22}$$

Recall that the shift-orthogonal pilot sequence has the property $a_m a_m^* = 1$. Since $\delta[k-m]\delta[k-m'] = \delta[m-m']$, after simplification:

$$R_b[k] = 1. \tag{2.23}$$

The IDFT is hence simply given by

$$R_b[n] = \delta[n]. \tag{2.24}$$

Therefore the autocorrelation of the shift-orthogonal pilot sequence is simply the Kronecker delta function. This pilot structure is referred to as "shift-orthogonal" due to this autocorrelation property. The cross-correlation of $b_M[n]$ with $b_N[n]$ can be found with the same approach. Let the cross-correlation function be given by $R_{bb}[n]$. Using Eq.(2.15), Eq.(2.12) and Eq.(2.21), the DFT is computed as:

$$R_{bb}[k] = \sum_{r=0}^{N_{\text{pre}}-1} e^{-j2\pi r/N_{\text{pre}}} \cdot B_M[k] \cdot B_M^*[k] = \sum_{r=0}^{N_{\text{pre}}-1} e^{-j2\pi r/N_{\text{pre}}} \cdot R_b[k] = \sum_{r=0}^{N_{\text{pre}}-1} e^{-j2\pi r/N_{\text{pre}}}. \tag{2.25}$$

The IDFT yields the cross-correlation function

$$R_{bb}[n] = \sum_{r=0}^{N_{\text{pre}}-1} \delta[n - rM] \tag{2.26}$$

where the fact that $M = N/N_{\text{pre}}$ has been used. The cross-correlation of $b_M[n]$ with $b_N[n]$ is found to just be N_{pre} repetitions of the autocorrelation of $b_M[n]$, where the distance between each repetition is M. Fig. 2.4 shows the cross-correlation for $M = 64$ and $N_{\text{pre}} = 16$.

With the pilot structure described a brief overview of the multipath channels that the pilot structure is meant to characterize is discussed next.

2.4 Multipath Channels as Linear Time-Variant (LTV) Systems

Let $s(t)$ be a bandpass signal transmitted through a linear time-varying channel of bandpass impulse response, $c(t, \tau)$, with observation time, t, and propagation delay,

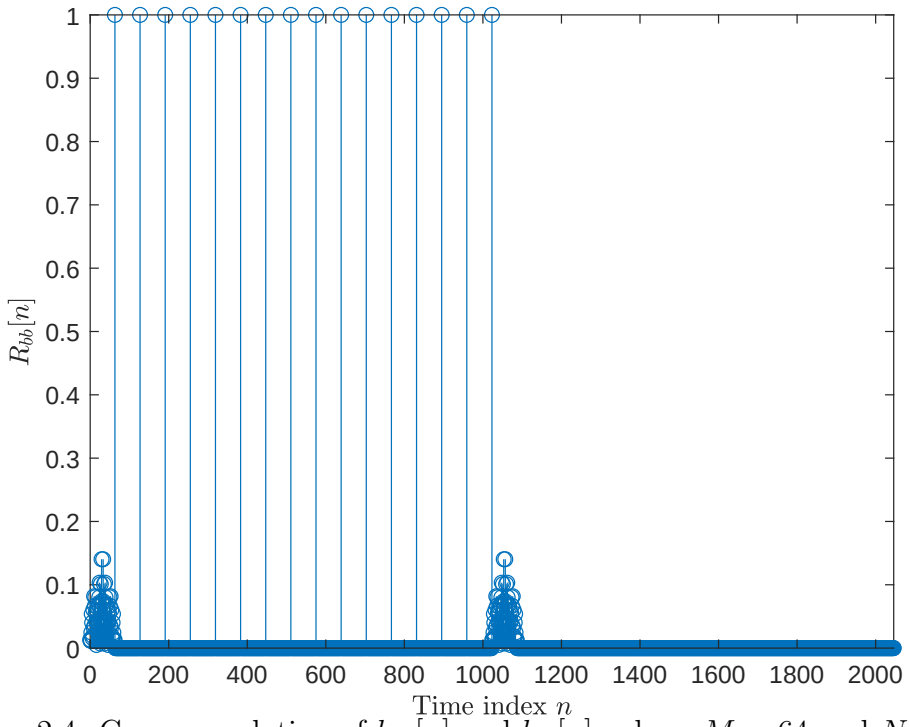

Figure 2.4: Cross-correlation of $b_M[n]$ and $b_N[n]$, where $M = 64$ and $N_{\text{pre}} = 16$.

τ. The channel output $r(t)$ is then given by:

$$r(t) = s(t) * c(t, \tau) + n(t) \tag{2.27}$$

where $n(t)$ is additive noise.

In a time-varying multipath channel, a transmitted impulse is received as a train of impulses due to dispersion (or spreading) in time. Due to time variations in the channel, a different impulse train is received for every transmitted impulse [31, p. 831]. Therefore, the path delay and attenuation factor are time-varying, with the number of impulses received differing each time. Taking all this into account, the received signal $r(t)$ can be written as:

$$r(t) = \sum_{p} c_p(t) s(t - \tau_p(t)) + n(t) \tag{2.28}$$

where p is the path delay index and $c_p(t)$ is the attenuation factor. In UWA channels, the attenuation factor is also frequency-dependent (see section 2.6) . It follows that the time-varying multipath channel, as a bandpass impulse response, is given by:

$$c(t,\tau) = \sum_p c_p(t)\delta(\tau - \tau_p(t)). \tag{2.29}$$

The impulse response $c(t,\tau)$ is the response of an impulse at time τ received at time t (transmission occurs at time $t-\tau$).

Since

$$s(t) = \mathrm{Re}\{x(t)e^{j2\pi f_c t}\} \tag{2.30}$$

where $x(t)$ is the lowpass equivalent of $s(t)$, $r(t)$ can be written as:

$$r(t) = \mathrm{Re}\left\{\sum_p c_p(t)x(t-\tau_p(t))e^{j2\pi f_c[t-\tau_p(t)]}\right\} + n(t).$$

Denoting the lowpass equivalent of $r(t)$ as $y(t)$, $y(t)$ can be given by:

$$y(t) = \sum_p c_p(t)e^{j\theta_p(t)}x(t-\tau_p(t)) + \tilde{n}(t). \tag{2.31}$$

Here, $\theta_p(t) = -2\pi f_c\tau_p(t)$ and $\tilde{n}(t)$ is the lowpass equivalent of $n(t)$. It follows that the lowpass impulse response is given by

$$h(t,\tau) = \sum_p h_p(t)\delta(\tau - \tau_p(t)) \tag{2.32}$$

where $h_p(t) = c_p(t)e^{j\theta_p(t)}$.

The attenuation factor $h_p(t)$ varies significantly with time only if there are large dynamic variations in the channel. If $\tau_p(t)$ changes by $1/f_c$, $\theta_p(t)$ changes by 2π radians, and since f_c is usually large compared to $1/\tau_p(t)$, this means even small

changes in $\tau_p(t)$ can cause $\theta_p(t)$ to vary rapidly (note that changes in $\tau_p(t)$ vary with path). Fading is a result of the random time variations experienced by $\theta_p(t)$, which can cause constructive or destructive interference of the quantities $\{h_p(t)e^{j\theta_p(t)}\}$. Destructive interference causes signals to "fade" out [31, p. 833] and constructive interference causes signal amplification.

A mathematical description of the multipath channels determines the channel propagation as impacted by its spatial variability. It is now appropriate to introduce the wide-sense stationary uncorrelated scattering (WSSUS) assumption which provides a simplified statistical model to capture the UWA channel's variability. The WSSUS assumption will prove useful in Chapter 6.

2.5 Statistical Description of the Channel: The WSSUS Assumption

WSSUS provides a framework to characterize the UWA channel with scattering functions like the Doppler power spectral density which is relevant for the thesis work. Generally, not all UWA channels can be modelled as WSSUS, and so it is not used too liberally in this work; it is used only to derive the Doppler power spectrum of the channels in Chapter 6. However, over short durations the WSS assumption can be satisfied, and over a limited frequency range the US approximation is satisfied. Following this rationale, the preambles used are of relatively short duration compared to the observation time. In this section the WSSUS approximation is applied to lowpass multipath channels.

Let $h(t, \tau)$ be a complex-valued random process at time t. The wide-sense stationary (WSS) assumption stipulates the second-order moments of a system are stationary. Mathematically, this can be expressed as:

$$\mathrm{E}\left[h(t,\tau)\right] = m_h(\tau) \tag{2.33}$$

$$R_h(t_1,t_2,\tau_1,\tau_2) = R_h(t_2-t_1,\tau_1,\tau_2) = R_h(\Delta t,\tau_1,\tau_2) \tag{2.34}$$

where $m_h(\tau)$ is the mean, or expected value, of $h(t,\tau)$, $R_h(t_1,t_2,\tau_1,\tau_2)$ is its autocorrelation function, and $\Delta t = t_2 - t_1$. Hence, the autocorrelation function under the WSS assumption with zero mean becomes:

$$R_h(\Delta t,\tau_1,\tau_2) = \mathrm{E}\left[h^*(t,\tau_1)h(t+\Delta t,\tau_2)\right]. \tag{2.35}$$

Uncorrelated scattering means $h_p(t)$ and $\theta_p(t)$ for path p are uncorrelated with those for path p' ($p \neq p'$), that is, the attenuation and phase shift at path delay τ_p are uncorrelated with those at $\tau_{p'}$. Therefore, for uncorrelated scattering of paths 1 and 2:

$$R_h(\Delta t,\tau_1,\tau_2) = R_h(\Delta t,\tau)\delta(\tau_2-\tau_1) \tag{2.36}$$

where τ can be τ_1 or τ_2.

The assumption of wide-sense stationarity (WSS) and uncorrelated scattering (US) is collectively called WSSUS. This assumption was applied for the channel analysis in Chapter 6; the justification will be explained in the next section. The WSSUS assumption makes it possible to cleanly extract channel scattering functions like the delay and Doppler power spectra. Integrating over Δt gives the delay power spectrum (or multipath intensity profile), $R_h(\tau)$, which is the average power output of the channel as a function of path delay. The duration τ for which $R_h(\tau) \neq 0$ is the delay or multipath spread, denoted by T_{m}. A more practical definition of delay spread is the square root of the second central moment of the normalized delay power spectrum - this is known as the rms delay spread.

Alternatively, the channel can be characterized in the frequency domain. Let $H(t, f)$ be the one-dimensional Fourier transform of $h(t, \tau)$. Since a WSS channel is assumed, it can be shown, using Fourier transform properties, that:

$$R_H(\Delta t, f_1, f_2) = \mathrm{E}\left[H^*(t, f_1)H(t + \Delta t, f_2)\right] \tag{2.37}$$

since $R_H(\Delta t, f_1, f_2)$ is the two-dimensional Fourier transform of $R_h(\Delta t, -\tau_1, \tau_2)$. Using the uncorrelated scattering assumption in Eq.(2.36), it is found, via Fourier transform properties, that

$$R_H(\Delta t, f_1, f_2) = R_H(\Delta t, \Delta f) \tag{2.38}$$

where $\Delta f = f_2 - f_1$ is the frequency spacing. Therefore, the uncorrelated scattering assumption in τ in the time domain is equivalent to the WSS assumption in f in the frequency domain.

As well, $R_H(\Delta t, \Delta f)$ is the one-dimensional Fourier transform of the delay power spectrum $R_h(t, \tau_1)$ from the τ_1 time domain to the Δf frequency domain. $R_H(\Delta t, \Delta f)$ is the spaced-frequency, spaced-time correlation function of the channel. If $\Delta t = 0$, $R_H(\Delta t, \Delta f)$ becomes the spaced-frequency correlation function, $R_H(\Delta f)$.

The domain length of Δf for which $R_H(\Delta f) \neq 0$ is the coherence bandwidth. The coherence bandwidth is denoted by B_{coh}. B_{coh} is approximately the inverse of the delay spread, i.e. $B_{\mathrm{coh}} \approx 1/T_{\mathrm{m}}$. Recall that T is the signal duration and let W be the signal bandwidth. A channel where $T_{\mathrm{m}} > T$ (or $B_{\mathrm{coh}} < W$) is said to be frequency-selective (or wideband), where the propagating signal is significantly distorted by the channel. A channel where $T_{\mathrm{m}} \ll T$ or $B_{\mathrm{coh}} \gg W$ is frequency-nonselective (or flat or narrowband).

In UWA communications, multipath in the channel causes large delay spreads, which disperses the waveform in time, and results in severe ISI. In shallow water environments, delay spread is typically $\approx O(10 \text{ ms})$, though there are scenarios where

it can be as large as 100 ms. In deep water environments, delay spread is $\approx O(\text{s})$ [38]. Thus UWA channels are generally frequency-selective.

It is also important to analyze the channel's time variations due to Doppler broadening and Doppler shifting of the signal to arrive at their scattering functions. The Doppler effects are characterized by the scattering functions $S_H(\nu, \Delta f)$ and $S_h(\nu, \tau)$, which are the 1-D Fourier transforms of $R_H(\Delta t, \Delta f)$ and $R_h(\Delta t, \tau)$ in the Δt domain, respectively.

Integrating over Δf yields the channel's Doppler power spectrum $S_H(\nu)$, which is the average power output of the channel as a function of Doppler frequency. The domain length, ν, for which $S_H(\nu) = 0$ is the Doppler spread (or Doppler broadening). The Doppler spread is denoted by B_d. A more practical definition of Doppler spread is the square root of the second central moment of the normalized Doppler power spectrum - this is known as the rms Doppler spread. Note that $S_H(\nu) = S_h(\nu)$. Integrating $S_h(\nu, \tau)$ over τ gives the Doppler power spectrum of the channel.

The duration of Δt for which $R_H(\Delta t) \neq 0$ is the coherence time, denoted T_coh, which is approximately the inverse of the Doppler spread, i.e. $T_\text{coh} \approx 1/B_\text{d}$. A channel where $B_\text{d} > W$ or $T_\text{coh} < T$ is referred to as fast fading (or time-selective), where the signal experiences severe Doppler effect due to rapid time variations during transmission. A channel where $B_\text{d} \ll W$ or $T_\text{coh} \gg T$ is referred to as slow fading.

In UWA communications, large Doppler shifts and spreads can easily occur from the relatively low speed of sound, which causes the waveform to disperse in frequency, resulting in severe ICI [38]. This makes UWA channels dynamic, so they are classified as fast fading channels.

As shown above, the uncorrelated assumption in τ is equivalent to assuming a WSS process in frequency. It is possible to find another equivalence relationship from this (along with Fourier transform properties). Let the 4-D Fourier transform of $R_h(t_1, t_2, \tau_1, \tau_2)$ be $S_H(\nu_1, \nu_2, f_1, f_2)$. Using Fourier transform properties and applying

the WSSUS assumption yields:

$$S_H(\nu_1, \nu_2, \Delta f) = S_H(\nu, \Delta f)\delta(\nu_2 - \nu_1) \tag{2.39}$$

where ν equals ν_1 or ν_2. This shows that a WSS process in time is equivalent to uncorrelated scattering in ν. The WSSUS assumption and the Fourier transform relationship between $S_H(\nu_1, \nu_2, \tau_1, \tau_2)$ and $R_h(t_1, t_2, \tau_1, \tau_2)$ can be used to arrive at the relationship:

$$S_H(\nu_1, \nu_2, \tau_1, \tau_2) = S_H(\nu_1, \nu_2, \tau)\delta(\tau_2 - \tau_1) = S_H(\nu, \tau)\delta(\nu_2 - \nu_1)\delta(\tau_2 - \tau_1). \tag{2.40}$$

Eq.(2.38) shows that WSSUS assumes a WSS process in both t and f while Eq.(2.40) shows that the WSSUS assumption only assumes unccorrelated scattering in both ν and τ.

So far justification for the WSSUS assumption is not presented. Furthermore, while the WSSUS assumption simplifies the statistical model of the UWA channel, it also impacts system performance. The next section addresses both of these crucial points.

2.5.1 Impact of the WSSUS Assumption on System Performance

The assumption of a WSSUS channel simplifies the mathematical model of the channel, however, the WSS assumption does not hold for long-term fading since the environment itself changes. The assumption holds approximately for short-term fading, which is of primary interest in the communication channel's performance. This means that, over short periods, it is assumed the environment does not change rapidly.

If the carrier phase changes rapidly during the symbol time T, it creates challenges. The frequency of the amplitude and phase variations during time t is on the order

of the maximum Doppler frequency, $\nu_{\max}$. The time constant for these variations is given by the correlation time $1/\nu_{\max}$. Thus transmission becomes possible when $T \ll 1/\nu_{\max}$, i.e. when the channel does not exhibit rapid time variations. This condition is usually necessary due to the unpredictable UWA channel dynamics. Furthermore, the correlation time, $1/\nu_{\max}$, must be large enough so there is high correlation between channel samples. This makes it possible to find an approximate expression to relate the variance of the Doppler power spectrum to the autocorrelation function of the channel. This will be shown next.

For channels with small Doppler shifts, the maximum Doppler frequency is a reasonable approximation for B_{d} and thus can be used to classify the channel. Estimation-wise, fast fading channels are quite challenging (sometimes impossible) to deal with, which is expecially the case for OFDM signals. As mentioned earlier, OFDM is the preferred modulation scheme as it is resilient to frequency selectivity. The way to make the estimation achievable is to modify the transmitted signal so the slowly-varying condition, $T \ll 1/\nu_{\max}$, is satisfied. Thus a flexible signal design scheme is the best way to combat fast fading channels.

For example, if a 64-point OFDM signal of bandwidth $W = 10$ kHz is transmitted with a 25-kHz carrier in a channel that introduces a maximum Doppler shift of 2.5 Hz, then $\nu_{\max}T = 0.016$. If the maximum Doppler shift introduced is 25 Hz then $\nu_{\max}T = 0.16$; though this does not mean the channel is fast fading, it does not necessarily mean the channel is slow fading either. If $\nu_{\max} = 250$ Hz then $\nu_{\max}T = 1.6$ and the channel is a fast fading channel. In such a situation one might consider a 16- or even an 8-point signal over a 64-point signal for transmission.

As mentioned earlier, the WSS assumption holds for small-scale analysis (short time durations) and thus one only needs to consider $R_h(t)$ for $t \ll 1/\nu_{\max}$. The Taylor

series for the autocorrelation function is:

$$R_h(t) = \sum_{n=0}^{\infty} \frac{1}{n!} t^n \frac{d^n}{dt^n} R_h(t)|_{t=0}. \tag{2.41}$$

Knowing that $R_h(t)$ is the inverse Fourier transform of $S_h(\nu)$, it is found that:

$$\frac{d^n}{dt^n} R_h(t)|_{t=0} = (j2\pi)^n \int_{-\infty}^{\infty} \nu^n S_h(\nu) d\nu. \tag{2.42}$$

The integral is identified as the nth moment of the Doppler power spectrum. Let the integral be given by μ_n. Since the process is zero-mean, $\mu_1 = 0$. Assuming a normalized Doppler power spectrum, $\mu_0 = 1$, and therefore:

$$R_h(t) = 1 - \frac{1}{2}(2\pi t)^2 \mu_2 + \sum_{n=3}^{\infty} \frac{1}{n!} t^n \frac{d^n}{dt^n} R_h(t)|_{t=0}. \tag{2.43}$$

Note that $\mu_n \leq (2\nu_{\max})^n$, and as a result:

$$\left| \sum_{n=3}^{\infty} \frac{1}{n!} t^n \frac{d^n}{dt^n} R_h(t)|_{t=0} \right| \leq \sum_{n=3}^{\infty} \frac{1}{n!} |4\pi\nu_{\max} t|^n. \tag{2.44}$$

Since these terms are very small for $t \ll 1/\nu_{\max}$, the result is:

$$R_h(t) \approx 1 - \frac{1}{2}(2\pi t)^2 \mu_2. \tag{2.45}$$

Therefore, it is concluded that the second moment determines largely the coherence time. Also, the second moment (equivalent to variance for zero-mean processes) of the Doppler power spectrum affects the performance of the digital communication system the most [32].

So far UWA channels have been discussed in the context of general multipath channels and scattering functions under the WSSUS assumption. The next section

delves into the physics of UWA channels, and the characteristics that make UWA channels unique compared to other channels.

2.6 Physics and Characteristics of the UWA Channel

As mentioned earlier, the UWA channel is classified as a linear time-variant channel. However, what differentiates UWA channels from most other communication channels is the frequency dependence of its attenuation factor. Thus transmitted signals in UWA channels experience increasingly severe attenuation with increasing frequency. This means UWA transmissions favour lower carrier frequencies at the cost of less bandwidth. The discussion of UWA channels presented in this chapter is similar to that in [33, 34, 35].

An acoustic wave experiences power reduction as it propagates through underwater environments. This is path loss or transmission loss due to spreading. Spreading loss is the energy loss due to the scattering of waves in a specific geometry and which is range-dependent. Subsequently, path loss is also range-dependent.

The power intensity of radiant energy is defined as acoustic power per unit area:

$$I(R) = \frac{P_A}{A(R)}. \tag{2.46}$$

Here P_A is acoustic power and $A(R)$ is the cross-sectional area, written as a function of range, R. Spreading loss is defined as the ratio of power intensity $I(0)$ at a reference location R_0 to power intensity $I(R)$ at the desired point R. Let the spreading loss in dB be given by $L_s(R)$. Then

$$L_s(R) = 10\log_{10}\left(\frac{R}{R_0}\right)^{\kappa} = \kappa(R_{dB} - R_{0,dB}) \tag{2.47}$$

where $1 \leq \kappa \leq 2$ and $R_{dB} = 10\log_{10}R$. At longer ranges, where the acoustic waves

reach the sea floor (a boundary), cylindrical spreading may be assumed depending on the source depth. For cylindrical spreading, $A(R)$ is proportional to R, which corresponds to the case $\kappa = 1$. At shorter ranges where the acoustic waves do not reach the sea floor, spherical spreading may be a better spreading model. For spherical spreading, $A(R)$ is proportional to R^2, which corresponds to the case $\kappa = 2$. In reality, the spreading geometry can be between cylindrical and spherical due to considerations like refraction, which occurs due to the sound speed dependence on depth. Thus $A(R)$ is proportional to R^κ in general. Since κ represents the spreading geometry, it is called the spreading loss exponent.

With acoustic absorption, a fraction of the acoustic energy is absorbed by the medium then transformed into heat while the rest is transferred through the medium. Absorption also contributes to path loss. Acoustic absorption is largely a function of frequency with some dependency on temperature, depth, salinity and acidity. It is measured in dB/meter. Many empirical models for acoustic absorption under different sea conditions have been proposed ([5, 6, 7, 8]). For frequencies up to about 50 kHz, the absorption coefficient $a(f)$ has a second-order approximation [33]:

$$a(f) \approx \alpha_0 + \alpha_1 f + \alpha_2 f^2. \tag{2.48}$$

Let the absorption loss in dB be given by $L_a(R, f)$. Then,

$$L_a(R, f) = a(f)(R - R_0). \tag{2.49}$$

Therefore, the overall path loss $L(R, f)$ can be written as:

$$L(R, f) = L_s(R) + L_a(R, f) = \kappa(R_{dB} - R_{0,dB}) + a(f)(R - R_0). \tag{2.50}$$

On a linear scale the overall path loss, given by $L(R, f)$, is:

$$L(R, f) = \left(\frac{R}{R_0}\right)^{\kappa} [a(f)]^{R-R_0}. \tag{2.51}$$

Due to path loss, the transmitted signal power in a given subchannel Δf is degraded to $\mathcal{S}(f)/L(R, f)$ where $\mathcal{S}(f)$ is the power spectral density (PSD) of the signal at the transmitter. Noise in UWA channels comes from wave motion, marine life, and anthropogenic sources like seismic exploration, shipping, sonars, etc. [30]. These sources contribute to a broadband background that is referred to as the ambient noise. The ambient noise is not white, so it is modelled as a colored Gaussian random process. If the noise power is $N(f)$, the range and frequency-dependent SNR under path loss is:

$$SNR(R, f) = \frac{\mathcal{S}(f)}{L(R, f)N(f)}. \tag{2.52}$$

Since $\mathcal{S}(f)$ is user-specified prior to transmission, variations in SNR arise from the term $1/[L(R, f)N(f)]$, so bandwidth will depend on transmission range, indicating that the SNR decreases with increasing range. Therefore bandwidth-efficient modulation schemes are important to achieve spectral efficiency greater than 1 bps/Hz [33].

To achieve a given SNR, the bandwidth and power required as a function of range can, respectively, be modelled by [34]:

$$W(R) = wR^{-\beta} \qquad \text{where} \quad \beta = 0, 1 \tag{2.53}$$

$$P_A(R) = pR^{\psi} \qquad \text{where} \quad \psi \geq 1 \tag{2.54}$$

where $\beta = 0$ if there is no path loss. It is important to note that since the channel's bandwidth is on the order of its carrier or center frequency, which is usually small, UWA channels are intrinsically wideband (i.e. frequency-selective).

Reflection and refraction of acoustic waves result in multipath. Refraction occurs due to the dependence of sound velocity profile with depth, which is significant in deep water, while reflections occur at the water surface and sea bottom, and from targets in the water column. Fig. 2.5 shows this [36, p. 2]. Let the total reflection

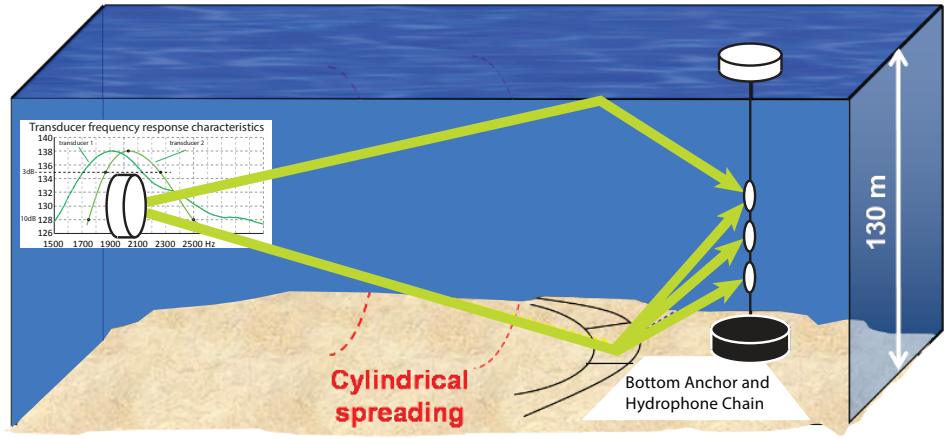

Figure 2.5: Multipath propagation in underwater environments.

coefficient for path p be given by Γ_p. Under ideal conditions, the reflection coefficient at the sea surface is -1, but the reflection coefficient at the sea bottom depends on the bottom cover and the wave's incident angle on it. The reflection coefficient yields the channel's attenuation factor, but the path loss should also be accounted for. The frequency-dependent attenuation factor is therefore given by [33]:

$$C_p(t,f) = \frac{\Gamma_p}{\sqrt{L(R_p(t),f)}}. \tag{2.55}$$

Thus each path is modelled as a lowpass filter, with a different dispersion for each path. Due to Doppler effects $R_p = R_p(t)$.

Given that each path has a time-varying delay, $\tau_p(t)$, the Fourier transform, $C(t,f)$, of the channel's bandpass impulse response is:

$$C(t,f) = \sum_p C_p(t,f)e^{-j2\pi f\tau_p(t)}. \tag{2.56}$$

Hence, when mapped back to the time domain, the bandpass impulse response of the channel becomes $c(t,\tau)$, and is given by

$$c(t,\tau) = \sum_p c_p(t, \tau - \tau_p(t)) \tag{2.57}$$

where $c_p(t,\tau)$ is the inverse Fourier transform of $C_p(t,f)$. The transmitted bandpass signal is given by $s(t) = \mathrm{Re}\{x(t)e^{j2\pi f_c t}\}$. Therefore, the received bandpass signal is: $r(t) = s(t) * c(t,\tau) + n(t)$. The received lowpass signal is $y(t) = x(t) * h(t,\tau) + \tilde{n}(t)$, where

$$H(t,f) = \sum_p C_p(t,f) e^{j\theta_p(t)} e^{-j2\pi f \tau_p(t)} \tag{2.58}$$

and $\theta_p(t) = -2\pi f_c \tau_p(t)$. Letting $H_p(t,f) = C_p(t,f)e^{j\theta_p(t)}$, the equivalent lowpass response can thus be written as

$$h(t,\tau) = \sum_p h_p(t, \tau - \tau_p(t)) \tag{2.59}$$

where $h_p(t,\tau) = c_p(t,\tau)e^{j\theta_p(t)}$.

The multipath model discussed in Section 2.4 is given by

$$c(t,\tau) = \sum_p c_p(t)\delta(\tau - \tau_p(t))$$

$$h(t,\tau) = \sum_p h_p(t)\delta(\tau - \tau_p(t)).$$

It is of interest sometimes to simplify the acoustic model to the form shown above. In OFDM this assumption can be valid and can often easily occur, which is explained below.

If the subcarrier signal's bandwidth Δf is small enough such that the channel's frequency response is almost flat or constant in the domain of that bandwidth, then

the flat fading model for each signal, or symbol, in the OFDM block can be assumed, and serves as a good approximation to the UWA channel. The number of subcarriers should be large enough for this condition to be satisfied. This is the narrowband assumption. For this reason, throughout the research, this simplified form of the UWA channel model was assumed.

Given the physics of the propagating signal through an UWA channel, the next section looks at how Doppler effects impact the propagating signals.

2.7 The Doppler Effect in UWA Channels

The UWA Doppler shift has two effects on a propagating signal. The first effect is a common (to the signal) shift in the carrier frequency of the signal. The second effect is dilation/contraction which manifests in the signal's time and frequency domain, causing time and frequency samples to shift. This effect is usually negligible in channels with small Mach numbers like radio channels, but is significant in UWA channels.

The following discussion describes how these Doppler effects arise. In an environment with Doppler shifts due to motion of the receiver and/or transmitter the received frequency is related to the transmitted frequency as follows:

$$f' = \left(1 + \frac{\Delta v}{c}\right) f \tag{2.60}$$

where f is the frequency at the transmitter, f' is the frequency at the receiver, c is the speed of sound, and Δv is the relative velocity between the transmitter and receiver platforms. The factor $\Delta v/c$ is the Mach number denoted by a. If the transmitting carrier frequency is f_c, then the carrier frequency is shifted by af_c.

Using the above expression for a channel with dominant Doppler effects, the transmitted signal, $s(t)$, is related to the received signal $r(t)$ as follows:

$$R(f') = R((1+a)f) = AS(f) \tag{2.61}$$

where A is the amplitude at the receiver, and $R(f)$ and $S(f)$ are the Fourier transforms of $r(t)$ and $s(t)$, respectively. Therefore,

$$R(f) = AS(f/(1+a)) \tag{2.62}$$

and in the time domain:

$$r(t) = (1+a)As((1+a)t) = A's((1+a)t) \tag{2.63}$$

such that $A' = A(1+a)$. The Doppler effect therefore scales the frequency domain by a factor of $1/(1+a)$ and the time domain by $1+a$. This means that when a is negative, the spectrum is broadened and the TD signal is compressed, and vice-versa. In underwater communications (in fact in all known physical channels), $|a| < 1$ and so the factor $1+a$ is always positive.

If a lowpass signal, $x(t)$, is transmitted, then the bandpass signal transmitted with carrier f_c, is:

$$s(t) = \mathrm{Re}\{x(t)e^{j2\pi f_c t}\}. \tag{2.64}$$

From the above discussion, the bandpass received signal is given by:

$$r(t) = A'\mathrm{Re}\{x((1+a)t)e^{j2\pi f_c(1+a)t}\}. \tag{2.65}$$

The complex equivalent lowpass received signal $y(t)$ is then:

$$y(t) = A'x((1+a)t)e^{j2\pi a f_c t}. \tag{2.66}$$

If $x(t)$ has duration T, then $y(t)$ will have duration $T/(1+a)$. Further, a complex lowpass independent and identically distributed (i.i.d.) additive white noise process, $\tilde{n}(t)$, completes the model:

$$y(t) = A'x((1+a)t)e^{j2\pi a f_c t} + \tilde{n}(t). \tag{2.67}$$

In the frequency domain:

$$Y(f) = AX\left(\frac{f - af_c}{1+a}\right) + \tilde{N}(f). \tag{2.68}$$

Let the UWA channel be given by the time-variant channel model in (2.29). Assume that the amplitude is constant (or experiences small variations) within an OFDM block, i.e. $c_p(t) = c_p$. Also, assume that the delay variation for each path $\tau_p(t)$ can be approximated by the first-order relation $\tau_p(t) \approx \tau_p(0) - a_p(t)t$. Since the relative platform velocity can vary with time, the Mach number will also. These assumptions are appropriate when $T < T_{\text{coh}}$, which is on the order $O(100$ ms$)$ at most [38, p. 12].

Also assume, and without loss of generality, that the Mach number has a weak dependence on p, i.e., there exists one common Mach number $a(t)$ in a short M-point burst. This assumption is common when the Doppler distortion due to platform motion is dominant or the angles of arrival experience small changes for the paths [40]. Alternatively, one can instead view $a(t)$ as the average of the path-dependent Mach numbers $a_p(t)$ (averaged over p); in this case $a(t)$ becomes the channel's average Mach number that needs to be estimated and eliminated.

At the transmitter each ith OFDM block occupies an interval $t \in [iT', (i+1)T']$ where T' is defined as $T+T_g$, with T_g being the guard interval or cyclic prefix duration.

The UWA bandpass CIR, in the presence of Doppler effects, is now given by:

$$c(t,\tau) = \sum_{p=1}^{P} c_p \delta(\tau - (\tau_p(0) - ta(t)). \tag{2.69}$$

The frequency response of the channel is then:

$$C(t,f) = e^{j2\pi a(t)ft} \sum_{p=1}^{P} c_p e^{-j2\pi f \tau_p(0)} = e^{j2\pi a(t)ft} C(f) \tag{2.70}$$

which shows time- and frequency-dependent phase shifts in the OFDM block.

According to (2.32), the lowpass equivalent of the channel is now given by

$$h(t,\tau) = e^{j2\pi a(t) f_c t} \sum_{p=1}^{P} c_p e^{-j2\pi f_c \tau_p(0)} \delta(\tau - (\tau_p(0) - ta(t))) \tag{2.71}$$

where $a(t)f_c$ is the Doppler shift present in the channel. Hence the frequency response is:

$$H(t,f) = e^{j2\pi a(t)(f+f_c)t} \sum_{p=1}^{P} c_p e^{-j2\pi (f+f_c)\tau_p(0)} = e^{j2\pi a(t)(f+f_c)t} C(f) \tag{2.72}$$

but it can also be expressed in other forms like:

$$H(t,f) = C(t, f+f_c) = e^{j2\pi a(t)(f+f_c)t} C(f+f_c). \tag{2.73}$$

The channel taps $\{c_p\}$ are not deterministic, rather they are random. For a large number of paths P, which often occurs in shallow water conditions, $h(t,\tau)$ can be approximated as a complex-valued Gaussian random process. The random variable of $|c_p|$ can be Rayleigh, Ricean, Nakagami, etc. Let $|\mathcal{C}_p|$ be the random variable representing $|c_p|$. Assuming that no line-of-sight component exists, one can assume

that $|\mathcal{C}_p|$ has a Rayleigh distribution [38, 43, 44].

This is not always the case however, as the taps may follow a different distribution under different transmission conditions and different water depths. In this case, one needs to find the distribution of channel taps with a kernel distrubtion, which is done via kernel density estimation. One of the reasons for this is due to the fact that a more general UWA channel model includes the random time-varying effects of the UWA channel on the channel taps as multiplicative noise (which is sometimes assumed Gaussian) [45]. Let the multiplicative noise be given by $M_p(t)$. Like c_p, if one assumes that $M_p(t)$ slowly varies in time for short durations, then the UWA channel is given by

$$h(t,\tau) = e^{j2\pi a(t) f_c t} \sum_{p=1}^{P} M_p c_p e^{-j2\pi f_c \tau_p(0)} \delta(\tau - (\tau_p(0) - t a(t)))$$

For the remainder of the thesis, M_p is assumed to be absorbed into c_p.

The bandpass received signal is

$$r(t) = s(t) * h(t,\tau) + n(t) \tag{2.74}$$

which is given by

$$r(t) = \sum_{p=1}^{P} c_p s((1+a(t))t - \tau_p(0)) + n(t). \tag{2.75}$$

Now, each ith OFDM block at the receiver occupies an interval $t \in [\frac{iT' + \tau_{p,i}(0)}{1+a_i(t)}, \frac{(i+1)T' + \tau_{p,i}(0)}{1+a_i(t)}]$ where $a_i(t)$ and $\tau_{p,i}(0)$ are the Mach number and reference delay for that block, respectively. It should be noted that since $|a(t)| < 1$, $1 + a(t) > 0$. Similarly, the

lowpass signal received can be written as:

$$y(t) = e^{j2\pi a(t) f_c t} \sum_{p=1}^{P} c_p e^{-j2\pi f_c \tau_p(0)} x((1+a(t))t - \tau_p(0)) + \tilde{n}(t) \tag{2.76}$$

where $t \in [\frac{iT' + \tau_{p,i}(0)}{1+a_i(t)}, \frac{(i+1)T' + \tau_{p,i}(0)}{1+a_i(t)}]$.

Assume $a(t)$ experiences small variations within the block. Then, the Fourier transform of $y(t)$, after simplifying, is given by:

$$Y(f) = \frac{1}{1+a} C\left(\frac{f}{1+a}\right) X\left(\frac{f - a f_c}{1+a}\right) + \tilde{N}(f). \tag{2.77}$$

Note the similarity of this expression with Eq.(2.68), which was derived in the absence of $c(t, \tau)$.

Recall that the OFDM representation of $x(t)$ is given by:

$$x(t) = \frac{1}{\sqrt{N}} \sum_{k=0}^{N-1} X[k] e^{j2\pi f_k t}. \tag{2.78}$$

Substituting this into Eq.(2.76) and simplifying gives an alternative representation of $y(t)$:

$$y(t) = \frac{1}{\sqrt{N}} e^{j2\pi a(t) f_c t} \sum_{m=0}^{M-1} C(f_k) X[k] e^{j2\pi f_k (1+a(t))t} + \tilde{n}(t). \tag{2.79}$$

A similar expression can be found in [41].

From the analysis so far two effects have persisted, which are more clearly seen in Equations (2.76) and (2.79). Firstly, the signal duration from each path is scaled by $1 + a(t)$. In UWA channels, $a(t)$ can reach $O(10^{-2})$ so the dilation/compression of the block duration is small. However in the frequency domain, since a large number of subcarriers is usually chosen, the ICI introduced is in most cases substantial, and Doppler compensation is needed.

Secondly, the frequency components in the signals experience a subcarrier-dependent Doppler shift of $a(t)(f_c+f_k)$, which effectively causes the bandwidth of each subcarrier signal (or the subchannel bandwidth) to increase. This breaks down the narrowband assumption discussed in the previous section. Doppler compensation resolves this issue.

After deriving the received signal in the time domain, the frequency domain of the received signal will now be analyzed.

2.8 Reception of Shift-Orthogonal Sequences in UWA Channels

In this section, assume the Mach number is slowly varying in the OFDM block to facilitate derivation, so $a(t) \approx a$. In terms of the shift-orthogonal pilot signals, the received signal is given by Eq.(2.79) but with the proposed M-point pilot structure; i.e.

$$y(t) = \frac{1}{\sqrt{M}} e^{j2\pi a f_c t} \sum_{m=0}^{M-1} C(f_m) B[m] e^{j2\pi f_m (1+a)t} + \tilde{n}(t) \tag{2.80}$$

where m is now the frequency index of the M-point pilots. Here $B_M[m]$ is written as $B[m]$ for simplicity. The frequency response (Fourier transform) $Y(f_k)$ (where $k \in [0, M-1]$) after the guard interval removal is given by:

$$Y(f_k) = \frac{1}{T} \int_{\frac{\tau_p}{1+a}}^{\frac{T+\tau_p}{1+a}} y(t) e^{-j2\pi f_k t} dt + \tilde{N}(f_k). \tag{2.81}$$

Simplifying yields

$$Y(f_k) = \frac{1}{1+a} \frac{1}{\sqrt{M}} C\left(\frac{f_k}{1+a}\right) \sum_{m=0}^{M-1} B[m] e^{-j\pi\alpha_{k,m}} \text{sinc } \alpha_{k,m} + \tilde{N}(f_k) \tag{2.82}$$

where $\alpha_{k,m}$ is given by

$$\alpha_{k,m} = \frac{f_k - (1+a) f_m - a f_c}{1+a} T. \tag{2.83}$$

In discrete time it can be shown that the DFT is given by:

$$Y[k] = \frac{1}{\sqrt{M}} C\left(\frac{f_k}{1+a}\right) \sum_{m=0}^{M-1} B[m] e^{-j\pi\left(1-\frac{1}{N}\right)\alpha_{k,m}} \frac{\sin \pi\alpha_{k,m}}{\sin \frac{\pi}{N}\alpha_{k,m}} + Z[k] \tag{2.84}$$

where $Z[k]$ is the DFT of $z[n]$, which is the filtered lowpass noise in discrete time. In terms of the frequency indices $\alpha_{k,m}$ is:

$$\alpha_{k,m} = \frac{k - mN_{\text{pre}} - a(f_c T + mN_{\text{pre}})}{1+a} \tag{2.85}$$

The energy spectral density (ESD) for $E[k]$ can now be computed from $E[k] = |Y[k]|^2$. Similar expressions are derived in [41]. The expressions show each tone shifts by: (i) the value af_cT, which is due to the common Doppler shift, and (ii) the value amN_{pre}, which is the pilot's sample drift and is different for each pilot. The factor $1/(1+a)$ narrows/broadens the spectrum as discussed previously.

One can also observe that, for a given pilot $k = mN_{\text{pre}}$, if $a(f_cT + mN_{\text{pre}}) \ll 1$, then the channel is slow fading, $\rho_{k,k} \approx 1$ and $|\rho_{k,m}| < |\rho_{k,k}|$. Therefore,

$$Y[k] = \frac{1}{\sqrt{M}} C\left(\frac{f_k}{1+a}\right) B[k] + \frac{1}{\sqrt{M}} C\left(\frac{f_k}{1+a}\right) \sum_{\substack{m=0 \\ mN_{\text{pre}} \neq k}}^{M-1} B[m]\rho_{k,m} + Z[k]. \tag{2.86}$$

The summation term in such a scenario is because of ICI, which is small due to assuming slow fading conditions, and can hence be viewed as additional noise.

Although the expressions derived in this section show the Doppler effects on the frequency spectrum of the received pilot signals, the derivation also motivates the concept of Doppler estimation and compensation in the time domain as opposed to the frequency domain. In this section slowly varying Mach numbers are assumed to find closed-form expressions for the frequency response. If no such assumptions for $a(t)$ are made then closed-form frequency domain expressions will no longer be

possible and the estimator would be based on approximate expressions. Furthermore, visually observing the time variations of $a(t)$ in the frequency domain is impossible, so visual analysis and intuition are severely limited. In the proposed estimator, the assumption of slowly varying Mach numbers is also applied, but only for short pilot bursts as shown in Chapter 4.

Now that the Doppler effect is properly understood in the context of UWA channels, the Doppler estimation problem can be properly approached and analyzed. Regardless of the estimator used, estimator performance needs to be properly defined with a suitable metric. The next section discusses how estimator performance will be quantified in the thesis and introduces the Cramer-Rao lower bound (CRLB)

2.9 Estimator Performance and the CRLB

The Doppler estimation problem is a parameter estimation problem that asks the question of how to estimate the Mach number, $a_i(t)$, from the ith received signal block. The ability of the estimator to output Mach number estimates accurately with small-enough errors is what defines the estimator's performance. In the case of UWA channels, ambient noise is the random process that affects the Doppler estimator. The likelihood function $L(a_i(t)|z_i(t))$ of $a_i(t)$ is the likelihood that the value of the unknown parameter is $a_i(t)$ given the noisy outcome $z_i(t)$ is observed ($z_i(t)$ is the filtered lowpass noise signal for the ith received signal block). It is defined as the joint probability density function (PDF) of the noisy outcome $z_i(t)$ given that the true value of the unknown parameter is $a_i(t)$; i.e.:

$$L(a_i(t)|z_i(t)) = f(z_i(t)|a_i(t)) \tag{2.87}$$

where $f(z_i(t)|a_i(t))$ is the joint PDF of signal and noise. The joint PDF, $f(z_i(t)|a_i(t))$, is viewed as a function of $z_i(t)$ with $a_i(t)$ fixed, while the likelihood function, $L(a_i(t)|z_i(t))$,

is used to view $f(z_i(t)|a_i(t))$ as a function of $a_i(t)$ with $z_i(t)$ fixed.

In decision theory, an estimator is a decision rule whose performance is evaluated via loss (also known as cost) functions. A loss function in statistics is a function of the difference between the estimated parameter value and the true parameter value for a given data instance. Quadratic loss functions are commonly used in estimation problems as they are symmetric in the sense that errors, with the same magnitude, above and below the true value of the parameter contribute to the same loss. As well, the variance properties of quadratic loss functions are, more often than not, mathematically more tractable than other loss functions. A quadratic loss function in terms of the estimated Mach number $\hat{a}_i(t)$ and the true Mach number $a_i(t)$ is of the form $(\hat{a}_i(t) - a_i(t))^2$.

The loss function here is a random variable because it depends on the estimates extracted from the received signal, which is contaminated by ambient noise. In this case the expected value of the loss function, $\mathrm{E}[(\hat{a}_i(t) - a_i(t))^2]$, becomes a better measure of estimator performance. But this is just the mean squared error (MSE) of the Mach number estimate. In fact the MSE metric (and variance metric for unbiased estimators) is the most commonly used metric for evaluating performance in channel or Doppler estimation problems.

It can be shown with some algebra that the MSE is related to variance via the equation

$$\mathrm{MSE}[\hat{a}_i(t)] = \mathrm{VAR}[\hat{a}_i(t)] + [\mathrm{bias}(\hat{a}_i(t), a_i(t))]^2 \tag{2.88}$$

where $\mathrm{VAR}[\hat{a}_i(t)]$ is the variance of the estimator (defined as $\mathrm{E}[(\hat{a}_i(t) - \mathrm{E}[\hat{a}_i(t)])^2]$) and $\mathrm{bias}(\hat{a}_i(t), a_i(t))$ is the bias of the estimator, defined as

$$\mathrm{bias}(\hat{a}_i(t), a_i(t)) = \mathrm{E}[\hat{a}_i(t)] - a_i(t). \tag{2.89}$$

An estimator is called unbiased if $\mathrm{bias}(\hat{a}_i(t), a_i(t)) = 0$. Unbiasedness is one of the

desirable properties of an estimator, since the average Mach number estimate would not be an overestimate or underestimate of the true value, i.e. the estimates on average are not biased away from the true value.

Another property desired for any estimator is efficiency, also known as minimum variance. It can be shown that if the estimator and the likelihood function satisfy two weak regularity conditions, then the variance of the estimator is subject to the following bound, called the Cramer-Rao lower bound (CRLB) [39]:

$$\mathrm{VAR}[\hat{a}_i(t)] \geq \frac{\left|1 + \frac{\partial}{\partial a_i}\mathrm{bias}(\hat{a}_i(t), a_i(t))\right|^2}{\mathcal{I}(a_i(t))} \tag{2.90}$$

where $\mathcal{I}(a_i(t))$ is known as the Fisher information, and is defined as

$$\mathcal{I}(a_i(t)) = \mathrm{E}\left[\left(\frac{\partial}{\partial a_i}\ln\, L(a_i(t)|z_i(t))\right)^2\right] \tag{2.91}$$

($\ln\, L(a_i(t)|z_i(t))$ is the log-likelihood function). A minimum variance estimator is an estimator whose variance equals the CRLB. A minimum variance unbiased estimator (MVUE) has a variance that equals the CRLB and has zero bias. It will be shown in Chapter 4 that the proposed Doppler estimator approaches the MVUE with increasing SNR.

As mentioned above, two regularity conditions need to be satisfied in order to derive the bound in Eq.(2.90). The first regularity condition states that the Fisher information is always defined, which means that $\frac{\partial}{\partial a_i}\ln\, L(a_i(t)|z_i(t))$, known as the score function, exists and is finite. The score functon has the useful property which states that the expectation of the score function is zero.

The second regularity condition states that, in the expectation of the estimator, the derivative with respect to a_i can be interchanged with the integral with respect to z_i. This can occur when (i) the joint PDF has infinite domain, is continuously

differentiable and its integral uniformly converges for all $a_i(t)$, or (ii) the joint PDF is bounded in z_i, with the bound being independent of $a_i(t)$. Let the Doppler estimator be given by the random process $T(Z_i(t)|a_i(t))$, where $Z_i(t)$ is the random process representing noise, and let the point estimate extracted be given by the statistic $T(z_i(t)|a_i(t))$. In other words, let $\hat{a}_i(t) = T(z_i(t)|a_i(t))$. Then the second regularity condition states:

$$\frac{\partial}{\partial a_i}\int T(z_i(t)|a_i(t))f(z_i(t)|a_i(t))\ dz_i = \int \frac{\partial}{\partial a_i}\left[T(z_i(t)|a_i(t))f(z_i(t)|a_i(t))\right]\ dz_i. \tag{2.92}$$

Note from Eq.(2.89) that $\mathrm{E}[T(z_i(t)|a_i(t))] = \mathrm{E}[\hat{a}_i(t)] = a_i(t) + \mathrm{bias}(\hat{a}_i(t), a_i(t))$. With this information in mind (regularity conditions and the expectation of the statistic), the CRLB can be derived by applying the Cauchy-Schwartz inequality on the covariance of the estimator and the score function. Furthermore, if the score function is differentiable (i.e. if the log-likelihood function is twice-differentiable), then the regularity conditions can be used to prove the following about the Fisher information [39]:

$$\mathcal{I}(\hat{a}_i(t)) = -\mathrm{E}\left[\frac{\partial^2}{\partial a_i^2}\ln\ L(a_i(t)|z_i(t))\right]. \tag{2.93}$$

That is, Eq.(2.91) and Eq.(2.93) are equivalent. This property proves to be useful in deriving the CRLB of the estimator in Chapter 4. Using Eq.(2.88), the CRLB for the MSE can be derived:

$$\mathrm{MSE}[\hat{a}_i(t)] \geq \frac{\left|1 + \frac{\partial}{\partial a_i}\mathrm{bias}(\hat{a}_i(t), a_i(t))\right|^2}{\mathcal{I}(a_i(t))} + [\mathrm{bias}(\hat{a}_i(t), a_i(t))]^2. \tag{2.94}$$

With this section, the necessary background that lays the foundation of this thesis is complete. The next chapter reviews the literature that was consulted when researching for this work.

Chapter 3

Literature Review

3.1 Introduction

The problems of Doppler estimation and compensation have been studied extensively. Many approaches have been suggested for each problem. One may expect that Doppler estimation and compensation go hand-in-hand, however many of the sources encountered treated exclusively one or the other. Related to Doppler estimation is the training sequence structure used at the transmitter. Doppler tracking is a feature present in some Doppler estimators or compensators. If present, it would be an intermediary stage that follows estimation and precedes compensation (like it is in this thesis), and it is usually studied as part of the estimation or compensation processes.

This chapter presents the state-of-the-art literature that the present research was informed by or that it built on. Then, these examples provide a basis to measure the proposed estimator and compensator's performance against. The chapter starts with a review of existing Doppler estimators and the pilot structures used in estimation for UWA channels. It follows with a review of Doppler compensators.

3.2 Doppler Estimation and Tracking

The Doppler estimation objective is to determine the time-varying Mach number (relative speed) between transmitter and receiver during transmission and thus quantify the time-varying UWA channel. Continuously determining the Mach number during

transmission gives rise to Doppler tracking. The particular Doppler estimation requirements are wide estimation range, high MSE performance and low computational complexity to provide accurate near-real-time solutions on platforms with potentially limited on-board processing.

There are many piloting structures available for pilot-aided estimation in UWA channel communications. They can be classified into three main categories: comb-, block- and scatter-type pilots.

Comb-type pilots, like the one proposed in [1] (and used in this thesis; see Chapter 2) occupy the entire time domain (TD) frame and a number of subcarriers in the corresponding frequency domain (FD) with a uniform distribution. Block-type pilots occupy the entire FD and a certain number of samples with a uniform distribution in the corresponding TD frame. Scatter-type pilots occupy a certain number of subcarriers and TD samples, though the choice of samples changes in n frames before repeating the same pattern again; i.e. given a frame duration of T seconds, this pilot structure is periodic with period nT and occupies the same subcarriers in a uniform distribution for all frames.

The suitability of each pilot type and its performance under different estimators is the subject of many papers [2], [3] [4]. It is shown that comb-type pilots perform best in tracking fast fading channels with smaller delay spreads, though they are sensitive to frequency selectivity, whereas block-type pilots perform best when there are longer delay spreads and when there is a high degree of frequency selectivity, though they are sensitive to fast fading. Scatter-type pilots perform well in both frequency selective and fast fading channels, though their receivers suffer from high computational requirements, making them slower compared to comb-type or block-type pilot receivers.

From the perspective of Doppler estimation, tracking the time variations of the channel is the primary interest. Since frequency selectivity does not significantly

hinder the proposed Doppler estimator (Chapter 4) comb-type pilots are appropriate and used for this work. The correlation properties of these pilots (see Chapter 2) play a major role in defining the proposed Doppler estimator.

There are several kinds of Doppler estimators, but most are based on grid searching, i.e. finding the Mach number that best satisfies an objective function subject to pre-defined constraints [10], [12] - [14], [17], [18], [21],[22] - [25]. Stojanovic [10] uses frequency grid searching on the narrowband cross-ambiguity function (CAF) to estimate the Doppler shift. The estimator accurately tracks the Mach number. Its main problem is its computational complexity which scales with increasing Doppler shift.

In [9] and [23] grid searching is also used on the narrowband CAF for Doppler estimation, where the main objective is to find the peak of the narrowband CAF. Both are capable of Doppler tracking, though unfortunately the narrowband CAF is not an adequate choice for many UWA channels, since UWA channels are wideband by nature.

In [22], [24] and [25] different methods are proposed to use wideband CAF for grid searching. A grid search algorithm based on finding the peak of the wideband CAF is presented in [22]. Two methods to estimate the Doppler effect: wideband CAF searching and fractional Fourier transform are presented in [25]. However MSE performance and Doppler tracking are not reported in [22] or [25]. The estimator in [24] is based on grid searching with warping functions derived from the wideband CAF, and it uses a backpropagation algorithm to accomplish this; unlike [22] and [25] it is capable of Doppler tracking, but the estimator is limited to shallow underwater environments.

The estimators in [12] - [14] are also based on grid searching, though they use the maximum correlation peaks of the received signal. However in [12] and [13], Doppler tracking is absent, while [14] does not provide MSE performance for their estimator.

Also, there does not appear to be any at-sea trials for their validation.

The grid search in [21] tries to find the maximum energy peak of the received signal, making it similar to [12] - [14] in intent and results. In [21] a grid-search-based FD estimator based on the maximum energy peak of the chirp-z transform is proposed, which can produce highly-accurate Mach number estimates; however the MSE has an error floor at low SNRs, so it is easily outperformed by many of the Doppler estimators discussed here.

In [17] four methods to estimate Doppler effects are outlined. These are null-subcarrier-based estimation, pilot-aided estimation, and decision-aided estimation for zero-padded OFDM, and cross-correlation-type estimation for CP-OFDM; all four estimators use grid searches to arrive at the Mach number estimates and use objective functions not unlike the CAF. However all approaches lack Doppler tracking.

Another popular approach to Doppler estimation is based on the autocorrelation of the received signal against the transmitted one [15], [18], [19]. This approach typically exploits the structure of the training sequence, which means that the estimator is only as good as the training sequence used.

In [15] a correlation-based approach similar to the one proposed in this thesis is used, but it is a one-shot estimator in that the estimates are not updated in real-time, which means that it can not track the Mach number. In [19] a correlation-type estimator is used, also similar to the one presented in this thesis, but the estimator's MSE performance is not reported. In [18] cyclo-stationarity is assumed (i.e. a periodic WSS process) to derive a grid-search-based estimator which detects the peak of the circular autocorrelation function. However MSE performance and sea trial results are not shown so performance comparison is not possible.

Another approach is the fractional Fourier transform to estimate the Mach number [20] [25]. In [20] the fractional Fourier transform is applied on linear frequency-modulated signals to estimate the Mach number. The MSE of the estimator however

has an error floor that starts at very low SNRs, which limits its performance. Doppler tracking is also absent.

Other methods to estimate the Mach number exploit the sparsity of UWA channels by using compressed sensing for channel estimation. In [11] delay-Doppler sparsity is exploited to arrive at a recursive estimation scheme based on compressed sensing to track the channel. However this approach to estimate the Mach number underperforms compared to other estimators, and is usually reserved only for channel estimation (estimating the channel taps) where it performs well.

It is also possible to use harmonic retrieval to estimate the Mach number [16], but it has low MSE performance compared to other estimators. Gradient descent methods have also been used [26] to find the peaks of the wideband CAF to reduce the computational complexity of standard methods based on ambiguity function grid searching, such as the ones outlined above. However MSE performance, or any other error performance of the estimator is not reported.

From reviewing other contributions, the following observations can be made about existing Doppler estimators.

For grid searchers, the objective functions are usually either narrowband or wideband CAFs. Other objective functions include cross-correlation functions and energy spectral densities. By their nature, grid searchers do not provide a closed-form solution to the Doppler estimation problem. In most cases the Mach number that maximizes the objective function is taken to be the desired estimate. Though this is sufficient to arrive at accurate estimates in most cases, there are cases where the Mach number falls outside the constraints of the objective functions, or more than one Mach number estimate equally satisfies the constraints. This means there is no solution with such estimators. Finally, these estimators suffer from high computational complexity since the search typically requires small resolutions to arrive at accurate estimates.

The novel approaches to Doppler estimation problem exploit the UWA channel sparsity so compressed sensing can be used to estimate the channel. Though these are classified as channel estimators, they can be used to indirectly find Mach number estimates. This method usually underperforms compared to estimators implemented as pre-processors to channel estimators. Fractional Fourier transform, harmonic retrieval, and gradient descent methods have also been proposed as possible solutions to the Doppler estimation problem for UWA channels.

For this thesis, the estimator is correlation-type which uses the shift-orthogonal pilot structure discussed in Chapter 2. It will be shown that this results in a very robust estimator with a wide estimation range, high MSE performance and low computational complexity. In fact, the estimator will be shown to handle Mach numbers as high as $O(10^{-2})$, which is higher than that possible with the existing approaches reviewed here. The estimator is sub-optimal though, in the sense that its MSE can be outperformed by existing estimators. Nonetheless, it has features that distinguish it from other estimators, namely high estimation range and relatively low computational complexity. Its performance is also validated with comprehensive at-sea experiments (Chapter 6).

3.3 Doppler Compensators

Since the Doppler effect dilates/compresses the transmitted signal, resampling is a natural step in Doppler compensation. The overwhelming majority of Doppler compensators, like the ones reviewed in this work, include some form of resampling in their design.

For Doppler compensation, Stojanovic in [10] details an adaptive decision feedback equalizer (DFE) that can track and compensate the Doppler effect. Resampling is performed with time-scale interpolators, then residual Doppler compensation is applied by implementing an equalizer with phase-locked loop (PLL). However as mentioned

in the previous section, it is computationally intensive, and the computational load increases with the Doppler shift. The compensator in [19] is similar to the one used in [10], but the MSE performance is not reported.

In [27] resampling is followed by reduction of preamble duration to mitigate the residual Doppler effect. It uses a time-varying interpolator to resample the received signal. However, the compensator does not take residual Doppler shifts into account, making it easily susceptible to performance degradation. A time-varying resampler is also used in [22] but it is followed by recursive least squares (RLS) equalization to compensate for, and track, the Doppler effect.

The problem with equalizers is that, like most other synchronization techniques, they are often unreliable in UWA communications, due in large part to multipath and fading. With PLL-aided DFEs [10], for example, the error loop filter bandwidth required to track higher Mach numbers in many scenarios is unachievable. Furthermore, the MSE degrades with increasing Doppler shifts, and subsequently, equalizer divergence occurs when attempting to equalize in fast fading channels. Due to these disadvantages equalizers are better applied to track slow fading channels.

In [13], residual carrier frequency offset (CFO) compensation is performed after resampling with a grid-search approach based on detecting the maximum autocorrelation peak of the training sequences used. It is however incapable of tracking the Mach number, and results from real-life tests are not presented.

In [21] resampling is followed by the bisection method to compensate the residual CFO, which is also based on grid searches. However, the MSE performance of the algorithm is not reported, although the compensator has been validated with at-sea trials.

In [24], warping functions are derived from the wideband CAF to derive a lag-Doppler filter to estimate and then compensate the Doppler effect. The filter uses

a backpropagation algorithm to accomplish this, which is another grid searching approach. As mentioned in the previous section, the filter is limited to shallow underwater environments, and is unable to track the Mach number.

In [15] resampling is followed by a cross-correlation-based approach using training sequences to estimate the residual CFO. This is similar to the compensation approach proposed in this thesis, but this compensator lacks a tracking mechanism, as the residual Doppler estimator is a one-shot estimator. The resampling factor is also fixed.

After reviewing the above sources, the following observations can be made about existing Doppler compensators.

Resampling, the first stage of Doppler compensation, was used in every source encountered. These papers have their contribution in the second stage of compensation, namely residual Doppler compensation. This requires residual Doppler estimation first. With respect to signal size, the residual Doppler shift has minimal impact if high-performance Doppler estimators are used i.e. the Mach number estimate is close enough to the true Mach number.

Some of the compensators reviewed only use resamplers as their Doppler compensator and do not address residual Doppler compensation. This is an issue in practical UWA channels because residual Doppler shifts, although orders of magnitude smaller than common Doppler shifts, limit communication systems performance (more relevant for underway platforms) in much the same way Doppler shifts limit performance if left uncompensated.

A number of Doppler compensators follow resampling with PLL-equipped equalizers to track and compensate the Doppler shift. As mentioned previously these compensators suffer from high computational complexity relative to other compensators, with the complexity increasing with the Doppler shift. The inherent issue with equalizers is their inability to track channels that suffer from severe multipath and

fading which is inherent in UWA channels. The PLL's error loop filter bandwidth to track larger Mach numbers is often difficult to achieve, with the MSE degrading with increasing Doppler shifts as well. Equalizer divergence is also a common issue in fast fading channels.

One of the novel approaches to residual Doppler compensation is using warping functions extracted from the wideband CAF to derive a grid-searching lag-Doppler filter which estimates and compensates common and residual Doppler shifts. Another approach found in literature is the use of the bisection method for regular and residual Doppler estimation, which is also a grid-searching algorithm.

Most of the Doppler estimators reviewed in the previous section can also be applied to residual CFO estimation. This is not generally the case, and it needs to be proven first. It will be later shown (Chapter 5) that after resampling, the residual CFO can be estimated with the proposed Doppler estimator. The residual CFO can then be eliminated via simple phase rotation.

Chapter 4

Time-Domain Doppler Estimation

4.1 Introduction

Doppler estimation is a research problem in UWA communications, because the Doppler effect is a direct consequence of the rapid variations that exist in UWA environments, which can destroy the signal if left untreated. This is especially the case when multicarrier modulation, like OFDM, is used to generate the transmit signal. It is therefore not surprising to find that many solutions are proposed to the problem, though they are not without their disadvantages and constraints. This is also true for the proposed estimator. There are no Doppler estimators which perfectly recover the Mach number for all UWA channels. Most, if not all, treatises on Doppler estimation make assumptions of the UWA channel, even when these assumptions are not completely satisfied.

As mentioned in Chapter 2, reducing the duration of the transmitted signal to be less than the channel's coherence time helps combat fast fading channels. In other words, the signal duration is made small enough so that the time variations in the channel can be tracked. This also means that if the signal is modified to satisfy this condition before or during transmission, the rapid variations of the UWA channel will have less impact. This leads to adopting the channel assumptions outlined in Section 2.7, namely:

- The delay variations can be approximated by $\tau_p(t) \approx \tau_p(0) - a(t)t$.
- The path-dependent channel gains, $c_p(t)$, and the Mach number, $a(t)$, vary

slowly within the OFDM pilot block. Therefore, it is valid to drop the dependence on t in parts of the derivations.

Once the channel assumptions and the signal structure are established, the Doppler estimator can be developed based on this. The assumption of short-time durations also justifies using the WSSUS assumption, though the assumption is not used too liberally in this work, and plays no part in deriving the proposed receiver, but it is used in Chapter 6 to generate the Doppler power spectrum of the analyzed UWA channels.

Other reported works make channel assumptions similar to the ones listed above, though the WSSUS assumption may not be explicitly stated.

In this chapter, a correlation-type estimator is proposed which exploits the shift-orthogonal pilot structure discussed in Chapter 2. This results in a highly-robust estimator with a wide estimation range, low MSE and low computational complexity. It will be shown that the estimator is capable of handling Mach numbers of $O(10^{-2})$, which is not possible in the references reviewed earlier. The proposed estimator is sub-optimal though, in the sense that its MSE can be outperformed by existing ones. Nonetheless it has strengths that distinguish it from other estimators, namely high estimation range and relatively low computational complexity. Its performance is also substantiated with comprehensive at-sea measurements (Chapter 6).

4.2 The Doppler Estimator: Derivation

The proposed Doppler estimator is a correlation-type estimator which relies on the periodicity of the transmitted lowpass shift-orthogonal pilot signal, $b(t)$. The estimator makes the following assumptions. Firstly, the M-point pilot sequence is sufficiently short so the Mach number does not vary significantly with time, and the dilation/-compression caused by the Mach number becomes small. Secondly, the M-point pilot

sequence is short enough that path gains do not vary significantly with time. In this way, when these pilot bursts are continuously transmitted in the form of preambles, channel time variations can be observed and tracked by the estimator. In most treatments, similar assumptions are made about variations in the channel gains and delays.

Assume an i.i.d. additive white noise process. This is a typical assumption when attempting to analyze performance under ideal, synthetic conditions. From Eq.(2.67), the received preambles in a Doppler-dominant environment is given by:

$$y(t) = Ab((1 + a(t))t)e^{j2\pi a(t) f_c t} + \tilde{n}(t). \tag{4.1}$$

Signal $b(t)$ is an N-point OFDM signal made of N_{pre} preambles. Thus for $n \in [0, N-1]$, it is M-periodic (recall $N = N_{\text{pre}}M$). Let the M-point OFDM pilot signal received due to a single preamble be given by:

$$y_i(t) = Ab_M((1 + a_i)t)e^{j2\pi a_i f_c t} + \tilde{n}_i(t) \tag{4.2}$$

where $a_i(t)$ can be represented by a_i, for now, due to the assumptions above. The lowpass received signal is multiplied with its conjugate delayed by MT_s, resulting in:

$$\begin{aligned} y_i(t)y_i^*(t - MT_s) = {} & A^2 e^{j2\pi a_i f_c MT_s} b_M(t + a_i t) b_M^*(t + a_i t - MT_s) \\ & + A\tilde{n}_i^*(t - MT_s)e^{j2\pi a_i f_c t} b_M(t + a_i t) \\ & + A\tilde{n}_i(t)e^{-j2\pi a_i f_c (t - MT_s)} b_M^*(t + a_i t - MT_s) + \tilde{n}_i(t)\tilde{n}_i^*(t - MT_s). \end{aligned}$$

The average is then calculated. Since an i.i.d. white noise process is assumed, the average taken over the ensembles approximately equals the one taken over time. Due to using short preamble durations, this is an approximation rather than an equality. One can thus approximate the time average of the second and third terms in the

equality to be equal to the ensemble average of $\tilde{n}_i(t)$ and $\tilde{n}_i(t - MT_s)$ respectively, which is 0 for both cases. Hence, one arrives at the expression:

$$\begin{aligned} & \frac{1}{MT_s}\int_{MT_s} y_i(t)y_i^*(t-MT_s)dt \\ = \; & A^2 e^{j2\pi a_i f_c MT_s}\frac{1}{MT_s}\int_{MT_s} b_M(t+a_it)b_M^*(t+a_it-MT_s)dt \\ & + \frac{1}{MT_s}\int_{MT_s} \tilde{n}_i(t)\tilde{n}_i^*(t-MT_s)\; dt. \end{aligned}$$

It should be noted that $b_M((1+a_i)t)$ is a periodic sequence like $b_M(t)$, for:

$$\begin{aligned} b_M((1+a_i)t - MT_s) &= \frac{1}{\sqrt{M}}\sum_{m=0}^{M-1} B[m]e^{j2\pi(1+a_i)f_m t}e^{-j2\pi f_m MT_s} \\ &= \frac{1}{\sqrt{M}}\sum_{m=0}^{M-1} B[m]e^{j2\pi m(1+a_i)f_m t} = b_M((1+a_i)t). \end{aligned}$$

since $f_m = mN_{\text{pre}}/T = m/(MT_s)$. Since the preamble size is assumed to be small enough for it not to experience significant dilation/compression, this also means that

$$\frac{1}{MT_s}\int_{MT_s} b_M(t+a_it)b_M^*(t+a_it-MT_s)\; dt = \frac{1}{MT_s}\int_{MT_s} |b_M((1+a_i)t)|^2\; dt \approx 1 \quad (4.3)$$

In discrete time, after Nyquist filtering and downsampling, the lowpass received sequence $y_i[n]$ is ideally given by:

$$y_i[n] = Ab_M[(1+a_i)n]e^{j2\pi a_i f_c nT_s} + z_i[n] \quad (4.4)$$

It can be shown by the Nyquist-Shannon sampling theorem that Eq.(4.4) is an appropriate discrete-time representation of $y_i(t)$.

The average of the differential product in discrete time becomes:

$$\begin{aligned}
&\frac{1}{M}\sum_{n=0}^{M-1} y_i[n]y_i^*[n-M] \\
&= A^2 e^{j2\pi a_i f_c M T_s}\frac{1}{M}\sum_{n=0}^{M-1} b_M[(1+a_i)n]b_M^*[(1+a_i)n-M] + \frac{1}{M}\sum_{n=0}^{M-1} z_i[n]z_i^*[n-M] \\
&= e^{j2\pi a_i f_c M T_s} D + \frac{1}{M}\sum_{n=0}^{M-1} z_i[n]z_i^*[n-M]
\end{aligned}$$

where

$$D = A^2\frac{1}{M}\sum_{n=0}^{M-1} b_M[(1+a_i)n]b_M^*[(1+a_i)n-M]. \tag{4.5}$$

Analogous to the continuous-time case, $b_M[(1+a_i)n]$ is still periodic, for:

$$\begin{aligned}
& b_M[(1+a_i)n-M] \\
=\ & \frac{1}{\sqrt{M}}\sum_{m=0}^{M-1} B[m]e^{j2\pi m(1+a_i)n/M}e^{-j2\pi mn} = \frac{1}{\sqrt{M}}\sum_{m=0}^{M-1} B[m]e^{j2\pi m(1+a_i)n/M} \\
=\ & b_M[(1+a_i)n].
\end{aligned}$$

Therefore,

$$\frac{1}{M}\sum_{n=0}^{M-1} b_M[(1+a_i)n]b_M^*[(1+a_i)n-M] = \frac{1}{M}\sum_{n=0}^{M-1} |b_M[(1+a_i)n]|^2 \approx 1. \tag{4.6}$$

Therefore the differential product of the shift-orthogonal pilots is 1, so $D = A^2$.

It should be noted that, while $\frac{1}{M}\sum_{n=0}^{M-1} z_i[n]z_i^*[n-M] \to \mathrm{E}[z_i[n]z_i^*[n-M]]$ for sufficiently large M (which evaluates to 0 given i.i.d. white noise), M may not always be large enough for the correlation samples to be 0. In this case the noise quantity, $\frac{1}{M}\sum_{n=0}^{M-1} z_i[n]z_i^*[n-M]$, while small, should not be neglected. This is confirmed by simulations of the estimator in this work.

Let:

$$\hat{\Delta}_i[n] = \arg \sum_{j=1}^{M} y_i[n+j] y_i^*[n-M+j] \tag{4.7}$$

(the factor $1/M$ is irrelevant to the phase). This was said of $y_i[n]y_i^*[n-M]$ above, and is also true for $y_i[n+j]y_i^*[n-M+j]$, since these are just shifted samples. The motive for this representation will be seen soon. It is observed that $\hat{\Delta}_i[n]$ yields a Doppler shift estimate. The proposed Doppler shift estimator is hence given by:

$$\widehat{\Delta f}_i[n] = \frac{W}{2\pi M} \arg \sum_{j=0}^{M-1} y_i[n+j] y_i^*[n-M+j] \tag{4.8}$$

and the Mach number estimator by:

$$\hat{a}_i[n] = \frac{W}{2\pi f_c M} \arg \sum_{j=0}^{M-1} y_i[n+j] y_i^*[n-M+j] \tag{4.9}$$

where $W = T_s^{-1}$. Now the reasoning to represent $\hat{\Delta}_i[n]$ by Eq.(4.7) can be justified. Note, in this form, the estimator is sample-based, which means it produces a Mach number estimate for every received signal sample. The estimator is simply a moving average (MA) model that updates the output estimate for every sample. Thus the estimator is also a Mach number tracker. However, since the estimator is tracking the estimates for every sample, it is computationally cumbersome to use these estimates for Doppler compensation. The proposed solution would be to extract just enough Mach number estimates for compensation and tracking without compromising accuracy. This is accomplished and described in Chapter 5. For real UWA channels, D in Eq.(4.5) takes on a different expression. Under the same assumptions discussed in Chapter 2, the discrete-time representation of the received signal in a UWA channel

is given by:

$$y_i[n] = e^{j2\pi a_i f_c n T_s} \sum_{p=1}^{P} c_p e^{-j2\pi f_c m_p T_s} b_M[(1+a_i)n - m_p] + z_i[n] \tag{4.10}$$

where $\{c_p\}$ are the channel path gains and $\{m_p\}$ are the discretized path delays. In such a channel,

$$D = \frac{1}{M} \sum_{n=0}^{M-1} \sum_{p=1}^{P} c_p e^{-j2\pi f_c m_p T_s} b_M[(1+a_i)n - m_p] \sum_{p'=1}^{P} c_{p'} e^{j2\pi f_c m_{p'} T_s} b_M^*[(1+a_i)n - M - m_{p'}] \tag{4.11}$$

and from the assumptions about a_i for short pilot sequences, the pilots are still (approximately) periodic. Using this, along with the property in Eq.(2.14) and some simplification yields:

$$D = |c_p|^2. \tag{4.12}$$

Therefore, the proposed estimator still stands for UWA channels since D does not contribute to the phase component.

The next section provides approximate models for the received signal under high SNRs whence the variance is derived.

4.2.1 Approximation for High SNRs

It is possible to derive a closed-form approximation for the variance of $y_i[n+j]y_i^*[n+j-M]$ under high SNRs. Let

$$\mu_i[n+j] = y_i[n+j]y_i^*[n+j-M]. \tag{4.13}$$

Then,

$$\begin{aligned}\mathrm{VAR}[\mu_i[n+j]] &= A^2|b_M[n]|^2\mathrm{VAR}[z_i^*[n+j-M]] \\ &\quad + A^2|b_M[n]|^2\mathrm{VAR}[z_i[n+j]] + \mathrm{VAR}[z_i[n+j]z_i^*[n+j-M]] \\ &= 2A^2|b_M[n]|^2\sigma_i^2 + \mathrm{VAR}[z_i[n+j]z_i^*[n+j-M]]\end{aligned}$$

where σ_i^2 is the variance of $z_i[n]$. Since $z_i[n+j]$ and $z_i^*[n+j-M]$ are independent, the transformations $|z_M[n+j]|^2$ and $|z_i^*[n+j-M]|^2$ are also independent; therefore,

$$\mathrm{VAR}\ [z_i[n+j]z_i^*[n+j-M]] = E[|z_i[n+j]|^2]E[|z_i^*[n+j-M]|^2] = (\sigma_i^2)^2 \quad (4.14)$$

and the result becomes:

$$\mathrm{VAR}\ [\mu_i[n+j]] = 2A^2|b_M[n]|^2\sigma_i^2 + (\sigma_i^2)^2. \quad (4.15)$$

Thus the variance depends on σ_i^2, as expected.

There is no closed-form expression relating $\mu_i[n+j]$ with $\arg\ \mu_i[n+j]$, hence no closed-form relationship exists relating VAR $[\mu_i[n+j]]$ to VAR $[\arg\ \mu_i[n+j]]$ (however, it is possible to find a lower bound for the variance, as shown in the next section). Instead, the objective is to find an approximate expression for sufficiently-high SNRs, which is how most Doppler estimators operate. This also provides new insight into the estimator. The following approximation to the model for high SNRs not only gives a closed-form expression for the proposed estimator, as above, but also provides closed-form expressions for the mean and variance of the proposed estimator.

Since the energy of the attenuated preamble is $A^2\sum_{n=0}^{N-1}|b_M[n]|^2 = MA^2$, its power is given by A^2. Let the SNR be defined as $SNR_i = A^2/\sigma_i^2$, i.e. the ratio of the attenuated signal power per preamble to the noise power per preamble. Thus the

received signal can be written as:

$$\begin{aligned} y_i[n] &= A\left(b_M[(1+a_i)n]e^{j2\pi a_i f_c n T_s} + \frac{1}{A}z_i[n]\right) \\ &= A\left(b_M[(1+a_i)n]e^{j2\pi a_i f_c n T_s} + \frac{1}{\sqrt{SNR_i}}z_{\text{norm}}[n]\right) \end{aligned} \tag{4.16}$$

such that $z_i[n] = \sqrt{\sigma_i^2}\ z_{\text{norm}}[n]$ where $z_{\text{norm}}[n]$ is the zero-mean, normally-distributed complex random variable.

As the noise component is comparatively small at high SNRs, the above model can be replaced with an approximate model which includes the direct effects of noise on the phase, $2\pi a_i f_c n T_s$, to get:

$$y_i[n] \approx A b_M[(1+a_i)n]e^{j(2\pi a_i f_c n T_s + 1/\sqrt{2\cdot SNR_i}\ w_{\text{norm}}[n])} \tag{4.17}$$

where $w_{\text{norm}}[n]$ is viewed as a normally-distributed, real, white noise process with zero-mean and variance = 1. Thus $1/\sqrt{2\cdot SNR_i}\ w_{\text{norm}}[n]$ is zero-mean and has a variance of $\sigma_i^2/(2A^2)$.

Since $w_{\text{norm}}[n]$ is real, the factor 1/2 is added to be consistent with the definitions of variance for real and complex Gaussian processes. The importance of this approximation is that it helps analyze the effects of noise on the phase directly and in a straightforward way. Note, while $1/\sqrt{2\cdot SNR_i}\ w_{\text{norm}}[n]$ is a real Gaussian process, $e^{j/\sqrt{2\cdot SNR_i}\ w_{\text{norm}}[n]}$ is a colored noise process. Thus for high SNRs, while the phase is viewed as being contaminated with a real white Gaussian noise, the received signal is viewed contaminated with a complex-valued colored noise (although it is approximately white at high SNRs). For high SNRs, it is noted that:

$$\frac{1}{M}\sum_{j=0}^{M-1} \arg\ \mu_i[n+j] = \arg\ \sum_{j=0}^{M-1} \mu_i[n+j]. \tag{4.18}$$

From Eq.(4.17):

$$\arg \sum_{j=0}^{M-1} \mu_i[n+j] = \arg \left\{ A^2 e^{j2\pi a_i f_c M T_s} \sum_{j=0}^{M-1} e^{j \cdot \frac{1}{\sqrt{2 \cdot SNR_i}} (w_{\text{norm}}[n+j] - w_{\text{norm}}[n+j-M])} \right\}$$
$$= 2\pi a_i f_c M T_s + \arg \sum_{j=0}^{M-1} e^{j \cdot \frac{1}{\sqrt{2 \cdot SNR_i}} (w_{\text{norm}}[n+j] - w_{\text{norm}}[n+j-M])}.$$

As the SNR is high, the noise difference is small so a first-order Taylor series approximation yields:

$$\arg \sum_{j=0}^{M-1} e^{j \cdot \frac{1}{\sqrt{2 \cdot SNR_i}} (w_{\text{norm}}[n+j] - w_{\text{norm}}[n+j-M])}$$
$$\approx \arg \sum_{j=0}^{M-1} \left(1 + j \frac{1}{\sqrt{2 \cdot SNR_i}} (w_{\text{norm}}[n+j] - w_{\text{norm}}[n+j-M]) \right)$$
$$\approx \arg \left[M \left(1 + j \frac{1}{\sqrt{2 \cdot SNR_i}} \sum_{j=0}^{M-1} \frac{1}{M} (w_{\text{norm}}[n+j] - w_{\text{norm}}[n+j-M]) \right) \right] \approx 0.$$

The mean and variance of the estimators can be inferred from the above analysis:

$$\text{E}[\widehat{\Delta f}_i[n]] = \frac{W}{2\pi M} \left(\frac{1}{M} \sum_{j=0}^{M-1} E[\arg \mu_i[n+j]] \right) = a_i f_c = \Delta f \tag{4.19}$$

$$\text{E}[\hat{a}_i[n]] = a_i \tag{4.20}$$

$$\text{VAR}[\widehat{\Delta f}_i[n]] = \left(\frac{W}{2\pi M} \right)^2 \left(\frac{1}{M^2} \sum_{j=0}^{M-1} \text{VAR} \left[\arg \mu_i[n+j] \right] \right) = \frac{\sigma_i^2}{MA^2} \left(\frac{W}{2\pi M} \right)^2 \tag{4.21}$$

$$\text{VAR}[\hat{a}_i[n]] = \frac{\sigma_i^2}{MA^2} \left(\frac{W}{2\pi f_c M} \right)^2. \tag{4.22}$$

The theoretical mean of the estimators show they are unbiased. The variance of the estimators is inversely proportional to the SNR A^2/σ_i^2 as is common in most

estimators.

The next section presents a derivation of the Cramer-Rao lower bound (CRLB) for the estimator for a lower limit on the variance, since as mentioned earlier a closed-form analytical expression is not possible.

4.2.2 CRLB Derivation and Analysis

First, the Fisher information is derived for a given unbiased Doppler shift estimator. Recall that the filtered lowpass Doppler-shifted signal in discrete time is given by:

$$y_i[n] = Ae^{j2\pi a_i f_c n T_s} b_M[(1+a_i)n] + z_i[n]. \tag{4.23}$$

Here, the noise $z_i[n]$ is assumed to be a zero-mean complex Gaussian noise. The likelihood function for $z_i[n]$ is given by:

$$L(a_i|z_i) = \prod_{n=0}^{M-1} \frac{1}{\sqrt{2\pi\sigma_i^2}} e^{-\frac{|z_i[n]|^2}{(2\sigma_i^2)}} = \frac{1}{\left(\sqrt{2\pi\sigma_i^2}\right)^M} \exp\left(-\frac{1}{2\sigma_i^2}\sum_{n=0}^{M-1}|z_i[n]|^2\right). \tag{4.24}$$

In terms of $y_i[n]$,

$$L(a_i|y_i[n]) = \frac{1}{\left(\sqrt{2\pi\sigma_i^2}\right)^M} \exp\left(-\frac{1}{2\sigma_i^2}\sum_{n=0}^{M-1}|y_i[n] - Ae^{j2\pi a_i f_c n T_s} b_M[(1+a_i)n]|^2\right). \tag{4.25}$$

The log-likelihood function in turn is given by:

$$\ln\, L(a_i|y_i[n]) = -\frac{1}{2\sigma_i^2}\sum_{n=0}^{M-1}|y_i[n] - Ae^{j2\pi a_i f_c n T_s} b_M[(1+a_i)n]|^2 - \frac{M}{2}\ln\, 2\pi\sigma_i^2. \tag{4.26}$$

Let $\nu_n = 2\pi f_c n T_s$. The score function $\frac{\partial}{\partial a_i}[\ln\, L(a_i|y_i[n])]$ can now be computed:

$$\begin{aligned}\frac{\partial}{\partial a_i}\ln\, L(a_i|y_i[n]) &= -\frac{A}{2\sigma_i^2}\sum_{n=0}^{M-1} j\nu_n[-e^{ja_i\nu_n}b_M[(1+a_i)n]\left(y_i[n] - Ae^{ja_i\nu_n}b_M[(1+a_i)n]\right)^* \\ &\quad + e^{-ja_i\nu_n}b_M^*[(1+a_i)n]\left(y_i[n] - Ae^{ja_i\nu_n}b_M[(1+a_i)n]\right)] \\ &= -\frac{A}{2\sigma_i^2}\sum_{n=0}^{M-1} j\nu_n(-e^{ja_i\nu_n}y_i^*[n]b_M[(1+a_i)n] + e^{-ja_i\nu_n}y_i[n]b_M^*[(1+a_i)n]).\end{aligned}$$

(It is easily verified that the expectation, E[·], of the score function is 0). Now, the second derivative can be computed as:

$$\begin{aligned}\frac{\partial^2}{\partial a_i^2}[\ln\, L(a_i|y_i[n])] &= -\frac{A}{2\sigma_i^2}\sum_{n=0}^{M-1}[j\nu_n(-j\nu_n e^{ja_i\nu_n}y_i^*[n]b_M[(1+a_i)n - \\ &\qquad\qquad j\nu_n e^{-ja_i\nu_n}y_i[n]b_M^*[(1+a_i)n])] \\ &= -\frac{A}{2\sigma_i^2}\sum_{n=0}^{M-1}\nu_n^2(e^{ja_i\nu_n}y_i^*[n]b_M[(1+a_i)n] + e^{-ja_i\nu_n}y_i[n]b_M^*[(1+a_i)n]).\end{aligned}$$

The Fisher information, $\mathcal{I}(a_i)$, can now be derived as:

$$\begin{aligned}\mathcal{I}(a_i) &= -\mathrm{E}\left[\frac{\partial^2}{\partial a_i^2}\ln\, L(a_i|y_i[n])\right] \\ &= \frac{A}{2\sigma_i^2}\sum_{n=0}^{M-1}\nu_n^2(e^{ja_i\nu_n}\mathrm{E}\,[y_i^*[n]]b_M[(1+a_i)n] + e^{-ja_i\nu_n}\mathrm{E}\,[y_i[n]]b_M^*[(1+a_i)n]) \\ &= \frac{A}{2\sigma_i^2}\sum_{n=0}^{M-1}\nu_n^2(Ab_M^*[(1+a_i)n]b_M[(1+a_i)n] + Ab_M[(1+a_i)n]b_M^*[(1+a_i)n]) \\ &= \frac{A^2}{\sigma_i^2}\sum_{n=0}^{M-1}\nu_n^2|b_M[(1+a_i)n]|^2.\end{aligned}$$

Given that $\nu_n = 2\pi f_c n T_s = 2\pi f_c n/W$, and the fact that the pilot duration is small enough such that the dilation/compression it experiences is negligible, the Fisher

information of the Doppler shift estimator is:

$$\mathcal{I}(a_i) = \frac{A^2}{\sigma_i^2}\left(\frac{2\pi f_c}{W}\right)^2 \sum_{n=0}^{M-1} n^2 |b_M[(1+a_i)n]|^2 \approx \frac{A^2}{\sigma_i^2}\left(\frac{2\pi f_c}{W}\right)^2 \sum_{n=0}^{M-1} n^2 |b_M[n]|^2$$
$$\approx SNR_i \cdot \left(\frac{2\pi f_c}{W}\right)^2 \sum_{n=0}^{M-1} n^2 |b_M[n]|^2 \tag{4.27}$$

which is independent of a_i. The reciprocal of $\mathcal{I}(a_i)$ is the CRLB of an unbiased estimator. Note that:

$$\sum_{n=0}^{M-1} n^2 |b_M[n]|^2 \leq \sum_{n=0}^{M-1} n^2 \sum_{n=0}^{M-1} |b_M[n]|^2. \tag{4.28}$$

But $\sum_{n=0}^{M-1} |b_M[n]|^2 = M$ (see Eq.(2.14)). Therefore,

$$\mathcal{I}(a_i) = SNR_i \cdot \left(\frac{2\pi f_c}{W}\right)^2 \sum_{n=0}^{M-1} n^2 |b_M[n]|^2 \leq SNR_i \cdot \left(\frac{2\pi f_c}{W}\right)^2 \frac{M^2(M-1)(2M-1)}{6}. \tag{4.29}$$

The bias of the estimator is given by bias $(\hat{a}_i, a_i) = \mathrm{E}\,[\hat{a}_i] - a_i$. In this case the bound is given as:

$$\mathrm{VAR}\,[\hat{a}_i] \geq \frac{\left[1 + \frac{\partial}{\partial a}\mathrm{bias}\,(\hat{a}_i, a_i)\right]^2}{I(a_i)}. \tag{4.30}$$

The estimator bias thus needs to be checked. Recall from Eq.(4.9) that:

$$\hat{a}_i[n] = \frac{W}{2\pi f_c M}\arg \sum_{j=0}^{M-1} \mu_i[n+j] \tag{4.31}$$

so

$$\mathrm{bias}\,(\hat{a}_i, a_i) = \frac{W}{2\pi f_c M}\mathrm{E}\left[\arg \sum_{j=0}^{M-1} \mu_i[n+j]\right] - a_i[n]. \tag{4.32}$$

The bias is expected to be very small since averaging the noise component in $\arg \sum_{j=0}^{M-1} \mu_i[n+j]$ over sufficiently many preambles mitigates it (the estimator is

shown to be unbiased for high SNRs in the previous section). The quantity:

$$1 + \frac{\partial}{\partial a_i}\text{bias } (\hat{a}_i, a_i) = \frac{W}{2\pi f_c M}\frac{\partial}{\partial a_i}\text{E } \left[\arg \sum_{j=0}^{M-1} \mu_i[n+j]\right] \tag{4.33}$$

was calculated numerically and found to be $1 + \frac{\partial}{\partial a_i}\text{bias } (\hat{a}_i, a_i) \approx 1$, i.e. the partial derivative is approximately 0, again confirming unbiasedness. Therefore, the bound for the estimator is given by:

$$\begin{aligned}\text{VAR } [\hat{a}_i] &\geq \left[SNR_i \cdot \left(\frac{2\pi f_c}{W}\right)^2 \sum_{n=0}^{M-1} n^2 |b_M[n]|^2\right]^{-1} \\ &\geq \left[SNR_i \cdot \left(\frac{2\pi f_c}{W}\right)^2 \frac{M^2(M-1)(2M-1)}{6}\right]^{-1}.\end{aligned} \tag{4.34}$$

It is interesting to note that the variance of $\hat{\Delta}_i$ is independent of W and f_c. For

$$\text{VAR } [\hat{\Delta}_i] = \left(\frac{2\pi f_c M}{W}\right)^2 \text{VAR } [\hat{a}_i] \geq \left[SNR_i \cdot \frac{(M-1)(2M-1)}{6}\right]^{-1}. \tag{4.35}$$

The relationship between MSE and variance is given by:

$$\text{MSE } [\hat{a}_i] = \text{VAR } [\hat{a}_i] + [\text{bias } (\hat{a}_i, \hat{a})]^2. \tag{4.36}$$

Note that the MSE and variance bounds are nearly the same due to the fact that the estimator is (approximately) unbiased, but it should be included for a more complete description. Thus,

$$\begin{aligned}\text{MSE } [\hat{a}_i] \geq &\left[SNR_i \cdot \left(\frac{2\pi f_c}{W}\right)^2 \frac{M^2(M-1)(2M-1)}{6}\right]^{-1} \\ &+ \left(\frac{W}{2\pi f_c M}\text{E } \left[\arg \sum_{j=0}^{M-1} \mu_i[n+j]\right] - a_i[n]\right)^2.\end{aligned} \tag{4.37}$$

In terms of $\hat{\Delta}_i$,

$$\text{MSE } [\hat{\Delta}_i] \geq \left[SNR_i \cdot \frac{(M-1)(2M-1)}{6} \right]^{-1} + \left(\text{E } \left[\arg \sum_{j=0}^{M-1} \mu_i[n+j] \right] - \Delta_i[n] \right)^2 . \tag{4.38}$$

The bounds in terms of $\sum_{n=0}^{M-1} n^2 |b_M[n]|^2$ are tighter, and they are the true CRLBs:

$$\begin{aligned} \text{MSE } [\hat{a}_i] \geq & \left[SNR_i \cdot \left(\frac{2\pi f_c}{W} \right)^2 \sum_{n=0}^{M-1} n^2 |b_M[n]|^2 \right]^{-1} \\ & + \left(\frac{W}{2\pi f_c M} \text{E } \left[\arg \sum_{j=0}^{M-1} \mu_i[n+j] \right] - a_i[n] \right)^2 . \end{aligned} \tag{4.39}$$

$$\text{MSE } [\hat{\Delta}_i] \geq \left[SNR_i \cdot \frac{1}{M^2} \sum_{n=0}^{M-1} n^2 |b_M[n]|^2 \right]^{-1} + \left(\text{E } \left[\arg \sum_{j=0}^{M-1} \mu_i[n+j] \right] - \Delta_i[n] \right)^2 . \tag{4.40}$$

The next section outlines the design criteria for the estimator.

4.3 Design Criteria

The proposed Doppler estimator is a TD estimator which relies on estimating the phase $2\pi a_i[n] f_c M T_s$. Recall that

$$\hat{a}_i[n] = \frac{W}{2\pi f_c M} \arg \sum_{j=0}^{M-1} \mu_i[n+j]. \tag{4.41}$$

Computing the argument involves an arctan operation, which takes on a value between $-\pi$ and π. One thus gets the condition:

$$\left| \frac{2a_i[n] f_c M}{W} \right| < 1 \tag{4.42}$$

or

$$|a_i[n]| < \frac{W}{2f_c M}. \tag{4.43}$$

If the above condition is not satisfied, there will be angle ambiguity, which means the estimator puts the phase estimates in the incorrect quadrant. Thus Eq.(4.43) is a necessary condition for the estimator to satisfy. For example, if $M = 64$, $f_c = 24.414$ kHz and $W = 10$ kHz, the pilot signals can be used with the Doppler estimator in channels where the Mach number can be as high as 3.2×10^{-3}.

The estimation range can be extended if the bandwidth is increased, carrier frequency is reduced, or shift-orthogonal pilot sequence length is reduced, thereby making the Doppler estimator applicable over more dynamic channels. For example, using a length of $M = 8$ $f_c = 24.414$ kHz and $W = 10$ kHz means the Doppler estimator can be used in channels where the Mach number is as high as 0.026.

However, it must be noted that there is a trade-off asscoiated with choosing the length of the M-point pilot sequence. If the preamble is shortened, then it will be able to handle faster time variations without experiencing pilot ambiguity, which as mentioned previously increases the range of the estimator. However, if the preamble is shortened to the point where it is less than the delay spread of the channel, then the channel estimator using these preambles will not be able to correctly capture the frequency selectivity of the channel. This trade-off needs to be kept in mind when choosing preamble size.

It should be noted that it is possible to transmit preambles with varying sizes as long as these sizes satisfy the design criterion, i.e. the preamble size M can vary with i. For example, 8-point, 16-point and 64-point preambles can be serially transmitted, and the estimator will be able to track the Mach number estimates across the preambles. It is also possible to vary the bandwidth of each transmitted preamble (W can vary with i) without hindering the performance of the estimator (provided

the design criterion is satisfied).

With the theory and design requirements of the proposed estimator established, next its performance will be benchmarked in simulations, in order to validate its theoretical framework and performance expectations in real channels. Later (Chapter 6) these performance expectations will be measured against at-sea trials.

4.4 Performance in Simulations

Shown in Fig. 4.1 is the proof-of-concept estimator, in the baseband, realized with MathWorks Simulink. It produces estimates of $\hat{\Delta}_i$, which are used to find $\hat{a}_i$ or $\widehat{\Delta f}_i$. Performance curves are presented for $\hat{\Delta}_i$.

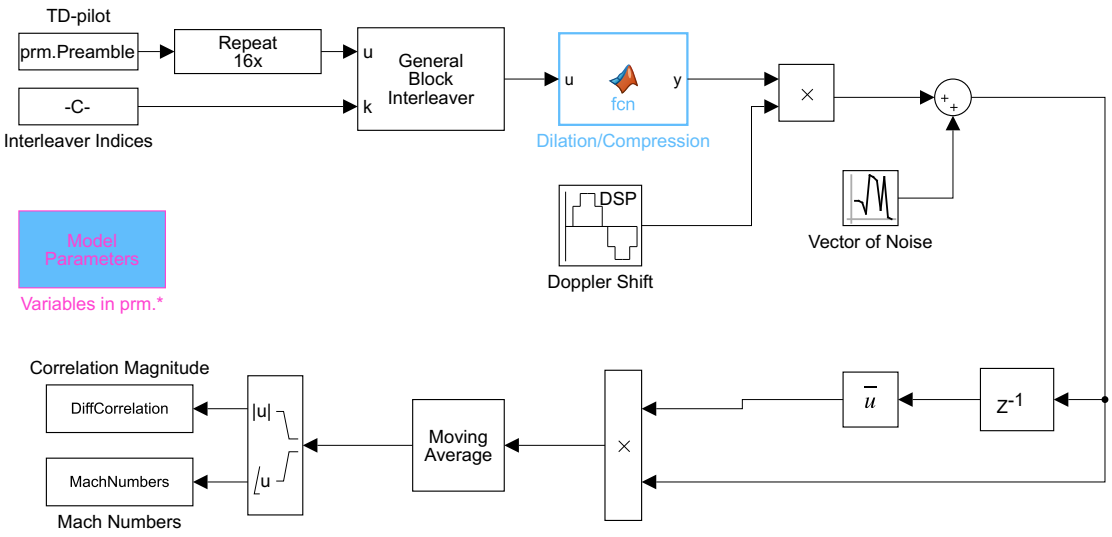

Figure 4.1: Simulink model used to test the Doppler estimator.

The model was first tested under noise-free conditions with only Doppler phase offsets to confirm the estimator performs as expected under such ideal conditions, before extending it to include noise, dilation/compression, etc.

After the M-point orthogonal pilot sequence is generated, the Doppler shift was added as a carrier frequency offset for Mach numbers $-10^{-3} < a < 10^{-3}$ and carrier frequencies of 2048 Hz and 24414 Hz. The estimator consistently produced perfect

phase estimates in the absence of noise. For example, with $W = 400$ Hz, $f_c = 2048$ Hz, and $a = -5 \times 10^{-5}$, the "MachNumbers" block (Fig. 4.1) produced phase estimates of $\hat{\Delta}_i[n] = -0.10294$. This results in the estimate $\hat{a}_i[n] = \hat{a} = -4.9998 \times 10^{-5}$. Another example with $W = 10$ kHz and $f_c = 24.414$ kHz, yield the same results.

Then the model was tested with a combination of noise and signal dilation/compression effects. The transmitted signal was checked to maintain a signal power of 1, meaning the SNR is given by $1/\sigma_i^2$. In Simulink, the SNR definition is based on the input sample size. When signals are handled on a per-sample basis, the signal power is normalized to 1 per sample (though it is not necessary for the proposed pilot signal as it has unit power) and the noise variance is also set on a per-sample basis.

For experimental purposes (Chapter 6), it is convenient to work with 64 samples (OFDM preamble sizes) or $64N_{\text{pre}}$ samples (OFDM block sizes); however when simulating the estimator with higher Mach numbers (greater than 10^{-3}), the preamble size was reduced to 8. These modes of operation do not affect the estimator's MSE, of course, rather they serve as a model reference, especially for the SNR calculations. The results presented below are for sample sizes of 64. As a result, signal power is normalized to 1 per 64 samples, and the AWGN block adds a 64-point noise sequence to each preamble with a power of σ_i^2.

The simulations were performed for Mach numbers $10^{-6} < a < 10^{-2}$. It was found that the estimator's performance has very weak dependence on the Mach number, i.e. the estimator is unbiased. Two Mach number values will be highlighted as representative of the range expected from Doppler effects, where the low value represents calm wave motion only and the high value repesents the relative platform motion scenario. The two Mach number values selected are: $a = -5 \times 10^{-5}$ and $a = -1 \times 10^{-3}$, and the results are shown for two combinations of bandwidth and carrier frequency.

Fig. 4.2 shows the Doppler estimator's performance, quantified by MSE, with SNR for $W = 400$ Hz, and $f_c = 2048$ Hz given the aforementioned two Mach numbers. As

shown, the performance is near-identical for both. For $|a| > 1.5 \times 10^{-3}$, the estimator experiences "angle ambiguity," i.e. the estimator yields bad estimates.

When $W = 10$ kHz and $f_c = 24.414$ kHz, near-identical performance is seen, again, for the two Mach numbers. This is expected as the variance of $\hat{\Delta}$ is independent of W or M. The estimator similarly experiences angle ambiguities for $|a| > 3 \times 10^{-3}$, which in practice is not too different from the previous case. Fig. 4.3 shows this.

These results are supported by the theory since 1 plus the derivative of the bias was numerically computed and found to be 1. Thus, the bias factor is simply a constant.

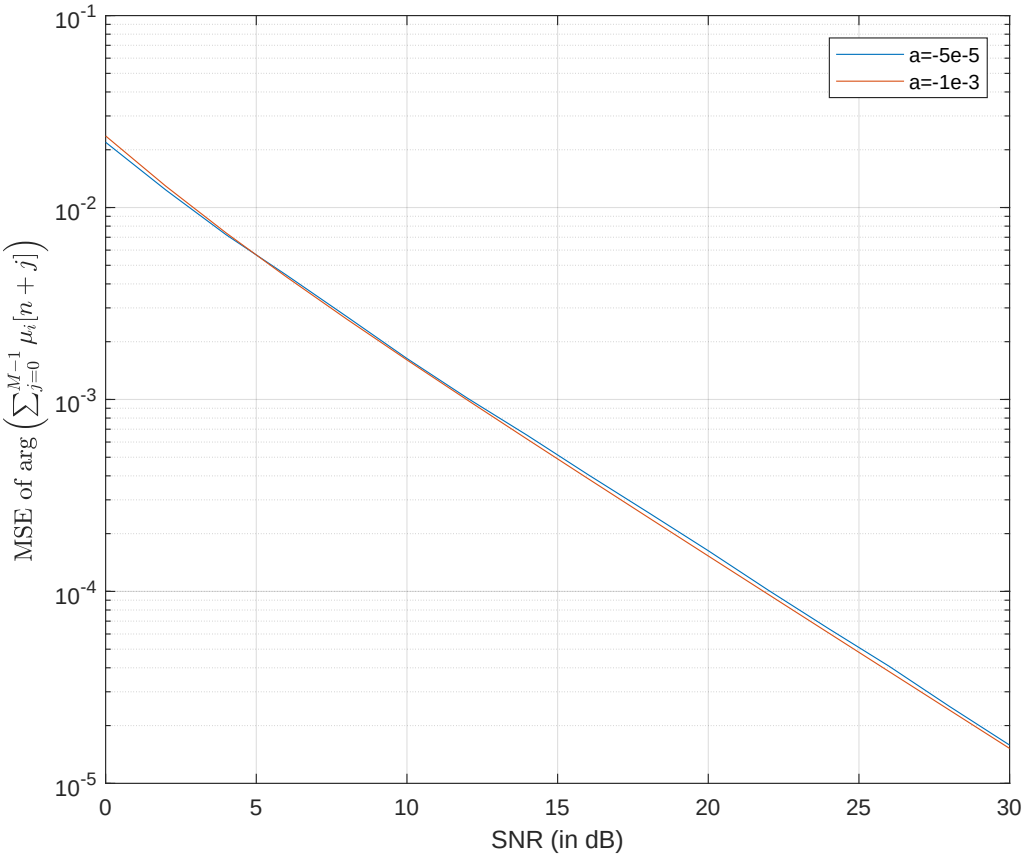

Figure 4.2: Simulated Doppler estimator performance of $\hat{\Delta}_i[n]$, quantified by MSE, for the two selected Mach numbers, given $W = 400$ Hz and $f_c = 2048$ Hz.

Finally, the CRLB of the estimator was computed for a lower bound on the variance (Eq.(4.40)). Fig. 4.4 shows the CRLB of the channel with $a = -5 \times 10^{-5}$ given $W = 400$ Hz and $f_c = 2048$ Hz. The measured MSE (Chapter 6) is sufficiently close to the theoretical CRLB, as it asymptotically approaches it with increasing SNR (as seen from the decreasing MSE separation with increasing SNR).

It is noted that for $SNR > 30$ dB, MSE $< 10^{-5}$ (≈ 0 as phase estimates will be near-perfect). Furthermore, the CRLB performance curve for the channel at $a = -10^{-3}$ is found to be the same. The CRLB performance curve of the channel, under any Mach number, is found to remain unchanged. Thus, the estimator is unbiased under these conditions. Again, since $\hat{\Delta}_i$ is independent of f_c and W, the MSE curves for $W = 10$ kHz and $f_c = 24.414$ kHz remain the same.

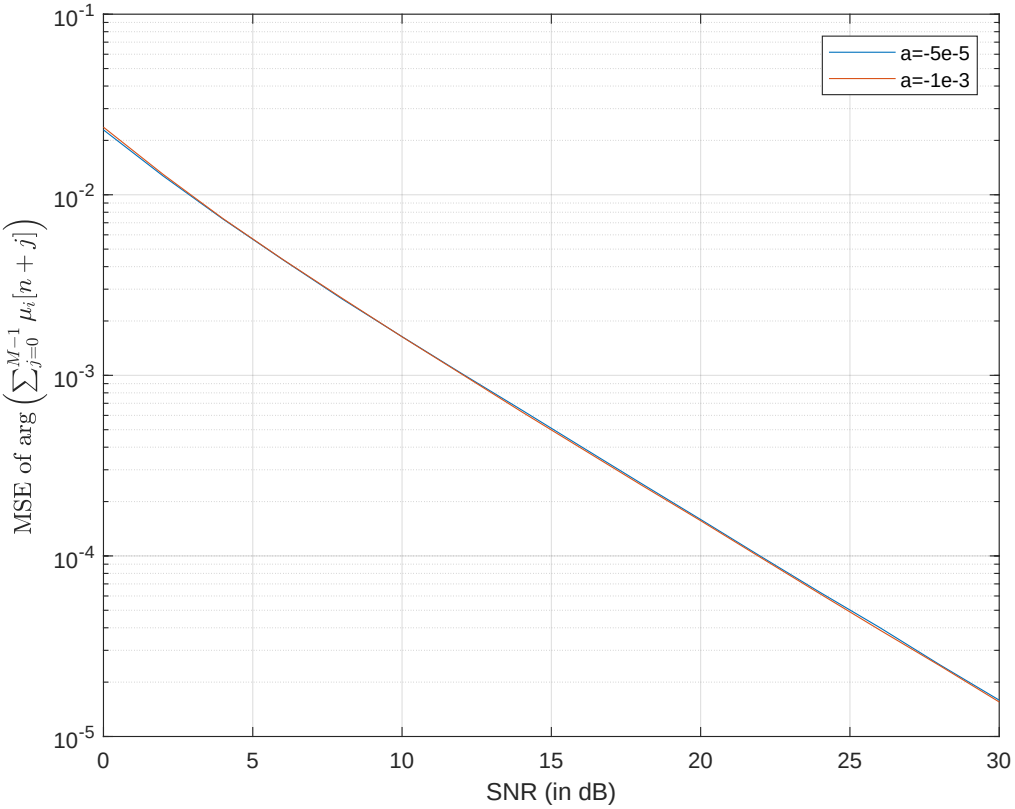

Figure 4.3: Simulated Doppler estimator performance of $\hat{\Delta}_i[n]$, quantified by MSE, for the two selected Mach numbers, given $W = 10$ kHz and $f_c = 24.414$ kHz.

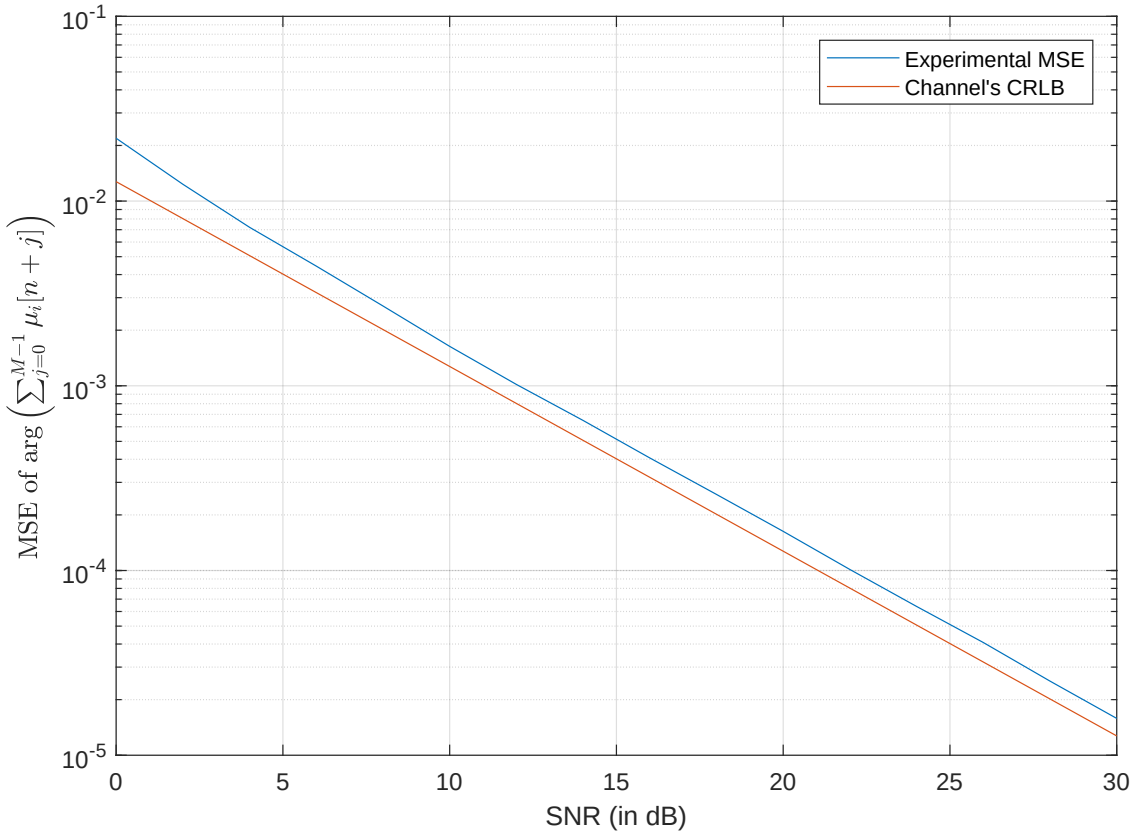

Figure 4.4: Simulated Doppler estimator performance of $\hat{\Delta}_i[n]$, quantified by MSE. Note that the measured MSE slowly approaches the theoretical CRLB.

If the MSE performance of $\hat{a}_i[n]$ is measured instead of $\hat{\Delta}_i[n]$ as above, the performance will depend on the parameters W, f_c and M, since MSE $[\hat{a}_i[n]] = \left(\frac{W}{2\pi f_c M}\right)^2$ MSE $[\hat{\Delta}_i[n]]$. Fig. 4.5 shows the MSE performance of $\hat{a}_i[n]$ when $W = 400$ Hz and $f_c = 2048$ Hz, while Fig. 4.6 shows the MSE performance of $\hat{a}_i[n]$ when $W = 10$ kHz and $f_c = 24.414$ kHz. Recall that results are presented for $M = 64$ in this section.

In the next section, the performance of the proposed Doppler estimator is compared against those reviewed in Chapter 3.

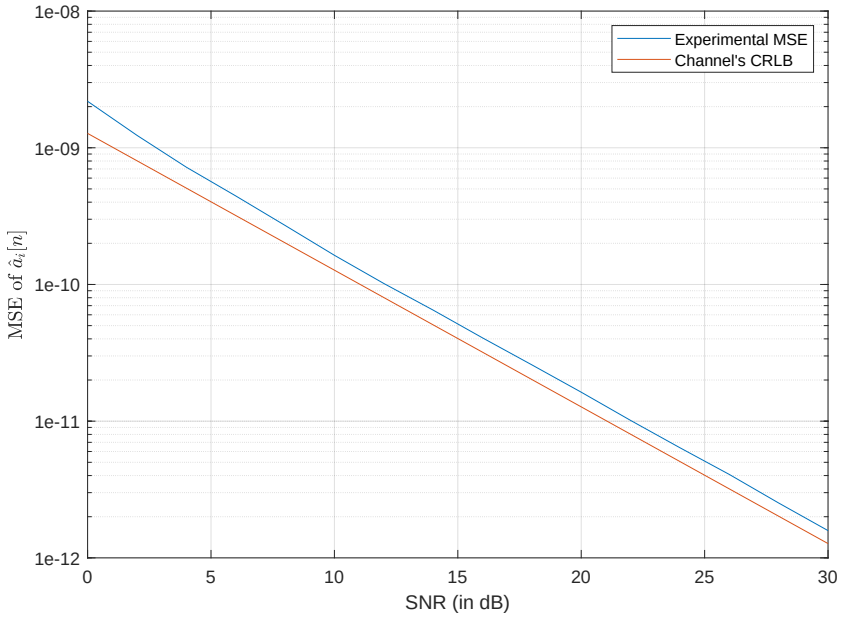

Figure 4.5: Simulated Doppler estimator performance of $\hat{a}_i[n]$, quantified by MSE, given $W = 400$ Hz and $f_c = 2048$ Hz. Note that the measured MSE slowly approaches the theoretical CRLB when shift-orthogonal pilots are used.

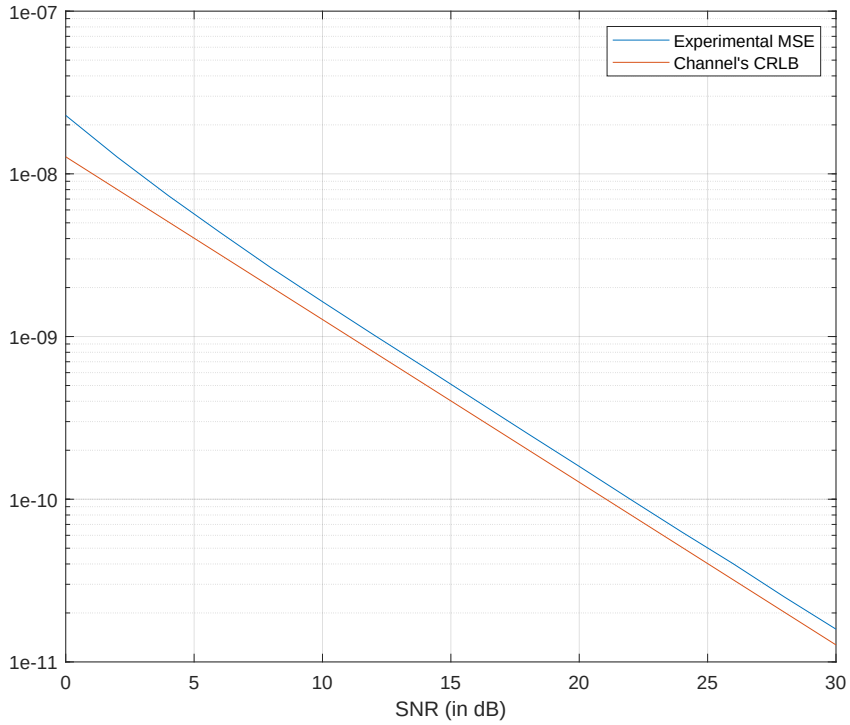

Figure 4.6: Simulated Doppler estimator performance of $\hat{a}_i[n]$, quantified by MSE, given $W = 10$ kHz and $f_c = 24.414$ kHz. Note that the measured MSE slowly approaches the theoretical CRLB when shift-orthogonal pilots are used.

4.5 Comparison to Existing Estimators

The proposed estimator performance is compared to others in the literature previously reviewed (Chapter 2). As mentioned in this chapter's introduction, it is sub-optimal as its MSE can be outperformed (i.e. other methods have lower MSE), but nonetheless, it has distinct strengths that contribute to its merit. It should be noted that none of the reviewed estimators demonstrate their viability for Mach numbers as high as $\approx O(10^{-2})$. The MSE vs SNR results encountered are overlayed on the MSE curves of the proposed estimator. All results are presented in terms of the MSE of the phase estimates $\hat{\Delta}_i[n]$, as phase estimates of the proposed estimator are blind to the sampling frequency and carrier frequency used, making for a fairer and more concise comparison with other estimators. Where the MSE performance of the Mach number is presented, the MSE is multiplied by the factor $(2\pi f_c M T_s)^2$ using the signal parameters presented in the paper to arrive at the MSE of the Doppler phase estimates.

Recall that the CRLB in this work is derived with the M-point shift-orthogonal pilots in mind. As such, the CRLB changes depending on the type of sequence used for transmission, and it represents the best unbiased estimator (MVUE) that uses the specified sequence. It is therefore not surprising to find estimators with MSEs falling below the CRLB documented here, since different sequences were used for transmission in the reviewed sources.

In terms of computational complexity, the proposed estimator has the lowest storage requirements as well as the fastest runtime when compared to optimization algorithms such as grid-searching algorithms. As mentioned previously, Eq. (4.7) is implemented using a sliding-window moving average. The MA recursive relation for the estimator is given by

$$\hat{\Delta}_i[n+1] = \hat{\Delta}_i[n] + \frac{\mu_i[n+M] - \mu_i[n]}{M}$$

From this expression, it is observed that each output requires three multiplications and two additions; as such, it uses a constant amount of space. Thus the storage requirement of each output value is of order $O(1)$. Since it is desired to store the output at each sample time, the storage complexity increases to $O(N)$. The time complexity for each output value is also a constant, and running the estimator across the entire frame also results in a time complexity of $O(N)$.

Optimization algorithms have higher time and space complexities as these algorithms typically rely on finding the parameter that best maximizes or minimizes a given objective function (under a set of constraints); as such, there is an element of "trial and error" involved where the objective function is calculated for every element in the constraint or search grid. These algorithms usually rely on high-resolution grids, so the search grid is expected to have a high number of samples. The memory required for the search grid is on the order of the search grid size, while the memory required for the objective function is proportional to the number of elementary operations required to compute each sample times the frame size; the number of elementary operations in these algortihms is usually not constant, as it tends to increase with increasing frame size. The time and storage complexities are thus of order $O(N_s N_o N)$ at best, where N_s is the size of the search grid, N_o is the number of elementary operations in the objective function, and N is the frame size.

The Doppler estimator of Stojanovic [10] is based on frequency grid searching using the narrowband CAF. The proposed Doppler estimator, on the other hand, gives estimates for every sample in closed form. Also, unlike [10], the estimator is sample-based and less intensive computationally. The paper does not provide the MSE performance of the estimator, however it does provide the performance of the compensator (compared in Chapter 5). Though the proposed estimator is not computationally intensive while estimating the Mach number compared to [10], it is computationally intensive during Doppler compensation mainly due to the resampling

step, though the computational intensity does not increase with Doppler shift, which is the case in [10]. This, however, becomes a non-issue since the Doppler effect correction is performed with a subset of the Mach number estimates. These estimates are systematically chosen without compromising accuracy (Chapter 5).

In [23] the grid searching algorithm is based on finding the peak of the narrowband CAF. It also compensates the Doppler effect by resampling and equalization, enabling Doppler tracking in the process. However, while the estimator is substantiated with sea trials, its MSE is not shown.

In [22] the grid searching algorithm is based on finding the peak of the wideband CAF. The Doppler effect is compensated via resampling and RLS equalization, which is capable of tracking the Doppler effect. However, their MSE performance is not presented.

The estimator in [24] is also based on grid searching using warping functions derived from the wideband CAF, and accomplishes this with a backpropagation algorithm. The estimator is limited to shallow underwater environments and outperform existing message passing algorithms. However, there is no in-water validation. MSE performance is not presented and tracking capabilities are not shown.

In [25] two methods are presented to estimate the Doppler effect: wideband CAF searching and fractional Fourier transform. Both estimators are substantiated by in-water measurements, with the fractional Fourier transform method outperforming the grid searching method. However, their MSE values and Doppler tracking are not reported.

In [20] the fractional Fourier transform is applied on linear frequency-modulated signals to estimate the Mach number, but it is severely outperformed by the proposed estimator; also the MSE of the estimator has an error floor that starts at very low SNR, which limits its performance. For $SNR > 0$ dB, it under-performs compared to the proposed estimator. Tracking is absent. Fig. 4.7 documents these results

In [21] a grid-search-based frequency domain estimator is proposed based on the maximum energy peak of the chirp-z transform, which can produce very accurate Mach number estimates; however like [20] the estimator is outperformed and the MSE has an error floor at very low SNRs. See Fig. 4.7.

In [12] - [14] correlation-type grid searching approaches are used that revolve around finding the maximum peak of the autocorrelation function of the received training sequence.

In [12] two such estimators are proposed, but they are both outperformed by the proposed estimator as measured by the MSE and they do not track. The MSE for the second method, claimed to be better, is presented, however it is documented in terms of simulation time rather than SNR, where SNR is fixed at 12 dB. The MSE of the Doppler phase estimates (estimates of $\hat{\Delta}_i[n]$) floors at -5 dB. This corresponds to an MSE of $10^{-5/10} \approx 0.316$. Due to the error floor present, the MSE stays at this value for the remainder of the simulation. Thus this MSE value is shown as a point at 12 dB in Fig. 4.7. It is worth noting that the first estimator outlined in [12] is conceptually similar to the proposed estimator but since the training sequences lack the orthogonality features adopted in this paper, closed-form estimates and tracking are not possible, which forces the use of grid searching. The second method however, which is based on equalization, is capable of Doppler tracking. The methods have not been validated by in-water tests.

In [13] Mach number tracking is absent, and the estimator has higher MSE than the proposed estimator when viewed in terms of phase estimates; furthermore there is an error floor at around 8 dB (see Fig. 4.7). This is partly due to the longer training sequences used in [13] for Doppler estimation, with the minimum length being 2560 (compared to 64 in the proposed estimator). The comparison however can still be considered fair, as the MSE performance of the proposed estimator improves when using longer sequences, albeit at the cost of smaller range of estimation. Recall that

the piloting structure proposed in this thesis requires shorter lengths to better track large magnitude channel dynamics. The estimator in [13] was also not shown tested against real-life channels.

The MSE performance and real-life measurements in [14] were not provided so it cannot be compared to the proposed estimator, though its performance is justified through simulations.

In [17] four methods commonly used to estimate the Doppler effect are provided. These are: null-subcarrier-based; pilot-aided; decision-aided for zero-padded OFDM, and cross-correlation-type estimation for cyclic prefix-OFDM; all four estimators perform grid searching for the Mach number estimates. Fig. 4.7 shows the performance of these four methods referenced to $\hat{\Delta}_i[n]$ corresponding to each estimator. The null-subcarrier-based estimator is shown to have a better MSE performance for the phase estimates, while the cross-correlation-based estimator is outperformed by the proposed estimator. For SNRs less than 13 dB, both the pilot-aided and decision-aided estimators have better MSE performance, but beyond that these estimators get outperformed due to the error floor they experience at 7 dB. All estimators are substantiated in real sea trials, however Doppler tracking is not demonstrated for any of these estimators.

In [15] a correlation-based approach similar to the one proposed in this thesis is used, albeit it is a one-shot estimator as the estimates are not updated in real-time, which means that it is unable to track the Doppler effect. [18] assumes cyclostationarity (i.e. a periodic WSS process) to derive a grid-search-based estimator that detects the peak of the circular autocorrelation function. MSE performance and sea trial results are not shown so comparisons against the proposed estimator is not possible. [19] uses a correlation-type estimator similar to the one presented here though MSE performance is not reported.

In [11], delay-Doppler sparsity (inherent in UWA channels) is exploited to arrive at a recursive estimation scheme based on compressed sensing that tracks the channel. However the channel tracker is quite outperformed by the proposed estimator and tracker. Furthermore, it is substantiated only with simulations; no measurements from in-water experiments are reported. A direct MSE comparison may be unfair as [11] tracks the channel delay taps and the Doppler shift simultaneously. The paper can thus be considered a case study that enforces the following statement: Doppler estimation and correction prior to channel estimation often has better performance than attempting to estimate the time-varying channel directly.

In [16] an approach based on harmonic retrieval is used, but it is outperformed by the proposed estimator as quantified through the MSE. Furthermore, the estimator fails at SNRs less than 15 dB due to the high MSE documented at this range; the estimator therefore has higher SNR requirements for good estimation (see Fig. 4.7).

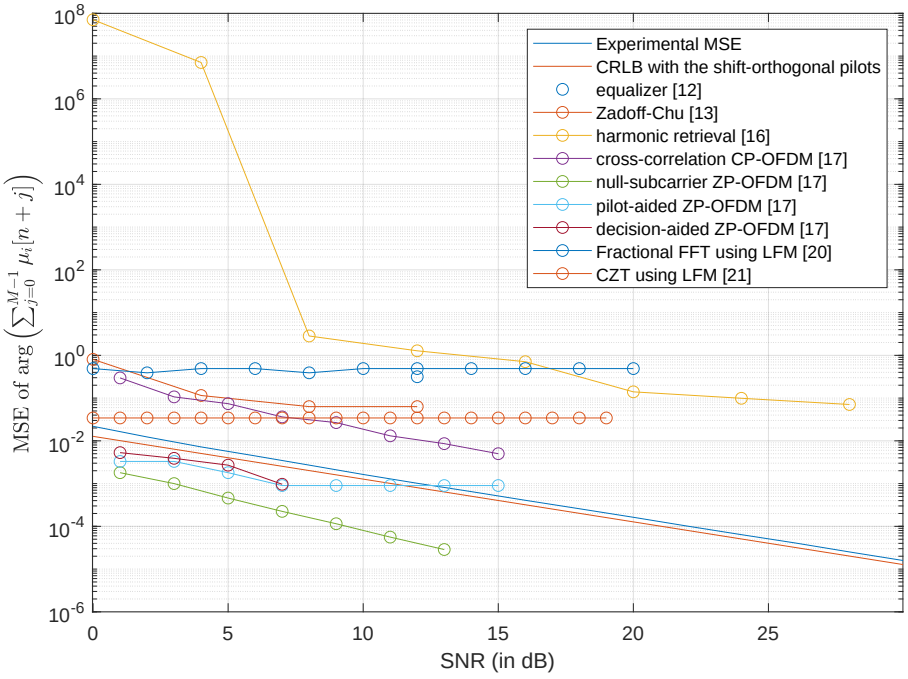

Figure 4.7: MSE performance comparison of existing estimators with the proposed Doppler estimator. All performance curves are referenced to MSE $[\hat{\Delta}_i[n]]$ in order to avoid dependence on signal parameters such as carrier frequency and sampling frequency.

In [26] the projected gradient method is used to find the peaks of the wideband cross-ambiguity function to reduce the computational complexity of standard methods based on ambiguity function grid searching, like the ones outlined, above. However, the MSE performance of the estimator is not demonstrated, and it is still more computationally intensive than the proposed estimator.

4.6 Concluding Remarks

The chapter proposes a correlation-type receiver that exploits the *apriori* known structure of the training sequence. The structure of the training sequence thus dictates the performance of this kind of estimator. In this thesis the shift-orthogonal pilot structure (Chapter 2) is chosen as it is more tolerant of fast fading channels than other pilot structures. The training sequence from this design is then autocorrelated at the receiver with a correlation delay, equal to the size of the training sequence, from which Mach number estimates are derived. The estimator yields a closed-form solution to the Doppler estimation problem and demonstrates low computational complexity. It is also capable of Doppler tracking.

As discussed in the previous section, the MSE of the proposed estimator is shown to outperform (be lower than) most grid-search-based estimators (when presented in the paper for comparison). It is also shown to be less intense computationally compared to grid searching, and as mentioned before, it produces a closed-form solution to the problem, thus avoiding the estimation ambiguity from which grid searchers suffer. Tracking is available in some of these estimators, but not sample-by-sample, as in the proposed estimator. The proposed estimator's MSE is lower than existing correlation-type estimators, fractional Fourier transform methods, sparsity methods, harmonic retrieval methods and gradient methods (when presented in the paper for comparison) and most of these estimators do not track the Mach number. Projected gradient estimators are also more computationally intensive.

Some estimators are found to have better MSE performance, however they suffer from other glaring issues, particularly their computational complexity, their inability to perform Doppler tracking, and estimation ambiguity in the case of most available grid searchers. In this regard, the proposed estimator excels.

Chapter 5

Doppler Compensation and Tracking

5.1 Introduction

After estimating the Mach number, the next task is to compensate the channel Doppler effects. Since the Mach number dilates/compresses the signal, resampling is a natural step in the Doppler compensation process. The overwhelming majority of Doppler compensators include some form of resampling in their design. Resampling results in mitigating signal dilation/compression as well as reducing the Doppler shift of the signal, though it does not fully mitigate due to estimation errors. This results in a small carrier frequency offset (CFO) known as the residual Doppler shift, which can be estimated and corrected in a variety of ways. In short, Doppler compensation is broken into the following steps:

- Perform signal resampling in the passband or baseband.
- Estimate residual Doppler shift, which manifests itself as a CFO.
- Perform CFO compensation to eliminate the residual Doppler shift.

Many approaches to Doppler compensation have been proposed, particularly for residual Doppler compensation since resampling is a staple in most compensators. In this chapter, it will be shown that after resampling, the residual CFO can be estimated with the proposed Doppler estimator (Chapter 4). This is followed by proposing an alternative Doppler tracking strategy to reduce the computational load on the resampler.

5.2 The Doppler Compensator

5.2.1 Stage I: Resampling

Recall that the linear time-varying multipath channel in the passband is generally given by:

$$c(t,\tau) = \sum_{p=1}^{N_p} c_p(t)\delta(\tau - \tau_p(t)) \tag{5.1}$$

where $c_p(t)$ is the time-varying path gain and $\tau_p(t)$ is the time-varying path delay model. Based on the assumptions in Section 2.7, the bandpass received signal can be written as:

$$r(t) = \sum_{p=1}^{N_p} c_p s((1+a(t))t - \tau_p(0)) + n(t) \tag{5.2}$$

where $s(t)$ is the bandpass transmitted signal and $n(t)$ is its noise component. In terms of the M-point shift-orthogonal pilot signals, the received signal is given by:

$$r_i(t) = \sum_{p=1}^{N_p} c_p b_M^{\mathrm{p}}((1+a_i(t))t - \tau_p(0)) + n(t) \tag{5.3}$$

where $b_M^{\mathrm{p}}(t)$ is the bandpass shift-orthogonal pilot sequence. The ith signal, $r_i(t)$, is a block extracted from $r(t)$ whose duration is $t = iMT_s$ seconds, where N_u is the transmitter's upsampling factor, $i \in [1, N_b]$ and N_b is the number of received blocks; $a_i(t)$ is the corresponding Mach number component extracted from $a(t)$ within that same duration. Recall that $a_i(t)$ is assumed to only experience small variations within the M-point preamble block. The lowpass impulse response for such a channel is given by:

$$h(t,\tau) = e^{j2\pi a_i(t) f_c t} \sum_{p=1}^{N_p} c_p e^{-j2\pi a_i(t) f_c \tau_p(0)} \delta(\tau - (\tau_p(0) - ta(t))) \tag{5.4}$$

and the N-point lowpass signal $y(t)$ is in general given by:

$$y(t) = e^{j2\pi a(t) f_c t} \sum_{p=1}^{N_p} c_p e^{-j2\pi a(t) f_c \tau_p(0)} x((1 + a(t))t - \tau_p(0)) + z(t) \tag{5.5}$$

where $x(t)$ is the lowpass transmitted signal and $z(t)$ is the filtered noise. Again, in terms of the M-point pilot signals:

$$y_i(t) = e^{j2\pi a_i(t) f_c t} \sum_{p=1}^{N_p} c_p e^{-j2\pi a_i(t) f_c \tau_p(0)} b_M((1 + a_i(t))t - \tau_p(0)) + z(t). \tag{5.6}$$

where $b_M(t)$ is the lowpass M-point pilot signal. Here, the lowpass signal, $y_i(t)$, is extracted from $y(t)$ for a duration of $t = iMT_s$ seconds; $a_i(t)$ is also extracted from $a(t)$ for the same duration. Looking at the expression for $r_i(t)$, the Doppler effect can be compensated by either resampling in the passband or baseband. Now, consider bandpass resampling and let the resampled signal be given by $r'_i(t)$. Then,

$$r'_i(t) = r_i\left(\frac{t}{1 + \hat{a}_i(t)}\right) = \sum_{p=1}^{N_p} c_p b_M^{\mathrm{p}}\left(\frac{1 + a_i(t)}{1 + \hat{a}_i(t)} t - \tau_p(0)\right) + n'_i(t) \tag{5.7}$$

where $n'_i(t)$ is the resampled noise.

Let

$$d_i(t) = \frac{1 + a_i(t)}{1 + \hat{a}_i(t)}. \tag{5.8}$$

$d_i(t)$ is the block's residual resampling factor. Note, an accurate Doppler estimate and an accurate resampling method mean that $d_i(t) \approx 1$, which should eliminate dilation/compression from the signal. Thus dilation/compression can be compensated

with high accuracy by simply resampling at the passband using any of the many tried-and-true resampling methods available. Downconverting $r_i'(t)$ yields:

$$y_i'(t) = e^{j2\pi \frac{a_i(t)-\hat{a}_i(t)}{1+\hat{a}_i(t)} f_c t} \sum_{p=1}^{N_p} c_p e^{-j2\pi a_i(t) f_c \tau_p(0)} b_M \left(t \cdot d_i(t) - \tau_p(0)\right) + z_i'(t). \tag{5.9}$$

After resampling, the second stage of compensation is residual Doppler compensation which is discussed next.

5.2.2 Stage II: Addressing the Residual Doppler

From Eq. (5.9) one can see the effects of resampling. Firstly, resampling $r_i(t)$ with the resampling factor $1+\hat{a}_i(t)$ reduces sample drift. Secondly, resampling in the passband yields a residual Doppler shift in the baseband that manifests itself as a CFO. This residual CFO should also be compensated. Let the residual Doppler shift be given by:

$$\delta_i(t) = \frac{a_i(t) - \hat{a}_i(t)}{1 + \hat{a}_i(t)} f_c. \tag{5.10}$$

Therefore,

$$y_i'(t) \approx e^{j2\pi\delta_i(t)t} \sum_{p=1}^{N_p} c_p e^{-j2\pi a_i(t) f_c \tau_p(0)} b_M(t - \tau_p(0)) + z_i'(t). \tag{5.11}$$

Let the estimated residual Doppler shift be $\hat{\delta}_i(t)$. After finding $\hat{\delta}_i(t)$ the CFO can be compensated by a simple phase rotation, allowing for recovery of the Doppler-free lowpass received signal:

$$y_i^{a=0}(t) \approx e^{-j2\pi\hat{\delta}_i(t)t} y_i'(t). \tag{5.12}$$

The proposed Doppler estimator (Chapter 4) can be used to find $\hat{\delta}_i[n]$, the discrete-time version of $\hat{\delta}_i(t)$. Recall $\delta_i(t)$ is assumed to experience only small variations within the block.

The sampled version of Eq. (5.11) is given by

$$y_i'[n] \approx e^{j2\pi\delta_i[n]nT_s} \sum_{p=1}^{N_p} c_p e^{-j2\pi a_i[n] f_c m_p} b_M[n - m_p] + z_i'[n] \tag{5.13}$$

where m_p is $\tau_p(0)$ rounded up to an integer. Now,

$$\frac{1}{M} \sum_{n=0}^{M-1} y_i'[n] y_i'^*[n - M] = e^{j2\pi\delta_i[n]MT_s} D + \frac{1}{M} \sum_{n=0}^{M-1} z_i'[n] z_i'^*[n - M] \tag{5.14}$$

where

$$D = \frac{1}{M} \sum_{n=0}^{M-1} \left[\left(\sum_{p=1}^{P} c_p e^{-j2\pi f_c m_p T_s} b_M[n - m_p] \right) \left(\sum_{p'=1}^{P} c_{p'} e^{j2\pi f_c m_{p'} T_s} b_M^*[n - M - m_{p'}] \right) \right]. \tag{5.15}$$

Using the property in Eq. (2.14) and simplifying yields

$$D = |c_p|^2 \tag{5.16}$$

which is the same as Eq. (4.12). Therefore,

$$\frac{1}{M} \sum_{n=0}^{M-1} y_i'[n] y_i'^*[n - M] = e^{j2\pi\delta_i[n]MT_s} |c_p|^2 + \frac{1}{M} \sum_{n=0}^{M-1} z_i'[n] z_i'^*[n - M]. \tag{5.17}$$

As noted in Section 4.2 the noise quantity $\frac{1}{M} \sum_{n=0}^{M-1} z_i[n] z_i^*[n-M]$, while small, cannot be neglected, mainly because of the small sample size used.

Now, following the same steps as in Section 4.2, the residual Doppler shift estimator is given by:

$$\hat{\delta}_i[n] = \frac{W}{2\pi M} \arg \sum_{j=1}^{M} \mu_i'[n + j] \tag{5.18}$$

where

$$\mu_i'[n] = y_i'[n] y_i'^*[n - M]. \tag{5.19}$$

Finally, the CFO can be compensated according to Eq. (5.12), resulting in the Doppler-free received signal.

Equivalently, one can resample at the baseband, as it is observed from Eq. (5.9) that:

$$y_i'(t) = e^{-j2\pi \frac{\hat{a}_i(t)}{1+\hat{a}_i(t)} f_c t} y_i \left(\frac{t}{1+\hat{a}_i(t)} \right). \tag{5.20}$$

The CFO term, here, is then added to the CFO $\frac{a_i(t)}{1+\hat{a}_i(t)} f_c$ inside $y_i(t/(1+\hat{a}_i(t)))$ which again yields the same residual CFO $\delta_i(t)$.

This concludes the Doppler compensation process. In its current state, Doppler compensation is computationally cumbersome since the Doppler estimator outputs Mach number estimates on a per-sample basis. Although this gives the estimator leverage compared to most other estimators since it can track the Mach number changes in the channel with great detail, it comes at the cost of overloading the resampler. The next section provides an alternative approach to track the Mach number, which then becomes an intermediary process between the estimation and compensation ones.

5.3 Efficient Mach Number Tracking

Since the estimator outputs $\hat{a}_i[n]$ for every sample n in a given block i, it is inherently able to track the Mach number sample-by-sample. Currently, this is followed by resampling using $\hat{a}_i[n]$, which means that the resampling factor changes for every sample in a given block.

Sample-by-sample compensation is computationally intensive. Instead of tracking Mach number evolution every sample, one can track its evolution every $I = N_{\text{track}} M/\alpha$ samples, where N_{track} and α are positive integer multiples of M and $\alpha \in [1, N_{\text{track}} M]$. For example, if $\alpha = 1$, the Mach number is tracked every $N_{\text{track}} M$ samples. This approach effectively amounts to downsampling the Mach number function $\hat{a}_i[n]$ by

the downsampling factor I, which is then fed to the compensator. Thus the Mach number tracker is now just a downsampling filter, and in terms of an FIR filter, is given by:

$$\hat{a}_i^I[n] = \sum_{\ell=0}^{K-1} h_i^I[\ell]\hat{a}_i[nI - \ell] \tag{5.21}$$

where $h_i^I[\ell]$ is the impulse response of the FIR filter for a given block and K is the filter order. The downsampling FIR filter can be implemented in various ways, for example, as polyphase filters. Doppler compensation using $\hat{a}_i^I[n]$ is referred to as block-by-block compensation; note that block-by-block resampling is a form of time-varying resampling.

A necessary condition that the compensator must satisfy is its ability to eliminate tap migrations in the channel impulse response (CIR). Channel tap migration is a consequence of sample drift in the received pilots due to Doppler dilation/compression. Thus the following approach is proposed:

- Attempt block-by-block compensation using $I = N_{\text{track}}M$ for a given N_{track} ($\alpha = 1$) and check if sample drift is eliminated from the CIR.

- If sample drift persists, increase α and repeat until sample drift is eliminated.

Since M is chosen sufficiently small so that $\hat{a}_i[n]$ slowly varies in the M-point OFDM block, sample drift should be eliminated by setting $I = M$. However, this may still be computationally intensive since a large number of preambles may be transmitted due to their short duration. Thus it is important to have a choice for N_{track}, which depends on the channel in question. This is a crucial step to ensure accurate tracking while simultaneously decreasing the computational load. Recall that the proposed Doppler estimator tracks estimates every sample, but sample-by-sample tracking is computationally cumbersome, whence the need for a more practical tracking mechanism arose.

Now that the proposed compensator is defined, its performance must be assesed in simulations to validate the theory and establish performance expectations for at-sea tests (Chapter 6).

5.4 Performance in Simulations

Simulations were performed under various Doppler scenarios. To demonstrate one such scenario, let $W = 10$ kHz, $f_c = 24.414$ kHz and assume that the channel has a fixed Mach number of $a = -0.001$. According to the estimator's design criterion,

$$\frac{|a| f_c M}{W} < \frac{1}{2} \tag{5.22}$$

so a Mach number this large requires a correlation delay, or preamble size, of $M < 204$.

Let $M = 64$ and recall the Simulink model used to test the estimator (Fig. 4.1). Assuming sufficiently high SNR, the Doppler estimator yields a Mach number estimate of $\hat{a} = -0.000999\cdots \approx -0.001$. In this example, the estimate does not vary at all within the block due to the high SNR and absence of multipath. Thus block-by-block compensation is not necessary and one can instead use the overall average Mach number estimate $\hat{a}$.

However, block-by-block compensation will be used here to demonstrate the approach. For channels with larger Mach numbers preamble size, carrier frequency, or bandwidth must be adapted accordingly. For example, if bandwidth and carrier frequency are set as above and it is desired to test the estimator in channels with Mach numbers on the order of 0.01, it is required that $M < 21$, so the pilot sequence's length needs to be reduced for more aggressive channels.

Now, on to compensation. The Simulink estimator model (Fig. 4.1) is a baseband model with no oversampling, so resampling can be viewed as performed on a downsampled, lowpass signal, followed by residual Doppler estimation.

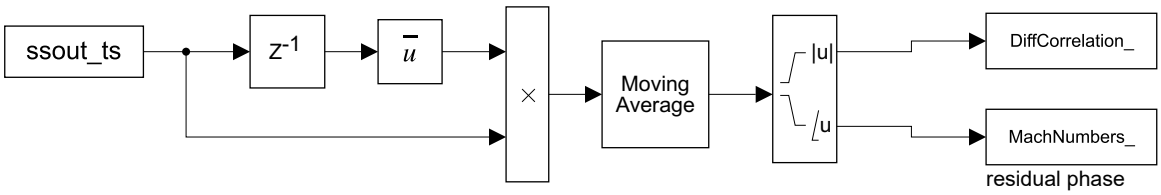

Figure 5.1: Residual Doppler estimator.

From Eq. (5.20), it is required to multiply the received signal by $e^{-j2\pi\hat{a}f_c t}$ before resampling. The resampling process takes the received signal and the set of Mach number estimates "MachNumbers" (both extracted from Simulink as time series variables) and performs block-by-block resampling. The MATLAB script that does this is shown in Appendix 1. Sample-by-sample resampling is included in Appendix 2 for comparison; the computation time is significantly longer, and a program crash is common. These scripts produce the resampled signal as a time series variable, which is fed again to the Doppler estimator Simulink model for residual Doppler estimation as shown in Fig. 5.1.

Since $\hat{a} = a = -0.001$ no residual Doppler shift is expected. This is indeed the case, as the average residual estimate is $\hat{\delta} \approx -2.42 \times 10^{-15}$ Hz. Since the Doppler compensator is essentially just a resampler followed by the proposed Doppler estimator to find the residual Doppler shift, the compensator performance is directly tied to these two elements. Analyzing the resampling algorithm is not a focus here, so compensation performance is viewed in lieu of the proposed Doppler estimator. The Doppler estimator's performance, along with the CRLB, have been documented extensively in Chapter 4.

In Chapter 6, the Doppler estimator, compensator and tracker are tested against real-life at-sea channels, where it is shown how the Mach number can be tracked and

dynamic effects removed in the CIR.

In the next section, the proposed Doppler compensator is compared against those reviewed in Chapter 3.

5.5 Comparison to Existing Compensators

The ultimate goal in compensation is the performance of the residual Doppler estimation step in the compensation process (where the proposed Doppler estimator is applied), because as mentioned earlier, although this work provides two different ways to resample, the focus of this work is not on resampling algorithms and their performance. These are well-documented in the literature and it is left to the designer to choose a suitable resampling technique (e.g. resampling with polyphase filters).

For Doppler compensation, Stojanovic in [10] uses an adaptive PLL-aided decision feedback equalizer capable of tracking and correcting the Doppler effect. However it is computationally intensive and has poorer MSE performance compared to the proposed estimator. Computational load also increases with Doppler shift. Since the proposed compensator uses block-by-block resampling, the proposed Doppler compensation process is significantly faster, compared to [10] which requires resolutions. The reported MSE is in terms of the PLL gain, and hence it cannot be overlayed on the MSE curve of the proposed compensator for comparison. However the MSE values documented are clearly higher. The SNR at which the equalizer is tested is also not documented.

In [19] a compensator similar to the one in [10] is used, but MSE values are not reported. Also similar to [10], the compensation process is slower than the block-by-block resampling proposed here. In [22] time-varying resampling is followed by linear RLS equalization to compensate and track the Doppler effect, though MSE is not documented.

It should be noted that equalizers, like most other synchronization techniques, are often unreliable in UWA communications, due to the ever-present multipath and fading. When using PLL-aided DFEs, the error loop filter bandwidth to track higher Mach numbers can also be difficult to achieve. This, coupled with the fact that the MSE degrades with increasing Doppler shifts, means equalizers are better applied to track slow fading channels. Also, equalizer divergence is possible when using equalizers in fast fading channels.

In [27] a time-varying interpolator is used to resample the received signal. However, the compensator does not take into account residual Doppler shifts, making it susceptible to performance degradation. Experimental MSE from simulations is not recorded, although the compensator is validated in undersea experiments.

In [13], residual CFO compensation is performed after resampling with a grid-search approach based on detecting the maximum autocorrelation peak of the training sequences used by the author. As discussed in Section 4.5, [13] is incapable of tracking the Mach number, and has higher MSE values than the proposed estimator, partly due to their training sequence [13] being of longer length. Also, there are no in-water tests presented. Fig. 5.2 documents the performance of the residual Doppler phase estimates of [13]

In [21] resampling is followed with the bisection method to compensate the residual Doppler, which is also based on grid searching. However their MSE performance is not reported, although their compensator has been validated at-sea.

In [24], warping functions are derived from the wideband CAF to derive a lag-Doppler filter to estimate and then compensate the Doppler effect. The filter uses a backpropagation algorithm to accomplish this, which is a grid searching approach. As mentioned in Section 4.5, the filter is limited to shallow underwater environments, and the MSE performance is inferior to the proposed estimator. The filter is unable to track the Mach number.

In [15] resampling is also employed but is followed by an iterative algorithm known as dichotomization for residual Doppler estimation. This compensator lacks a tracking mechanism, as the residual Doppler estimator is a one-shot estimator. The resampling factor is also fixed. MSE performance of the residual Doppler estimator is not presented.

The performance curves in the previous chapter can also be used here since the proposed estimator is used for find the residual Doppler shift. The comparisons of the previous chapter therefore apply here if one excludes the resampling stage.

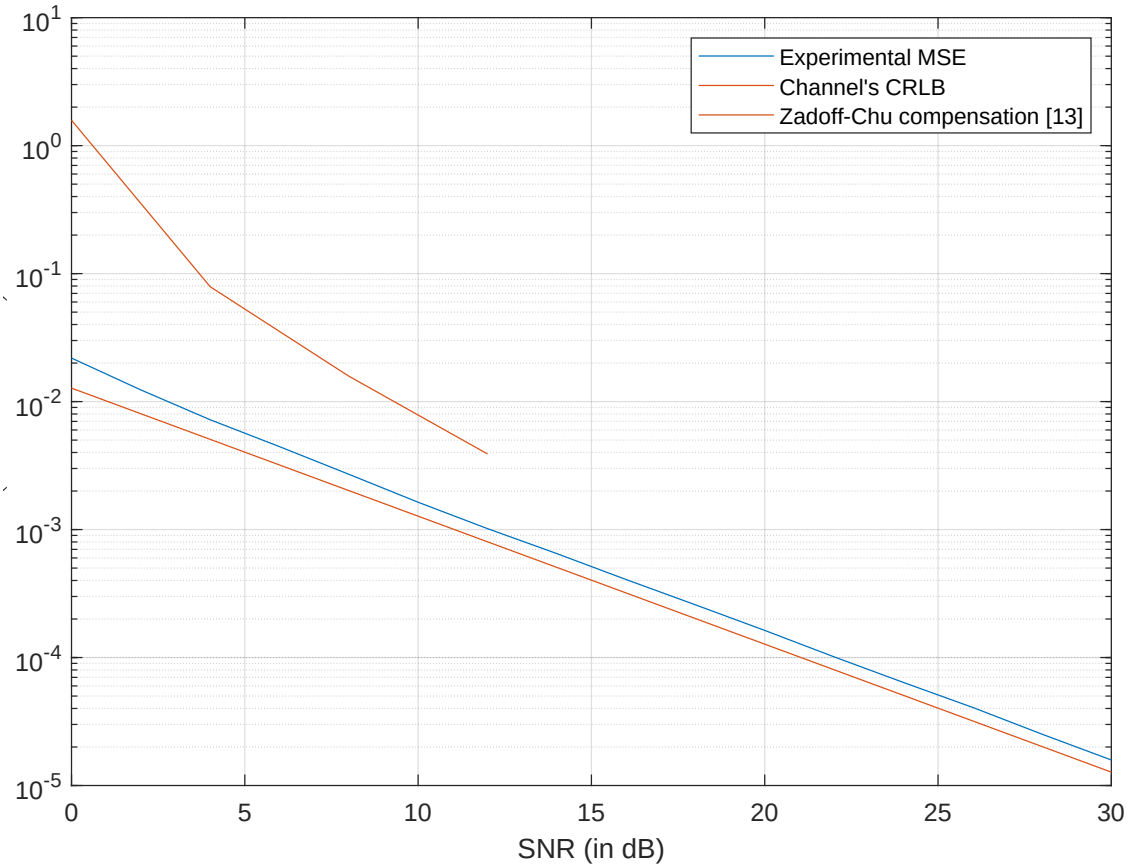

Figure 5.2: MSE performance comparison of the residual Doppler estimator in [13] with the proposed Doppler estimator. All performance curves are referenced to MSE $[\hat{\Delta}_i'[n]]$ in order to avoid dependence on signal parameters such as carrier frequency and sampling frequency. Fig. 4.7 is also applicable here to demonstrate the performance of the residual Doppler estimation process.

5.6 Concluding Remarks

Many authors implement the same techniques for Doppler estimation to perform residual Doppler estimation, namely the grid searchers and correlation-type estimators encountered in Chapter 4. This is due to the residual Doppler shift appearing as a CFO just like the common Doppler shift, though it still needs to be proven that this is indeed the case for their particular estimator. This thesis uses the same approach, insofar as the Doppler estimator proposed in Chapter 4 is also used as the residual Doppler estimator. This was proven in detail in this chapter. The proposed Doppler compensation performance is thus directly linked to the proposed Doppler estimator. As mentioned earlier, the resampler is left to the designer as it is not the thesis' main focus. Thus the resampler performance is not taken into consideration. This treatment is also adopted in Doppler compensation papers that include resampling as part of Doppler compensation.

It was shown that the proposed Doppler compensator outperforms most existing compensators as quantified by the MSE (when available for comparison). Furthermore, the proposed compensator does not suffer the issues of PLL-equipped equalizers. If the received signal is resampled block-by-block, it also performs faster than these types of compensators. It was also observed that the proposed compensator, even when outperformed by others, has unique strengths that distinguish it like the ability to track the Mach number and its confirmed performance in at-sea trials.

Finally, although the proposed Doppler estimator tracks estimates every sample, sample-by-sample tracking is computationally cumbersome. This motivated the need for a more practical Doppler tracker. The proposed tracker downsamples the Mach number estimates, with the choice of downsampling factor depending on the channel in question. The downsampling factor is chosen so that significant changes in the Mach number estimates can be tracked without overloading the resampler.

The next chapter demonstrates how this approach is applied in practice with at-sea measurements of the end-to-end estimator, compensator and tracker subsystem.

Chapter 6

Sea Experiments, Trials and Results

6.1 Introduction

The proposed Doppler estimator and compensator were tested under various underwater channel conditions. Doppler effects are the cumulative results of wave motions, relative platform (boat or buoy) motions if a transmitter or receiver is deployed from it, and the inherent CFO from the transmitter and receiver carrier frequency mismatch (i.e. the transmitter and receiver are not frequency-synchronized). The inherent CFO must be compensated prior to receiver processing to isolate the wave and platform motion effects from the effect of transmitter/receiver carrier mismatch. The CFO, $f_{c,RX} - f_{c,TX}$, inherent in the equipment is ≈ -14 Hz, which corresponds to a system Mach number of -5.7×10^{-4}.

A series of in-water experiments of increasing complexity was performed. The first two trials were deployed off the piers near the Centre for Ocean Venture Enterprises (COVE, Dartmouth, Nova Scotia) in 6 m of water. The third (final) at-sea experiment culminated in the in-situ application and validation of the proposed estimator and Doppler compensator developed. These were deployed in deep water (90 m) from a boat offshore of Nova Scotia on the Scotian Shelf (Chebucto Head). The trials shared resources (e.g. equipment, boat, labour, etc.) with Acoubit Communications Inc. (Nova Scotia, Canada).

The setup for all three trials was similar in that the transmitter was deployed to the same depth as the receiver. The transmitter-receiver separation and water depth were varied for a variety of transmitted signals. The transmitter was housed in a custom

pressure vessel, which was lowered over-the-side of the pier or boat. The receiver used was Acoubit Communication's experimental gateway buoy, "AquaGate," custom built by Turbulent Research Inc. (Dartmouth, Canada). The AquaGate system (Fig. 6.1) consisted of a free-floating surface buoy with a vertical line array of hydrophones tethered at some depth beneathe the buoy. The hydrophones were separated by 20 cm.

Generally, the distance between adjacent hydrophones should be greater than $\frac{\lambda}{4}$ to capture significant change in field distribution, but not at multiples of λ. However, to avoid coupling effects between hydrophones, the minimum distance suggested in practice is $\frac{\lambda}{2}$. In the case here, $\lambda = 1500/24414 = 6.1$ cm. Thus the minimum distance is 3.05 cm. In practice the separation is larger, typically around $3\lambda - 8\lambda$. In all trials, the separation was 20 cm, which is about 3.28λ. This was observed in the shallow and deep water trials. Five hydrophones were used in the shallow water trials and two in the deep water ones.

The receiver array was wired to the above-water Wi-Fi antenna on the gateway buoy so it was possible to observe the received signals in near real-time. The received Wi-Fi signals were analyzed as soon as they were received. In this way, subsequent runs could be modified based on the analysis towards better achieving the trial's goals.

The residual Doppler shift in all these trials was very small. This implies high accuracy in estimating Mach numbers. The long-range sea trials focused on UWA channels where wave motion produces the only time variations in the channel, i.e. no platform motion was introduced. The goal of this chapter is to present a comprehensive analysis of the proposed receiver and its viability to estimate and track the channel wave dynamics and efficiently compensate for it. These results serve as the foundation for planned future work in which the Doppler impact of deliberate motions on platforms like autonomous underwater vehicles will be investigated.

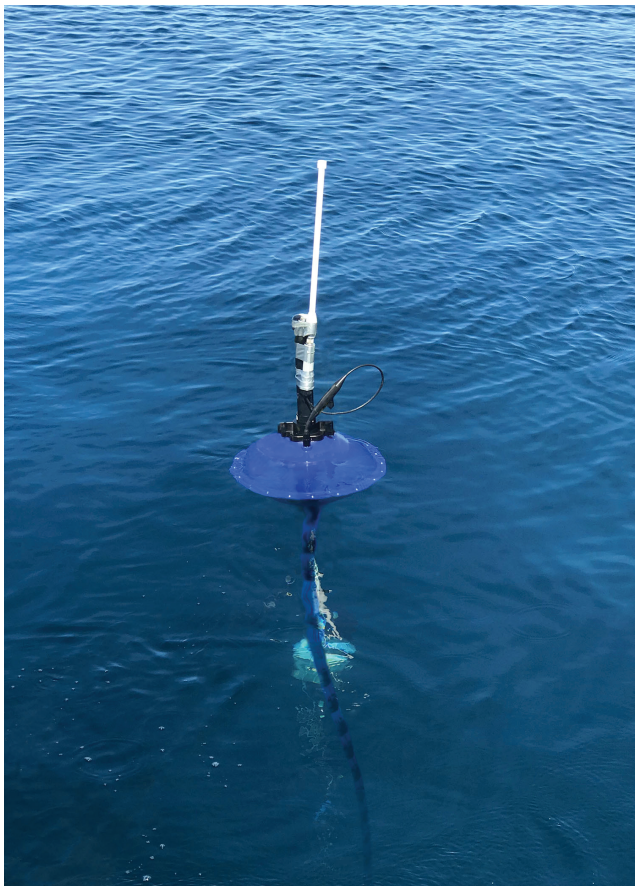

Figure 6.1: Acoubit Communication's "AquaGate" gateway receiver.

As the objective was to have the waves induce Doppler effects no mitigation measures were applied to decouple the surface motions from the ship to transmitter or gateway buoy to receivers.

6.2 Preparations for Scotian Shelf At-Sea Experiments: Short-Range Pier-to-Pier Trials

Prior to the at-sea experiments, short-range work-up trials were conducted to ensure that the transmitter, receiver, auxiliary equipment and signal generation methods used work as intended and to gain familiarity with their operations. These trials were conducted pier-to-pier in shallow water environments ($\approx$ 6 m depths) meaning the transmitter and receiver were deployed off the pier. Five hydrophones in a vertical

line array were the receivers as shown in Fig. 6.2.

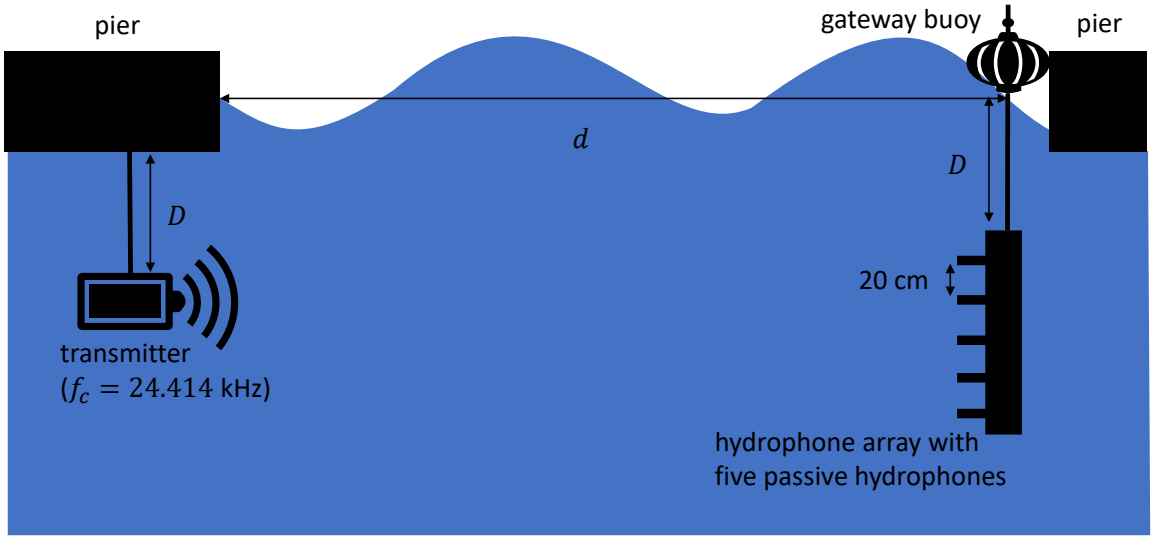

Figure 6.2: Layout for short range, shallow water at-sea validation

Next, the two short-range shallow water trials are discussed.

6.2.1 Proof-Of-Concept: 15-m Short-Range Shallow Water Trials

sampling frequency, f_s (kHz)	carrier frequency, f_c (kHz)	power level, PL	range, d (m)	depth, D (m)	transmission time (s)
9.766	24.414	1	15	6	6
9.766	24.414	2	15	6	6
9.766	24.414	3	15	6	6
9.766	24.414	4	15	6	6

Table 6.1: Trials plan for shallow water work-ups at 15 m range separation between transmitter and receiver (6 m deep water) off piers at the COVE

These trials were conducted on the 21st of August, 2019. The weather was warm (ambient temperature of 20 °C) and the sea condition was fair (small sea swells). The trials plan is summarized in Table 6.1. $d = 15$ m and $D = 6$ m in Fig. 6.2. Preambles made of the shift-orthogonal pilot sequence have a QPSK constellation and a sampling frequency of 9.766 kHz. The transmitted signal has bandwidth of $W = 4.883$ kHz.

As will be seen in the long-range trials, more test bandwidths ranging from 2 kHz to 20 kHz will be used.

In long-range sea trials it is expected that at some range, the signal will fade. The signals with the highest energy will be concentrated in specific time blocks. It is thus not always beneficial to process all the received blocks. This channel will be used to illustrate the approach for this series of tests. To achieve this, the received signal blocks in the first 3 seconds of transmission will be analyzed.

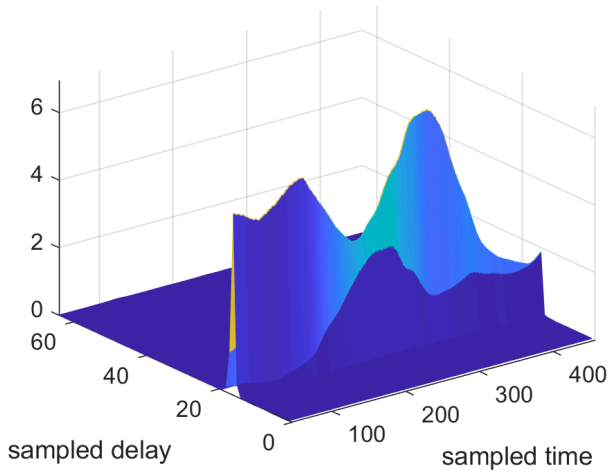

Figure 6.3: CIR for the 15-m short-range UWA channel tests. The channel is shown for a duration of $\Delta t = 3$ s. Sampled time and sampled delay axes are unitless.

Fig. 6.3 shows the 3-second channel's impulse response (CIR). Channel estimates were provided courtesy of Acoubit Communications Inc.

The channel Doppler effects are more apparent in the CIR when it is viewed in terms of its time axes t and τ (observation time and path delay, respectively). This is depicted as a plane view of Fig. 6.3, in the form of a spectrogram (Fig. 6.4).

Fig. 6.4 shows the channel is quasi-stationary since the delay time, τ, for a channel tap remains fixed for all sample times, t, analyzed. Quasi-stationary channels do not require Doppler compensation. Doppler estimation is performed on the 3-second received blocks, followed by tracking, to arrive at the results in Fig. 6.5.

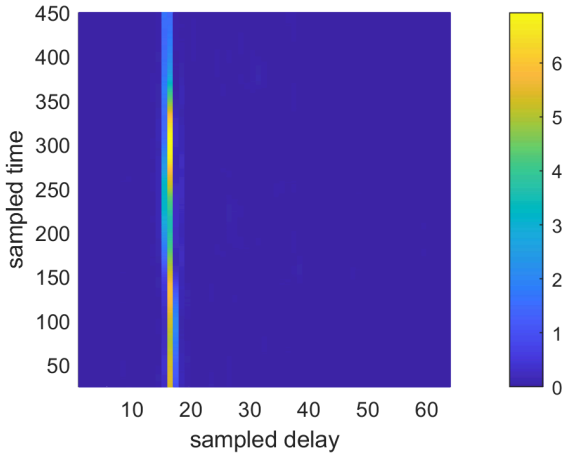

Figure 6.4: Plane view of the CIR in Fig. 6.3. Channel taps with the highest energy are yellow while the green / gray hues correspond to the low-energy taps (see colorbar). The vertical yellow line in Fig. 6.4 shows these channel taps are static. In other words, a channel tap's delay position remains approximately constant for any observation time.

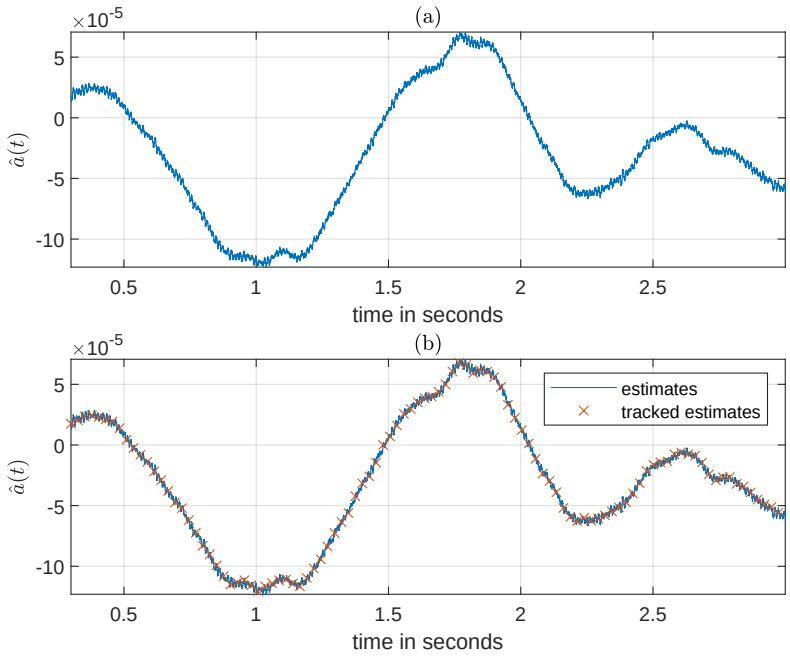

Figure 6.5: 15 m range results for: (a) Mach number estimator and (b) tracker outputs for the proposed receiver. Note how in real UWA channels, the Doppler shifts vary with time. This gives rise to Doppler spread, which can be estimated as $(\hat{a}_{\max} - \hat{a}_{\min})f_c = 3.76$ Hz. This Doppler spread is small w.r.t the subcarrier spacing $9766/64 \approx 152.6$ Hz. The Doppler spread is $3.76 \times 64/9766 = 2.5\%$ of f_s/M. The average Mach number estimate of the channel is -2.6113×10^{-5}.

Fig. 6.5 shows the time variations of the Mach number. Thus the amount of signal shift varies with variations in time t. This gives rise to Doppler spread, which can defined as [38]:

$$B_{\mathrm{d}} = \max_{i,j}\{|a_i(t) - a_j(t)|f_c\} \tag{6.1}$$

This is an alternative definition to Doppler spread, and is different than the one introduced in Chapter 2: the root-mean-square of the Doppler power spectrum. This definition is used later in this chapter when analyzing Doppler power spectrums for the entire channel. However the definition above allows us to have a rough estimate of the Doppler spread from $\hat{a}(t)$ vs t graphs for the RX blocks of interest. Thus rough estimates of the Doppler spread can be extracted for RX blocks of interest without the need to regenerate the Doppler spectrum for every cluster of RX blocks one wants to analyze.

From Fig. 6.5 the Doppler spread of the analyzed signal block is around 3.76 Hz. This corresponds to $3.76/9766 = 0.038\%$ of the sampling frequency or, more importantly $0.038\% \times 64 = 2.5\%$ of the subcarrier spacing. Thus the Doppler spread of the channel over the 3-s duration has minimal effect on the signal. The average Mach number of the channel is estimated to be -2.6113×10^{-5}, which corresponds to an average CFO (which is the average common Doppler shift) of 0.64 Hz (0.0026% of f_c). This, along with the result presented in Fig. 6.4, confirms that such a channel does not require Doppler compensation.

Also of interest is comparing the Doppler analysis of received blocks, for specific durations, to the overall channel Doppler content. This is most apparent in the Doppler power spectrum of the overall channel (Fig. 6.6). Bin 8 corresponds to 0 Doppler frequency. The Doppler power spectrum is shifted by roughly $4.7789 \times 10^{-4} \times 9.5367 = 4.557 \times 10^{-3}$ Hz and the rms Doppler spread is $0.71068 \times 9.5367 = 6.778$ Hz.

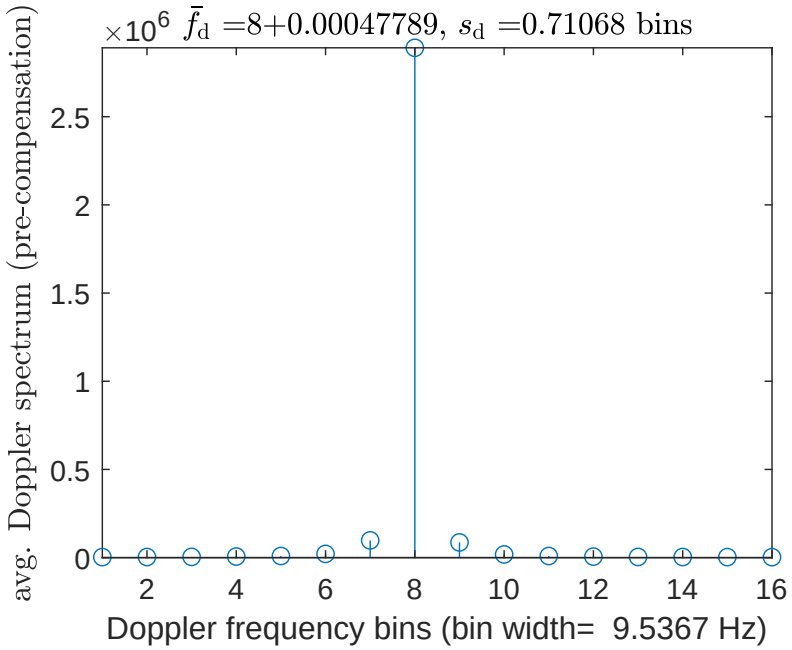

Figure 6.6: For the 15-m channel the spectrum is shifted by roughly $4.7789 \times 10^{-4} \times 9.5367 = 4.557 \times 10^{-3}$ Hz while the rms Doppler spread is about $0.71068 \times 9.5367 = 6.778$ Hz. Thus the overall channel has a smaller average common Doppler shift and a larger spread.

Thus the overall channel has a smaller (almost zero) common Doppler shift and a larger Doppler spread. Although this can give rough average estimates of $\hat{a}$ and B_{d} for the overall channel, the accuracy of these estimates are generally worse than the proposed estimator, especially at longer ranges. This is because the channel estimator provided by Acoubit Communications is a standard cross-correlation-type estimator (i.e. matched filter) which is not ideal for UWA channels, although it has acceptable performance in quasi-stationary UWA channels where there is little wave activity, with the requirement of sufficiently high SNR. In the next series of trials, the effect of Doppler compensation on these parameters is explored.

The scatter plot of the demodulated pilots, after channel equalization, is shown in Fig. 6.7. The constellation has a QPSK structure which suggests the pilots were correctly recovered.

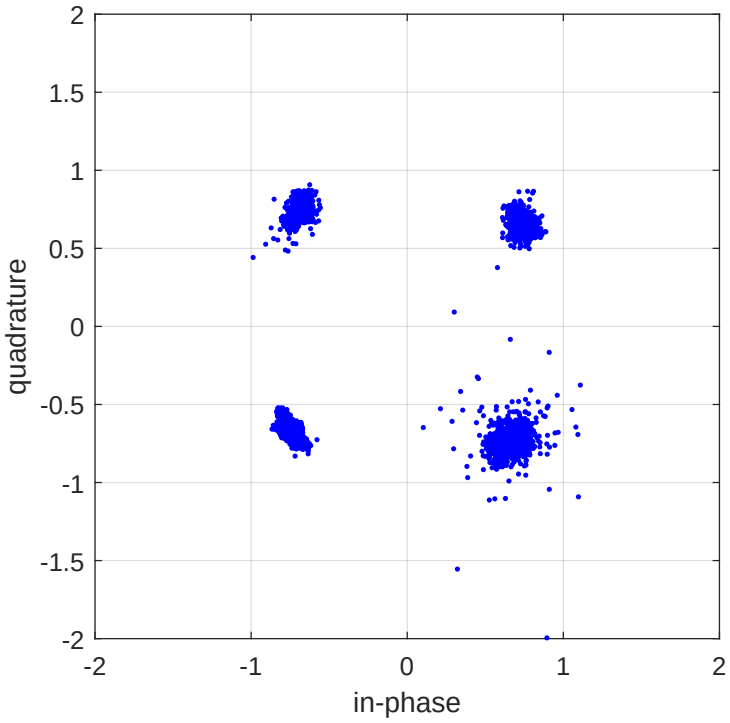

Figure 6.7: Scatter plot of the received QPSK pilots after channel equalization. The tight clustering shows successful channel estimation and recovery of the pilots.

6.2.2 Proof-Of-Concept: 200-m Short-Range Shallow Water Trials

These trials were conducted on the 28$^{\text{th}}$ of August, 2019. The weather was warm (ambient temperature of 20 °C) and the sea condition was fair (small sea swells). The setup is as shown in Fig. 6.2 with $d = 200$ m and $D = 6$ m. The plan for this trial is summarized in Table 6.2.

sampling frequency, f_s (kHz)	carrier frequency, f_c (kHz)	power level, PL	range, d (m)	depth, D (m)	transmission time (s)
9.766	24.414	1	200	6	6
9.766	24.414	2	200	6	6
9.766	24.414	3	200	6	6
9.766	24.414	4	200	6	6

Table 6.2: Trials plan for shallow water work-ups at 200 m range separation between transmitter and receiver (6 m deep water) off piers at the COVE.

Preambles made of the shift-orthogonal pilot sequence have a bandwidth of 4.883 kHz. The total observation time in the channel is 6 seconds. Received blocks from $t = 0$ to $t = 5$ s are used for this analysis. Fig. 6.8 shows the 5-second CIR and the t vs τ spectrogram is shown in Fig. 6.9.

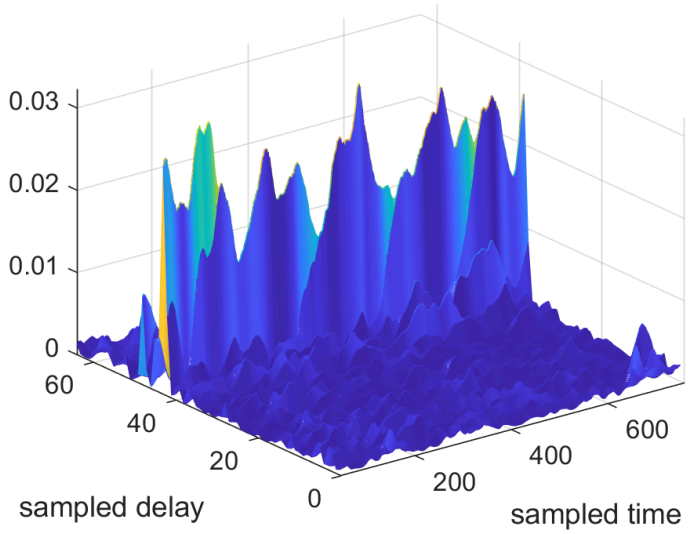

Figure 6.8: CIR for the 200-m short-range UWA channel.

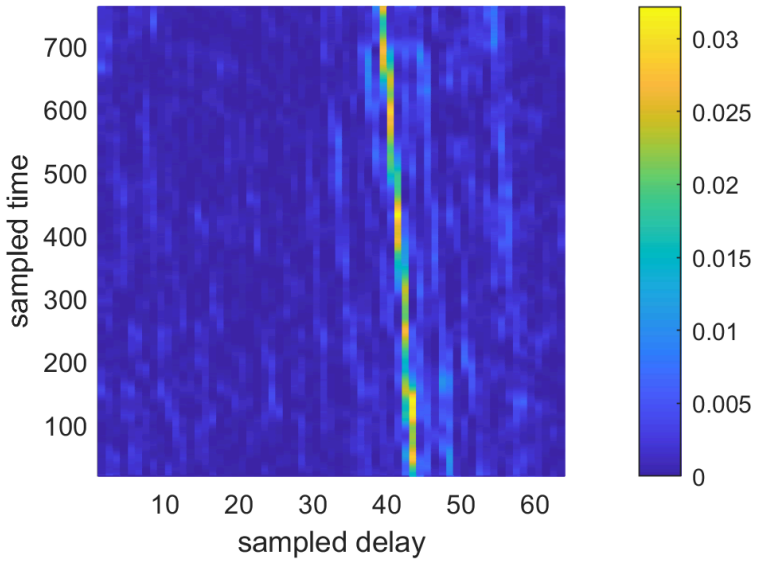

Figure 6.9: Top view of the CIR. The largest channel taps are colored yellow while the green/gray hues corresponds to the low-energy taps (see colorbar). The vertical yellow line is not straight, showing channel tap migrations during transmission.

Fig. 6.9 shows that the channel tap positions shift during transmission. This phenomenon is tap migration and is a manifestation of the Doppler shift. This type of UWA channel requires Doppler compensation over the specific interval, t. Doppler estimation is applied to the 5-second received blocks, followed by tracking, to arrive at the results in Fig. 6.10. The average Mach number estimated for the channel over the 5-s duration is -9.096×10^{-5}, which corresponds to an average common Doppler shift of 2.22 Hz; this is 0.009% of f_c; although the average shift is small, over relatively long durations the received signal will nonetheless be dilated/compressed, resulting in the tap migrations seen in Fig. 6.9. The Doppler spread, estimated using Eq. (6.2), is 4.87 Hz, which is 0.05% of f_s and 3.2% of the carrier spacing f_s/M.

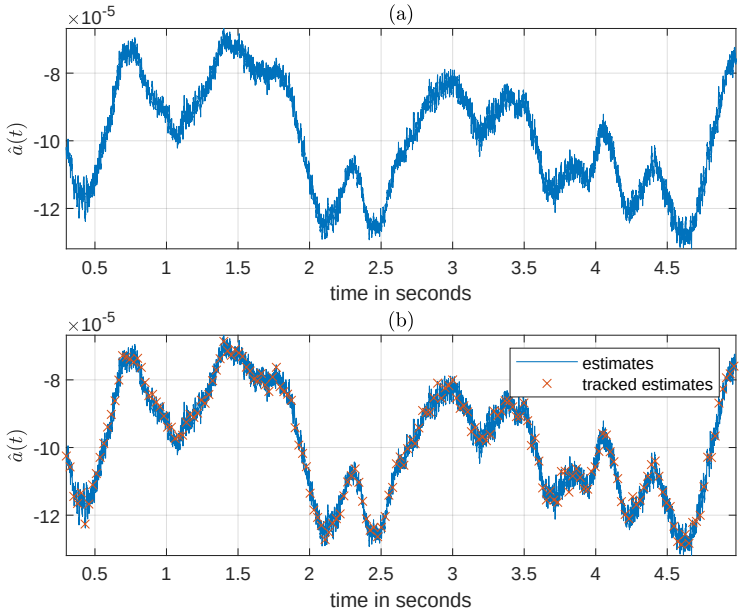

Figure 6.10: At 200 m transmitter-receiver separation: (a) Mach number estimator and (b) tracker outputs for the proposed receiver. Note, in real UWA channels, Doppler shifts vary with time which gives rise to Doppler spread estimated as $(\hat{a}_{\max} - \hat{a}_{\min})f_c = 4.87$ Hz. This Doppler spread is small w.r.t the subcarrier spacing $9766/64 \approx 152.6$ Hz. The Doppler spread is $4.87 \times 64/9766 = 3.2\%$ of f_s/M. The average channel Mach number estimate is -9.096×10^{-5}.

To compare this to the Doppler content of the overall channel, Fig. 6.11 shows the Doppler power spectrum of the channel for the full 6-second duration.

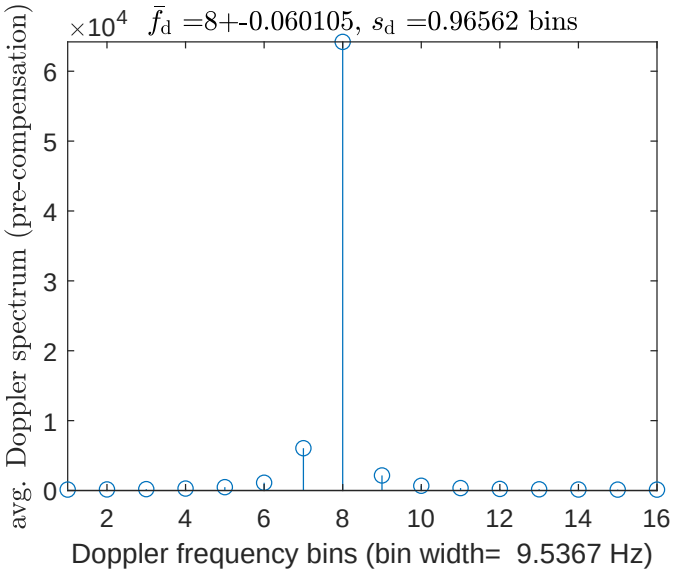

Figure 6.11: For the 200-m channel the spectrum is shifted by roughly $-0.060105 \times 9.5367 = -0.57$ Hz while the rms Doppler spread is about $0.96562 \times 9.5367 = 9.21$ Hz. Thus the overall channel has a smaller average common Doppler shift and a larger spread.

The Doppler shift given by the Doppler power spectrum is -0.57 Hz, which is smaller than the estimated common Doppler shift for the 5-s channel. The spread of the 6-s channel however is 9.21 Hz which is larger than the one estimated from the 5-s channel. Doppler compensation is needed to compensate the channel in Fig. 6.9. The result is shown in Fig. 6.12.

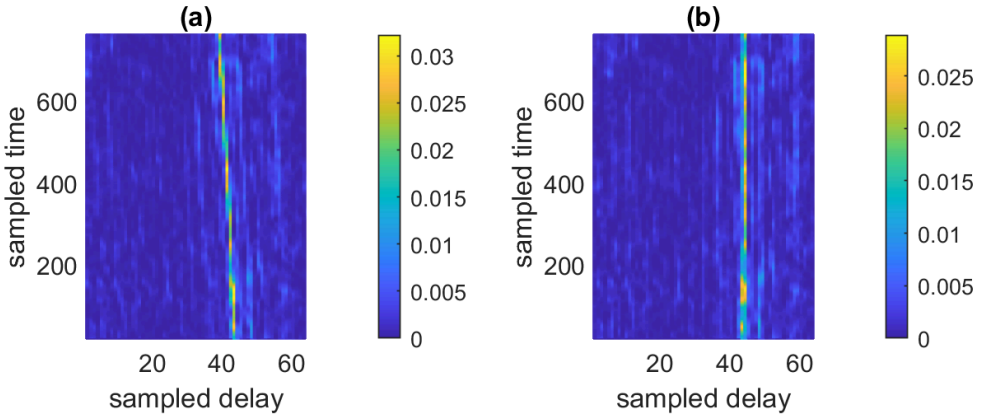

Figure 6.12: Channel impulse response: (a) before and (b) after Doppler compensation. The slanted lines become vertical after compensation, which indicates successful correction of the channel tap migrations.

The corrected CIR shows that the CIR tap locations are returned to their vertical pattern. This shows, visually, that the Doppler effects in the 5-s channel are successfully mitigated. The Doppler power spectrum of the overall channel after compensation is shown in Fig. 6.13. From a comparison of Figs. 6.11 and 6.13, it is apparent that a collateral benefit from compensating the 5-s channel, where most channel taps are located, is that the Doppler shift and spread of the overall 6-s channel are also mitigated. This is due to reducing the dynamic effects in the overall channel.

The scatter plot of the demodulated pilots, after channel equalization, is shown in Fig. 6.14, which shows the QPSK mapping retained at the receiver as expected.

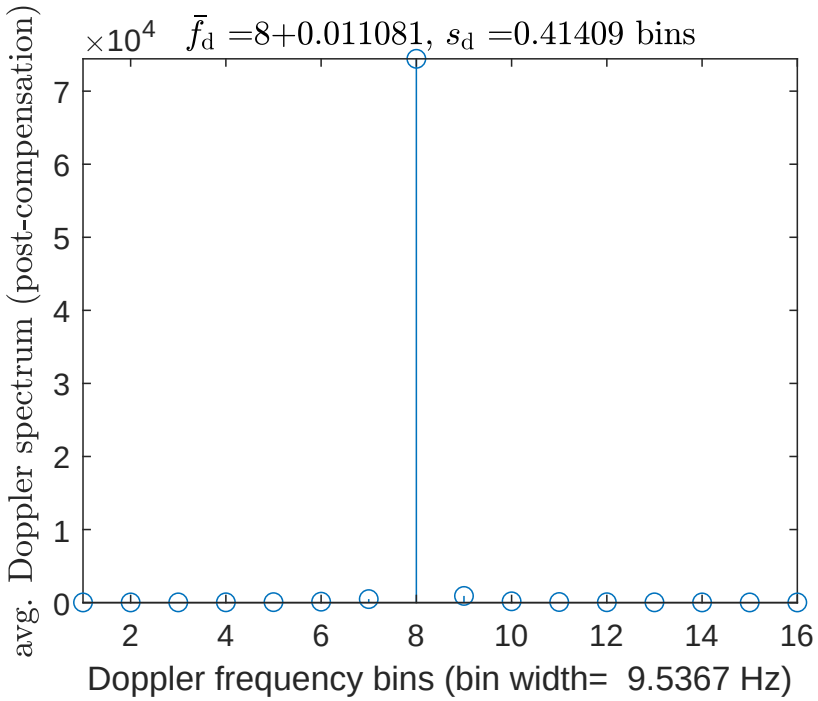

Figure 6.13: For the 200-m channel after compensation the spectrum is shifted by roughly $0.011081 \times 9.5367 = -0.1$ Hz while the rms Doppler spread is about $0.41409 \times 9.5367 = 3.95$ Hz. Comparing with Fig. 6.11 shows that the overall channel is also corrected by the Doppler compensation.

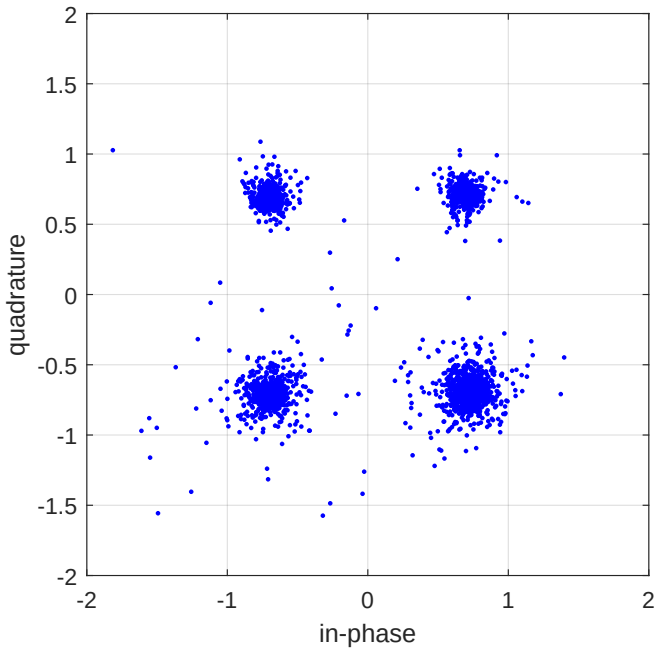

Figure 6.14: Scatter plot of the received QPSK pilots after channel equalization. The tight clustering shows successful channel estimation and recovery of the pilots.

6.3 Validation: Long-Range Deep Water Trials

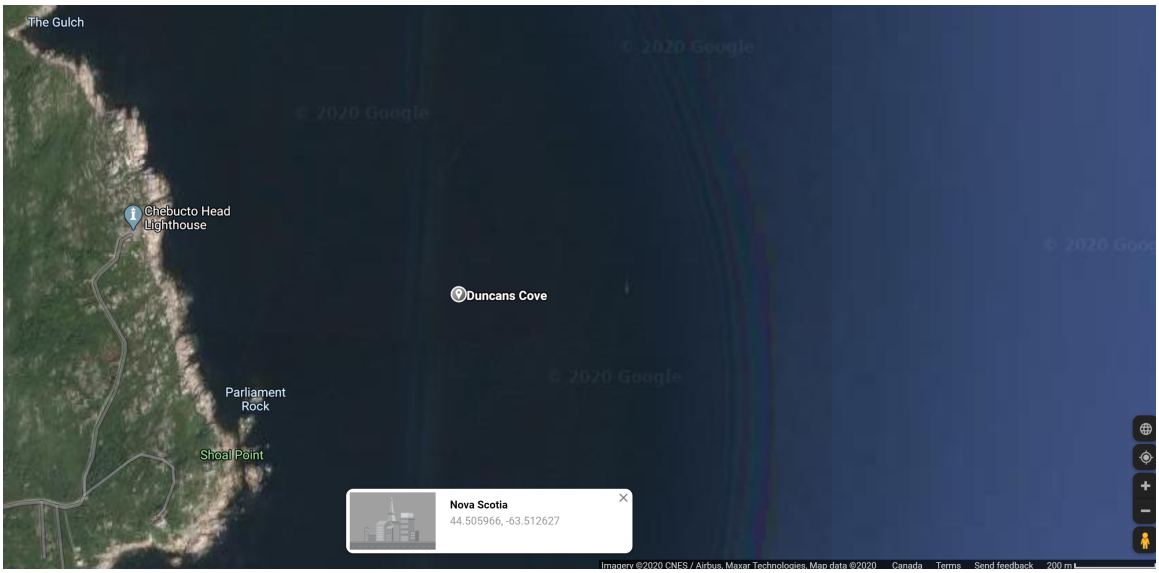

Figure 6.15: Location of the validation experiments on the Scotian Shelf at Chebucto Head.

These trials were performed from 10 a.m. to 5 p.m on October 16th, 2019. The work area (Fig. 6.15) was located just off Chebucto Head (44.505966 ° N, 63.512627 ° W), over an average 90 m water depth. The weather was moderate with 14 km/hr winds and sea swells of 1 m, which will create the desired Doppler effects, since the dominant motions for these experiments were intended to be sea surface ones. The average ambient temperature was 14°C. The experimental configuration in deep water (Fig. 6.16) was similar to what was trialed in shallow waters (Fig. 6.2), the main difference being the transmitter was deployed from a support boat (Fig. 6.17) and two hydrophones were used at the receiver instead of five.

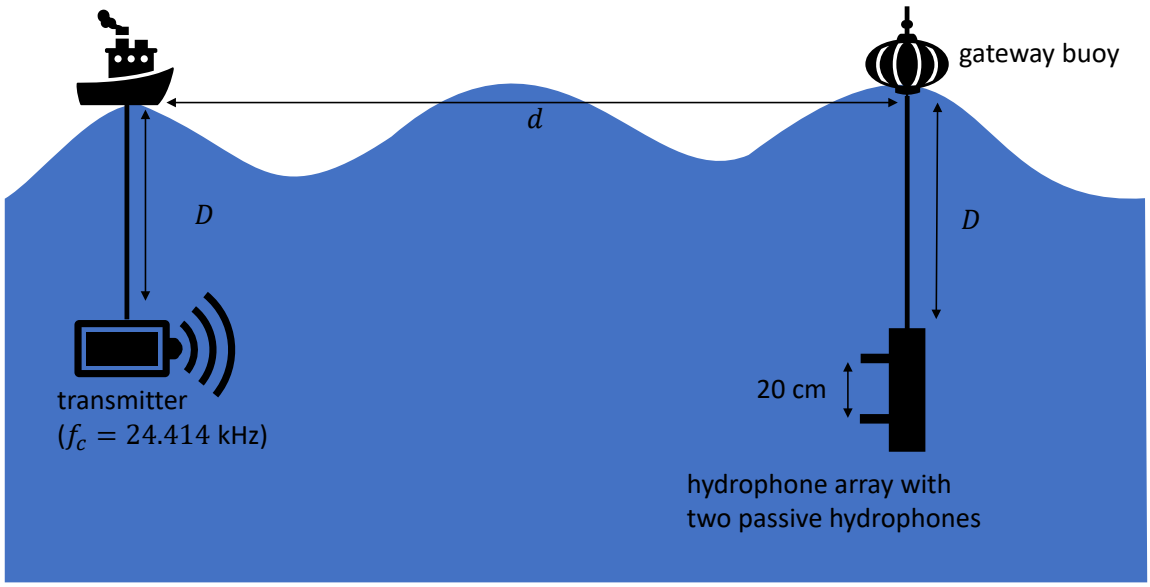

Figure 6.16: Experimental configuration for long range, deep water at-sea validation

For these trials, the transmitter depth was 30 m for $d = 500 - 5$ m, and 60 m for $d = 5$ km. Receiver depth was fixed at 30 m. The detailed trials plan is summarized in Table 6.3. The transmitter carrier frequency was 24.414 kHz. In the transmissions, each preamble was a 64-point shift-orthogonal pilot sequence with a 1 second guard band between preambles.

Figure 6.17: Support boat used for the October 16$^{\text{th}}$, 2019 validation trials offshore of Nova Scotia (in collaboration with Acoubit Communications, Inc.).

The preambles were transmitted at four different power levels where each level was separated by 4 dB (e.g. power level 2 is 4 dB higher than power level 1 and so on). Note that the transmitter's depth was 30 m for all transmission ranges except for the 5-km ranges, where the depth was increased to 60 m. Two hydrophones were used at the receiver to allow for the potential of limited beam-forming. The proposed receiver is designed for single receiver; thus outside of channel estimation, having all hydrophones open was not necessary. Future work will look at extending the proposed receiver for multiple hydrophones.

The transmitted files were designed beforehand and saved as .wav files. At sea, these .wav files were used to drive the transmitter. The transmitted preambles contain the shift-orthogonal pilot sequences discussed earlier in Chapter 2. The preambles have a QPSK constellation. The transmitter upconverts the preambles with a carrier

frequency of $f_c = 24.414$ kHz prior to transmission. Over 60 runs were conducted. The received signals were saved in a .wav format. These files were converted to digital data using the Simulink block"From Multimedia File" Simulink block (see Fig. 6.18) and analyzed using Simulink. The results from a run for a channel are captured by the following:

1. The channel impulse response is displayed in the $t - \tau$ plane to highlight Doppler effects affecting the channel. The plot duration is chosen so that the high-energy channel samples are apparent.
2. The average Doppler power spectrum is shown in discrete time again, defined as the discrete average sum (over τ) of the Fourier transform of the 2-D auto-correlation function $R_h(t, \tau)$. The discrete Doppler frequency axis is normalized to 16 bins for all channels.
3. The Doppler estimator output is shown, where $a(t) = v(t)/c$, and $v(t)$ is the relative velocity between the transmitter and receiver. Since the trials were conducted with no relative platform motion, $v(t)$ represents the water waves' average relative velocity only. The Doppler tracker output is also shown.
4. The QPSK constellations of the demodulated pilots are shown for the entire transmission duration. These are extracted after channel estimation and equalization, but before QPSK demodulation.

6.4 Analysis Methodology

This section describes how the measurements from individual channels (runs), collected as described in the previous section, are reduced, processed and interpreted for the deep-water and long-range validation experiments on the Scotian Shelf. Some detailed examples are presented at the end of the section.

run #	f_s (kHz)	d (km)	D (m)	power level (PL) (1 – 4)
1	1.953	0.5	30	4
2		1.0	30	2
3				3
4				4
5		2	30	1
6		5	60	4
7	4.883	0.5	30	2
8		1	30	4
9		2	30	4
10		5	60	4
11	9.766	0.5	30	1
12				2
13				3
14				4
15		1	30	3
16				4
17		2	30	3
18				4
19	19.531	0.5	30	3
20				4
21		1	30	2
22				3
23		2	30	4

Table 6.3: Support boat used for the October 16$^{\text{th}}$, 2019 validation trials offshore of Nova Scotia (in collaboration with Acoubit Communications, Inc.).

After filtering and downconverting the received signals, the resulting lowpass and downsampled signal passes through the Doppler estimator. Fig. 6.18 shows the Simulink model that accomplishes this processing.

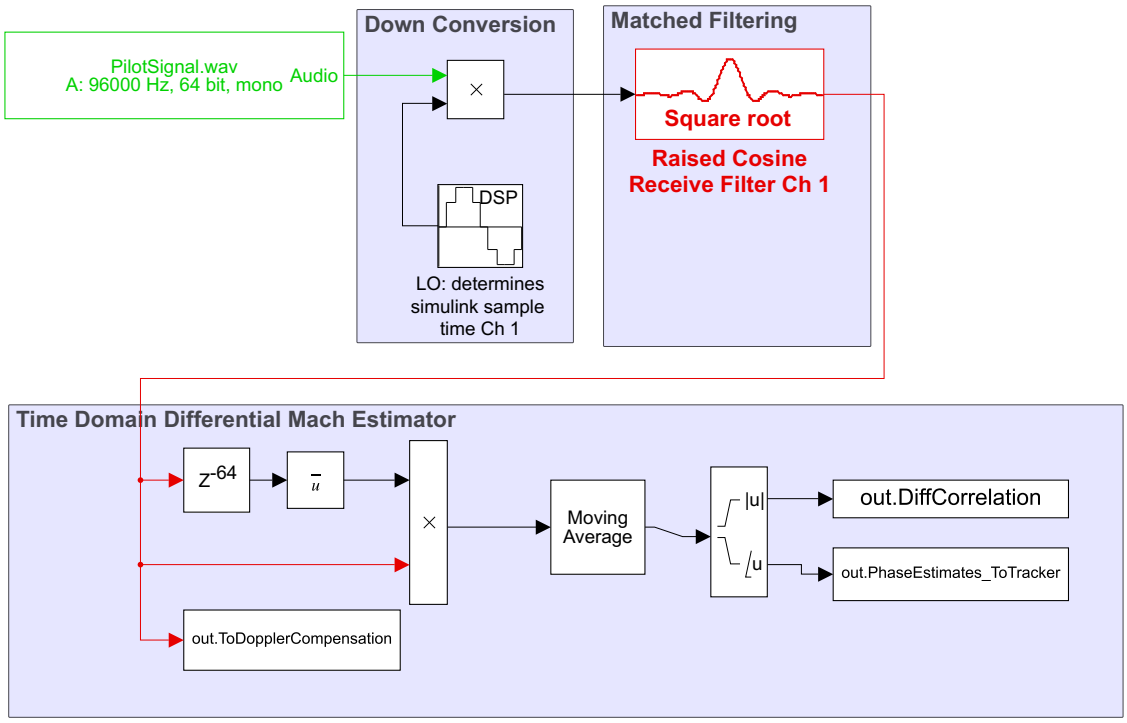

Figure 6.18: Simulink analysis to estimate the Mach number for one hydrophone. The Mach number estimates are tracked in MATLAB by downsampling (Chapter 6). The lowpass and downsampled signal is also fed to MATLAB, where the tracked estimates are used to resample the signal block-by-block.

The proposed receiver is designed for one receiving hydrophone, hence the output of one of the hydrophones is used for the analysis. Then, the Doppler tracker reduces the array length of the Mach number estimates for more efficient compensation. These tracker values are used to resample the signal block-by-block (script in Appendix A-1). After resampling, the signal is fed to the Simulink model in Fig. 5.1 to estimate the residual Doppler shift. Lastly, the output is modulated by $e^{-j2\pi\hat{\delta}[n]nT_s}$ to recover the Doppler-mitigated signal.

As discussed in the previous section, the most revealing information from the analysis of individual channels are the CIR (t vs τ), Doppler power spectrum, Mach number and tracker estimates, and the constellation diagram of the demodulated pilots. Appendix B shows these graphically for twenty-three of the channels acquired during the Scotian Shelf experiment. Out of the sixty trials, these were the most successful. The remaining trials either had corrupted files or experienced severe fading to the point where the received signal was undetectable.

Table 6.4 summarizes the runs and lists averaged values that represent the results, namely, the sample average of the Mach number estimates, sample average of the residual Doppler shift and the rms Doppler spread of the average Doppler power spectrum. The Mach number estimator results are shown as $\hat{a}(t)$ vs t plots. The tracked estimates are overlaid on the $\hat{a}(t)$ vs t plots. Average Mach numbers in this work have an order of magnitude between 10^{-5} and 10^{-4}.

Mach numbers on the order of 10^{-5} are considered "small" and Mach numbers on the order of 10^{-4} are classed as "large" by comparison. The downsampler to track the Mach number has a downsampling factor of 256, meaning that a Mach number estimate is extracted every four preambles.

The results of the Doppler compensation process are shown in lieu of CIR and Doppler power spectrum plots. The CIR is shown in terms of t vs τ where time variations of the channel taps due to Doppler effects are more apparent.

In Appendix B, CIR and Doppler power spectrum plots are shown before and after compensation to highlight the Doppler compensation effectiveness. In the CIR, the Doppler effect manifests as a migration of channel taps; ideally in the absence of channel dynamics, at a given delay $\tau = \tau_0$, a channel tap's position should remain at τ_0 for all times t, and thus high-energy channel taps should appear as vertical lines in a t vs τ spectrogram. Therefore, Doppler compensation should mitigate channel tap migration and restore the CIR to this static behavior.

The average Doppler power spectrum plots in Appendix B are computed by averaging the Fourier transform of the channel's autocorrelation function over τ. In such plots, the Doppler effect manifests itself as a shift in the Doppler power spectrum (equals the average Doppler shift in the entire channel) as well as a spread to other Doppler frequencies. Walree et al.[37] show that the Doppler power spectrum in UWA channels can be represented by an empirical stretched exponential model. That is, the average Doppler power spectrum $\bar{S}_H(\nu)$ in UWA channels barring noise effects is of the form:

$$\bar{S}_H(\nu) = Ae^{-(|\nu-\nu_0|/v)^\lambda} \tag{6.2}$$

where ν is Doppler frequency, ν_0 is the shift in the spectrum, v and A are scaling factors and λ is the stretching exponent ($\lambda > 0$). This hints at one crucial aspect of power content vs Doppler frequency, that being the power is concentrated around the mean and decays away from the mean. This is found to be the case in all the runs displayed in Appendix B, such as Fig. B-14.4 (shown in Fig. 6.20 below).

The shift ν_0 is the average common Doppler shift of the overall channel. Note that Doppler compensation is performed on signal blocks that include higher-energy channel taps, and so the average common Doppler shift af_c and spread (Eq. (6.2)) of the analyzed blocks are in general not equal to ν_0 and B_d.

Though the main goal of Doppler compensation is mitigating af_c (along with sample drift), it also reduces ν_0 and B_d as a side benefit. The Doppler power spectra from Appendix B, such as Figs. 6.20(a) and 6.20(b), represent the Doppler content before and after compensation for the entire channel, and are therefore not representative of the Doppler compensation performance. The discretized Doppler power spectrum is used in the results instead of $S_H(\nu)$.

experimental parameters				Doppler analysis				
run #	W (kHz)	d (km)	PL (1 – 4)	estimation $\hat{a}$		compensation $\widehat{\delta}$ ($\times 10^{-5}$ Hz)	spread B_d (Hz)	Appendix
				$\times 10^{-4}$	($\sim 10^{-4}$)			
1	0.977	0.5	4	-1.2957	✓	-370	3.2024	B-1
2		1.0	2	-0.76964		2.2632	3.2081	B-2
3			3	-0.80691		-1.5696	3.1490	B-3
4			4	-0.95010	✓	23.713	3.4886	B-4
5		2	1	-0.27641		-61.718	5.0873	B-5
6		5	4	-1.5804	✓	120	3.1324	B-6
7	2.441	0.5	2	-1.4458	✓	-61.644	6.5837	B-7
8		1	4	-0.66986		-62.958	6.4144	B-8
9		2	4	-0.63162		-45.686	5.7907	B-9
10		5	4	-1.4432	✓	-210	7.3581	B-10
11	4.888	0.5	1	-0.80060		-15.759	10.1375	B-11
12			2	-1.2850	✓	-20.413	11.4736	B-12
13			3	-0.79488		-71.881	10.0078	B-13
14			4	-0.76510		-7.6450	9.6378	B-14
15		1	3	-0.92101	✓	-72.206	10.4265	B-15
16	4.888	1	4	-0.44963		-0.91021	9.3985	B-16
17		2	3	-0.47873		-71.514	12.7553	B-17
18			4	-0.36252		-30.248	9.0891	B-18
19	9.766	0.5	3	-1.0175	✓	-11.911	14.3482	B-19
20			4	-0.38944		-6.8015	10.8387	B-20
21		1	2	-1.0445	✓	-420	18.0317	B-21
22			3	-0.8846		-380	14.7692	B-22
23		2	4	-0.11636		-560	18.9764	B-23

Table 6.4: Summary of results in Appendix B. $\hat{a}$ and $\hat{\delta}$ are sample averages of $\hat{a}(t)$ and $\hat{\delta}(t)$, respectively. Doppler spread values correspond to the pre-compensation channels. Post-compensation values are not taken into consideration as compensation was applied to the higher-energy channel taps to reduce computational complexity. Thus Doppler spread after compensation is not an indicator of compensation performance.

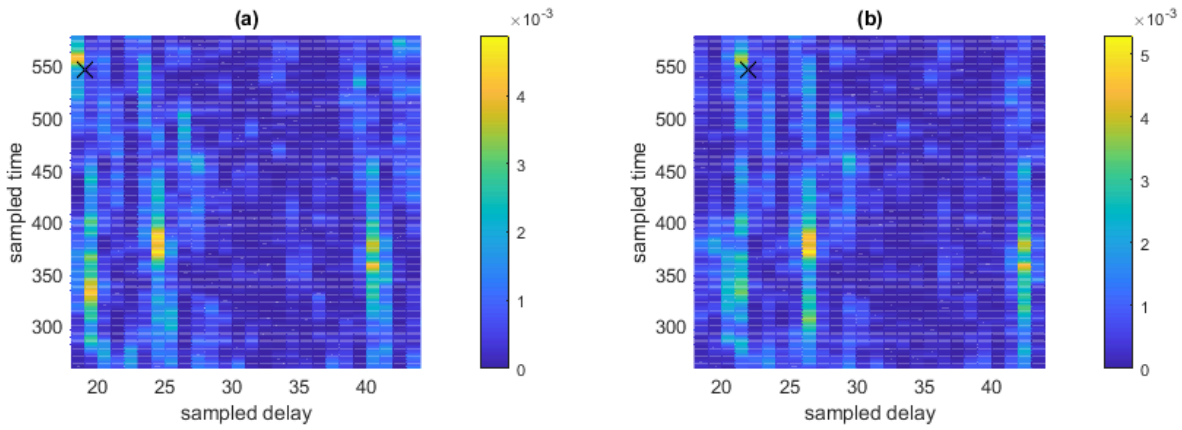

Figure 6.19: CIR comparison (a) before and (b) after Doppler compensation for $W = 4.883$ kHz, $d = 500$ m and PL $= 4$. The CIR is projected onto t vs τ where the effect of Doppler compensation is more evident. High-energy (yellow) taps are compensated. 'x' shows a test tap location before and after compensation. The taps are aligned vertically after compensation, demonstrating proper recovery of channel tap locations.

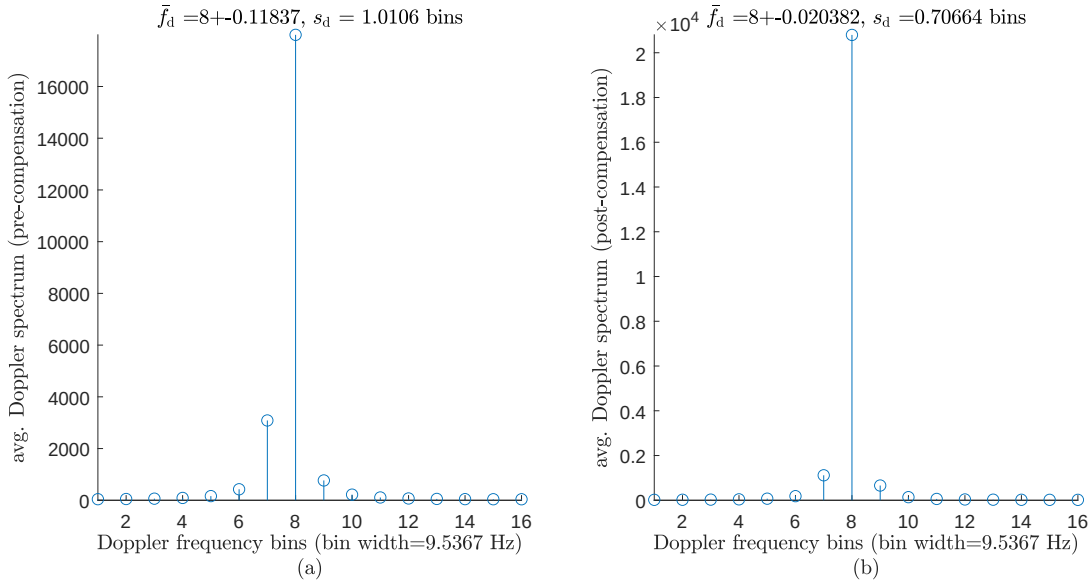

Figure 6.20: Average Doppler power spectrum comparison (a) before and (b) after compensation for the entire channel ($W = 4.883$ kHz, $d = 500$ m, power level 4). The average is computed over channel delays. The spectrum is shifted so that the Doppler frequency of 0 corresponds to bin 8. Doppler spread is small. The centroid of the spectrum is returned to bin 8 after compensation.

The average common Doppler shift of the discrete spectrum is given by $\bar{f}_{\mathrm{d}}$ while the Doppler spread is given by s_{d}. These values are respectively the Doppler shift ν_0 and Doppler spread B_{d} in bins (rather than Hz).

Scatter plots of the demodulated pilots are produced after performing channel estimation (cross-correlation-type) on the Doppler-mitigated signals and equalizing the channel (channel estimator and equalizer are provided courtesy of Acoubit Communications Inc.). These scatter plots confirm whether the QPSK structure of the pilots are properly recovered. As a scatter plot, if the scatter is tightly clustered then the pilots were recovered correctly.

The Mach number estimates from the runs indicate that the Mach number of the UWA channels encountered varied between -1.58e-4 and -1.12e-5. Larger Mach numbers mean that the water waves encountered during transmission were more energetic.

To demonstrate the analysis approach, consider three UWA channels from Appendix B. The selected channels are examples of extreme cases tested: (1) shortest range and smallest bandwidth (B-1); (2) longest range, and (3) highest bandwidth. The processing for all cases was identical however, case (2) provided challenges with longer ranges since there were not as many taps due to fading.

1. B-1: $W = 0.977$ kHz, $d = 0.5$ km, PL $= 4$, $\Delta t = 3.6$ s (shortest range, lowest bandwidth):

   The received signal is taken from $t = 1.4$ s to $t = 5$ s ($\Delta t = 3.6$ s), where highly-correlated channel taps can be observed. Fig. B-1.1 shows the Mach number estimator and tracker, with the Mach number oscillating between -3e-4 and 0. The sample mean $\hat{a} = \frac{1}{N}\sum \hat{a}[n]$ is -1.2957e-4. A downsampling factor of 256 means that the Mach number is tracked every four preambles, i.e. every $256/1953 = 0.13$ s. It can be seen from Fig. B-1.1(b) that the low-frequency

envelope of the Mach number wave is successfully tracked with this approach, ensuring that there will be no substantial loss of accuracy during compensation.

Fig. B-1.3 shows the CIR before and after Doppler compensation for the 3.5-s transmission window. The Doppler effect gives rise to sample drift in the received signal that dilates/compresses the signal, which causes channel tap migration in our channel estimates. Fig. B-1.3(a) clearly shows these migrations. The Doppler compensator successfully mitigates this effect as is seen in Fig. B-1.3(b). The channel's Doppler power spectrum for the entire 5-s channel is shown in Fig. B-1.4. The 8th bin corresponds to zero Doppler frequency. Comparing Fig. B-1.4(a) to Fig. B-1.4(b), it is observed that the overall channel's average Doppler shift is reduced from -1.5 bins (-2.85 Hz) to 0.074 bins (0.14 Hz), effectively eliminating Doppler shift.

The rms Doppler spread of the channel is relatively small (around 0.17% of f_s and 10.9% of f_s/M). The Doppler compensator does not eliminate the spread in general as it only compensates for select signal blocks where high-energy channel taps are located. Consequently, the Doppler spread remains largely unchanged (3.2 Hz estimated before compensation and 3.3 Hz estimated after compensation). Nonetheless, Doppler spread provides insight on how dynamic the UWA channel is.

Fig. B-1.2 shows the pilot signals recovered after Doppler compensation and channel equalization does indeed have a QPSK constellation, indicating successful signal recovery.

2. B-10: $W = 2.442$ kHz, $d = 5$ km, PL $= 4$, $\Delta t = 5$ s (longest range, moderate bandwidth):

   For this channel, the entire 5-s signal is taken. Fig. B-10.1 shows the Mach

number estimator and tracker, with the Mach number oscillating between -2.5e-4 and 0.5e-4. The sample mean $\hat{a} = \frac{1}{N}\sum \hat{a}[n]$ is -1.4432e-4. A downsampling factor of 256 means the Mach number is tracked every four preambles, i.e. every $256/4883 = 0.052$ s. It can be seen from Fig. B-10.1(b) that the low-frequency envelope of the Mach number wave is successfully tracked with this approach, ensuring minimal loss of accuracy during compensation.

Fig. B-10.3 shows the CIR before and after Doppler compensation for the 5-s transmission window. The Doppler effect gives rise to sample drift in the received signal that dilates / compresses the signal, which causes channel tap migration in the channel estimates. Fig. B-10.3(a) clearly shows these migrations. The Doppler compensator successfully mitigates this effect as is seen in Fig. B-10.3(b). The channel's Doppler power spectrum for the entire 5-s channel is shown in Fig. B-10.4. The 8th bin corresponds to zero Doppler frequency. Comparing Fig. B-10.4(a) to Fig. B-10.4(b), it is observed that the overall channel's average Doppler shift is reduced from -0.7 bins (-3.35 Hz) to 0.03 bins (0.14 Hz), effectively eliminating Doppler shift.

The rms Doppler spread of the channel is relatively small (around 0.15% of f_s or 9.6% of f_s/M); the Doppler compensator does not eliminate the spread in general as it only compensates for select signal blocks where high-energy channel taps are located. However in this case, the Doppler spread is slightly reduced from 1.54 bins (7.36 Hz) to 1.26 bins (6 Hz).

Fig. B-10.2 shows the pilot signals recovered after Doppler compensation and channel equalization do indeed have a QPSK constellation, indicating successful signal recovery.

3. B-20: $W = 9.766$ kHz, $d = 0.5$ km, PL $= 4$, $\Delta t = 0.7$ s (shortest range, highest bandwidth):

Here, the received signal is taken from $t = 3.3$ s to $t = 4$ s ($\Delta t = 0.7$ s). Fig. B-20.1 shows the Mach number estimator and tracker, with the Mach number oscillating between -1.5e-4 and 5e-5. The sample mean $\hat{a} = \frac{1}{N}\sum \hat{a}[n]$ is -3.8944e-5. A downsampling factor of 256 means the Mach number is tracked every four preambles, i.e. every $256/19531 = 0.013$ s. It can be seen from Fig. B-20.1(b) that the low-frequency envelope of the Mach number wave is successfully tracked with this approach, ensuring minimal loss of accuracy during compensation.

Fig. B-20.3 shows the CIR before and after Doppler compensation for the 0.7-s transmission window. The Doppler effect gives rise to sample drift in the received signal that dilates / compresses the signal, which causes channel tap migration in the channel estimates. Fig. B-20.3(a) clearly shows these migrations. The Doppler compensator successfully mitigates this effect as is seen in Fig. B-20.3(b). The channel's Doppler power spectrum for the entire 5-s channel is shown in Fig. B-20.4. The 8th bin corresponds to zero Doppler frequency. Comparing Fig. B-20.4(a) to Fig. B-20.4(b), it is observed that the overall channel's average Doppler shift is reduced from -0.0135 bins (-0.26 Hz) to -0.002983 bins (-0.057 Hz), effectively eliminating Doppler shift.

The rms Doppler spread of this channel is relatively small (around 0.055% of f_s or 3.5% of f_s/M); the Doppler compensator does not eliminate the spread in general as it only compensates for selected signal blocks where high-energy channel taps are located. However in this case, the Doppler spread is slightly reduced from 0.57 bins (10.8 Hz) to 0.5 bins (9.58 Hz).

Fig. B-20.2 shows that the pilot signals recovered after Doppler compensation and channel equalization do indeed have a QPSK constellation, indicating successful signal recovery.

The analysis of these channels is summarized in Table 6.4 with performance quantified against the average Mach number $\hat{a}$, rms Doppler spread (in Hz) and average residual Doppler shift $\hat{\delta}$ (in Hz). These parameters are compared with the experimental parameters f_s, d and PL.

6.4.1 Aggregate Analysis

The previous section analyzed the channels individually and provided an overview of the collected in-water measurements. This section will organize the analysis to observe how the channel dynamics vary with parameters like transmission bandwidth, range achievable and power level.

The Doppler compensation is directly affected by the signal-to-noise ratio of the received signals. If the signal excess is zero then there is no signal compensation to consider. Therefore, it is assumed that there will be sufficient SNR before Doppler effects can be perceived and then compensated for. This can be an issue at the longer transmitter-receiver ranges tested like 2 km and 5 km.

The next subsections organize the processed in-water measurements to observe Doppler spread dependencies and validate the performance of the proposed Doppler estimation, tracking and compensation.

i. Mach Number

The expectation was Doppler spread is independent of the Mach number. The percentage of Doppler spread and mean Mach number estimates $\hat{a}$ in Table 6.4 are plotted in Fig. 6.21. As expected, there is no discernible relationship between the magnitude of the channel's Mach number and the effect of Doppler spread on the propagating signal. That is, increasing Mach number does not impact Doppler spread.

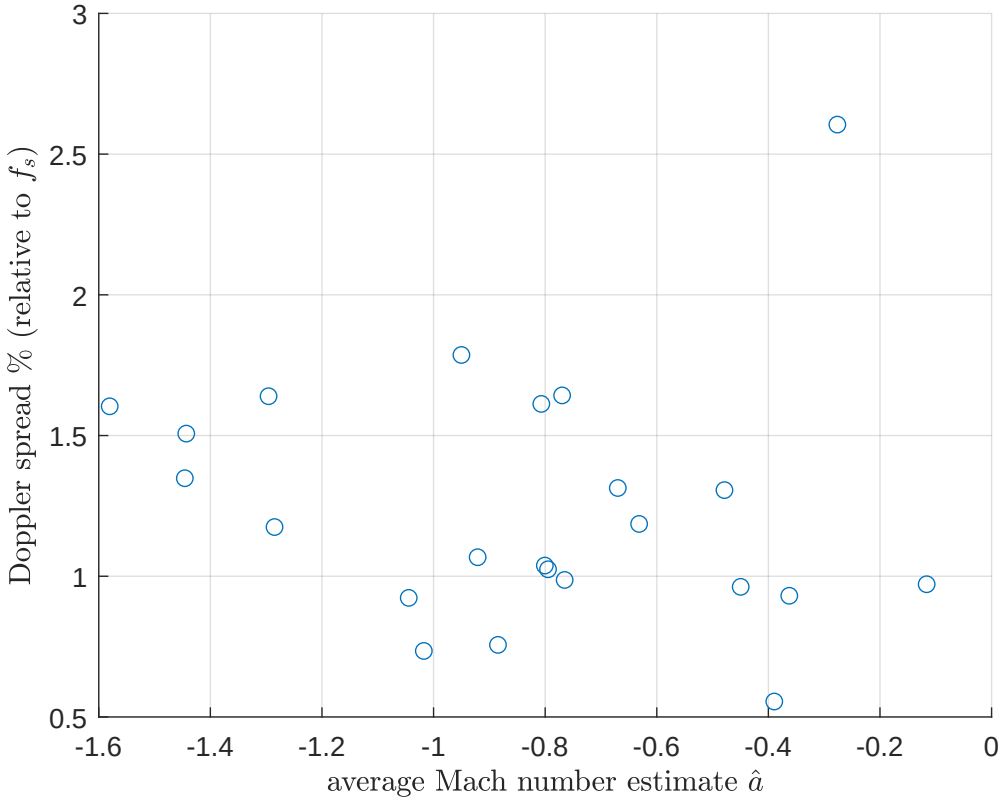

Figure 6.21: No relationship is apparent between Mach number and Doppler spread.

The Mach number depends on the relative motion between transmitter and receiver. Doppler spread on the other hand depends on time variations resulting from propagation (environmental) factors such as scattering from surface waves and small targets like fish, air bubbles, etc. It can also depend on the sound speed profile. If there was a minimum (inflection) in the sound speed profile with depth, the acoustic waves would propagate mostly horizontally around the depth of the inflection point. Unfortunately, it was not clear what the sound speed profile was like in the work area as no in-water sound speed measurements were made.

The micropaths spawned by scattering sources were not captured. This may have a larger contribution than anticipated. This will be addressed in future modelling and measurements.

ii. Range

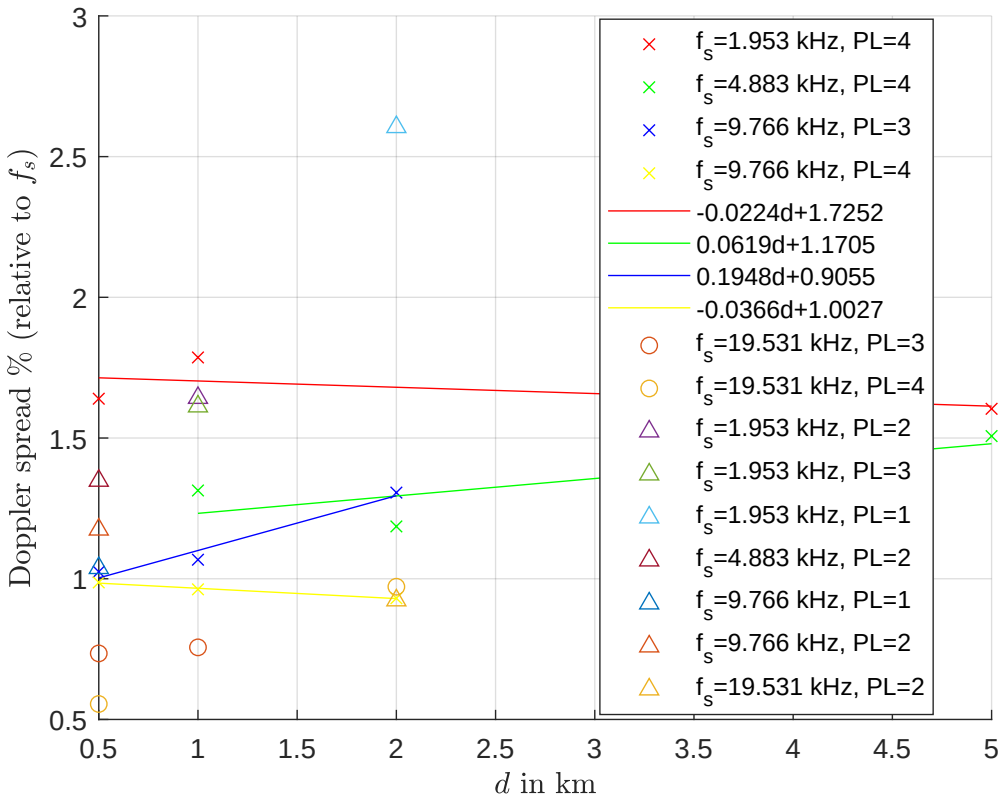

Figure 6.22: Data sets denoted by '×' are linearly fitted as they contain three or more points. The effect of Doppler spread decreases with transmission range with the exception of two outliers (red and yellow lines).

It is known from physics that Doppler spread generally gets smaller with transmission range because at larger distances the propagation paths experience smaller grazing angles at the moving sea surface. This geometrical trend results in smaller Doppler contributions from these paths. Fig 6.22 shows two lines conforming to this relationship, namely $W = 0.9766$ kHz and PL $= 4$, and $W = 4.883$ kHz and PL $= 4$. The other two lines ($W = 2.442$ kHz and PL $= 4$, and $W = 4.883$ kHz and PL $= 3$) shows the opposite behavior. This is because Doppler spread does not depend only on range; other factors that contribute to Doppler spread include surface scattering at sea surface and ocean bottom.

iii. Transmission Bandwidth

The expectation is that with increasing transmission bandwidth the Doppler spread would be lower. Doppler spread percentage and transmission bandwidth (W) in Table 6.4 are plotted in Fig. 6.23, where range (d) and transmission power level (PL) are held constant.

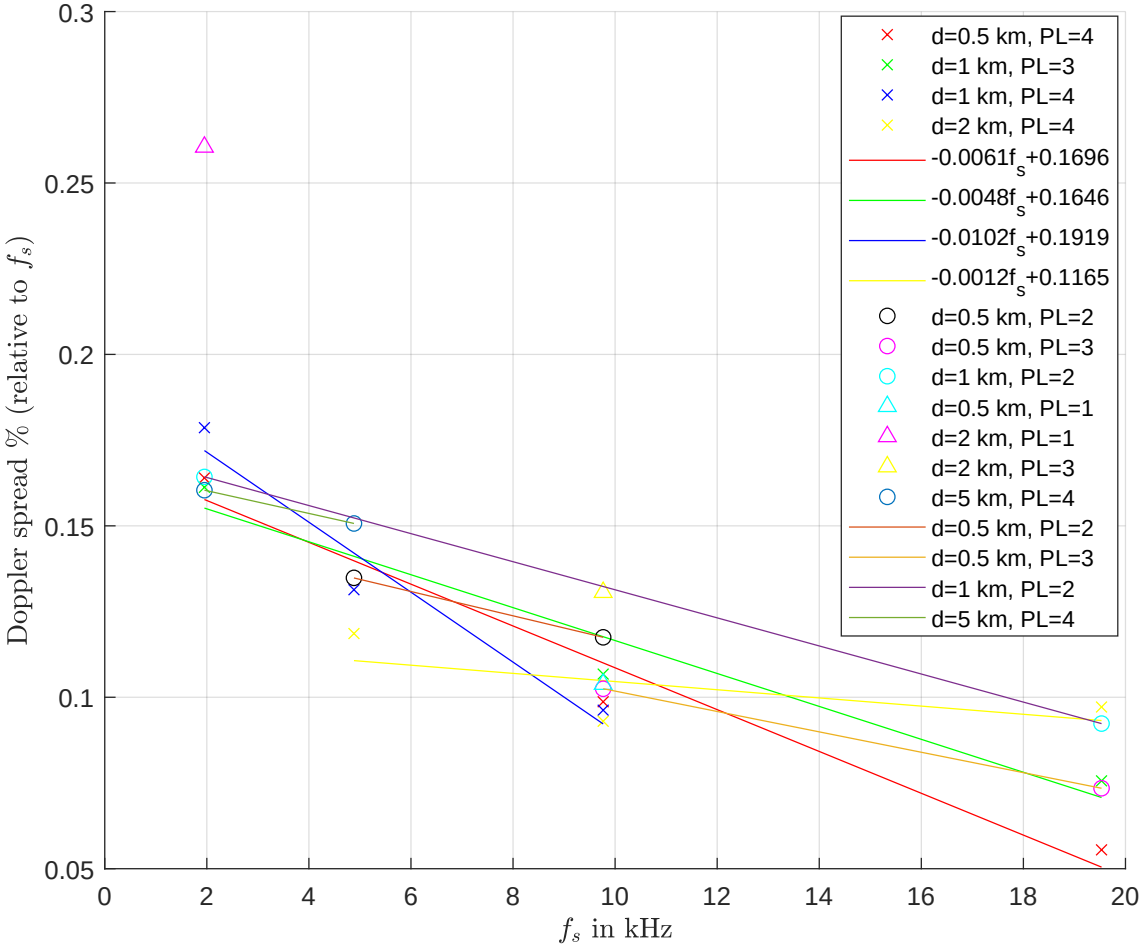

Figure 6.23: Data sets denoted by '×' are linearly fitted as they have three or more points. The effect of Doppler spread on the signal reduces when transmission bandwidth is increased. The first-order coefficients of the lines are in %/kHz while the zero-order ones are in %.

Fig. 6.23 shows that Doppler spread percentage decreases with respect to bandwidth. In other words, although the Doppler spread, in Hz, increases with bandwidth,

as observed in Table 6.4, transmission signals with larger bandwidths are more resilient against Doppler effects. As Fig. 6.23 shows, the impact of Doppler spread diminishes with increasing bandwidth. This is due to the subcarrier spacing increasing when bandwidth is increased, which better combats Doppler spread.

The expectation is that the signals will always be transmitted with sufficient bandwidth. Beyond a certain bandwidth the benefit of doing so (which is to mitigate Doppler effects) is not there. The reason bandwidth is a consideration at all is because it is computationally expensive to work with very high bandwidth transmissions. Furthermore, the maximum bandwidth we are allowed to use is a little less than the carrier frequency, as aliasing occurs beyond that. The result is hence useful for ensuring sufficient bandwidth to significantly reduce Doppler effects (especially when there is deliberate motion between transmitter and receiver).

For very dynamic (low coherence time) channels, the preamble can be adapted to be within the channel coherence time to better track the channel variations. Given a higher bandwidth the preamble can be made correspondingly shorter so it is possible to be within the channel coherence time. For the proposed approach, the shift-orthogonal OFDM pilots are more effective in dynamic channels for channel and Doppler estimation.

iv. Transmission Range Achievable

The previous subsection showed that signals transmitted with sufficient bandwidth combat Doppler spread better. Mach number effects are only from waves which have semi-random relative back-and-forth motions between the transmitter and receiver. The expectation is that the channel Mach number does not impact the transmission range achievable. Transmission range is more impacted by propagation conditions. Therefore, the common Doppler shift due to waves should not impact the transmission range achievable.

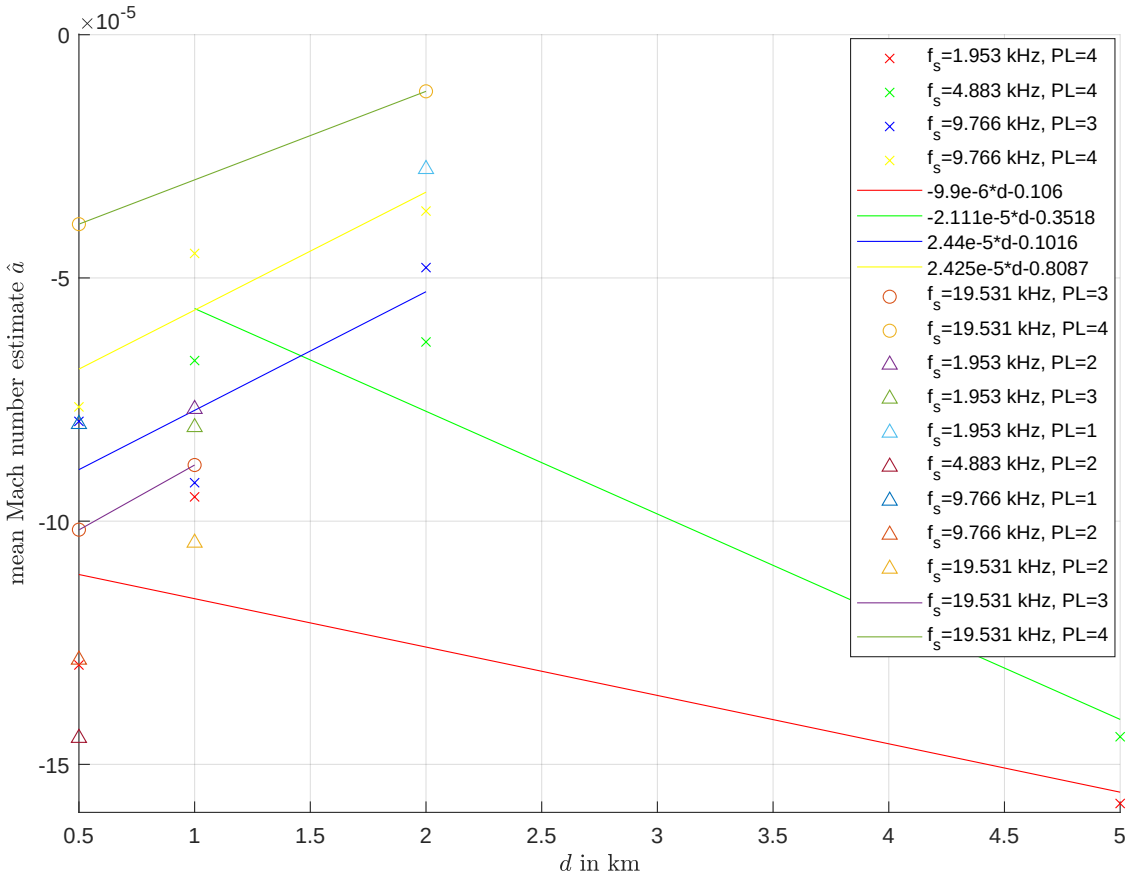

Figure 6.24: Data sets denoted by '×' are linearly fitted as there are 3 or more points. No correlation is observed between $\hat{a}$ and d which is as expected.

The Mach number estimate ($\hat{a}$) and transmission range (d) in Table 6.4 are plotted in Fig. 6.24, where the transmission bandwidth (W) and power level (PL) are held constant. Fig. 6.24 supports the assertion that there is no correlation between the signal Doppler shifts and transmission range (given sufficient bandwidth) for the Mach numbers studied. In the limiting case of high Mach numbers one encounters more turbulent flows, which can create hydrodynamic flow noise, or pseudo-sound [29]; this raises the ambient noise level and makes signal detection difficult but it should not impact transmission range.

v. Transmission Power Level

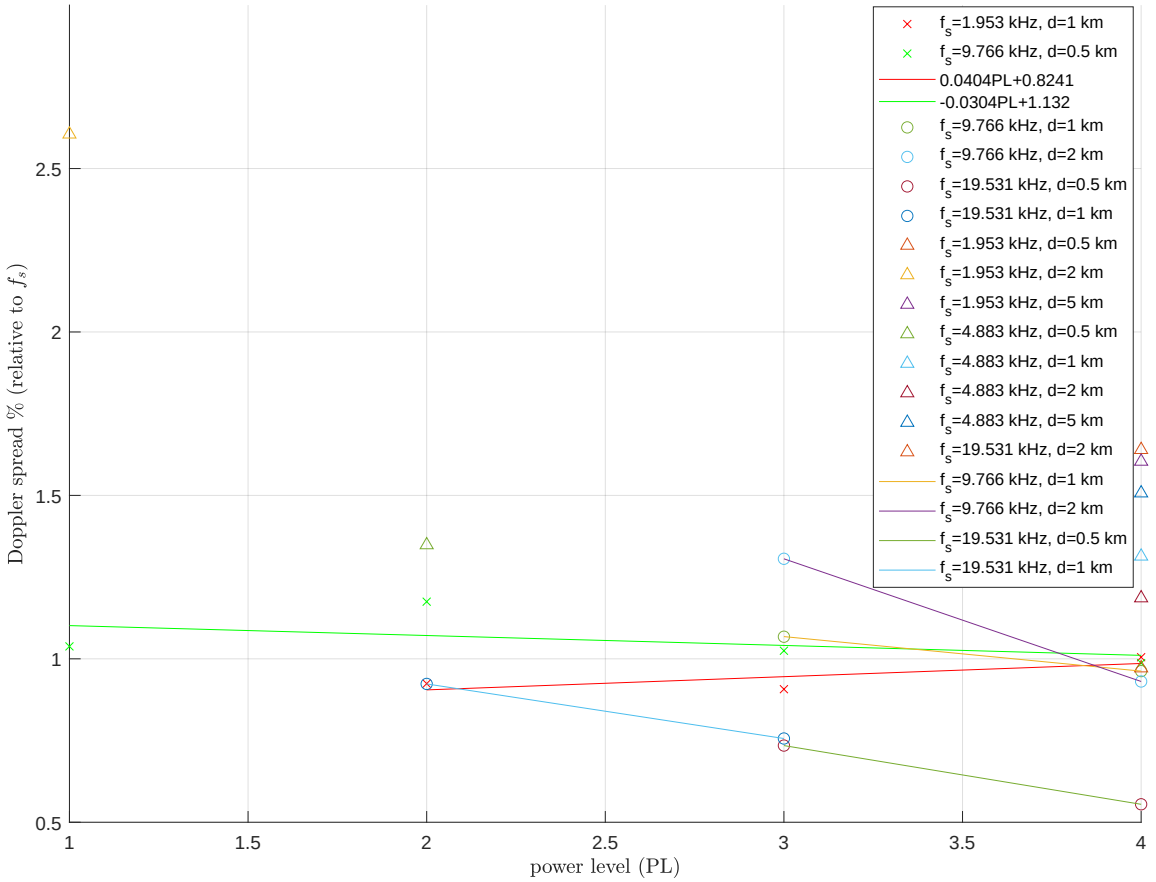

Figure 6.25: Data sets denoted by '×' are linearly fit since they contain three or more points. The effect of Doppler spread decreases when power level is increased (with the exception of the red line).

The expectation is that the Doppler spread should be less for increasing transmission power. The Doppler spread percentage and power level (PL) in Table 6.4 are plotted in Fig. 6.25, where bandwidth (W) and range (d) are held constant. Barring the outlier case with $W = 0.977$ kHz and $d = 1$ km, the measurements show the effect of Doppler spread on the propagating signal can be reduced by increasing the signal power.

This confirms that the developed system is correctly predicting and conforming to the physics of the underwater channel. It is also possible to plot the spread percentage

in terms of SNR, since the SNR can be measured from the received signals (see Fig. 6.26 below). The trends observed in Fig. 6.25 are observed here again.

Having investigated the Doppler spread correlations, the next subsections address the compensator performance.

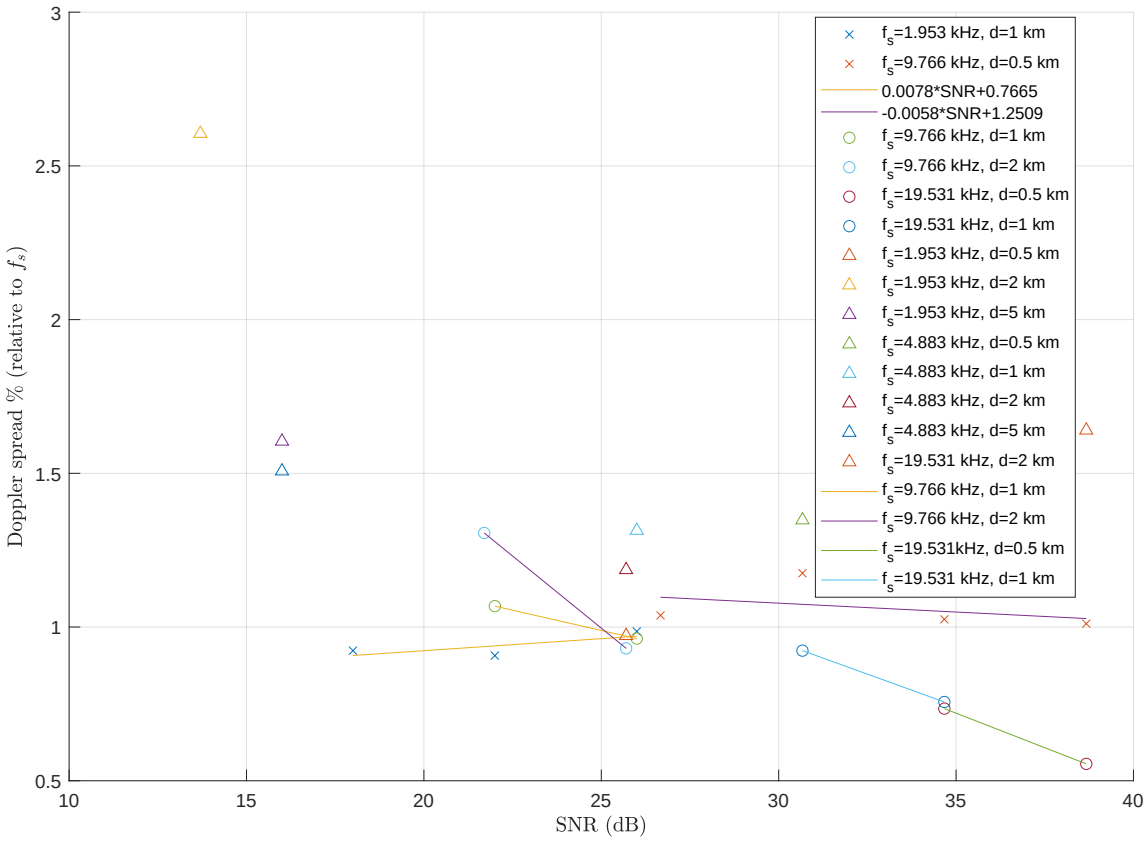

Figure 6.26: Data sets denoted by '×' are linearly fit since they contain three or more points. The effect of Doppler spread decreases when power level is increased (with the exception of the red line).

vi. Mach Number and Residual Doppler Shift

The residual Doppler shift is what remains after compensation is applied to the Doppler shifted signals. Its magnitude could be a measure of the compensator's performance. Given the Mach numbers measured in-water are not high (purposely so) it is not expected that the residual Doppler shift should be high.

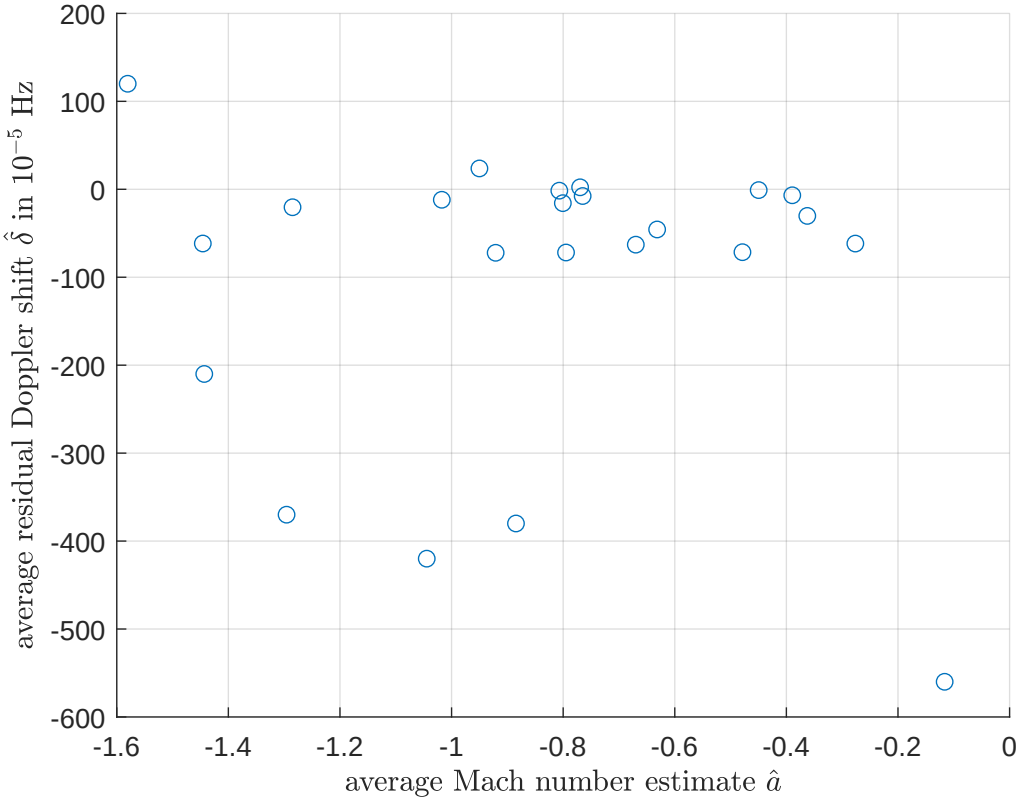

Figure 6.27: Each scatter point corresponds to a channel with its own Mach number a. No single-variable relationship is found between $\hat{\delta}$ and $\hat{a}$ which is as expected.

While the Mach numbers successfully captured by the proposed receiver are bounded by $W/(2f_cM)$, (which is 6.2×10^{-4} - 0.0062 depending on transmission bandwidth), the receiver performance is independent of channel Mach numbers less than the bound. For higher Mach numbers, the estimator breaks down due to experiencing angle ambiguity and, as shown in Chapter 5, higher Mach numbers are best addressed through shorter preamble lengths (assuming bandwidth and carrier frequency are pre-defined for the application).

The Mach number estimate ($\hat{a}$) and estimated residual Doppler shift ($\hat{\delta}$) in Table 6.4 are plotted in Fig. 6.27. Fig. 6.27 shows no discernible correlation between $\hat{\delta}$ and

$\hat{a}$. This agrees with the theory where:

$$\delta(t) = \frac{a(t) - \hat{a}(t)}{1 + \hat{a}(t)} f_c = \delta(a, \hat{a}). \tag{6.3}$$

The residual Doppler shift depends on both a and $\hat{a}$ and consequently, there should not be a single-variable relationship between residual Doppler shift and Mach number. This confirms the hypothesis but more importantly, follows what the theory suggests.

Fig. 6.27 also shows that for these trials, the resampling stage of Doppler compensation yielded residual errors in the range of 0.056 Hz $\leq |\hat{\delta}| \leq 9.1021 \times 10^{-6}$ Hz. These errors are relatively small with respect to the transmission bandwidth used and do not significantly impact performance.

vii. Residual Doppler Shift

Generally, the hypothesis is that with greater Doppler spread, a larger Doppler shift residue is observed at the output of typical compensators. Recall the rms Doppler spread, in Hz, is B_{d} such that B_{d}/W is the fractional Doppler spread normalized to the bandwidth (alternatively we can consider $B_{\mathrm{d}}/\Delta f$; this will not change our observations however since $B_{\mathrm{d}}/\Delta f = N \cdot B_{\mathrm{d}}/W$). This quantity offers insight into the severity of the Doppler spread. The Mach number estimate ($\hat{a}$) and Doppler spread percentage in Table 6.4 are plotted in Fig. 6.28.

However, Fig. 6.28 does not support the general hypothesis. There is no discernible correlation between $\hat{\delta}$ and B_{d}. This is because the resampling in our case accounts for Doppler shift variations (i.e. Doppler spread). This is a contribution from the thesis over the standard static resampling used. The resampling factor $1+\hat{a}$, which varies block-by-block, accounts for Doppler shift variations, thereby mitigating Doppler spread. In fact, its effectiveness will be pronounced in dynamic channels with deliberate relative motions between the transmitter and receiver (future work).

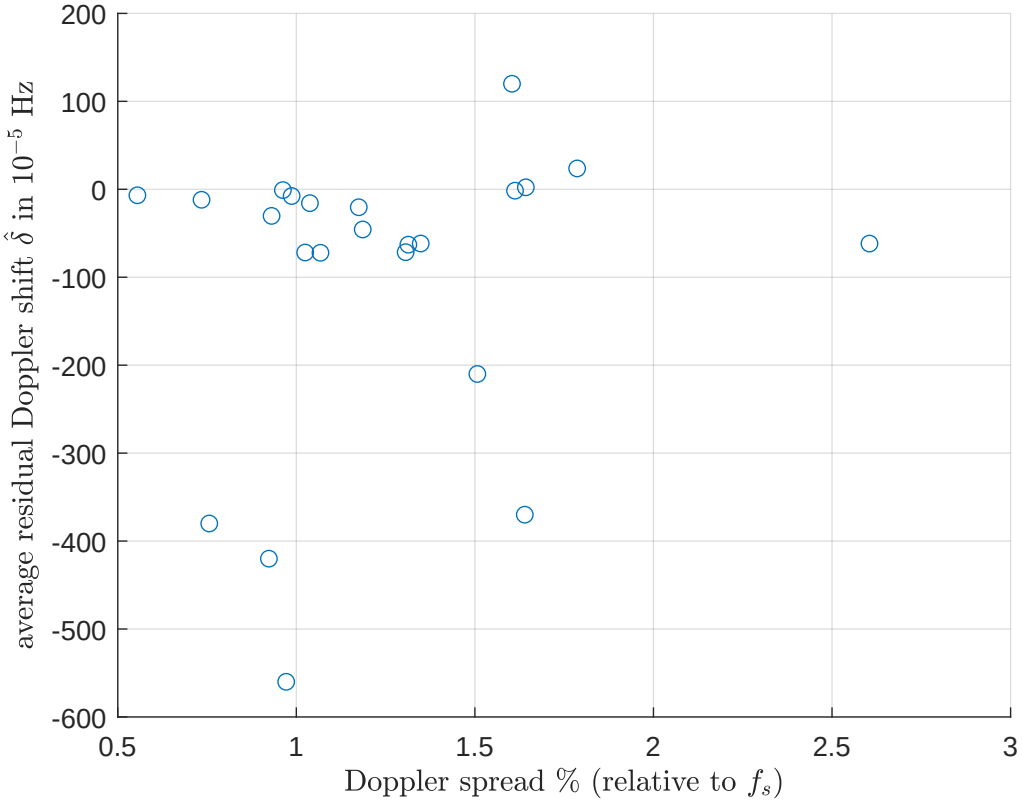

Figure 6.28: Scatter plot of the residual Doppler shift estimates versus percentage of Doppler spread. No single-variable relationship is found between $\hat{\delta}$ and s_{d}.

Given smaller Mach numbers to start and a resampling process that addresses Doppler shift variations, it is acceptable that there is very little Doppler shift left. The Doppler spread therefore does not significantly impact the residual Doppler estimator. As shown earlier, with increasing bandwidth, W, the Doppler spread decreases. This confirms the ability of the proposed resampler to address dynamic channel variations. It is a testament to the compensation process's effectiveness that the residual Doppler shift is in the noise to the point where there is no apparent relationship between the residual Doppler shift and the spread.

6.5 Concluding Remarks

A detailed analysis of 23 channels proves the proposed receiver's successful performance in UWA channels where the dominant source of Doppler effects is wave motion. The tracker's ability to accurately extract the Mach number estimates and the compensator's ability to eliminate Doppler effects from the channel are demonstrated in Appendix B. The relatively small residual Doppler shifts estimated for each channel are clear indications of the receiver's high performance.

The results also show the dependence of Doppler spread on some of the transmission parameters. It is shown that the effects of Doppler spread can be mitigated by increasing the bandwidth of the transmitted signal. This observation has not been seen recorded in existng literature, and in our trials it seems to hold true for shift-orthogonal pilot signals. Increasing the signal power also reduces the effects of Doppler spread. The results also imply that the effects of Doppler spread worsen when the range of transmission is increased (though there have been two outliers to this observation).

Finally the results show that transmission range does not affect the Mach number of the channel. Thus the induced common Doppler shift due to gravity waves during transmission is independent of the range of transmission.

In all these experiments, the Doppler spread generally had a small effect on the propagating signal. This will not be the case in the presence of platfom motion (to be tested in future work), which introduces more Doppler content to the problem.

Chapter 7

Conclusions and Future Work

A shift-orthogonal pilot strucutre was proposed for Doppler estimation in UWA channels. The correlation properties of the proposed pilot structure is the main motivator behind using it in Doppler estimation, as the autocorrelation function of these pilots is simply a Kronecker delta function. This means that the energy of the autocorrelation output is concentrated at just one tap. This shift-orthogonal property facilitates Doppler estimation as well as channel estimation in dynamic channels such as UWA channels. Furthermore, if the duration of the propagating signal is less than the channel's Doppler spread, then the WSSUS assumption can be validated for UWA channels.

The impulse response of the UWA channel was derived from first principles. The model was then simplified by assuming a first-order model for the time- and path-dependent delays and assuming that the preamble duration is small enough such that the path attenuations and the Mach number vary slowly in time within the preamble block.

The proposed Doppler estimator autocorrelates the shift-orthogonal pilots at the receiver with a correlation delay equal to the size of the sequence, from which Mach number estimates can be extracted. The estimator yields a closed-form solution to the Doppler estimation problem, allowing us to avoid ambiguity problems other estimators suffer from, such as grid-search-based estimators. The estimator also boasts low computational complexity and is capable of Doppler tracking. The MSE of the estimator was shown to outperform most estimators found in literature.

The proposed Doppler compensator uses resampling for the first stage of compensation as is common in most compensators. Resampling however is time-varying, where the resampling factor is varied block by block to account for the different dilations/compressions experiences by each receiver block. Although the Doppler estimator output is capable of tracking Mach number variations sample by sample, the size of the data array at the output results in high computational complexity, making the resampling process time-consuming. The proposed Doppler tracker downsamples the time-varying Mach number estimates while simultaneously tracking the envelope of the Mach number wave in order to minimize compensation errors. This gives rise to block-by-block resampling.

The second stage of compensation, namely residual Doppler compensation, involves the use of the proposed Doppler estimator to estimate the residual Doppler shift. This is due to the fact that the residual Doppler shift appears as CFO just like the common Doppler shift, and it was proven that the proposed estimator can be applied in both cases. Doppler compensation performance is thus the same as the Doppler estimation performance as well as the performance of the resampling algorithm used.

It was shown that the proposed Doppler compensation approach outperforms most existing compensators in terms of MSE. If the received signal is resampled block by block (using a sufficiently large block size), it also outspeeds most existing compenstors. It was also observed that the propsed compensator, even when outperformed, has unique features that can make it more viable, such as its ability to track the Mach number and its confirmed performance in real-life sea trials.

The proposed receiver was verified via MATLAB and Simulink. More importantly, the receiver was also validated via real sea experiments. It was shown to perform well for short-range as well as long-range transmissions. The analysis proved the proposed receiver's success in UWA channels where the dominant source of Doppler effects is

wave motion. The tracker's ability to accurately extract the Mach number estimates and the compensator's ability to eliminate Doppler effects from the channel were shown in the graphs plotted in Appendix B as well as the data recorded in Table 7.1. The relatively small residual Doppler shifts estimated for each channel show the receiver's high performance in the experiments and trials conducted with minimal errors generated by the receiver.

The channel's Doppler spread was shown to be mitigated by increasing the bandwidth of the transmitted signal. This result was not observed in existing literature and serves as a new discovery that is proven for shift-orthogonal pilot signals. Increasing the signal power also reduces the effects of Doppler spread; furthermore the effects of Doppler spread seem to worsen when the range of transmission is increased, though a concrete statement cannot be made due to the existence of two outliers.

Finally the results show that transmission range does not influence the Mach number of the channel, indicating that range does not impact the common Doppler shift due to gravity waves during transmission. Doppler spread was relatively small during for each analyzed channel.

The proposed receiver is now fully justified for UWA channels where platform motion is absent and wave motion is the prime contributor to Doppler effects. In the future, new experiments will be conducted where platform motion will be induced on the transmitter and/or receiver sides. This is expected to increase Doppler shift as well as Doppler spread. After confirming the receiver's success in these experiments, AUVs will be used to fully implement the proposed receiver.

Appendix A

MATLAB Scripts

A-1 MATLAB script for block-by-block compensation

Below is the script developed for block-by-block resampling. Signals are frame-based. "simout" is the received signal extracted as a timeseries variable.

```
M=64;
Fs=10000
corr_delay=1; %correlation delay in blocks; e.g. a value of 1 means a delay of M
                      %samples

%mean estimate
a_hat=mean(mean(squeeze(MachNumbers.Data(:,1,1+corr_delay:end))))*Fs/(2*pi*24414*...
                        corr_delay)

aa=squeeze(MachNumbers.Data)*Fs/(2*pi*24414*corr_delay); %estimates per sample
a_h=mean(squeeze(MachNumbers.Data(:,1,corr_delay:end)))*Fs/(2*pi*24414*1);
%estimates per block

sout=zeros(length(simout.Data)-corr_delay,M);

%initialize resampled output array and ignore the zero row vectors
ssout=zeros(length(simout.Data)-corr_delay,M);

for i=1:length(simout.Data)-corr_delay
    n=0+M*corr_delay:M-1+M*corr_delay;
    n=n+M*(i-1)*ones(1,64);

    %multiply by the carrier exp(-j*2pi*mach estimate*fc*t)
    sout(i,:)=simout.Data(i+corr_delay,:).*exp(-j*2*pi*24414/Fc*aa(:,i+...
                                    corr_delay)'.*n);
    [ni,di]=rat(1+a_h(i));
    sout1=resample(sout(i,:),ni,di); %block-by-block resampling
    if length(sout1)<M
        ssout(i,:)=padarray(sout1,[0 M-length(sout1)],'post');
    else ssout(i,:)=sout1(1:M);
    end
end
ssout_ts=timeseries(ssout); %convert array to time series
```

A-2 MATLAB script for sample-by-sample compensation

Below is the script developed for sample-by-sample resampling. Signals are sample-based. "RxBaseSamples.Data" is the received signal extracted as a timeseries variable.

```
Fs=10000;

%correlation delay in samples; e.g. a delay of 64 corresponds to a delay of 64
%samples
corr_delay=64;

%mean estimate
a_hat=mean(squeeze(MachNumbers.Data(:,1,startpoint:edpoint)))*Fs/(2*pi*24414*...
                        corr_delay)
[nn,dd]=rat(1+a_hat);
aa=squeeze(MachNumbers.Data)*Fs/(2*pi*24414*corr_delay); %estimates per sample

sout=zeros(1:endpoint-startpoint+1,1);

%a larger array for the resampled signal is used in order to take into account the
%extra samples in case of dilation
ssout=zeros(1:64+endpoint-startpoint+,1);

for i=startpoint:endpoint-startpoint+1
    n=startpoint;
    n=n+1*(i-1);
    sout(i-startpoint+1)=squeeze(RxBaseSamples.Data(1,1,n)).*exp(-j*2*pi*...
                                        24414/10000*aa(i)*n);
    [ni,di]=rat(1+aa(i));
    sout1=resample(sout(i-startpoint+1),ni,di);
    if length(sout1)>1
        ssout(i-startpoint+1:length(sout1)+i-startpoint)=sout1;
    else ssout(i-startpoint+1)=sout1;
    end
end
ssout_ts=timeseries(ssout);
```

Appendix B

Chebucto Head's Sea Experiments' Results ($f_c = 24.414$ **kHz**)

B-1 $W = 0.9766$ **kHz,** $d = 500$ **m,** PL $= 4$, $\Delta t = 3.6$ **s**

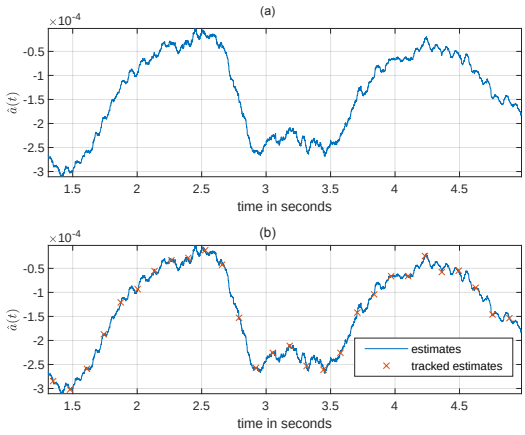

Figure B-1.1: Mach number estimator (a) and tracker (b) with $W = 0.9766$ kHz, $d = 500$ m and PL $= 4$. 'x' indicates every 256th sample retained due to downsampling (sample is extracted every 4 preambles). Relative velocity is given by $1500 \cdot a(t)$. This data reduction facilitates practical compensation. Note, the downsampled representation captures the Mach number such that no lower frequency features relevant to tracking are neglected. This practically tracks the Mach number variations.

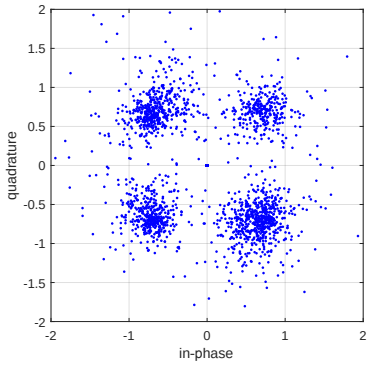

Figure B-1.2: Scatter plot of the compensated and demodulated RX pilots sampled at $W = 0.9766$ kHz for a range of $d = 500$ m amd power level 4. The plot indicates that the QPSK symbols have been properly recovered.

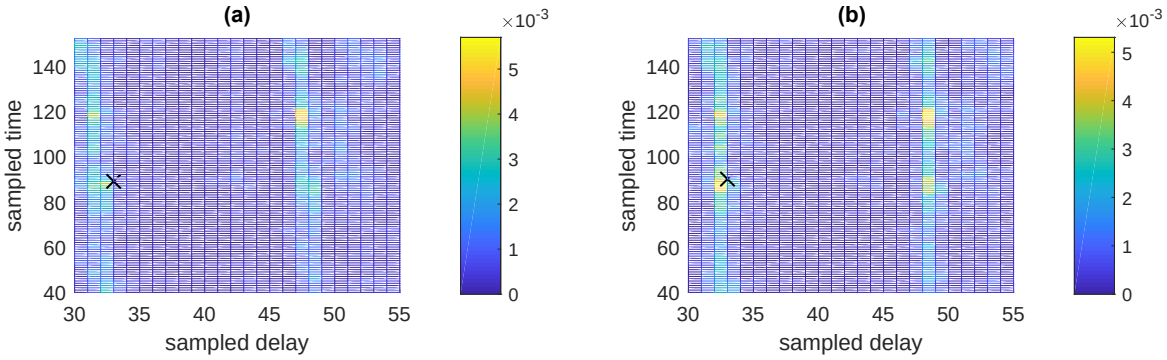

Figure B-1.3: CIR comparison (a) before and (b) after Doppler compensation for $W = 0.9766$ kHz, $d = 500$ m and PL $= 4$. The CIR is projected onto t vs τ where the effect of Doppler compensation is more evident. Channel taps with the highest energy content (colored yellow) are shown. 'x' shows a test tap location before and after compensation. The taps are aligned vertically after compensation, demonstrating proper recovery of channel tap locations.

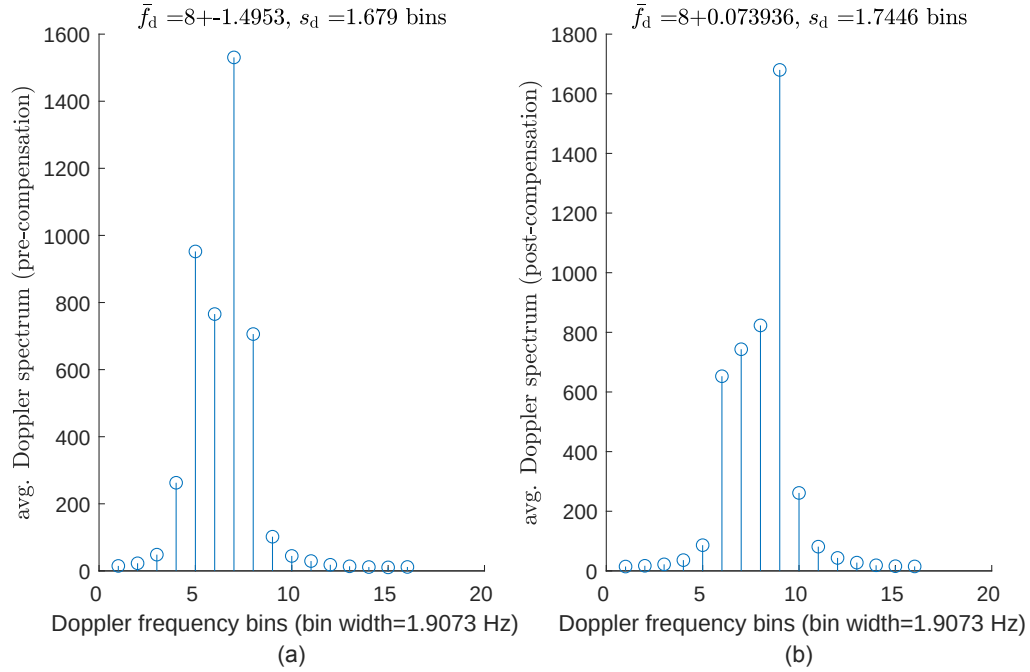

Figure B-1.4: Average Doppler power spectrum comparison (a) before and (b) after compensation for the entire channel ($W = 0.9766$ kHz, $d = 500$ m, power level 4). The average is computed over channel delays. The spectrum is shifted so that the Doppler frequency of 0 corresponds to bin 8. Doppler spread is severe. The centroid of the spectrum is returned to bin 8 after compensation. Only the higher-energy taps were corrected, so the Doppler spread of the channel was not mitigated.

B-2 $W = 0.9766$ **kHz,** $d = 1$ **km,** PL $= 2$**,** $\Delta t = 5$ **s**

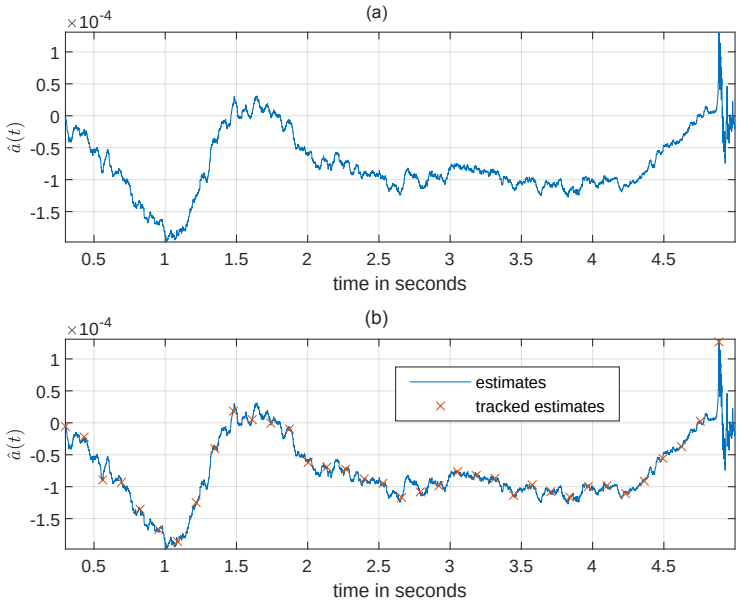

Figure B-2.1: Mach number estimator (a) and tracker (b) with $W = 0.9766$ kHz, $d = 1$ km and PL $= 4$. 'x' indicates every 256th sample retained due to downsampling (sample is extracted every 4 preambles). Relative velocity is given by $1500 \cdot a(t)$. This data reduction facilitates practical compensation. Note, the downsampled representation captures the Mach number such that no lower frequency features relevant to tracking are neglected. This practically tracks the Mach number variations.

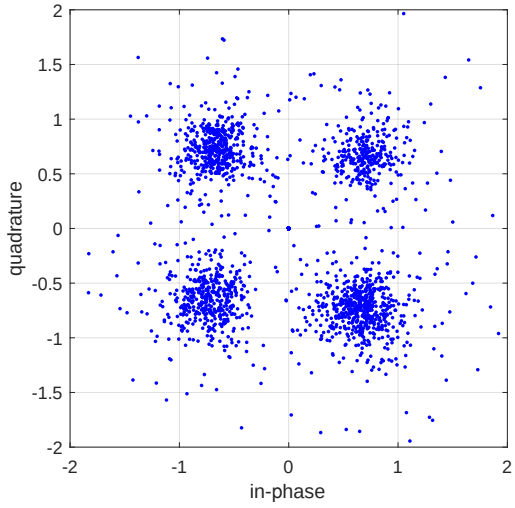

Figure B-2.2: Scatter plot of the compensated and demodulated RX pilots sampled at $W = 0.9766$ kHz for a range of $d = 1$ km amd power level 2. The plot indicates that the QPSK symbols have been properly recovered.

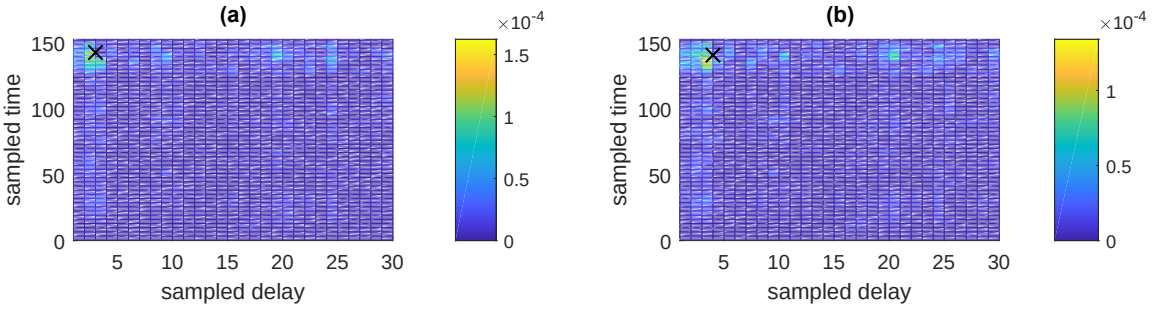

Figure B-2.3: CIR comparison (a) before and (b) after Doppler compensation for $W = 0.9766$ kHz, $d = 1$ km and PL = 2. The CIR is projected onto t vs τ where the effect of Doppler compensation is more evident. Channel taps with the highest energy content (colored yellow) are shown. Only two high-energy taps exist in the entire channel. 'x' shows a test tap location before and after compensation. The taps are aligned vertically after compensation, demonstrating proper recovery of channel tap locations.

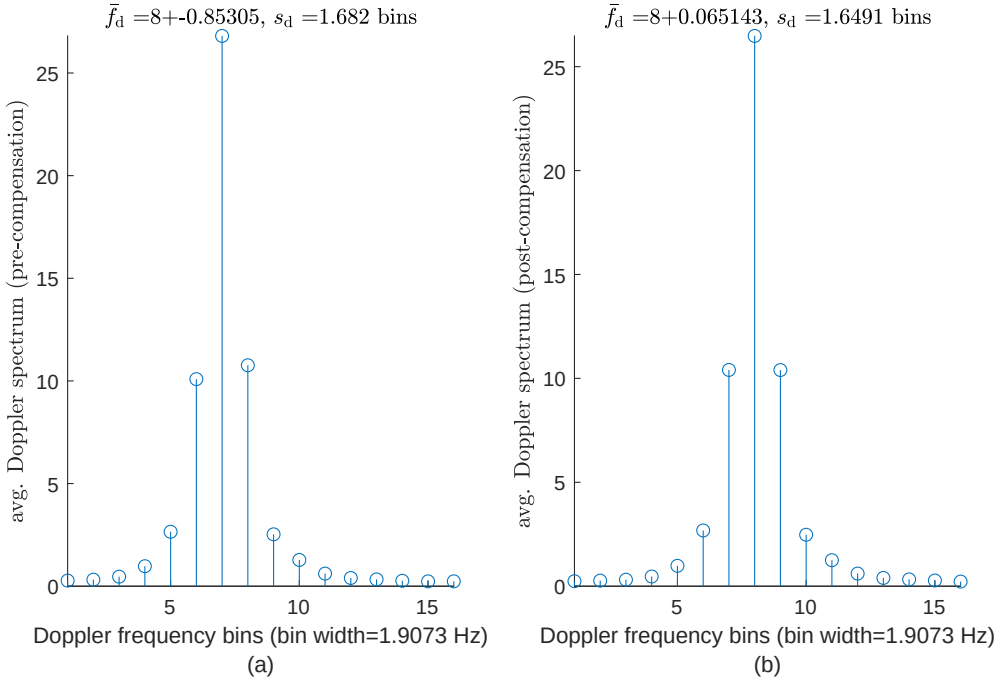

Figure B-2.4: Average Doppler power spectrum comparison (a) before and (b) after compensation for the entire channel ($W = 0.9766$ kHz, $d = 1$ km, power level 2). The average is computed over channel delays. The spectrum is shifted so that the Doppler frequency of 0 corresponds to bin 8. Doppler spread is moderate. The centroid of the spectrum is returned to bin 8 after compensation. Only the higher-energy taps were corrected, so the Doppler spread of the channel was not mitigated.

B-3 $W = 0.9766$ **kHz,** $d = 1$ **km,** PL $= 3$**,** $\Delta t = 5$ **s**

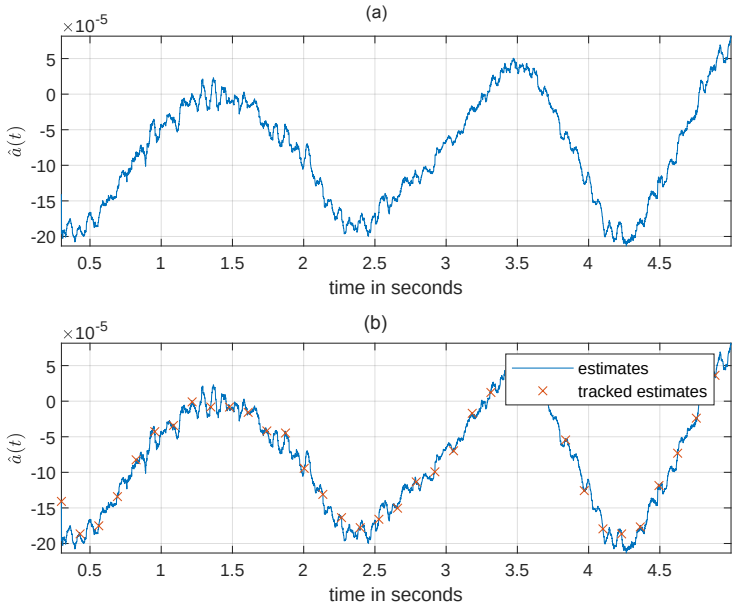

Figure B-3.1: Mach number estimator (a) and tracker (b) with $W = 0.9766$ kHz, $d = 1$ km and PL $= 3$. 'x' indicates every 256th sample retained due to downsampling (sample is extracted every 4 preambles). Relative velocity is given by $1500 \cdot a(t)$. This data reduction facilitates practical compensation. Note, the downsampled representation captures the Mach number such that no lower frequency features relevant to tracking are neglected. This practically tracks the Mach number variations.

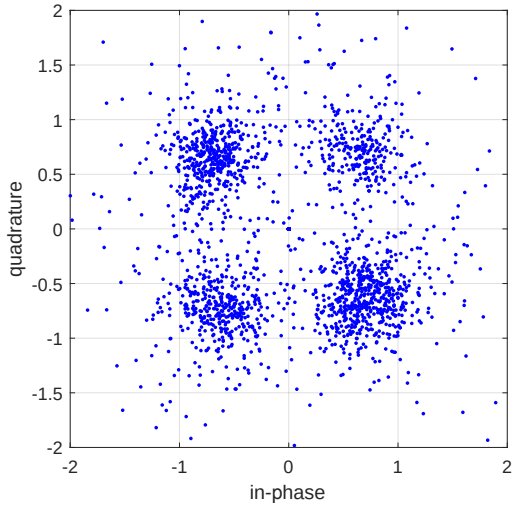

Figure B-3.2: Scatter plot of the compensated and demodulated RX pilots sampled at $W = 0.9766$ kHz for a range of $d = 1$ km amd power level 3. The plot indicates that the QPSK symbols have been properly recovered.

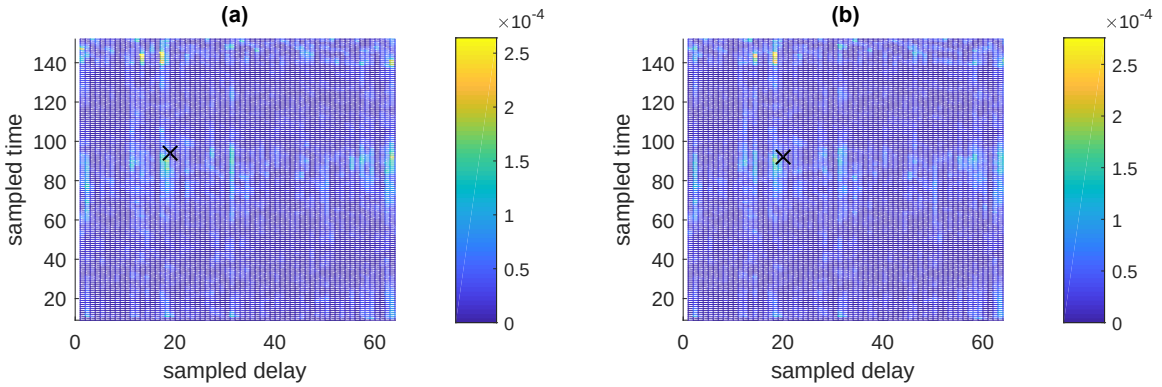

Figure B-3.3: CIR comparison (a) before and (b) after Doppler compensation for $W = 0.9766$ kHz, $d = 1$ km and PL $= 3$. The CIR is projected onto t vs τ where the effect of Doppler compensation is more evident. Channel taps with the highest energy content (colored yellow) are shown. Only a few high-energy taps exist in the entire channel. 'x' shows a test tap location before and after compensation. The taps are aligned vertically after compensation, demonstrating proper recovery of channel tap locations.

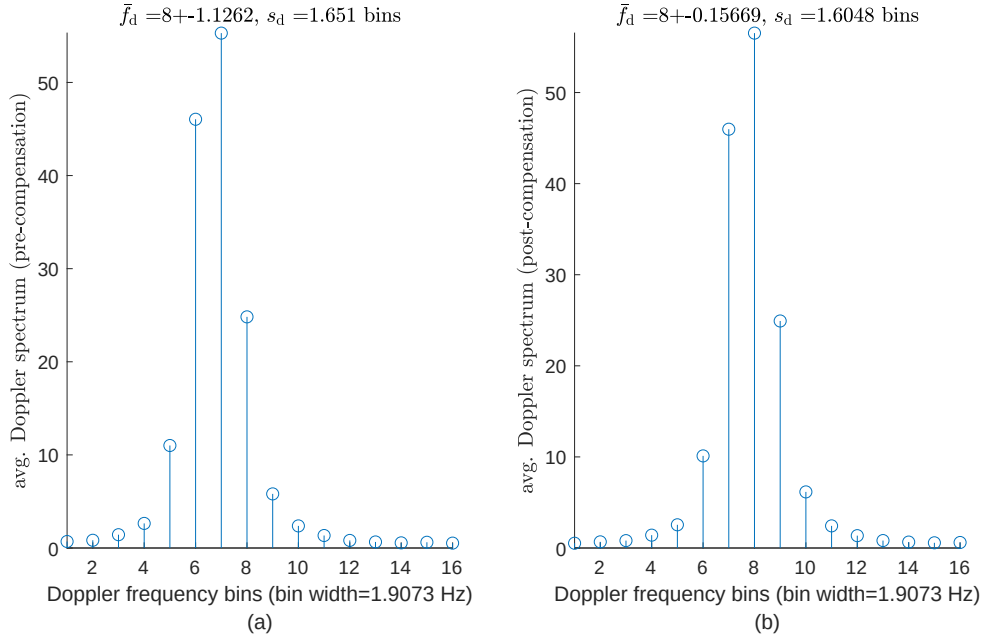

Figure B-3.4: Average Doppler power spectrum comparison (a) before and (b) after compensation for the entire channel ($W = 0.9766$ kHz, $d = 1$ km, power level 3). The average is computed over channel delays. The spectrum is shifted so that the Doppler frequency of 0 corresponds to bin 8. Doppler spread is severe. The centroid of the spectrum is returned to bin 8 after compensation. Only the higher-energy taps were corrected, so the Doppler spread of the channel was not mitigated.

B-4 $W = 0.9766$ **kHz,** $d = 1$ **km,** PL $= 4$**,** $\Delta t = 3.4$ **s**

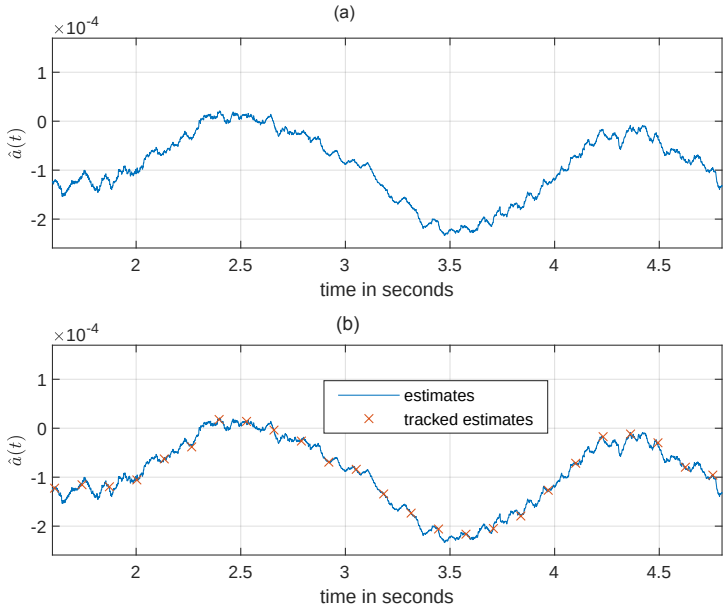

Figure B-4.1: Mach number estimator (a) and tracker (b) with $W = 0.9766$ kHz, $d = 1$ km and PL $= 4$. 'x' indicates every 256th sample retained due to downsampling (sample is extracted every 4 preambles). Relative velocity is given by $1500 \cdot a(t)$. This data reduction facilitates practical compensation. Note, the downsampled representation captures the Mach number such that no lower frequency features relevant to tracking are neglected. This practically tracks the Mach number variations.

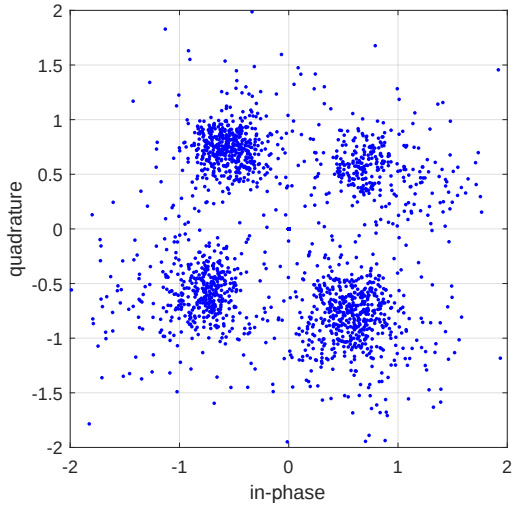

Figure B-4.2: Scatter plot of the compensated and demodulated RX pilots sampled at $W = 0.9766$ kHz for a range of $d = 1$ km amd power level 4. The plot indicates that the QPSK symbols have been properly recovered.

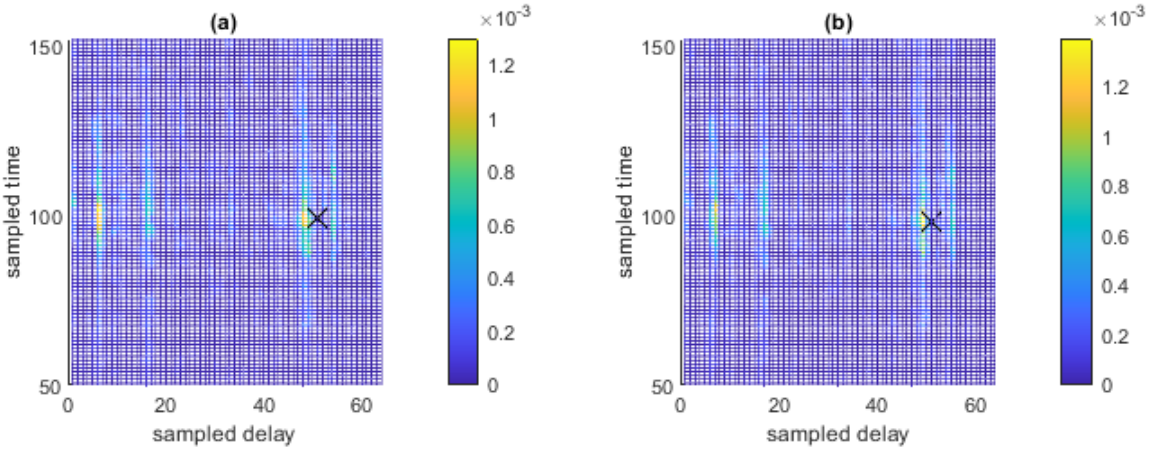

Figure B-4.3: CIR comparison (a) before and (b) after Doppler compensation for $W = 0.9766$ kHz, $d = 1$ km and PL $= 4$. The CIR is projected onto t vs τ where the effect of Doppler compensation is more evident. High-energy (yellow) taps are compensated. 'x' shows a test tap location before and after compensation. The taps are aligned vertically after compensation, demonstrating proper recovery of channel tap locations.

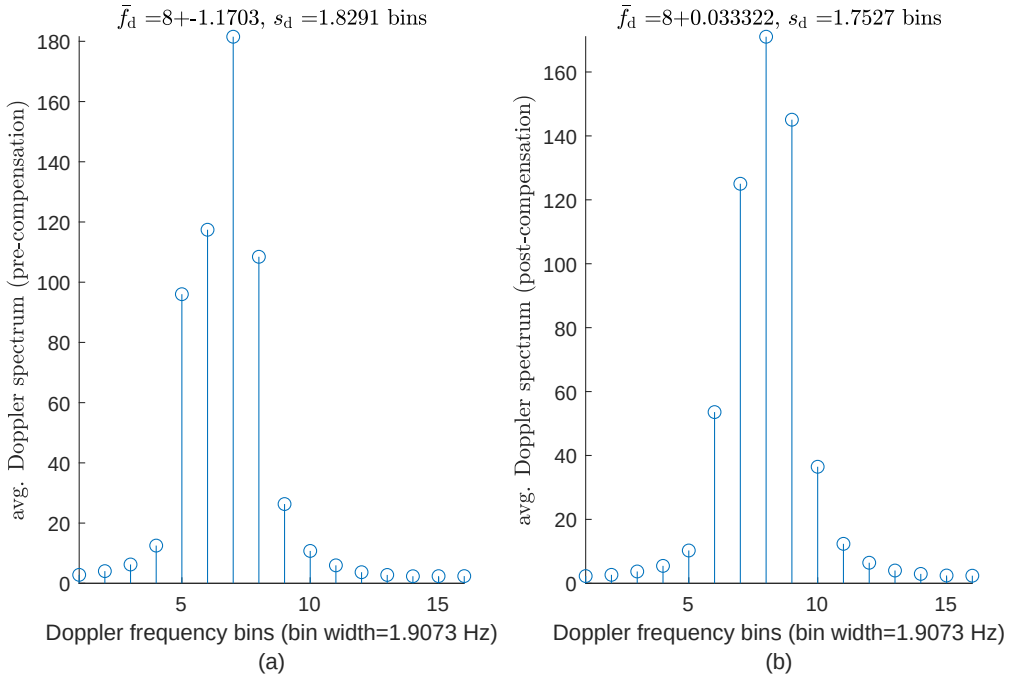

Figure B-4.4: Average Doppler power spectrum comparison (a) before and (b) after compensation for the entire channel ($W = 0.9766$ kHz, $d = 1$ km, power level 4). The average is computed over channel delays. The spectrum is shifted so that the Doppler frequency of 0 corresponds to bin 8. Doppler spread is severe. The centroid of the spectrum is returned to bin 8 after compensation. Only the higher-energy taps were corrected, so the Doppler spread of the channel was not mitigated.

B-5 $W = 0.9766$ **kHz,** $d = 2$ **km,** PL $= 1$, $\Delta t = 0.7$ **s**

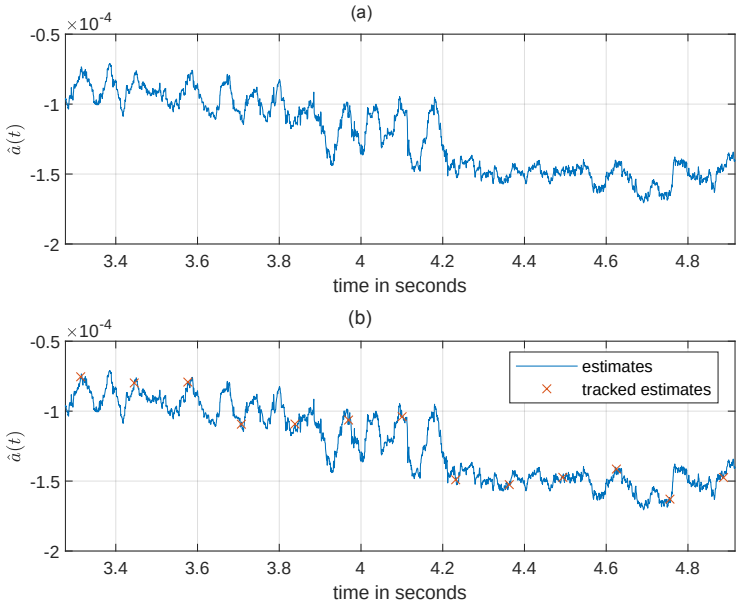

Figure B-5.1: Mach number estimator (a) and tracker (b) with $W = 0.9766$ kHz, $d = 2$ km and PL $= 1$. 'x' indicates every 256th sample retained due to downsampling (sample is extracted every 4 preambles). Relative velocity is given by $1500 \cdot a(t)$. This data reduction facilitates practical compensation. Note, the downsampled representation captures the Mach number such that no lower frequency features relevant to tracking are neglected. This practically tracks the Mach number variations.

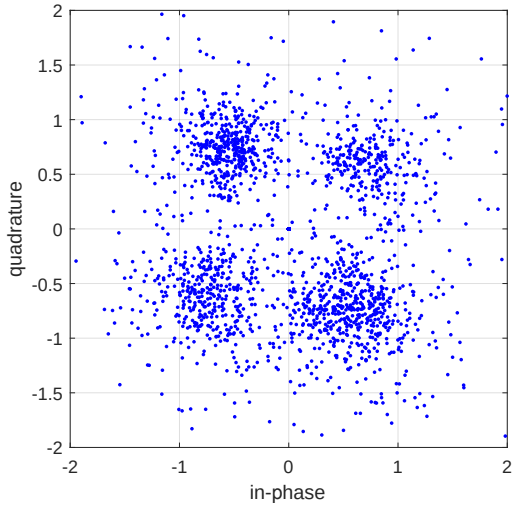

Figure B-5.2: Scatter plot of the compensated and demodulated RX pilots sampled at $W = 0.9766$ kHz for a range of $d = 2$ km amd power level 1. The plot indicates that the QPSK symbols have been properly recovered.

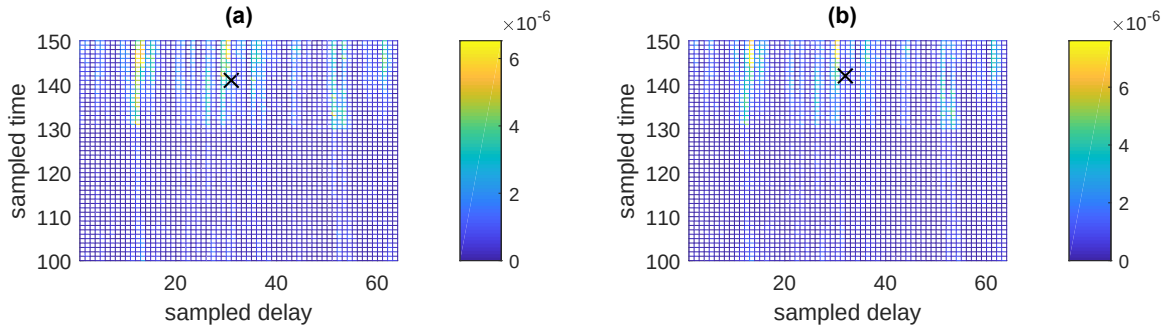

Figure B-5.3: CIR comparison (a) before and (b) after Doppler compensation for $W = 0.9766$ kHz, $d = 2$ km and PL = 1. The CIR is projected onto t vs τ where the effect of Doppler compensation is more evident. High-energy (yellow) taps are compensated. 'x' shows a test tap location before and after compensation. The taps are aligned vertically after compensation, demonstrating proper recovery of channel tap locations.

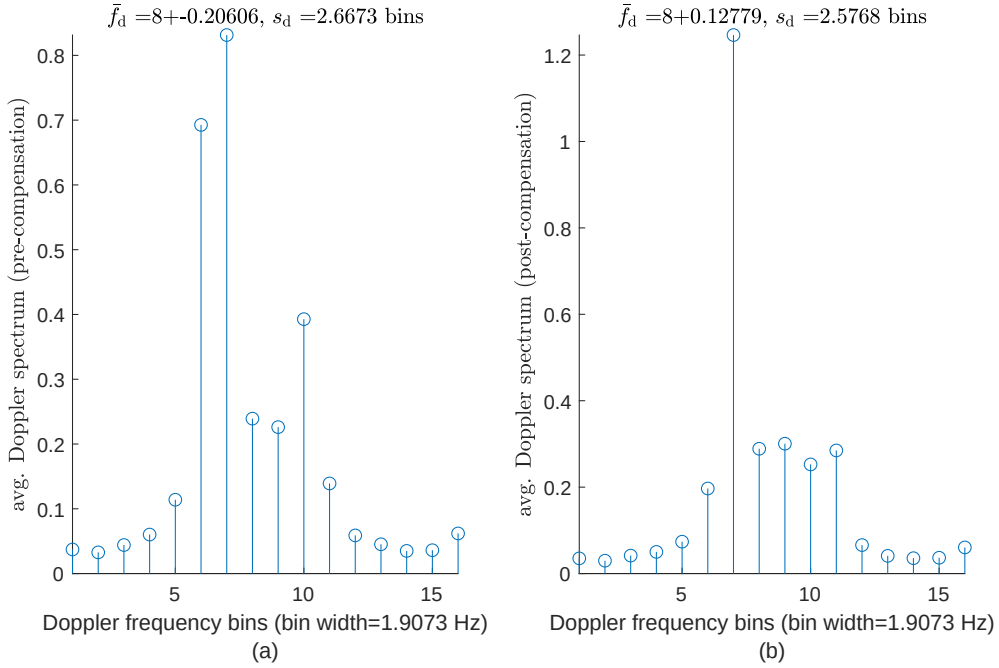

Figure B-5.4: Average Doppler power spectrum comparison (a) before and (b) after compensation for the entire channel ($W = 0.9766$ kHz, $d = 2$ km, power level 1). The average is computed over channel delays. The spectrum is shifted so that the Doppler frequency of 0 corresponds to bin 8. Doppler spread is severe. The centroid is close to bin 8 before and after compensation. Only the higher-energy taps were corrected, so the Doppler spread of the channel was not mitigated.

B-6 $W = 0.9766$ **kHz,** $d = 5$ **km,** PL $= 4$**,** $\Delta t = 5$ **s**

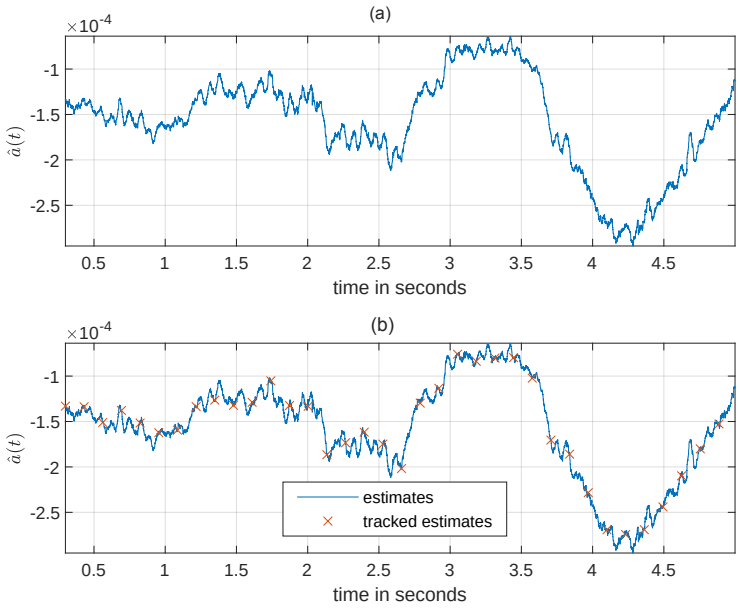

Figure B-6.1: Mach number estimator (a) and tracker (b) with $W = 0.9766$ kHz, $d = 5$ km and PL $= 4$. 'x' indicates every 256th sample retained due to downsampling (sample is extracted every 4 preambles). Relative velocity is given by $1500 \cdot a(t)$. This data reduction facilitates practical compensation. Note, the downsampled representation captures the Mach number such that no lower frequency features relevant to tracking are neglected. This practically tracks the Mach number variations.

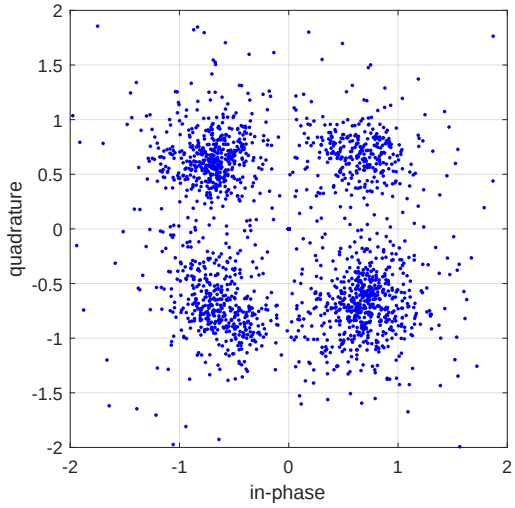

Figure B-6.2: Scatter plot of the compensated and demodulated RX pilots sampled at $W = 0.9766$ kHz for a range of $d = 5$ km amd power level 4. The plot indicates that the QPSK symbols have been properly recovered.

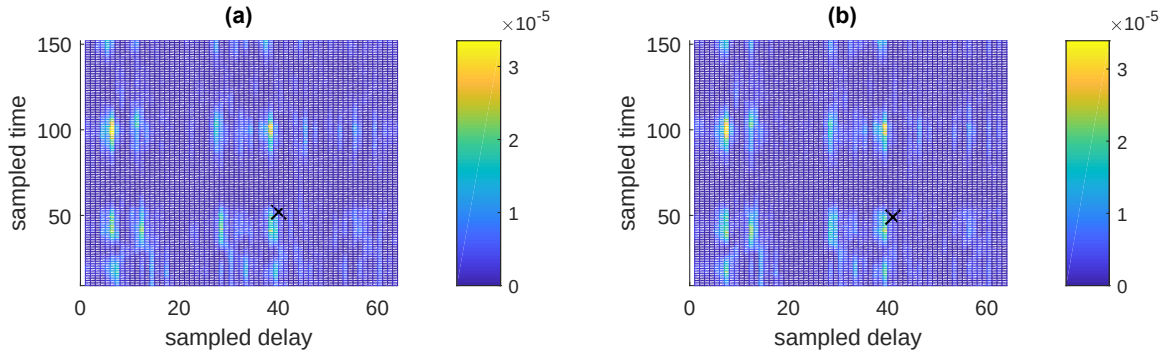

Figure B-6.3: CIR comparison (a) before and (b) after Doppler compensation for $W = 0.9766$ kHz, $d = 5$ km and PL $= 4$. The CIR is projected onto t vs τ where the effect of Doppler compensation is more evident. High-energy (yellow) taps are compensated. 'x' shows a test tap location before and after compensation. The taps are aligned vertically after compensation, demonstrating proper recovery of channel tap locations.

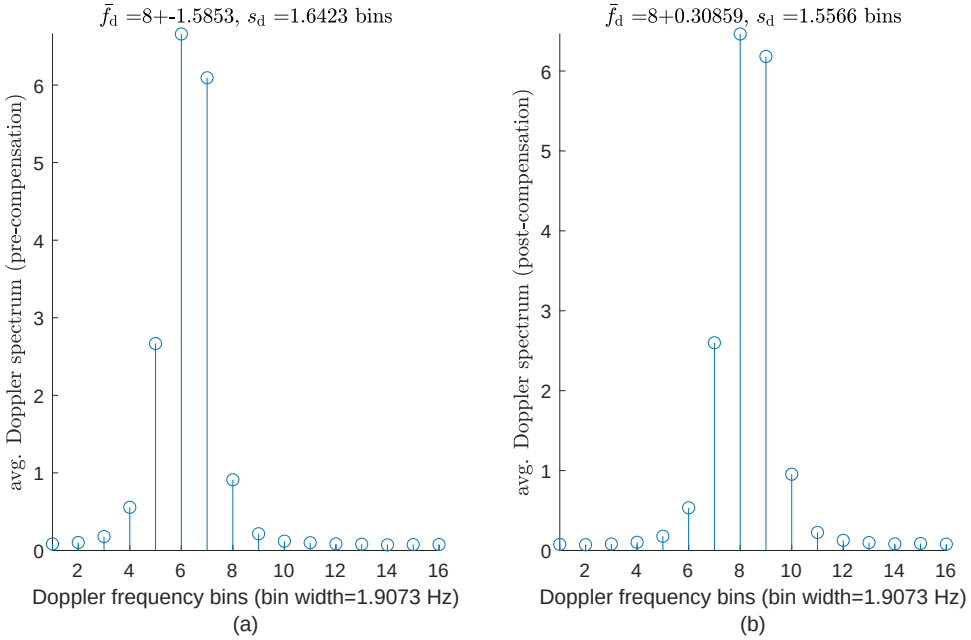

Figure B-6.4: Average Doppler power spectrum comparison (a) before and (b) after compensation for the entire channel ($W = 0.9766$ kHz, $d = 5$ km, power level 4). The average is computed over channel delays. The spectrum is shifted so that the Doppler frequency of 0 corresponds to bin 8. Doppler spread is severe. The centroid of the spectrum is returned to bin 8 after compensation. Only the higher-energy taps were corrected, so the Doppler spread of the channel was not mitigated.

B-7 $W = 2.442$ **kHz,** $d = 500$ **km,** PL $= 2$**,** $\Delta t = 3.7$ **s**

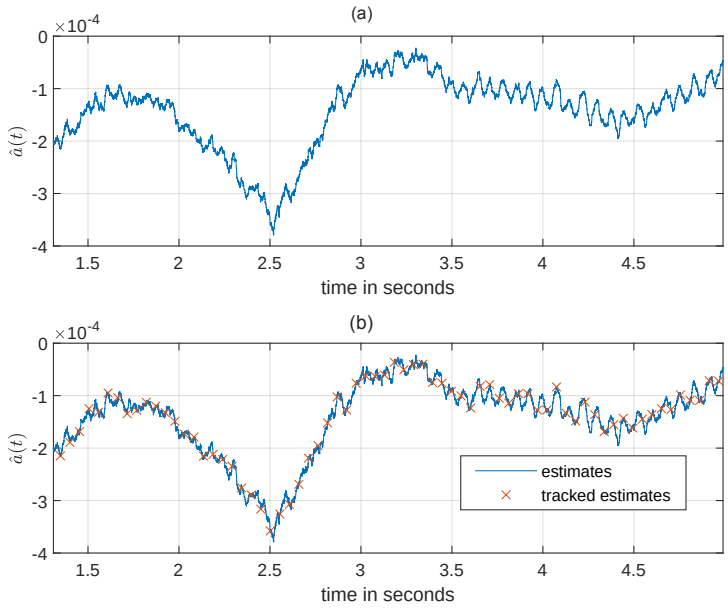

Figure B-7.1: Mach number estimator (a) and tracker (b) with $W = 2.442$ kHz, $d = 500$ m and PL $= 2$. 'x' indicates every 256th sample retained due to downsampling (sample is extracted every 4 preambles). Relative velocity is given by $1500 \cdot a(t)$. This data reduction facilitates practical compensation. Note, the downsampled representation captures the Mach number such that no lower frequency features relevant to tracking are neglected. This practically tracks the Mach number variations.

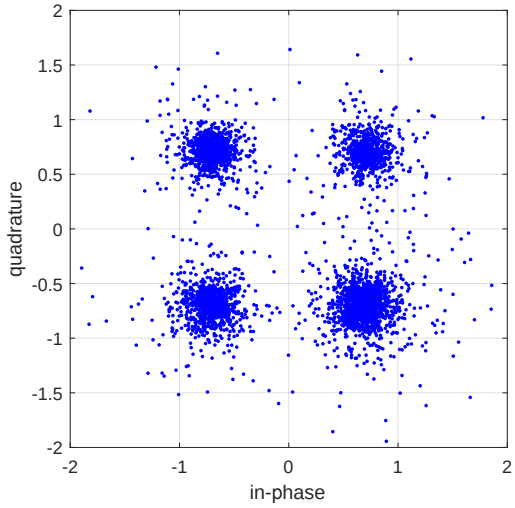

Figure B-7.2: Scatter plot of the compensated and demodulated RX pilots sampled at $W = 2.442$ kHz for a range of $d = 500$ m amd power level 2. The plot indicates that the QPSK symbols have been properly recovered.

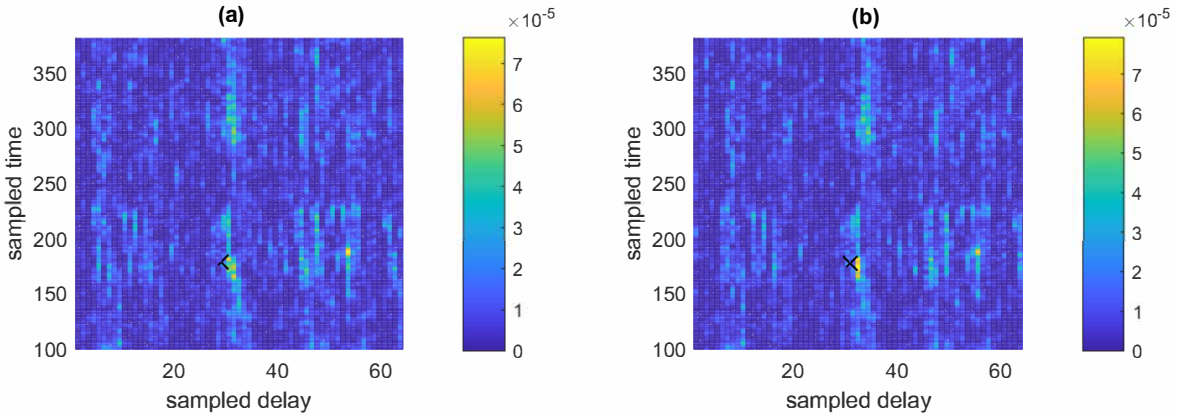

Figure B-7.3: CIR comparison (a) before and (b) after Doppler compensation for $W = 2.442$ kHz, $d = 500$ m and PL = 2. The CIR is projected onto t vs τ where the effect of Doppler compensation is more evident. High-energy (yellow) taps are compensated. 'x' shows a test tap location before and after compensation. The taps are aligned vertically after compensation, demonstrating proper recovery of channel tap locations.

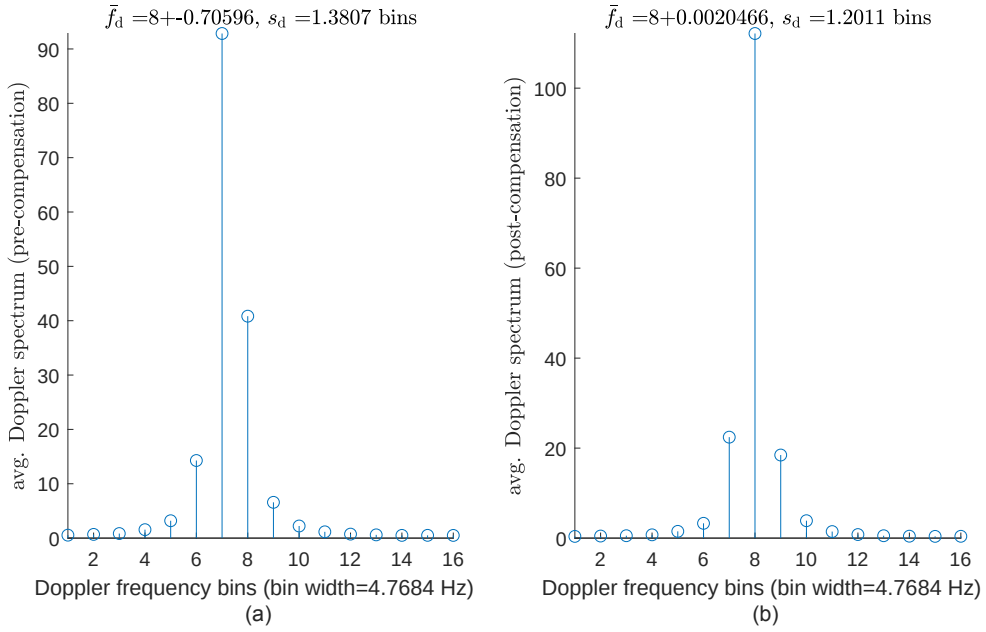

Figure B-7.4: Average Doppler power spectrum comparison (a) before and (b) after compensation for the entire channel ($W = 2.442$ kHz, $d = 500$ m, power level 2). The average is computed over channel delays. The spectrum is shifted so that the Doppler frequency of 0 corresponds to bin 8. Doppler spread is moderate. The centroid of the spectrum is returned to bin 8 after compensation. Only the higher-energy taps were corrected, so the Doppler spread of the channel was not mitigated.

B-8 $W = 2.442$ **kHz,** $d = 1$ **km,** PL $= 4$, $\Delta t = 5$ **s**

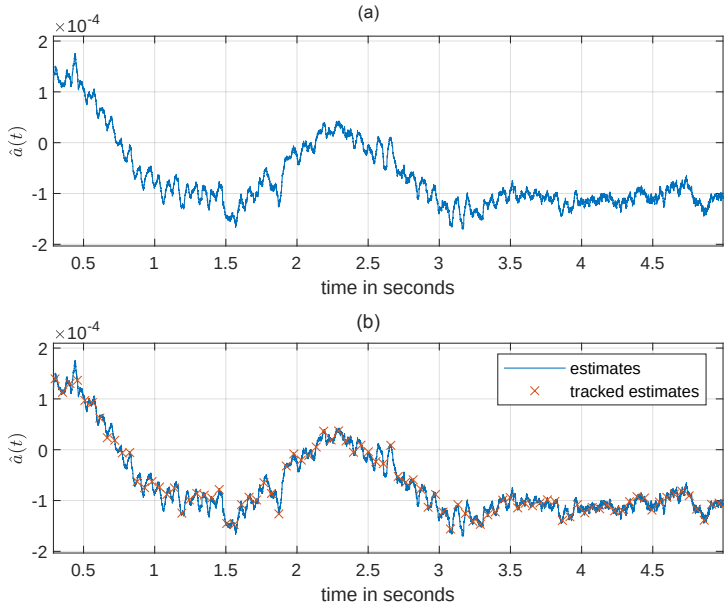

Figure B-8.1: Mach number estimator (a) and tracker (b) with $W = 2.442$ kHz, $d = 1$ km and PL $= 4$. 'x' indicates every 256th sample retained due to downsampling (sample is extracted every 4 preambles). Relative velocity is given by $1500 \cdot a(t)$. This data reduction facilitates practical compensation. Note, the downsampled representation captures the Mach number such that no lower frequency features relevant to tracking are neglected. This practically tracks the Mach number variations.

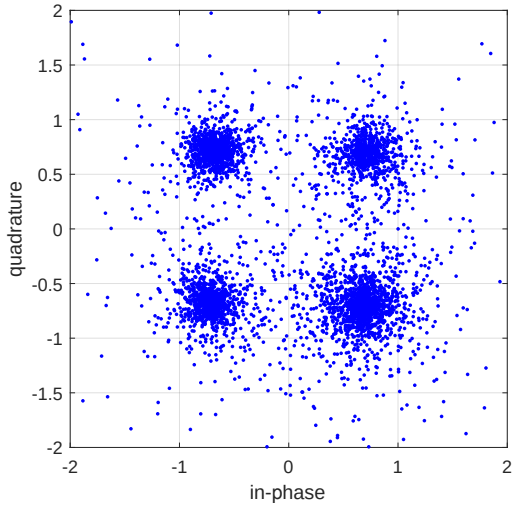

Figure B-8.2: Scatter plot of the compensated and demodulated RX pilots sampled at $W = 2.442$ kHz for a range of $d = 1$ km amd power level 4. The plot indicates that the QPSK symbols have been properly recovered.

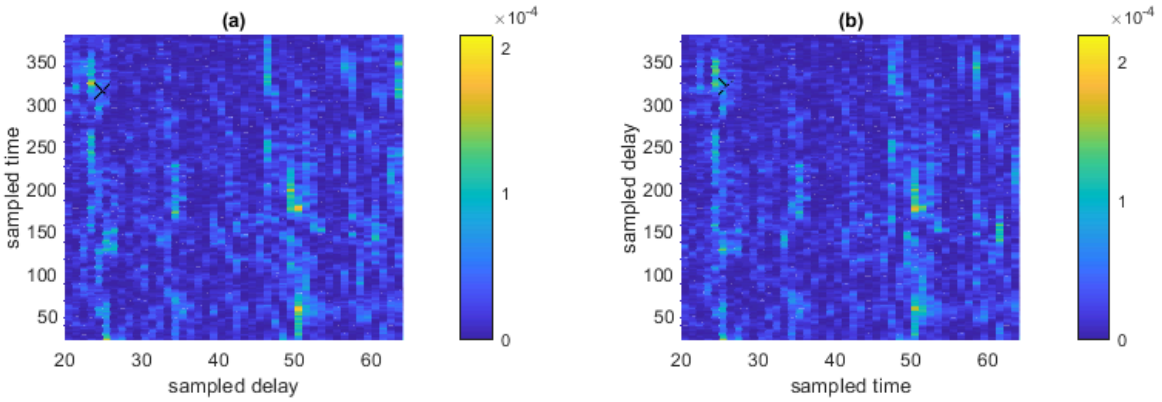

Figure B-8.3: CIR comparison (a) before and (b) after Doppler compensation for $W = 2.442$ kHz, $d = 1$ km and PL $= 4$. The CIR is projected onto t vs τ where the effect of Doppler compensation is more evident. High-energy (yellow) taps are compensated. 'x' shows a test tap location before and after compensation. The taps are aligned vertically after compensation, demonstrating proper recovery of channel tap locations.

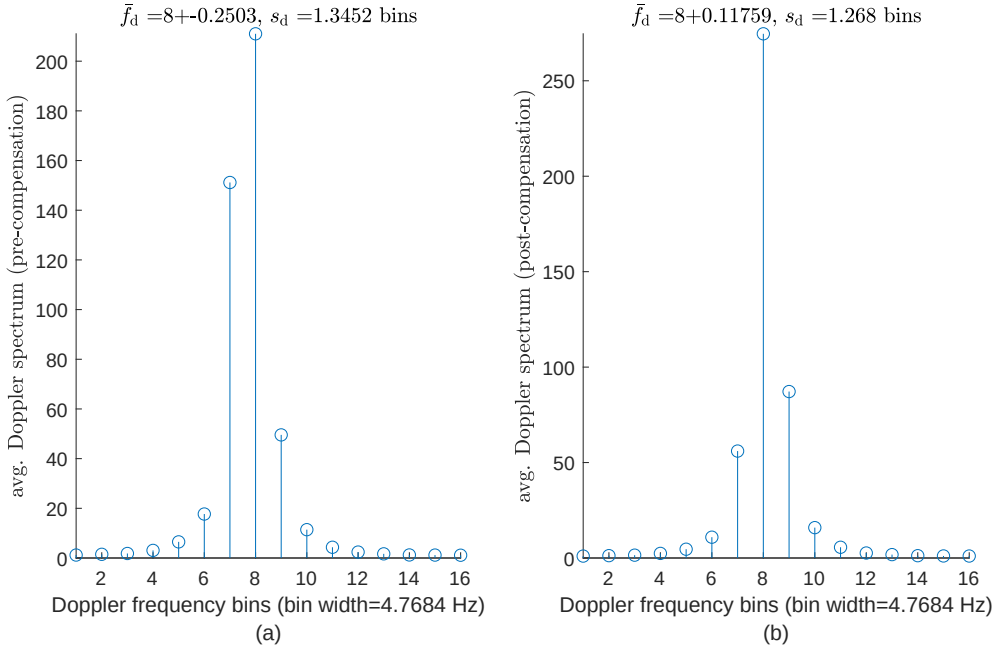

Figure B-8.4: Average Doppler power spectrum comparison (a) before and (b) after compensation for the entire channel ($W = 2.442$ kHz, $d = 1$ km, power level 4). The average is computed over channel delays. The spectrum is shifted so that the Doppler frequency of 0 corresponds to bin 8. Doppler spread is moderate. The centroid of the spectrum is close to bin 8 before and after compensation. Only the higher-energy taps were corrected, so the Doppler spread of the channel was not mitigated.

B-9 $W = 2.442$ **kHz,** $d = 2$ **km,** PL $= 4$**,** $\Delta t = 4.3$ **s**

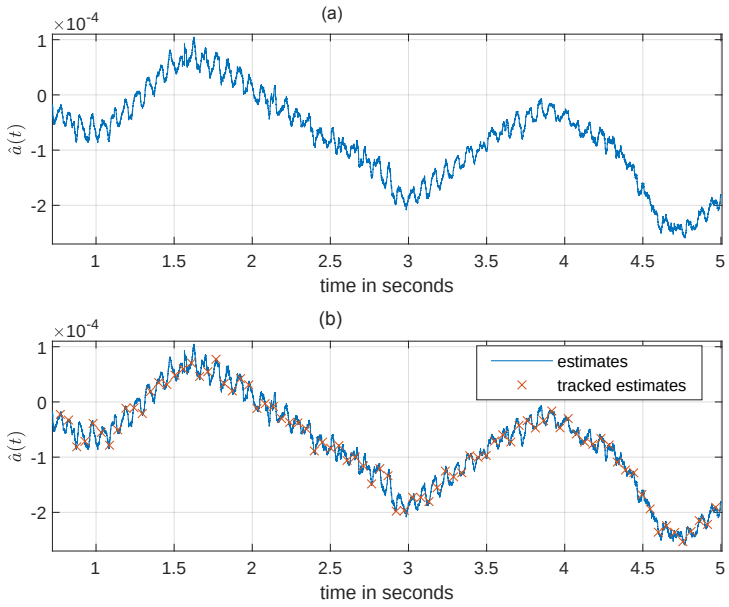

Figure B-9.1: Mach number estimator (a) and tracker (b) with $W = 2.442$ kHz, $d = 2$ km and PL $= 4$. 'x' indicates every 256th sample retained due to downsampling (sample is extracted every 4 preambles). Relative velocity is given by $1500 \cdot a(t)$. This data reduction facilitates practical compensation. Note, the downsampled representation captures the Mach number such that no lower frequency features relevant to tracking are neglected. This practically tracks the Mach number variations.

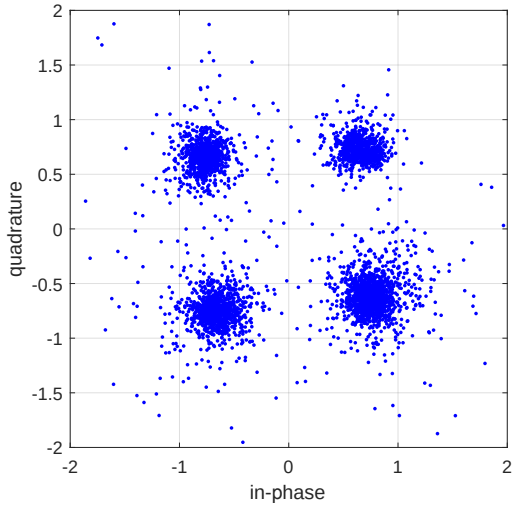

Figure B-9.2: Scatter plot of the compensated and demodulated RX pilots sampled at $W = 2.442$ kHz for a range of $d = 2$ km amd power level 4. The plot indicates that the QPSK symbols have been properly recovered.

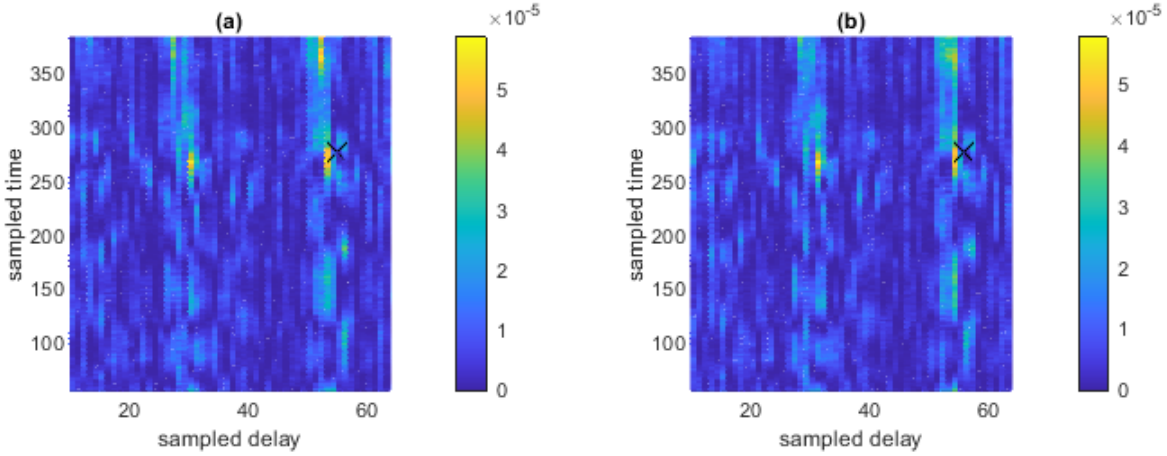

Figure B-9.3: CIR comparison (a) before and (b) after Doppler compensation for $W = 2.442$ kHz, $d = 2$ km and PL $= 4$. The CIR is projected onto t vs τ where the effect of Doppler compensation is more evident. High-energy (yellow) taps are compensated. 'x' shows a test tap location before and after compensation. The taps are aligned vertically after compensation, demonstrating proper recovery of channel tap locations.

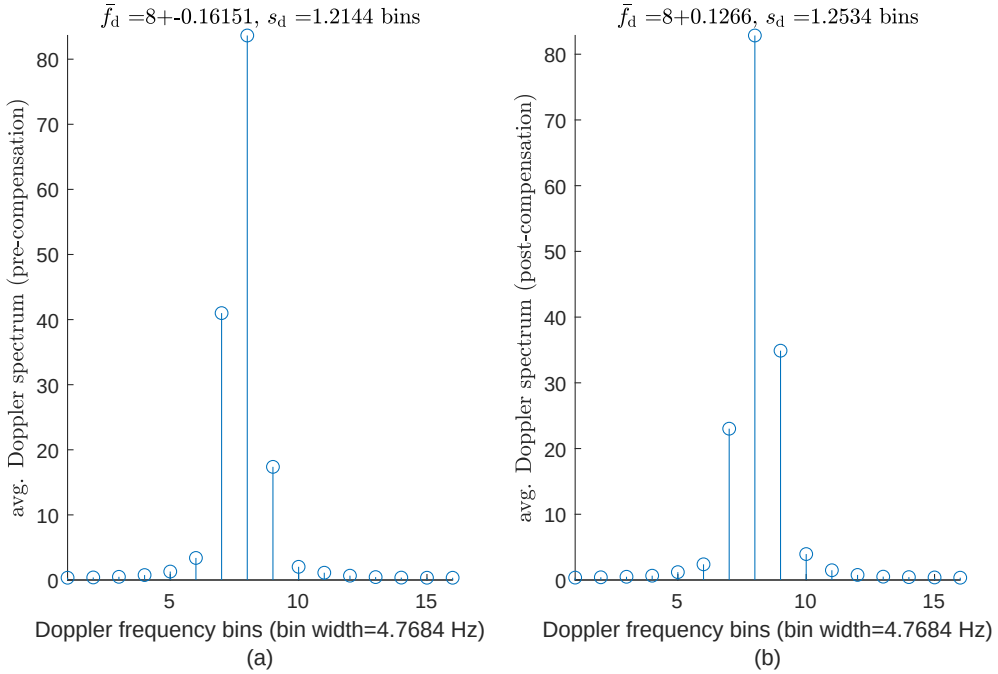

Figure B-9.4: Average Doppler power spectrum comparison (a) before and (b) after compensation for the entire channel ($W = 2.442$ kHz, $d = 2$ km, power level 4). The average is computed over channel delays. The spectrum is shifted so that the Doppler frequency of 0 corresponds to bin 8. Doppler spread is moderate. The centroid of the spectrum is close to bin 8 before and after compensation. Only the higher-energy taps were corrected, so the Doppler spread of the channel was not mitigated.

B-10 $W = 2.442$ **kHz,** $d = 5$ **km,** PL $= 4$**,** $\Delta t = 5$ **s**

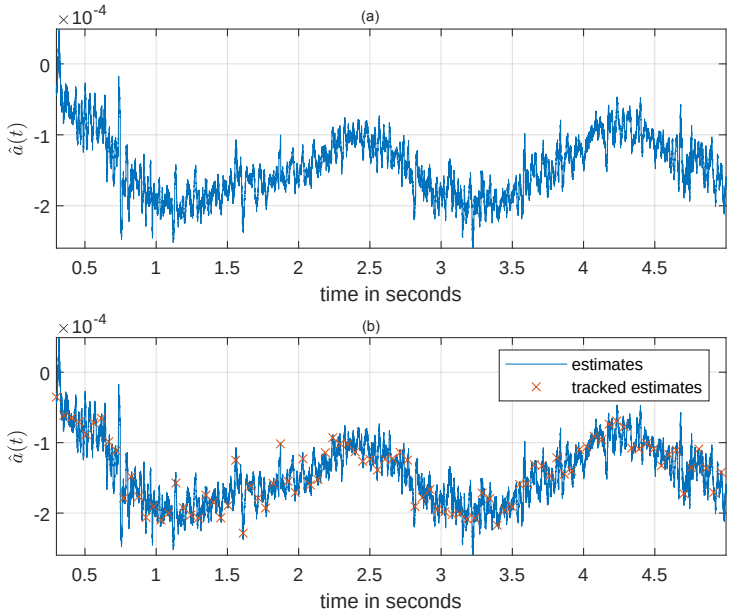

Figure B-10.1: Mach number estimator (a) and tracker (b) with $W = 2.442$ kHz, $d = 5$ km and PL $= 4$. 'x' indicates every 256th sample retained due to downsampling (sample is extracted every 4 preambles). Relative velocity is given by $1500 \cdot a(t)$. This data reduction facilitates practical compensation. Note, the downsampled representation captures the Mach number such that no lower frequency features relevant to tracking are neglected. This practically tracks the Mach number variations.

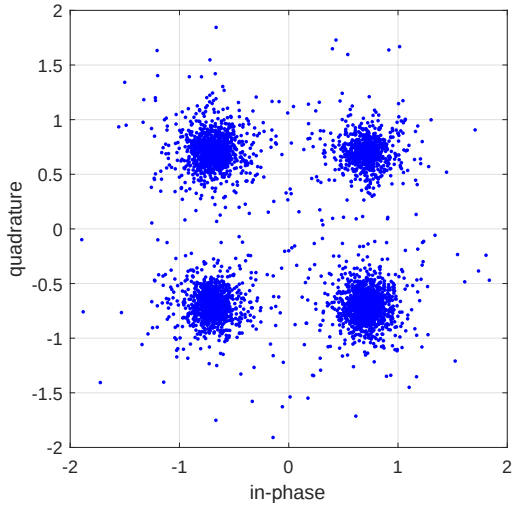

Figure B-10.2: Scatter plot of the compensated and demodulated RX pilots sampled at $W = 2.442$ kHz for a range of $d = 5$ km amd power level 4. The plot indicates that the QPSK symbols have been properly recovered.

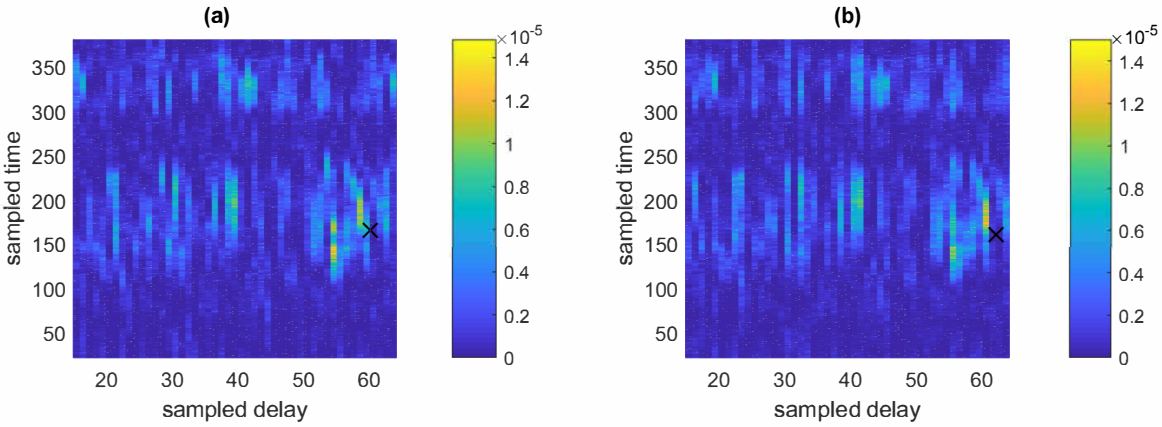

Figure B-10.3: CIR comparison (a) before and (b) after Doppler compensation for $W = 2.442$ kHz, $d = 5$ km and PL $= 4$. The CIR is projected onto t vs τ where the effect of Doppler compensation is more evident. High-energy (yellow) taps are compensated. 'x' shows a test tap location before and after compensation. The taps are aligned vertically after compensation, demonstrating proper recovery of channel tap locations.

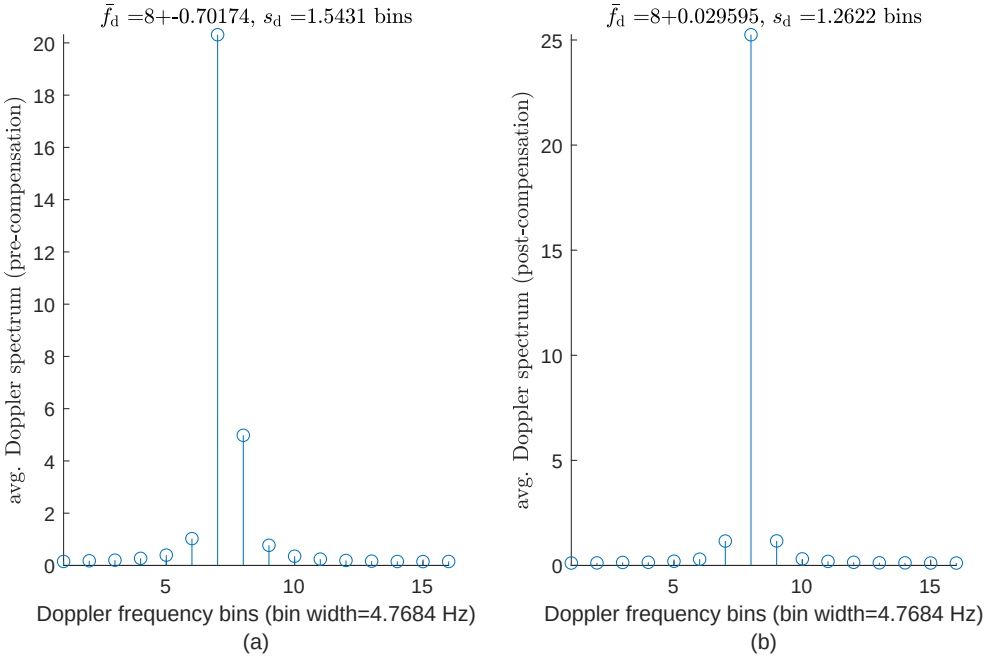

Figure B-10.4: Average Doppler power spectrum comparison (a) before and (b) after compensation for the entire channel ($W = 2.442$ kHz, $d = 5$ km, power level 4). The average is computed over channel delays. The spectrum is shifted so that the Doppler frequency of 0 corresponds to bin 8. Doppler spread is small. The centroid of the spectrum is returned to bin 8 after compensation.

B-11 $W = 4.883$ **kHz,** $d = 500$ **m,** PL $= 1$, $\Delta t = 5$ **s**

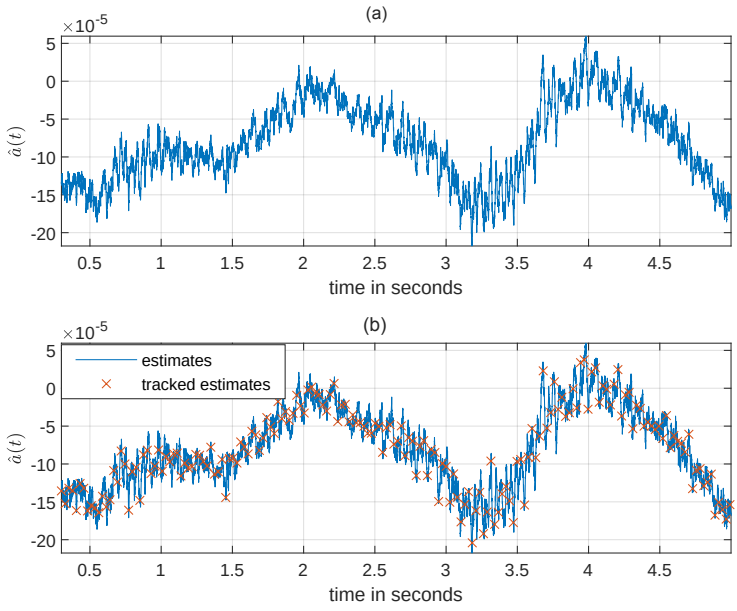

Figure B-11.1: Mach number estimator (a) and tracker (b) with $W = 4.883$ kHz, $d = 500$ m and PL $= 1$. 'x' indicates every 256th sample retained due to downsampling (sample is extracted every 4 preambles). Relative velocity is given by $1500 \cdot a(t)$. This data reduction facilitates practical compensation. Note, the downsampled representation captures the Mach number such that no lower frequency features relevant to tracking are neglected. This practically tracks the Mach number variations.

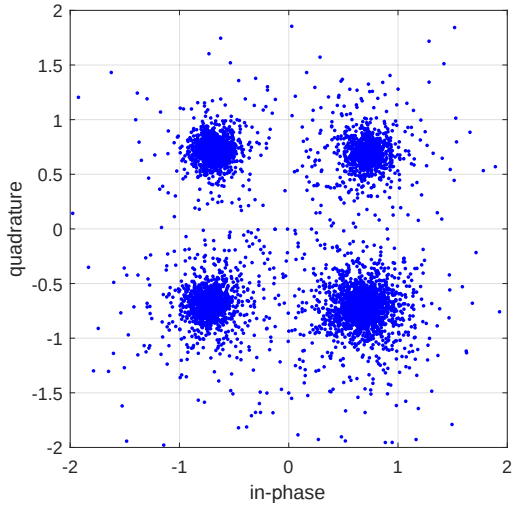

Figure B-11.2: Scatter plot of the compensated and demodulated RX pilots sampled at $W = 4.883$ kHz for a range of $d = 500$ m amd power level 1. The plot indicates that the QPSK symbols have been properly recovered.

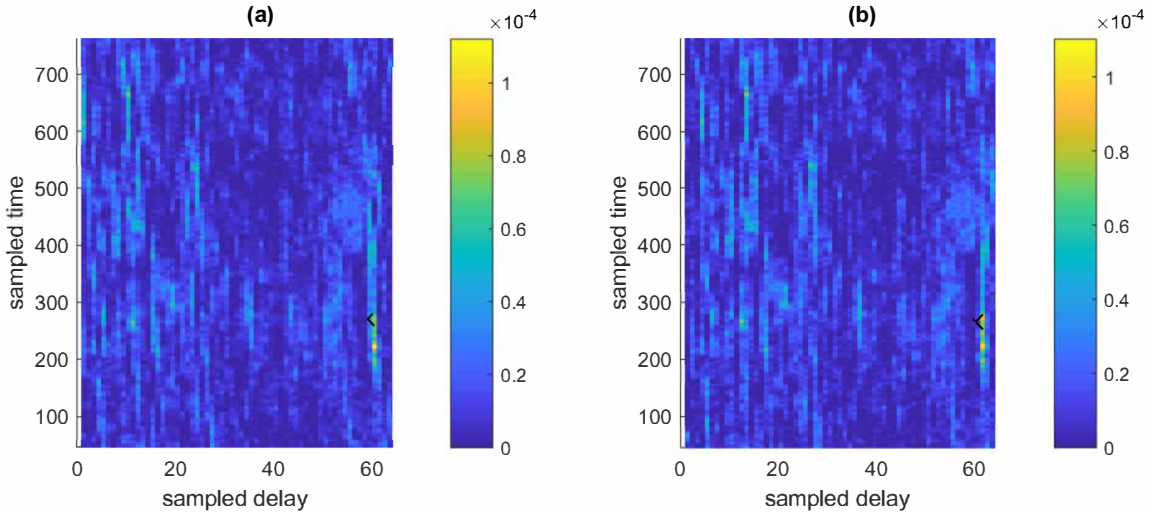

Figure B-11.3: CIR comparison (a) before and (b) after Doppler compensation for $W = 4.883$ kHz, $d = 500$ m and PL = 1. The CIR is projected onto t vs τ where the effect of Doppler compensation is more evident. High-energy (yellow) taps are compensated. 'x' shows a test tap location before and after compensation. The taps are aligned vertically after compensation, demonstrating proper recovery of channel tap locations.

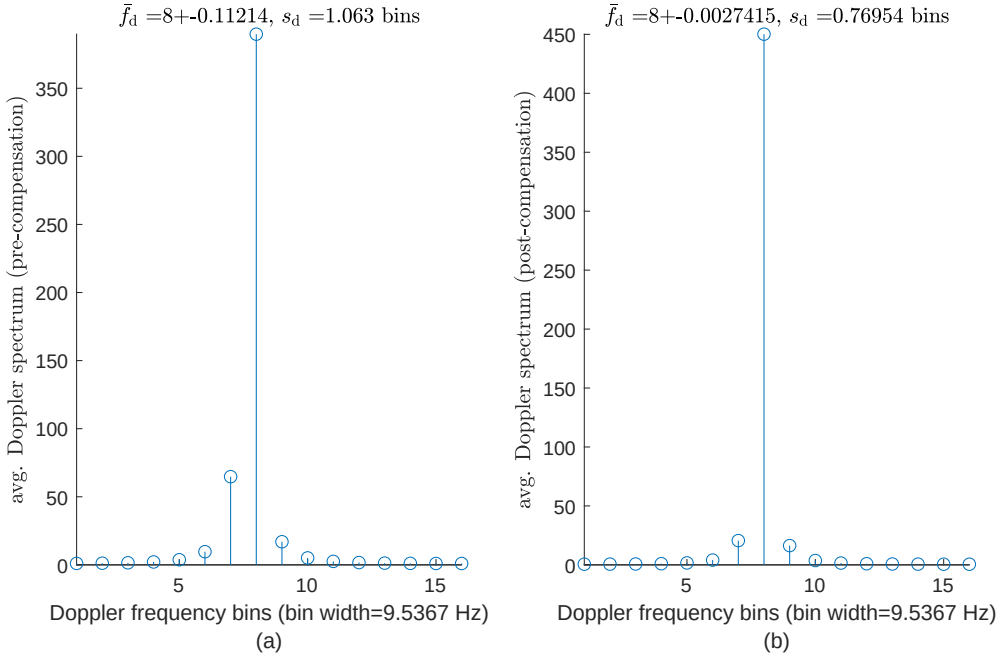

Figure B-11.4: Average Doppler power spectrum comparison (a) before and (b) after compensation for the entire channel ($W = 4.883$ kHz, $d = 500$ m, power level 1). The average is computed over channel delays. The spectrum is shifted so that the Doppler frequency of 0 corresponds to bin 8. Doppler spread is small. The centroid of the spectrum is returned to bin 8 after compensation.

B-12 $W = 4.883$ **kHz,** $d = 500$ **m,** PL $= 2$**,** $\Delta t = 5$ **s**

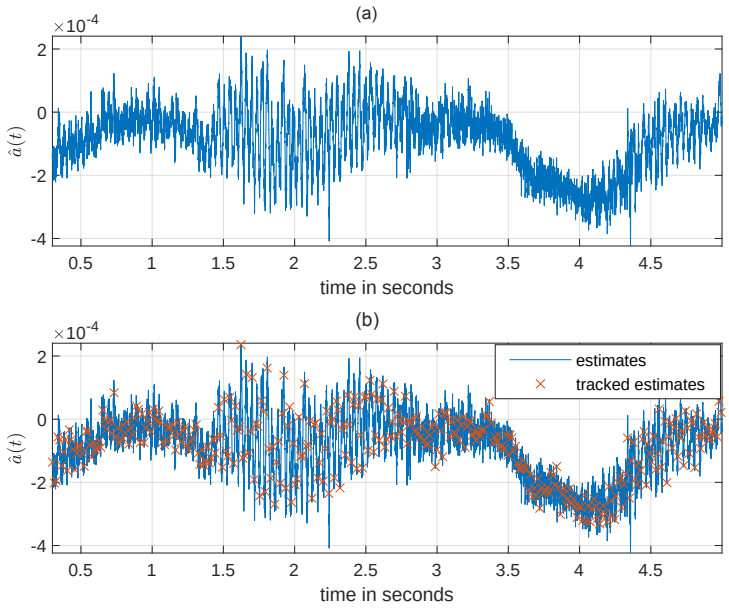

Figure B-12.1: Mach number estimator (a) and tracker (b) with $W = 4.883$ kHz, $d = 500$ m and PL $= 2$. 'x' indicates every 256th sample retained due to downsampling (sample is extracted every 4 preambles). Relative velocity is given by $1500 \cdot a(t)$. This data reduction facilitates practical compensation. Note, the downsampled representation captures the Mach number such that no lower frequency features relevant to tracking are neglected. This practically tracks the Mach number variations.

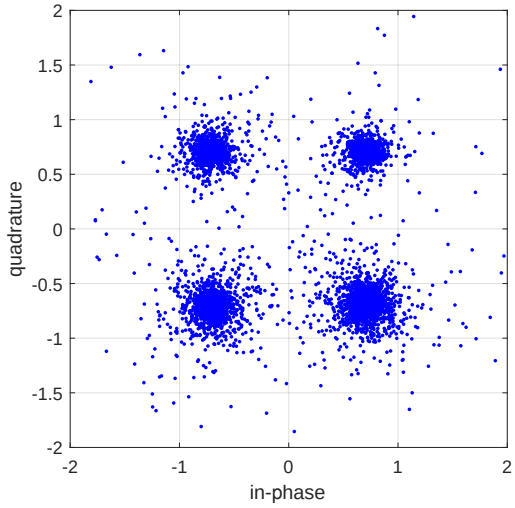

Figure B-12.2: Scatter plot of the compensated and demodulated RX pilots sampled at $W = 4.883$ kHz for a range of $d = 500$ m amd power level 2. The plot indicates that the QPSK symbols have been properly recovered.

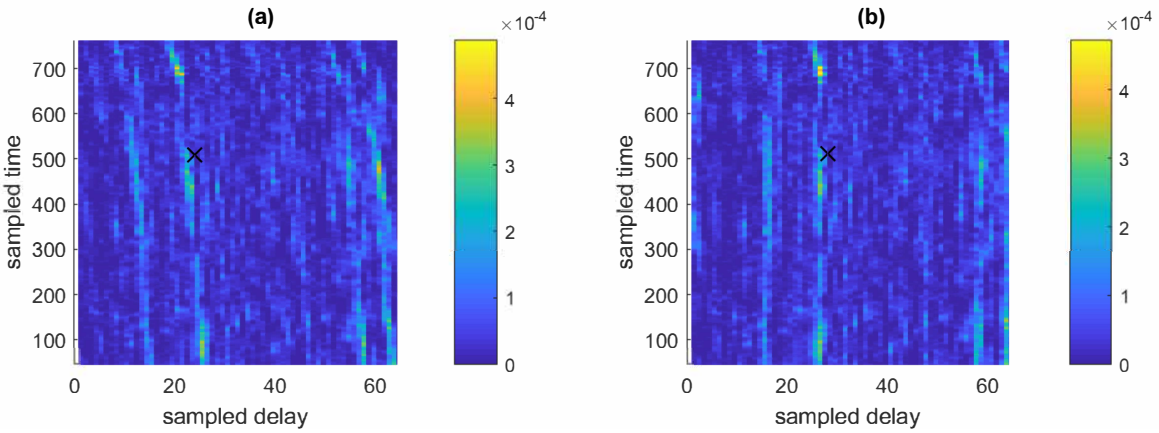

Figure B-12.3: CIR comparison (a) before and (b) after Doppler compensation for $W = 4.883$ kHz, $d = 500$ m and PL $= 2$. The CIR is projected onto t vs τ where the effect of Doppler compensation is more evident. High-energy (yellow) taps are compensated. 'x' shows a test tap location before and after compensation. The taps are aligned vertically after compensation, demonstrating proper recovery of channel tap locations.

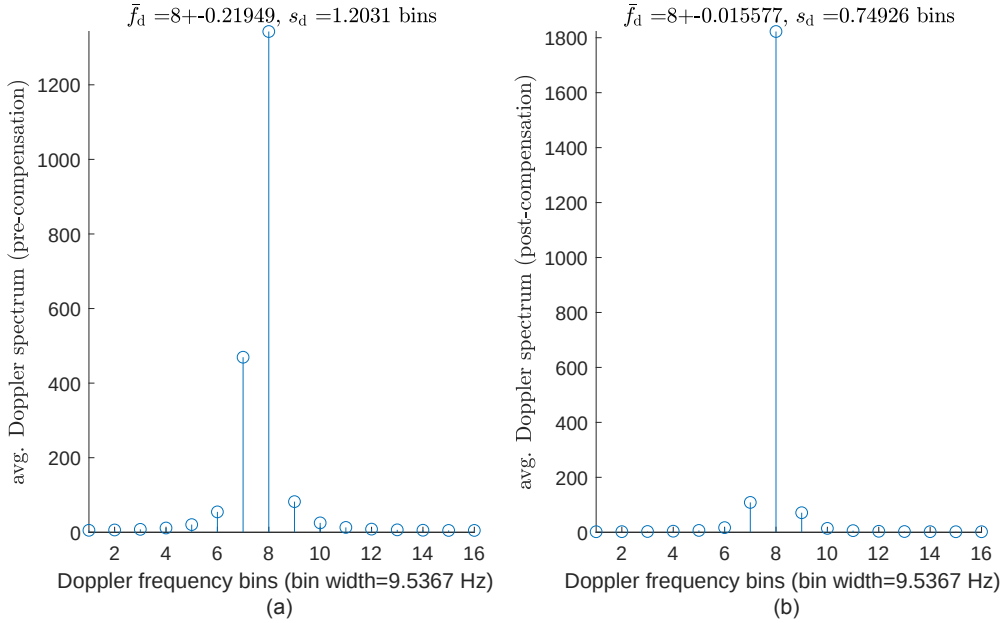

Figure B-12.4: Average Doppler power spectrum comparison (a) before and (b) after compensation for the entire channel ($W = 4.883$ kHz, $d = 500$ m, power level 2). The average is computed over channel delays. The spectrum is shifted so that the Doppler frequency of 0 corresponds to bin 8. Doppler spread is small. The centroid of the spectrum is returned to bin 8 after compensation.

B-13 $W = 4.883$ **kHz,** $d = 500$ **m,** PL $= 3$**,** $\Delta t = 5$ **s**

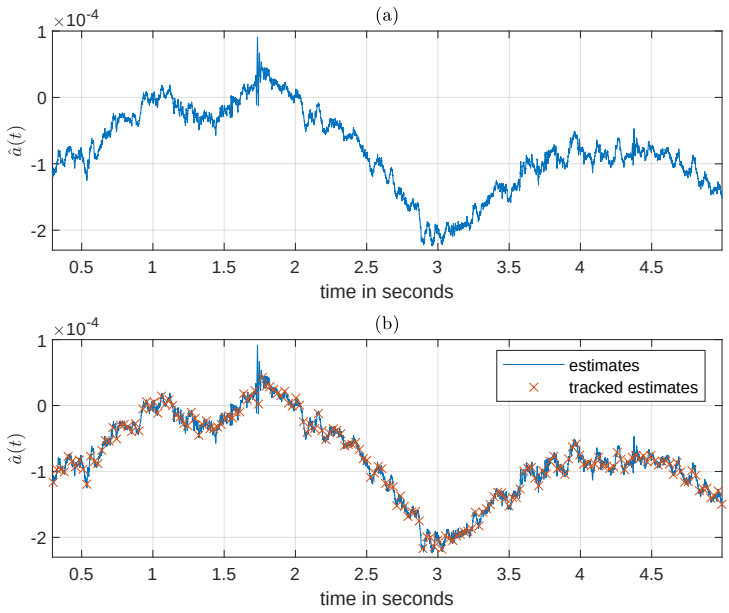

Figure B-13.1: Mach number estimator (a) and tracker (b) with $W = 4.883$ kHz, $d = 500$ m and PL $= 3$. 'x' indicates every 256th sample retained due to downsampling (sample is extracted every 4 preambles). Relative velocity is given by $1500 \cdot a(t)$. This data reduction facilitates practical compensation. Note, the downsampled representation captures the Mach number such that no lower frequency features relevant to tracking are neglected. This practically tracks the Mach number variations.

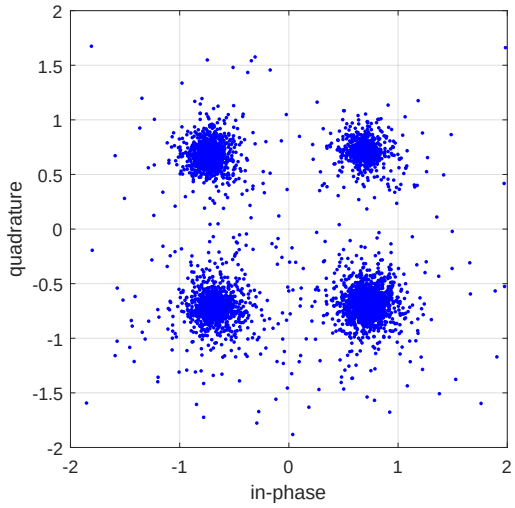

Figure B-13.2: Scatter plot of the compensated and demodulated RX pilots sampled at $W = 4.883$ kHz for a range of $d = 500$ m amd power level 3. The plot indicates that the QPSK symbols have been properly recovered.

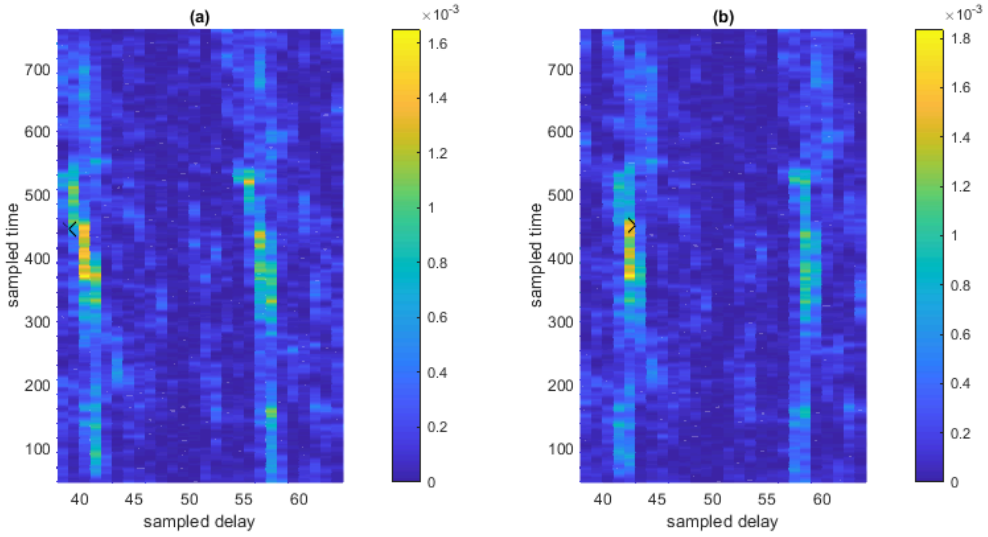

Figure B-13.3: CIR comparison (a) before and (b) after Doppler compensation for $W = 4.883$ kHz, $d = 500$ m and PL $= 3$. The CIR is projected onto t vs τ where the effect of Doppler compensation is more evident. High-energy (yellow) taps are compensated. 'x' shows a test tap location before and after compensation. The taps are aligned vertically after compensation, demonstrating proper recovery of channel tap locations.

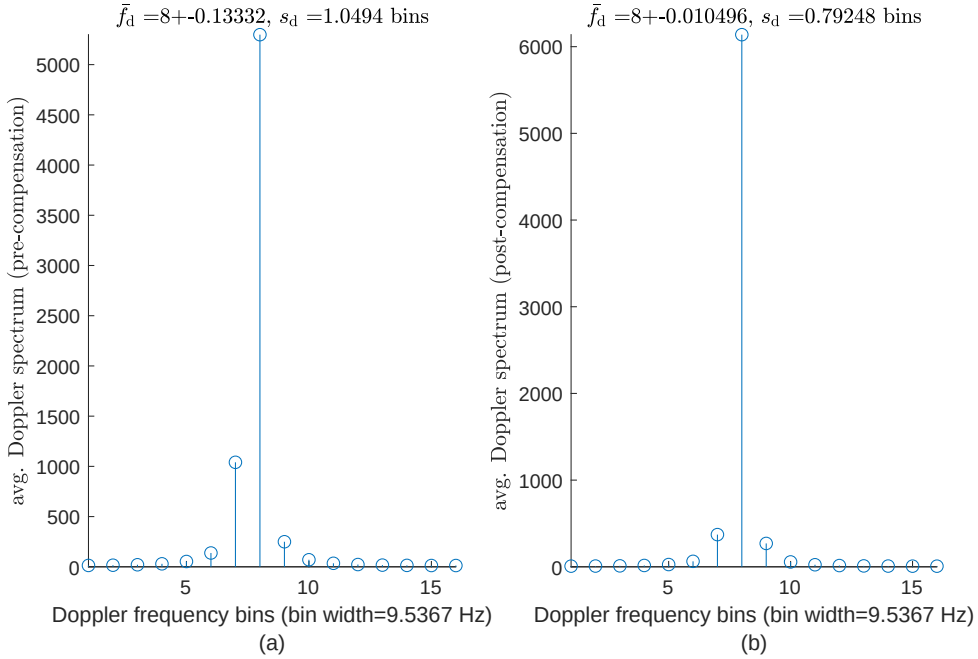

Figure B-13.4: Average Doppler power spectrum comparison (a) before and (b) after compensation for the entire channel ($W = 4.883$ kHz, $d = 500$ m, power level 3). The average is computed over channel delays. The spectrum is shifted so that the Doppler frequency of 0 corresponds to bin 8. Doppler spread is small. The centroid of the spectrum is returned to bin 8 after compensation.

B-14 $W = 4.883$ **kHz,** $d = 500$ **m,** PL $= 4$**,** $\Delta t = 2.1$ **s**

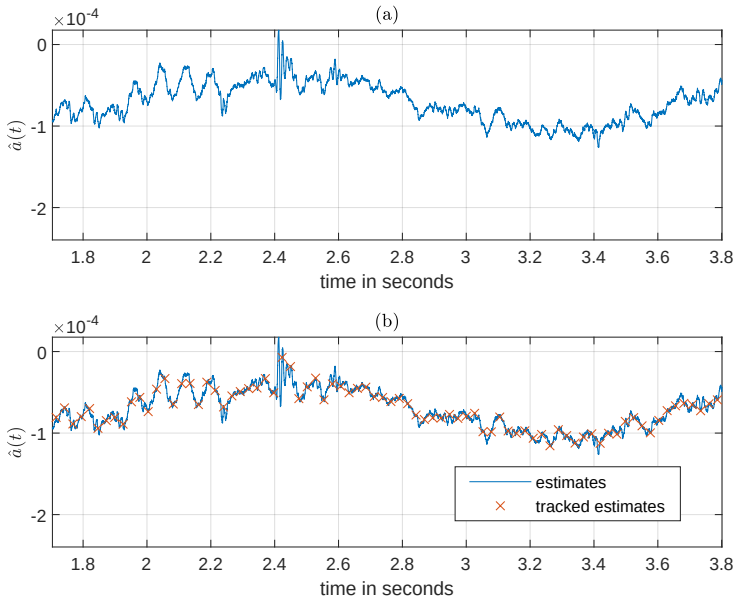

Figure B-14.1: Mach number estimator (a) and tracker (b) with $W = 4.883$ kHz, $d = 500$ m and PL $= 4$. 'x' indicates every 256th sample retained due to downsampling (sample is extracted every 4 preambles). Relative velocity is given by $1500 \cdot a(t)$. This data reduction facilitates practical compensation. Note, the downsampled representation captures the Mach number such that no lower frequency features relevant to tracking are neglected. This practically tracks the Mach number variations.

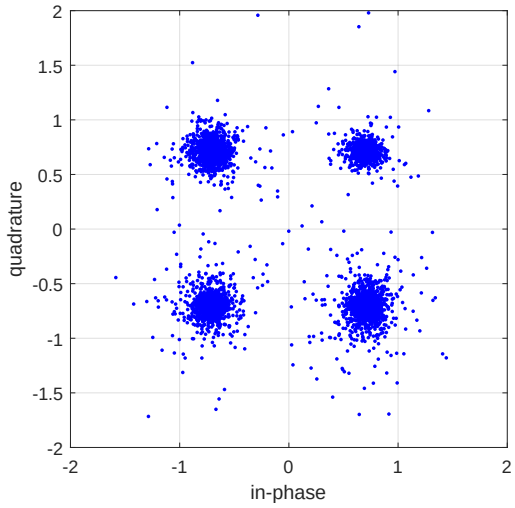

Figure B-14.2: Scatter plot of the compensated and demodulated RX pilots sampled at $W = 4.883$ kHz for a range of $d = 500$ m amd power level 4. The plot indicates that the QPSK symbols have been properly recovered.

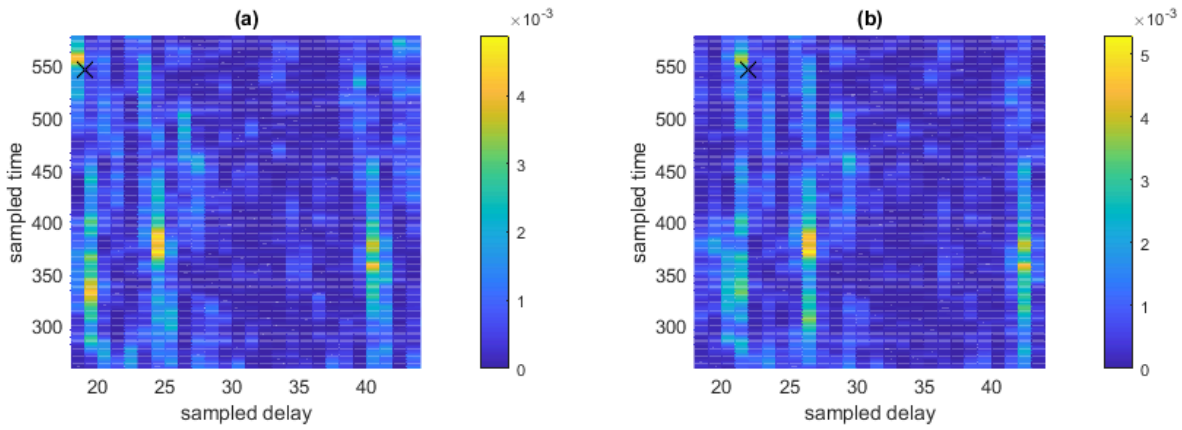

Figure B-14.3: CIR comparison (a) before and (b) after Doppler compensation for $W = 4.883$ kHz, $d = 500$ m and PL $= 4$. The CIR is projected onto t vs τ where the effect of Doppler compensation is more evident. High-energy (yellow) taps are compensated. 'x' shows a test tap location before and after compensation. The taps are aligned vertically after compensation, demonstrating proper recovery of channel tap locations.

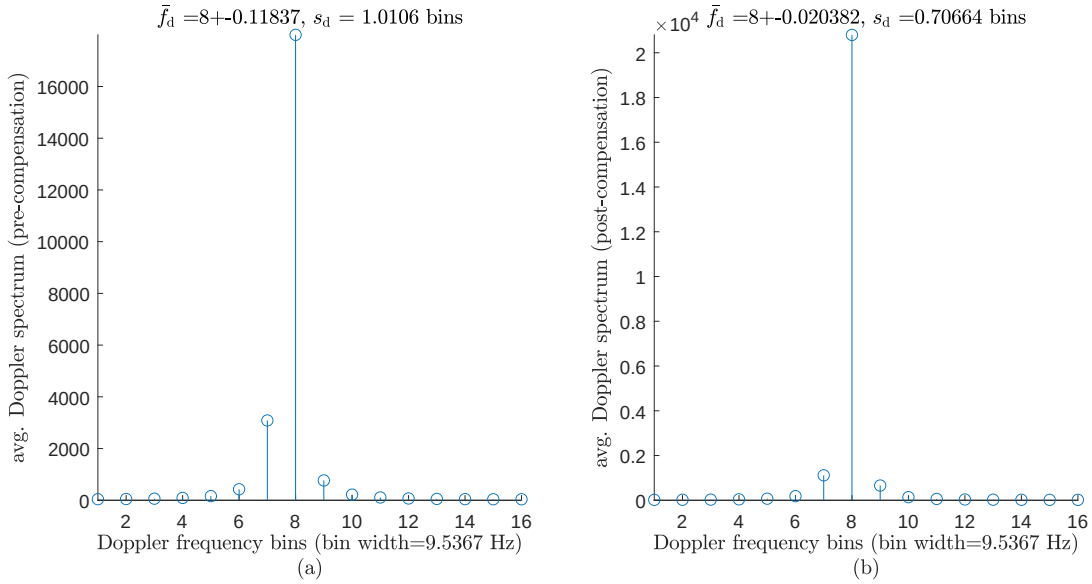

Figure B-14.4: Average Doppler power spectrum comparison (a) before and (b) after compensation for the entire channel ($W = 4.883$ kHz, $d = 500$ m, power level 4). The average is computed over channel delays. The spectrum is shifted so that the Doppler frequency of 0 corresponds to bin 8. Doppler spread is small. The centroid of the spectrum is returned to bin 8 after compensation.

B-15 $W = 4.883$ **kHz,** $d = 1$ **km,** PL $= 3$**,** $\Delta t = 2$ **s,** $\Delta t = 2$ **s**

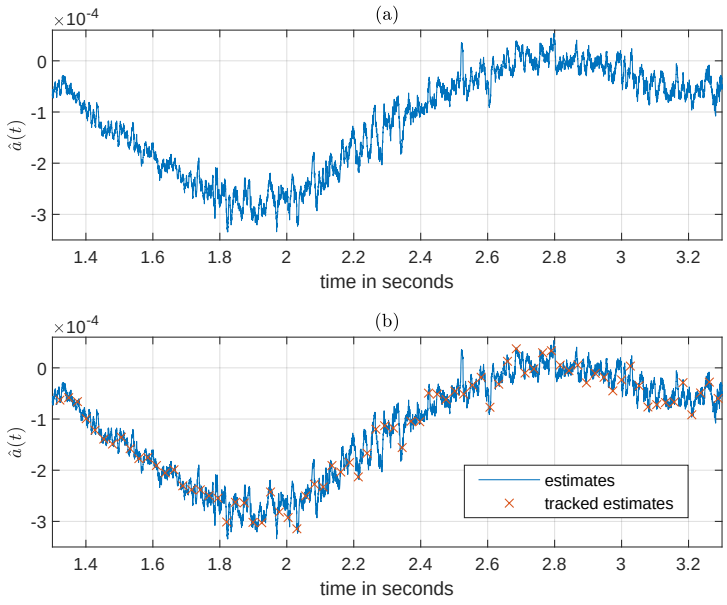

Figure B-15.1: Mach number estimator (a) and tracker (b) with $W = 4.883$ kHz, $d = 1$ km and PL $= 3$. 'x' indicates every 256th sample retained due to downsampling (sample is extracted every 4 preambles). Relative velocity is given by $1500 \cdot a(t)$. This data reduction facilitates practical compensation. Note, the downsampled representation captures the Mach number such that no lower frequency features relevant to tracking are neglected. This practically tracks the Mach number variations.

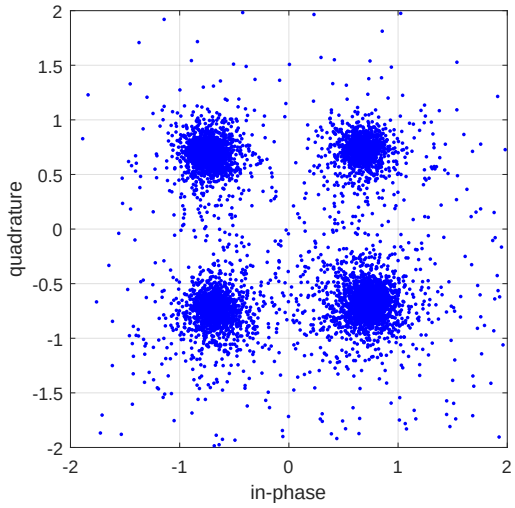

Figure B-15.2: Scatter plot of the compensated and demodulated RX pilots sampled at $W = 4.883$ kHz for a range of $d = 1$ km amd power level 3. The plot indicates that the QPSK symbols have been properly recovered.

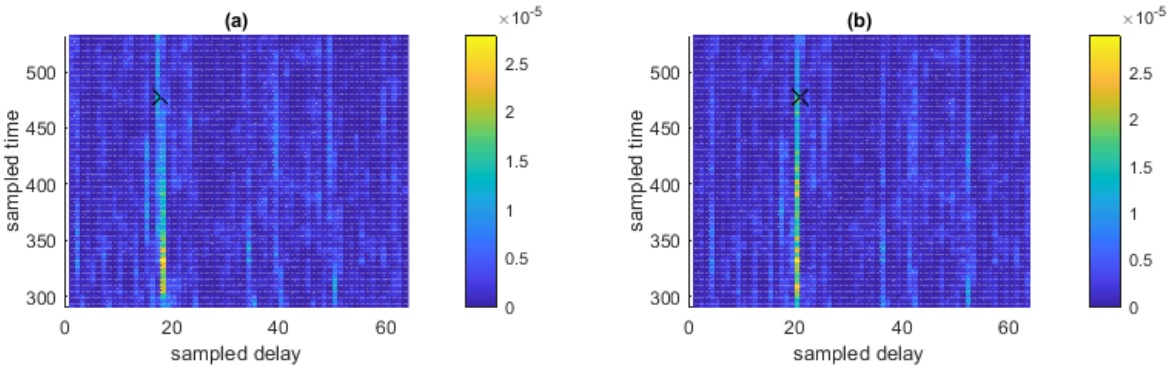

Figure B-15.3: CIR comparison (a) before and (b) after Doppler compensation for $W = 4.883$ kHz, $d = 1$ km and PL = 3. The CIR is projected onto t vs τ where the effect of Doppler compensation is more evident. High-energy (yellow) taps are compensated. 'x' shows a test tap location before and after compensation. The taps are aligned vertically after compensation, demonstrating proper recovery of channel tap locations.

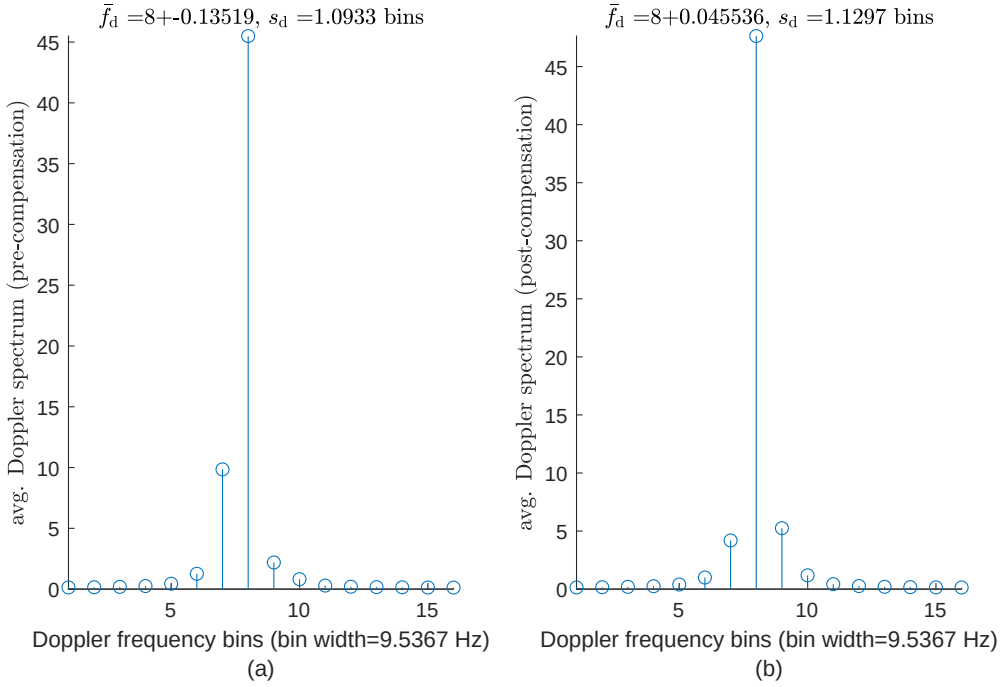

Figure B-15.4: Average Doppler power spectrum comparison (a) before and (b) after compensation for the entire channel ($W = 4.883$ kHz, $d = 1$ km, power level 3). The average is computed over channel delays. The spectrum is shifted so that the Doppler frequency of 0 corresponds to bin 8. Doppler spread is small. The centroid of the spectrum is returned to bin 8 after compensation.

B-16 $W = 4.883$ **kHz,** $d = 1$ **km,** PL $= 4$**,** $\Delta t = 1.6$ **s**

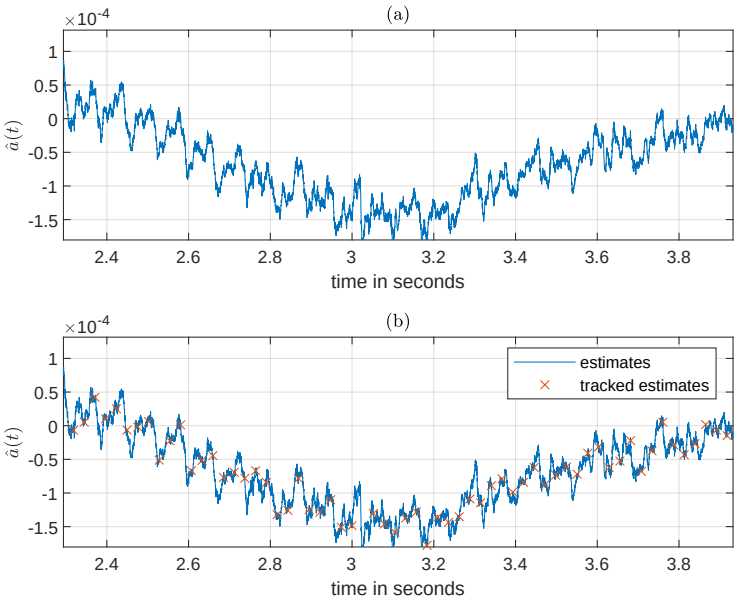

Figure B-16.1: Mach number estimator (a) and tracker (b) with $W = 4.883$ kHz, $d = 1$ km and PL $= 4$. 'x' indicates every 256th sample retained due to downsampling (sample is extracted every 4 preambles). Relative velocity is given by $1500 \cdot a(t)$. This data reduction facilitates practical compensation. Note, the downsampled representation captures the Mach number such that no lower frequency features relevant to tracking are neglected. This practically tracks the Mach number variations.

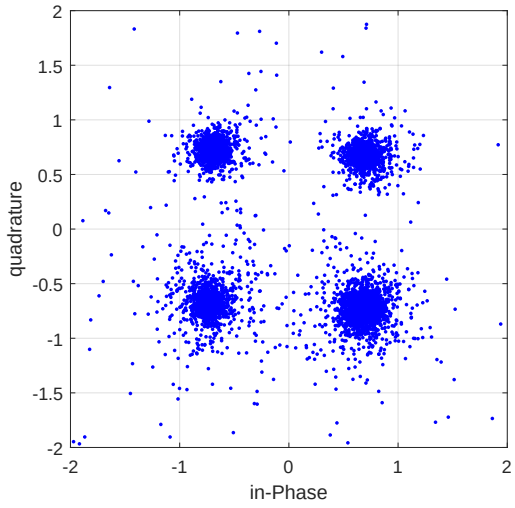

Figure B-16.2: Scatter plot of the compensated and demodulated RX pilots sampled at $W = 4.883$ kHz for a range of $d = 1$ km amd power level 4. The plot indicates that the QPSK symbols have been properly recovered.

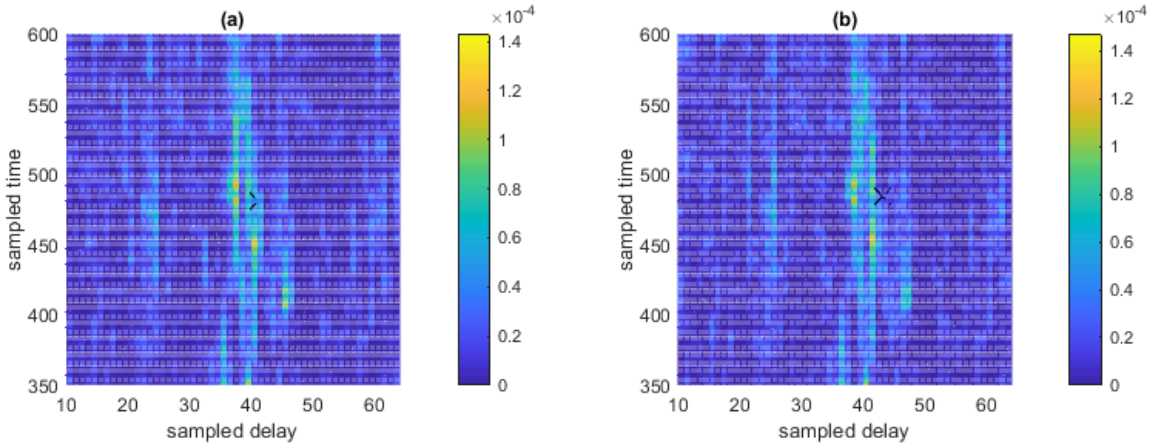

Figure B-16.3: CIR comparison (a) before and (b) after Doppler compensation for $W = 4.883$ kHz, $d = 1$ km and PL $= 4$. The CIR is projected onto t vs τ where the effect of Doppler compensation is more evident. High-energy (yellow) taps are compensated. 'x' shows a test tap location before and after compensation. The taps are aligned vertically after compensation, demonstrating proper recovery of channel tap locations.

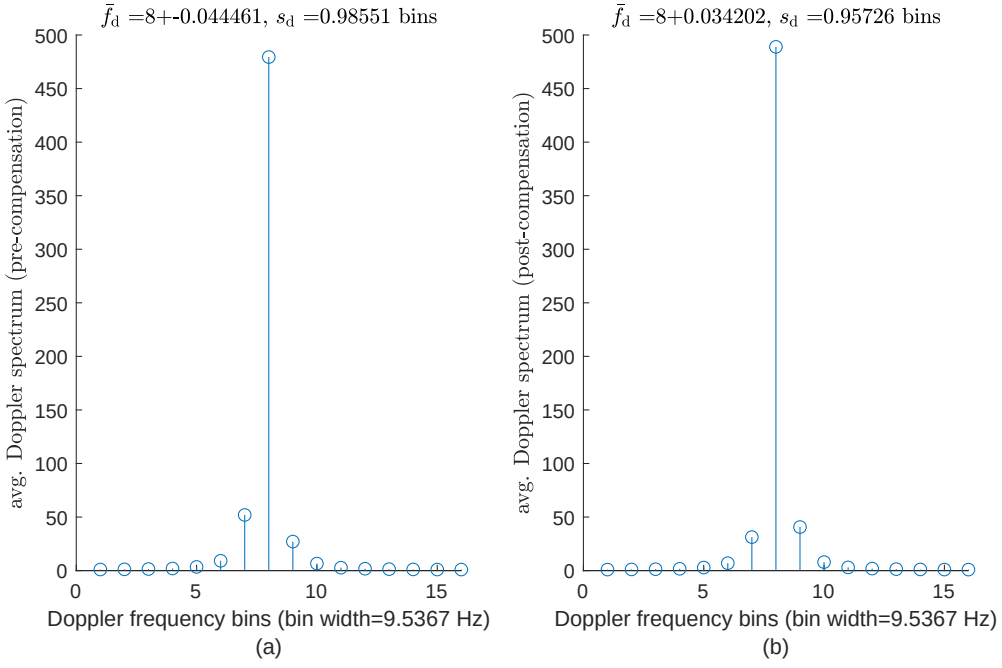

Figure B-16.4: Average Doppler power spectrum comparison (a) before and (b) after compensation for the entire channel ($W = 4.883$ kHz, $d = 1$ km, power level 4). The average is computed over channel delays. The spectrum is shifted so that the Doppler frequency of 0 corresponds to bin 8. Doppler spread is small. The centroid of the spectrum is close to bin 8 before and after compensation.

B-17 $W = 4.883$ **kHz,** $d = 2$ **km,** PL $= 3$**,** $\Delta t = 5$ **s**

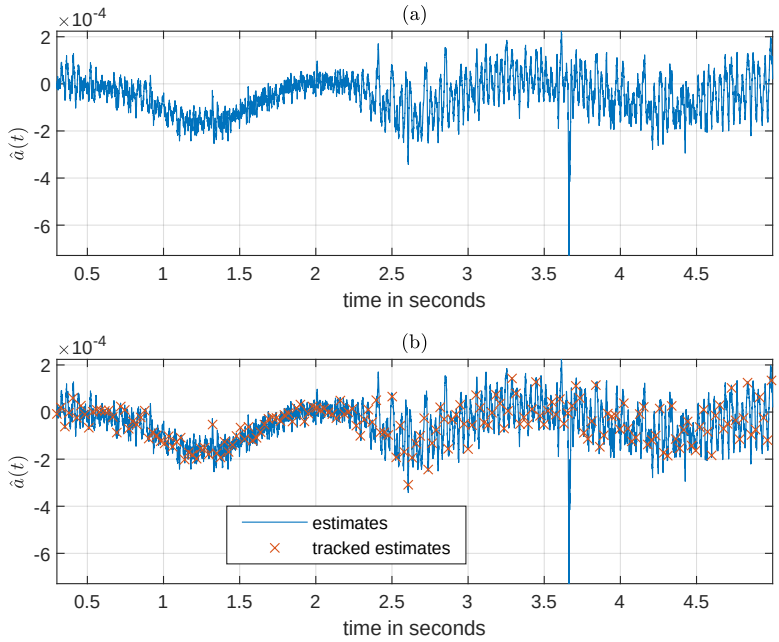

Figure B-17.1: Mach number estimator (a) and tracker (b) with $W = 4.883$ kHz, $d = 2$ km and PL $= 3$. 'x' indicates every 256th sample retained due to downsampling (sample is extracted every 4 preambles). Relative velocity is given by $1500 \cdot a(t)$. This data reduction facilitates practical compensation. Note, the downsampled representation captures the Mach number such that no lower frequency features relevant to tracking are neglected. This practically tracks the Mach number variations.

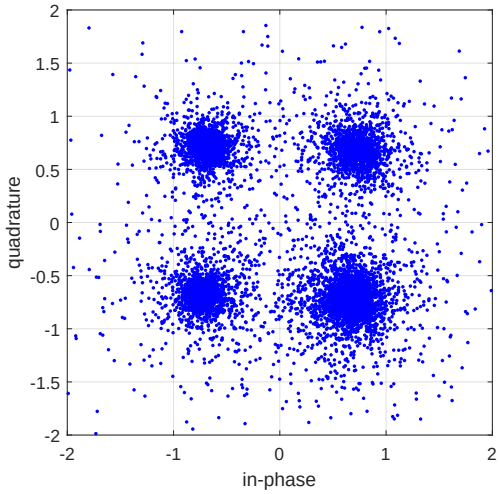

Figure B-17.2: Scatter plot of the compensated and demodulated RX pilots sampled at $W = 4.883$ kHz for a range of $d = 2$ km amd power level 3. The plot indicates that the QPSK symbols have been properly recovered.

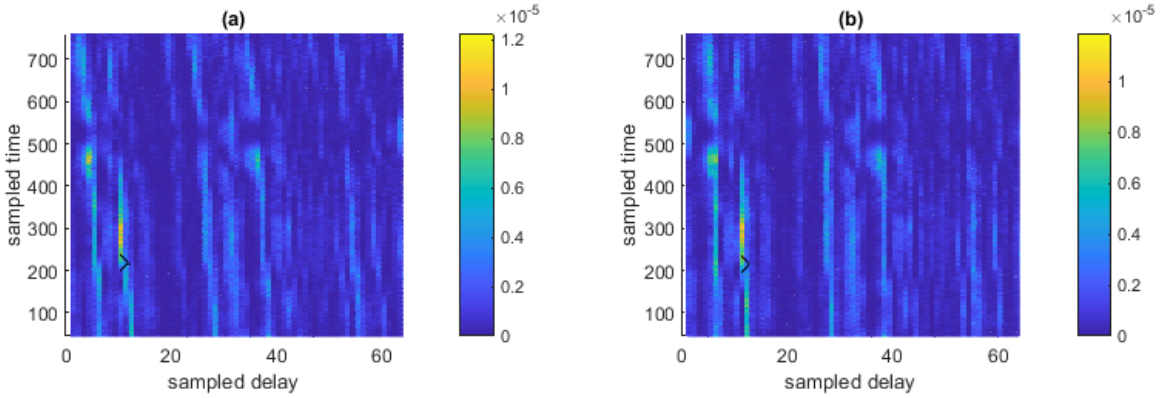

Figure B-17.3: CIR comparison (a) before and (b) after Doppler compensation for $W = 4.883$ kHz, $d = 2$ km and PL = 3. The CIR is projected onto t vs τ where the effect of Doppler compensation is more evident. High-energy (yellow) taps are compensated. 'x' shows a test tap location before and after compensation. The taps are aligned vertically after compensation, demonstrating proper recovery of channel tap locations.

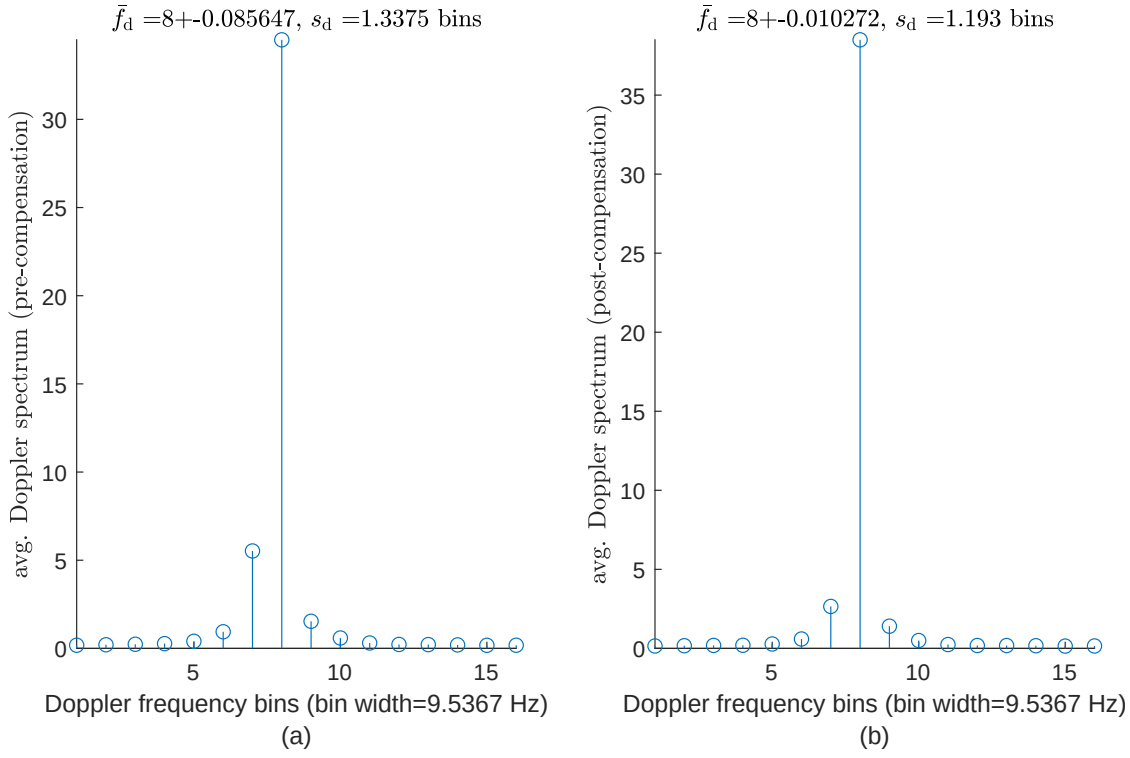

Figure B-17.4: Average Doppler power spectrum comparison (a) before and (b) after compensation for the entire channel ($W = 4.883$ kHz, $d = 2$ km, power level 3). The average is computed over channel delays. The spectrum is shifted so that the Doppler frequency of 0 corresponds to bin 8. Doppler spread is small. The centroid of the spectrum is returned to bin 8 after compensation.

B-18 $W = 4.883$ **kHz,** $d = 2$ **km,** PL $= 4$**,** $\Delta t = 5$ **s**

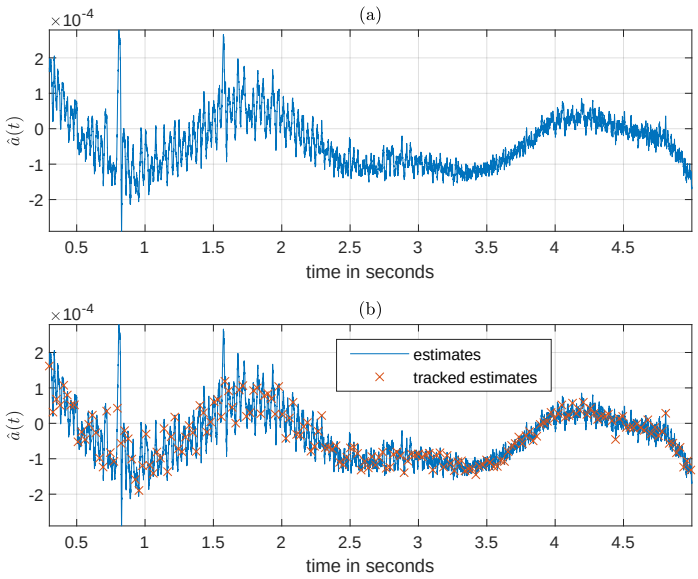

Figure B-18.1: Mach number estimator (a) and tracker (b) with $W = 4.883$ kHz, $d = 2$ km and PL $= 4$. 'x' indicates every 256th sample retained due to downsampling (sample is extracted every 4 preambles). Relative velocity is given by $1500 \cdot a(t)$. This data reduction facilitates practical compensation. Note, the downsampled representation captures the Mach number such that no lower frequency features relevant to tracking are neglected. This practically tracks the Mach number variations.

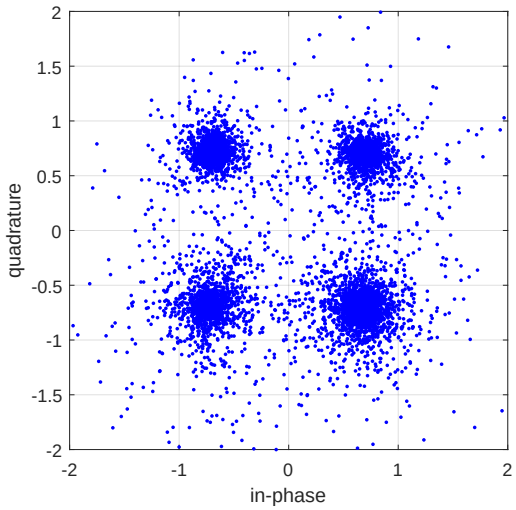

Figure B-18.2: Scatter plot of the compensated and demodulated RX pilots sampled at $W = 4.883$ kHz for a range of $d = 2$ km amd power level 4. The plot indicates that the QPSK symbols have been properly recovered.

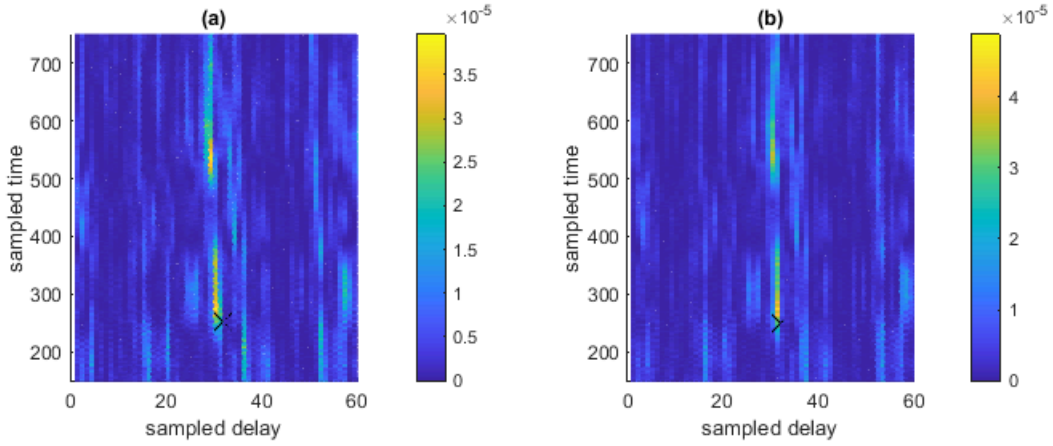

Figure B-18.3: CIR comparison (a) before and (b) after Doppler compensation for $W = 4.883$ kHz, $d = 2$ km and PL $= 4$. The CIR is projected onto t vs τ where the effect of Doppler compensation is more evident. High-energy (yellow) taps are compensated. 'x' shows a test tap location before and after compensation. The taps are aligned vertically after compensation, demonstrating proper recovery of channel tap locations.

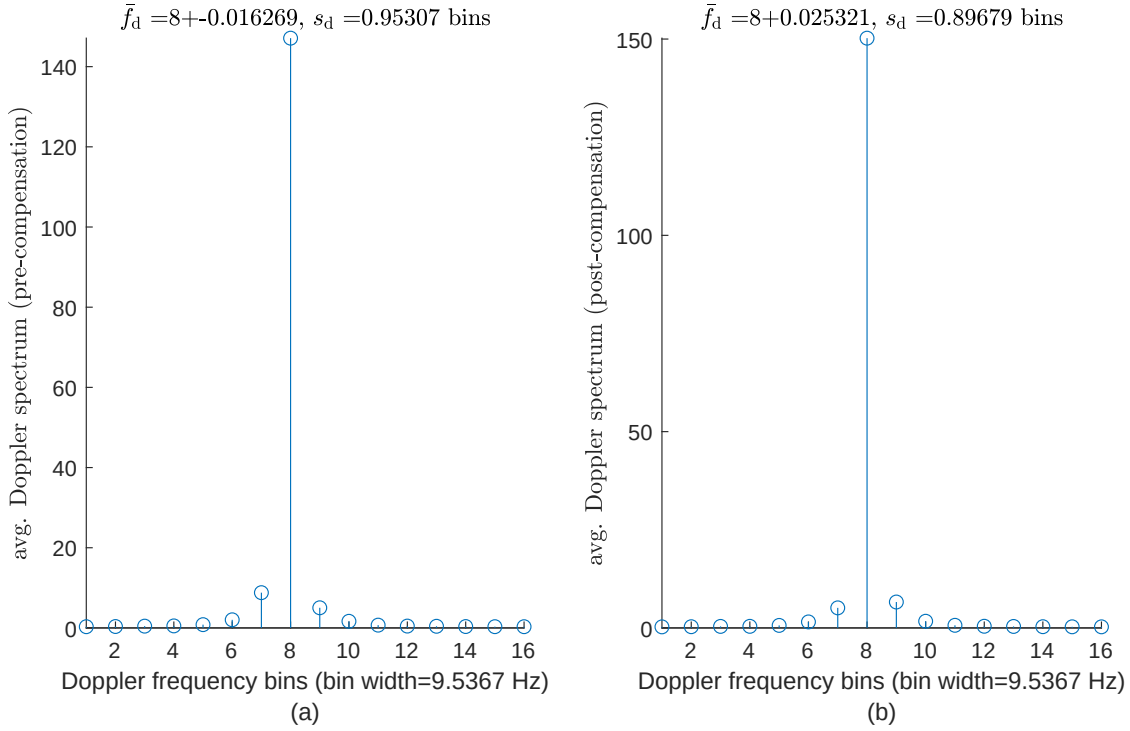

Figure B-18.4: Average Doppler power spectrum comparison (a) before and (b) after compensation for the entire channel ($W = 4.883$ kHz, $d = 2$ km, power level 4). The average is computed over channel delays. The spectrum is shifted so that the Doppler frequency of 0 corresponds to bin 8. Doppler spread is small. The centroid of the spectrum is close to bin before and after compensation.

B-19 $W = 9.766$ **kHz,** $d = 500$ **m,** PL $= 3$**,** $\Delta t = 5$ **s**

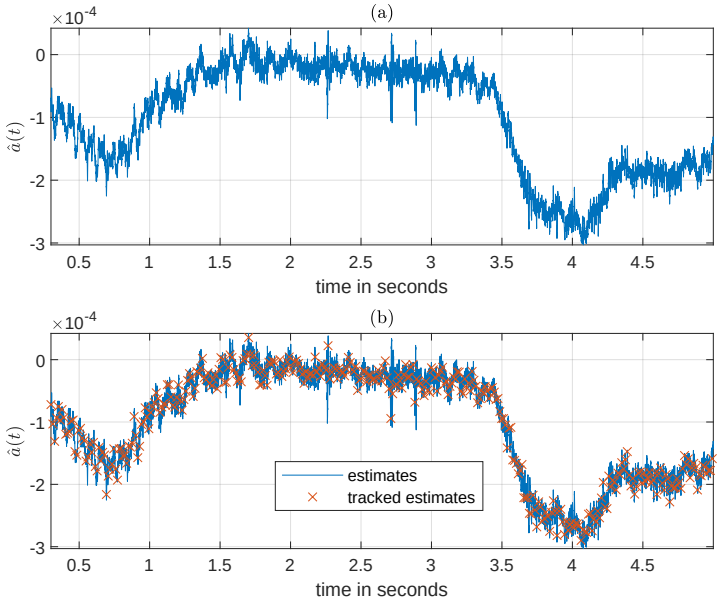

Figure B-19.1: Mach number estimator (a) and tracker (b) with $W = 9.766$ kHz, $d = 500$ m and PL $= 3$. 'x' indicates every 256th sample retained due to downsampling (sample is extracted every 4 preambles). Relative velocity is given by $1500 \cdot a(t)$. This data reduction facilitates practical compensation. Note, the downsampled representation captures the Mach number such that no lower frequency features relevant to tracking are neglected. This practically tracks the Mach number variations.

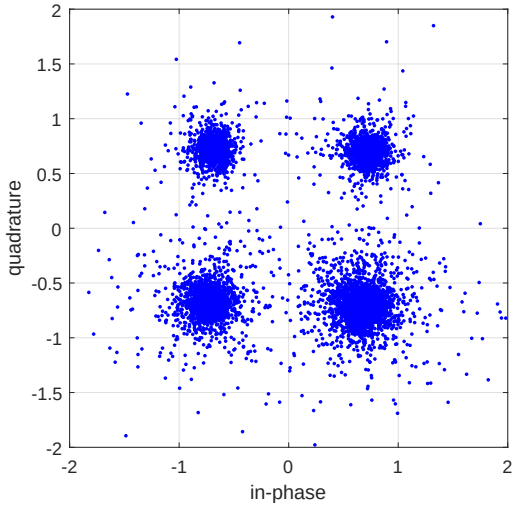

Figure B-19.2: Scatter plot of the compensated and demodulated RX pilots sampled at $W = 9.766$ kHz for a range of $d = 500$ m amd power level 3. The plot indicates that the QPSK symbols have been properly recovered.

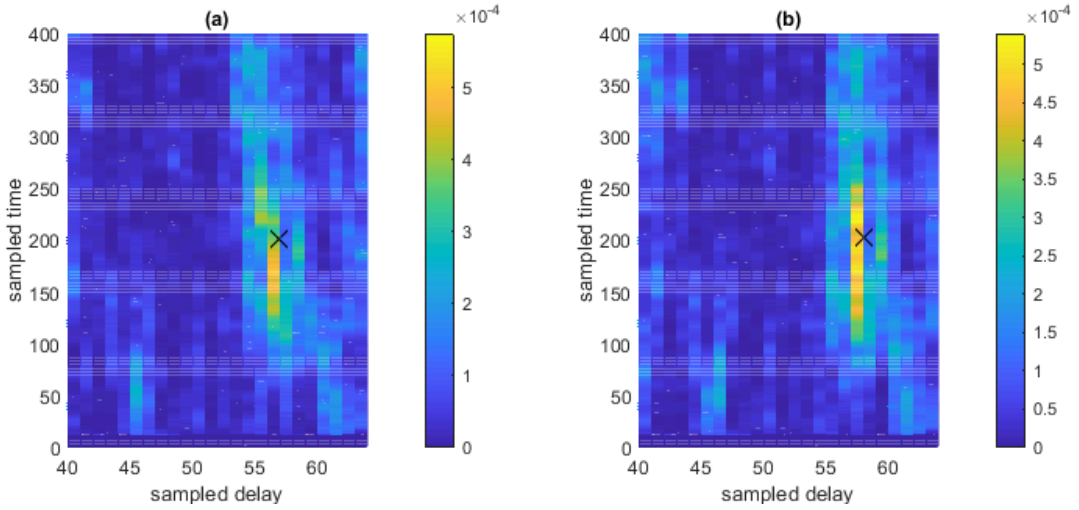

Figure B-19.3: CIR comparison (a) before and (b) after Doppler compensation for $W = 9.766$ kHz, $d = 500$ m and PL $= 3$. The CIR is projected onto t vs τ where the effect of Doppler compensation is more evident. High-energy (yellow) taps are compensated. 'x' shows a test tap location before and after compensation. The taps are aligned vertically after compensation, demonstrating proper recovery of channel tap locations.

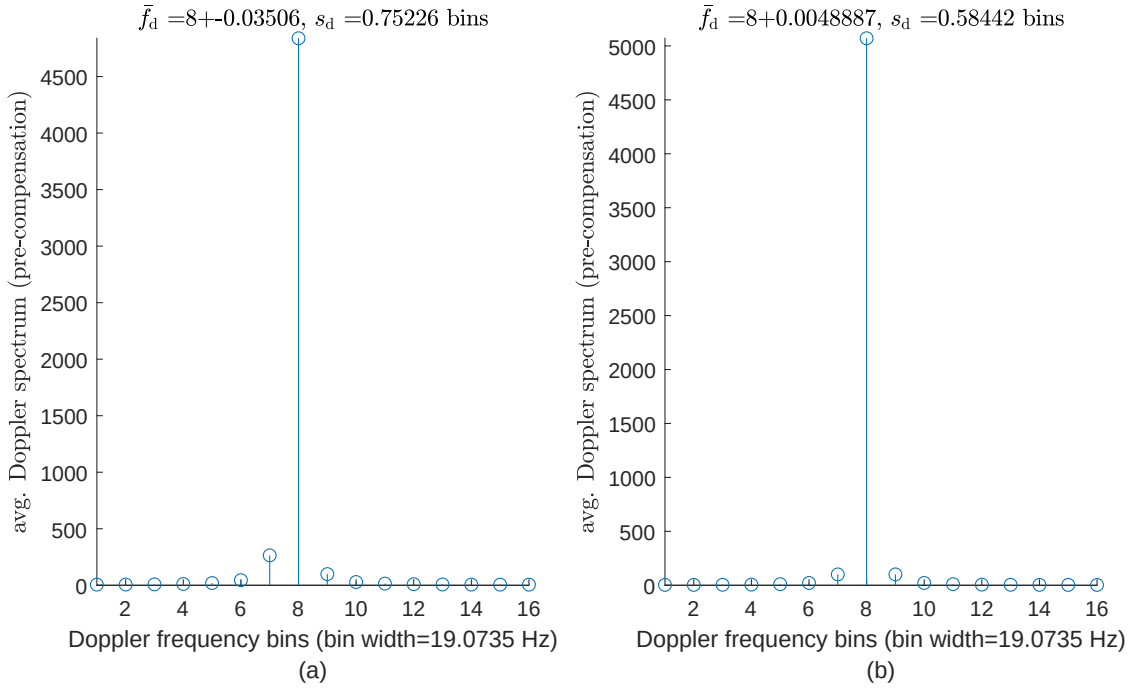

Figure B-19.4: Average Doppler power spectrum comparison (a) before and (b) after compensation for the entire channel ($W = 9.766$ kHz, $d = 500$ m, power level 3). The average is computed over channel delays. The spectrum is shifted so that the Doppler frequency of 0 corresponds to bin 8. Doppler spread is small. The centroid of the spectrum is returned to bin 8 after compensation.

B-20 $W = 9.766$ **kHz,** $d = 500$ **m,** PL $= 4$**,** $\Delta t = 0.7$ **s**

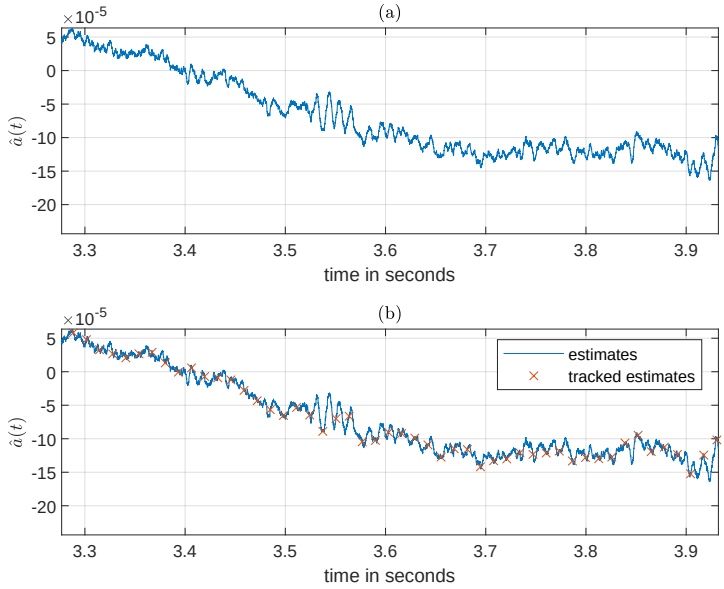

Figure B-20.1: Mach number estimator (a) and tracker (b) with $W = 9.766$ kHz, $d = 500$ m and PL $= 4$. 'x' indicates every 256th sample retained due to downsampling (sample is extracted every 4 preambles). Relative velocity is given by $1500 \cdot a(t)$. This data reduction facilitates practical compensation. Note, the downsampled representation captures the Mach number such that no lower frequency features relevant to tracking are neglected. This practically tracks the Mach number variations.

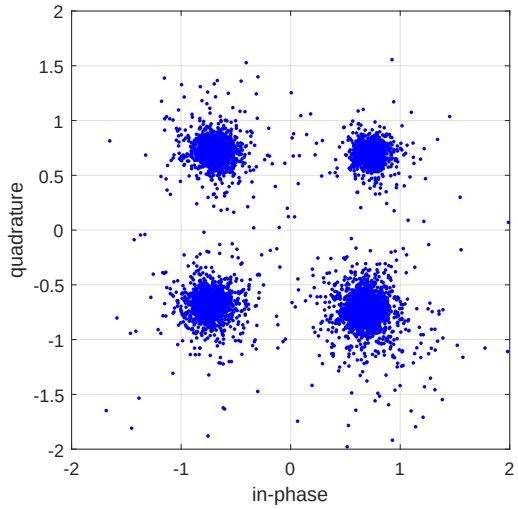

Figure B-20.2: Scatter plot of the compensated and demodulated RX pilots sampled at $W = 9.766$ kHz for a range of $d = 500$ m amd power level 4. The plot indicates that the QPSK symbols have been properly recovered.

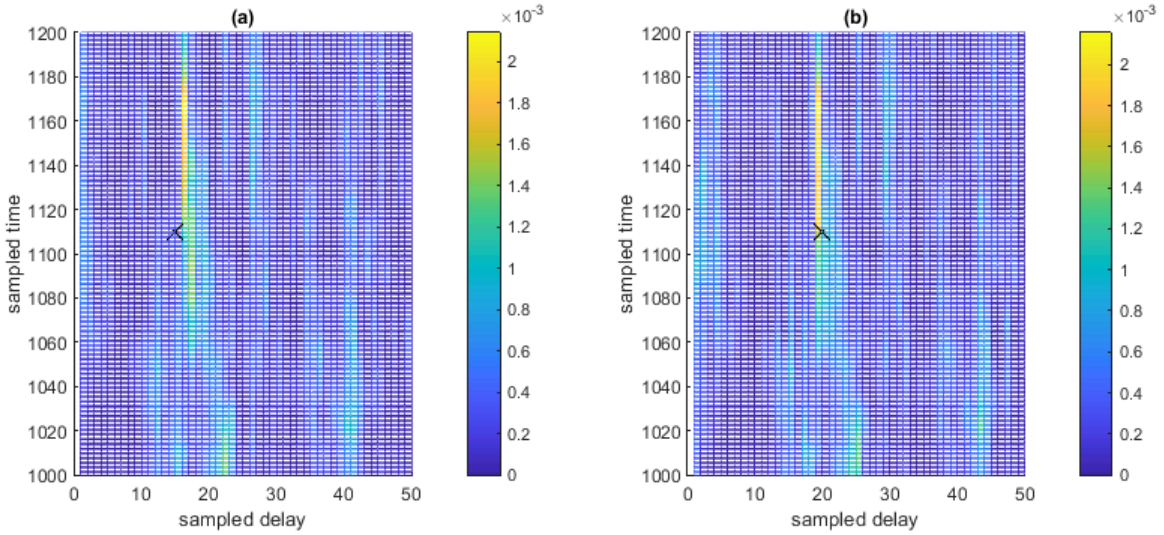

Figure B-20.3: CIR comparison (a) before and (b) after Doppler compensation for $W = 9.766$ kHz, $d = 500$ m and PL $= 4$. The CIR is projected onto t vs τ where the effect of Doppler compensation is more evident. High-energy (yellow) taps are compensated. 'x' shows a test tap location before and after compensation. The taps are aligned vertically after compensation, demonstrating proper recovery of channel tap locations.

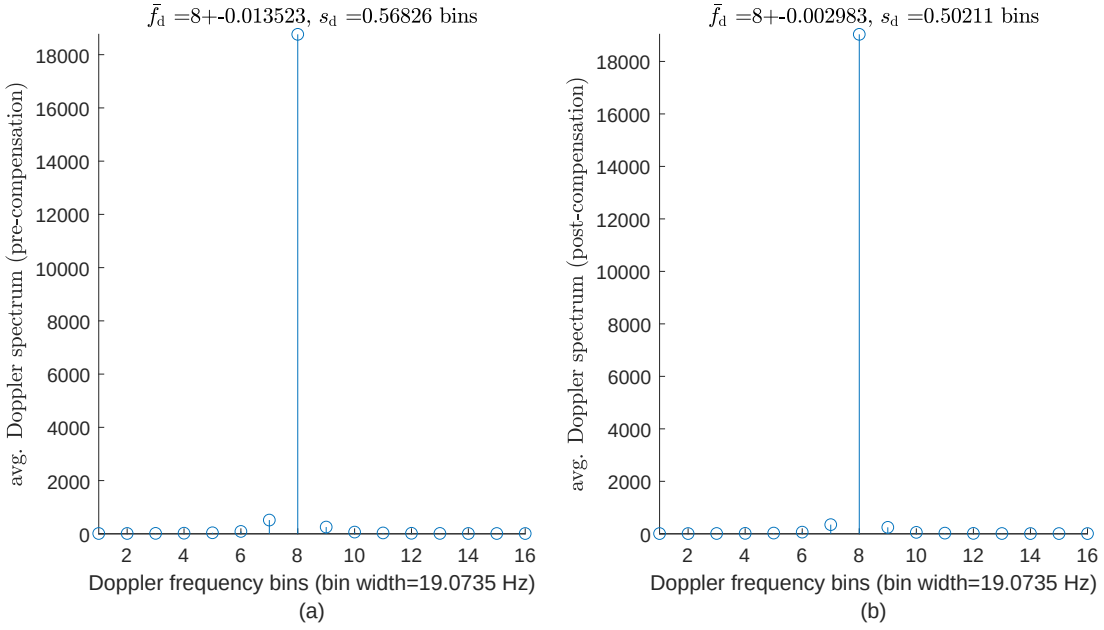

Figure B-20.4: Average Doppler power spectrum comparison (a) before and (b) after compensation for the entire channel ($W = 9.766$ kHz, $d = 500$ m, power level 4). The average is computed over channel delays. The spectrum is shifted so that the Doppler frequency of 0 corresponds to bin 8. Doppler spread is small. The centroid of the spectrum is returned to bin 8 after compensation.

B-21 $W = 9.766$ **kHz,** $d = 1$ **km,** PL $= 2$**,** $\Delta t = 4.5$ **s**

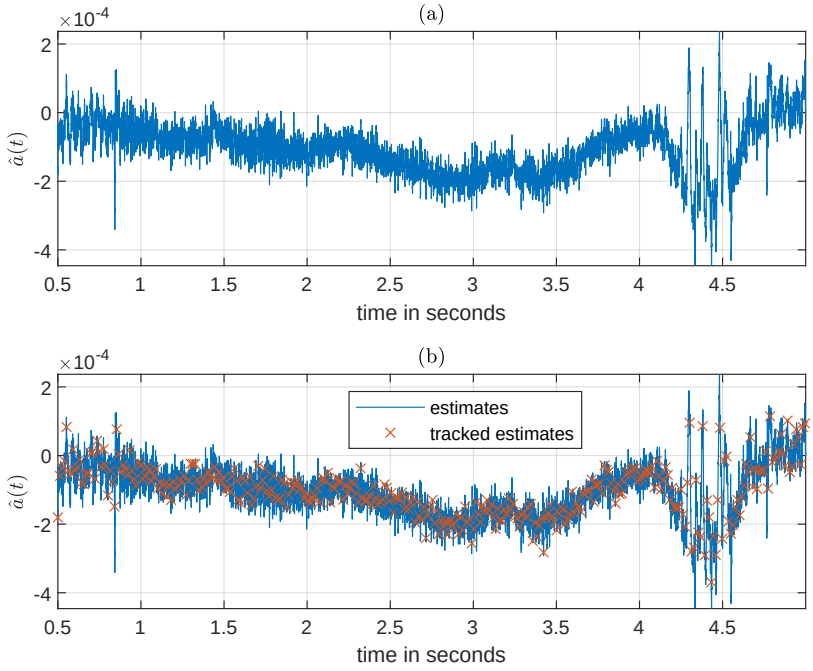

Figure B-21.1: Mach number estimator (a) and tracker (b) with $W = 9.766$ kHz, $d = 1$ km and PL $= 2$. 'x' indicates every 256th sample retained due to downsampling (sample is extracted every 4 preambles). Relative velocity is given by $1500 \cdot a(t)$. This data reduction facilitates practical compensation. Note, the downsampled representation captures the Mach number such that no lower frequency features relevant to tracking are neglected. This practically tracks the Mach number variations.

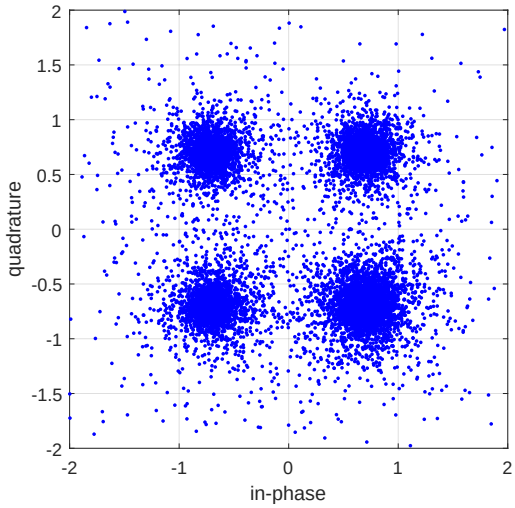

Figure B-21.2: Scatter plot of the compensated and demodulated RX pilots sampled at $W = 9.766$ kHz for a range of $d = 1$ km amd power level 2. The plot indicates that the QPSK symbols have been properly recovered.

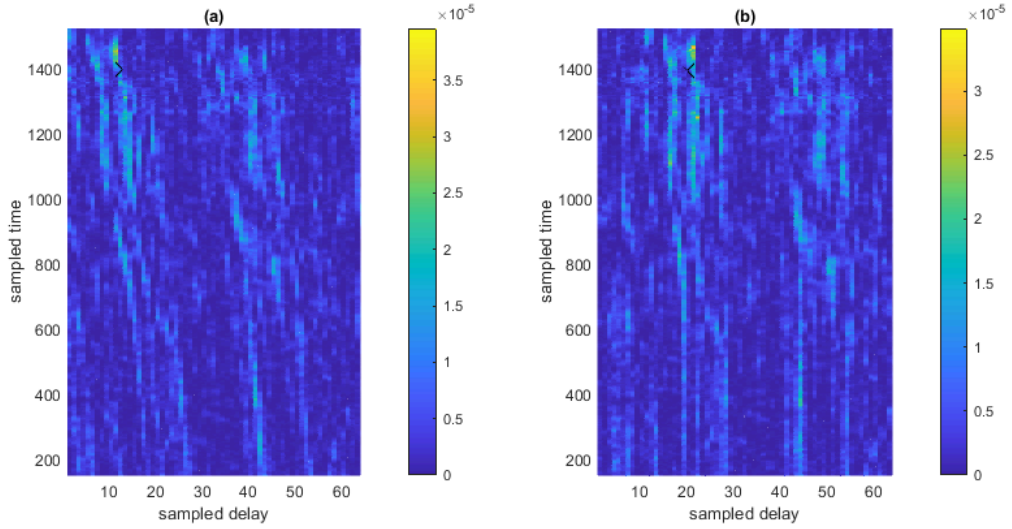

Figure B-21.3: CIR comparison (a) before and (b) after Doppler compensation for $W = 9.766$ kHz, $d = 1$ km and PL $= 2$. The CIR is projected onto t vs τ where the effect of Doppler compensation is more evident. High-energy (yellow) taps are compensated. 'x' shows a test tap location before and after compensation. The taps are aligned vertically after compensation, demonstrating proper recovery of channel tap locations.

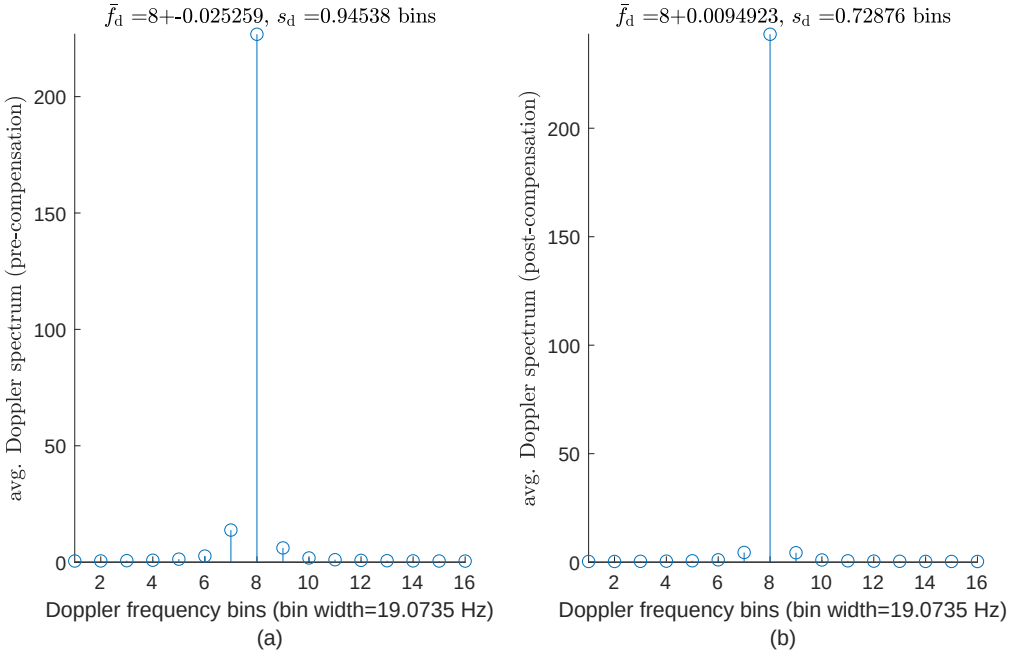

Figure B-21.4: Average Doppler power spectrum comparison (a) before and (b) after compensation for the entire channel ($W = 9.766$ kHz, $d = 1$ km, power level 2). The average is computed over channel delays. The spectrum is shifted so that the Doppler frequency of 0 corresponds to bin 8. Doppler spread is small. The centroid of the spectrum is returned to bin 8 after compensation.

B-22 $W = 9.766$ **kHz,** $d = 1$ **km,** PL $= 3$**,** $\Delta t = 1.6$ **s**

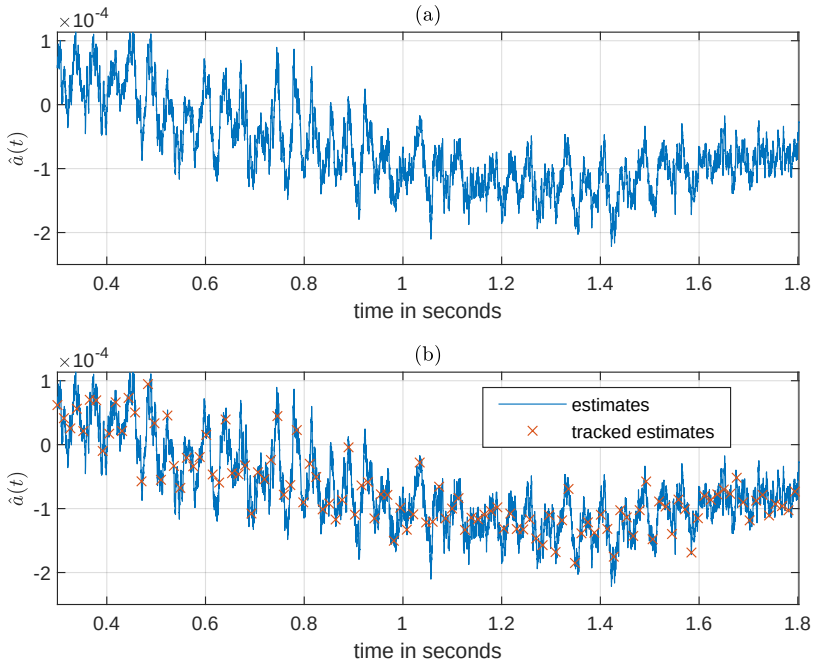

Figure B-22.1: Mach number estimator (a) and tracker (b) with $W = 9.766$ kHz, $d = 1$ km and PL $= 3$. 'x' indicates every 256th sample retained due to downsampling (sample is extracted every 4 preambles). Relative velocity is given by $1500 \cdot a(t)$. This data reduction facilitates practical compensation. Note, the downsampled representation captures the Mach number such that no lower frequency features relevant to tracking are neglected. This practically tracks the Mach number variations.

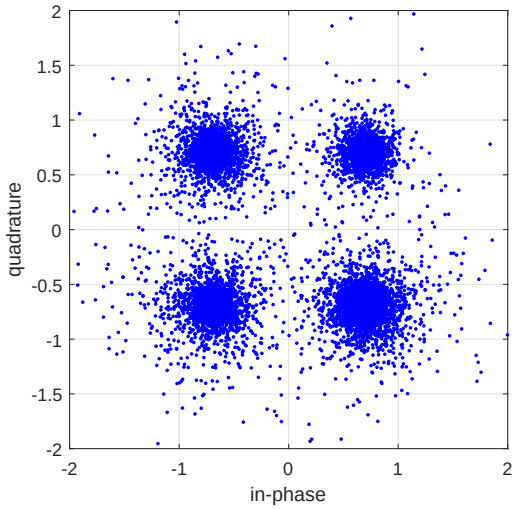

Figure B-22.2: Scatter plot of the compensated and demodulated RX pilots sampled at $W = 9.766$ kHz for a range of $d = 1$ km amd power level 3. The plot indicates that the QPSK symbols have been properly recovered.

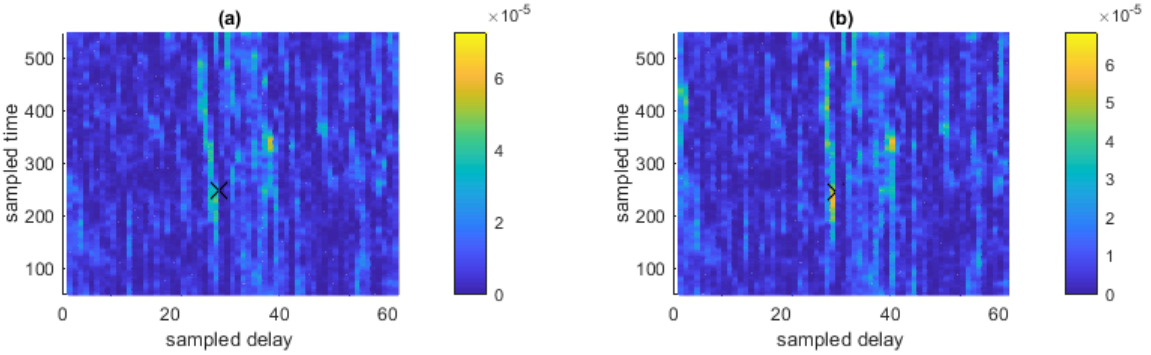

Figure B-22.3: CIR comparison (a) before and (b) after Doppler compensation for $W = 9.766$ kHz, $d = 1$ km and PL = 3. The CIR is projected onto t vs τ where the effect of Doppler compensation is more evident. High-energy (yellow) taps are compensated. 'x' shows a test tap location before and after compensation. The taps are aligned vertically after compensation, demonstrating proper recovery of channel tap locations.

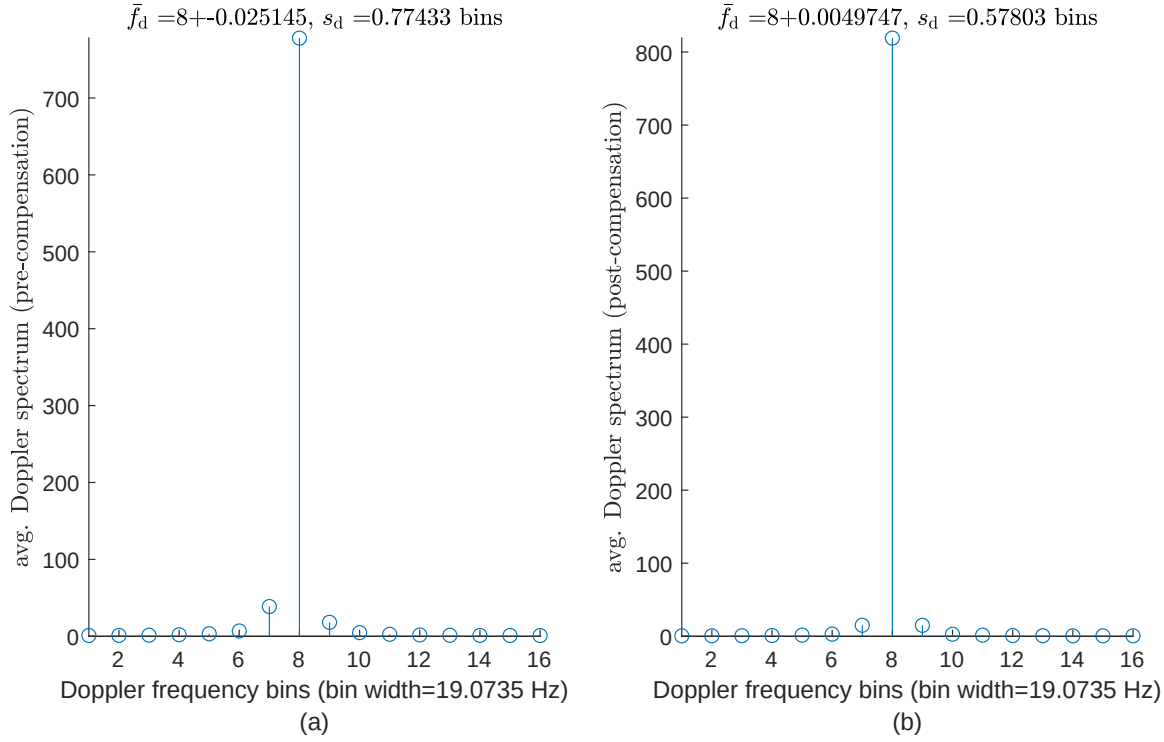

Figure B-22.4: Average Doppler power spectrum comparison (a) before and (b) after compensation for the entire channel ($W = 9.766$ kHz, $d = 1$ km, power level 3). The average is computed over channel delays. The spectrum is shifted so that the Doppler frequency of 0 corresponds to bin 8. Doppler spread is small. The centroid of the spectrum is returned to bin 8 after compensation.

B-23 $W = 9.766$ **kHz,** $d = 2$ **km,** PL $= 4$**,** $\Delta t = 1.3$ **s**

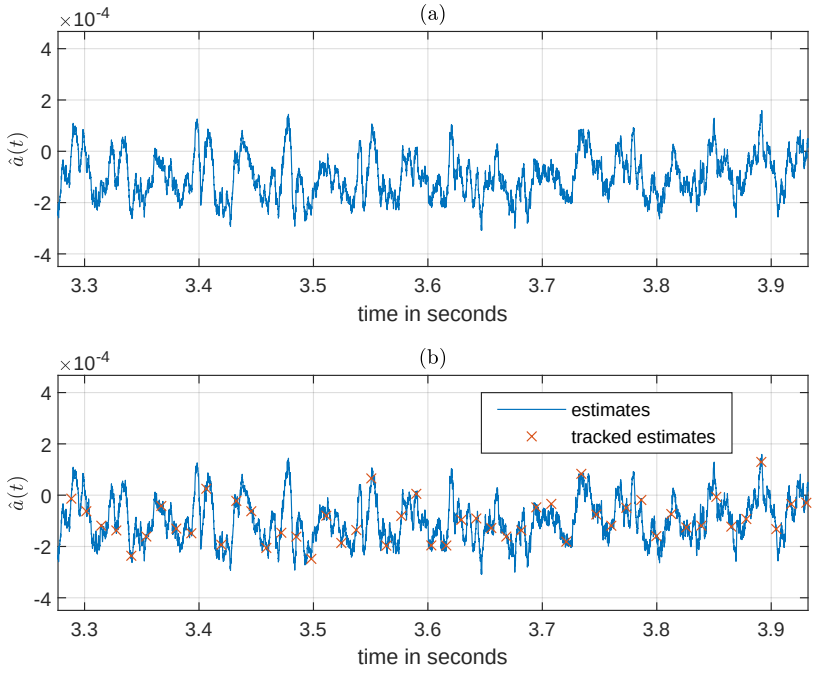

Figure B-23.1: Mach number estimator (a) and tracker (b) with $W = 9.766$ kHz, $d = 2$ km and PL $= 4$. 'x' indicates every 256th sample retained due to downsampling (sample is extracted every 4 preambles). Relative velocity is given by $1500 \cdot a(t)$. This data reduction facilitates practical compensation. Note, the downsampled representation captures the Mach number such that no lower frequency features relevant to tracking are neglected. This practically tracks the Mach number variations.

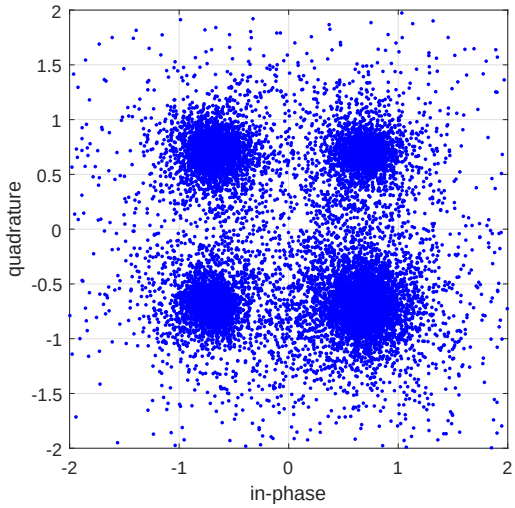

Figure B-23.2: Scatter plot of the compensated and demodulated RX pilots sampled at $W = 9.766$ kHz for a range of $d = 2$ km amd power level 4. The plot indicates that the QPSK symbols have been properly recovered.

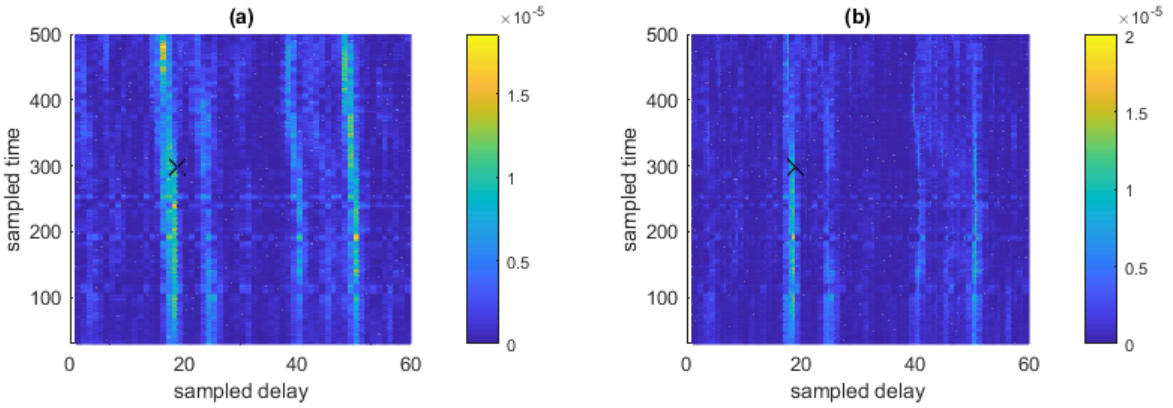

Figure B-23.3: CIR comparison (a) before and (b) after Doppler compensation for $W = 9.766$ kHz, $d = 2$ km and PL $= 4$. The CIR is projected onto t vs τ where the effect of Doppler compensation is more evident. High-energy (yellow) taps are compensated. 'x' shows a test tap location before and after compensation. The taps are aligned vertically after compensation, demonstrating proper recovery of channel tap locations.

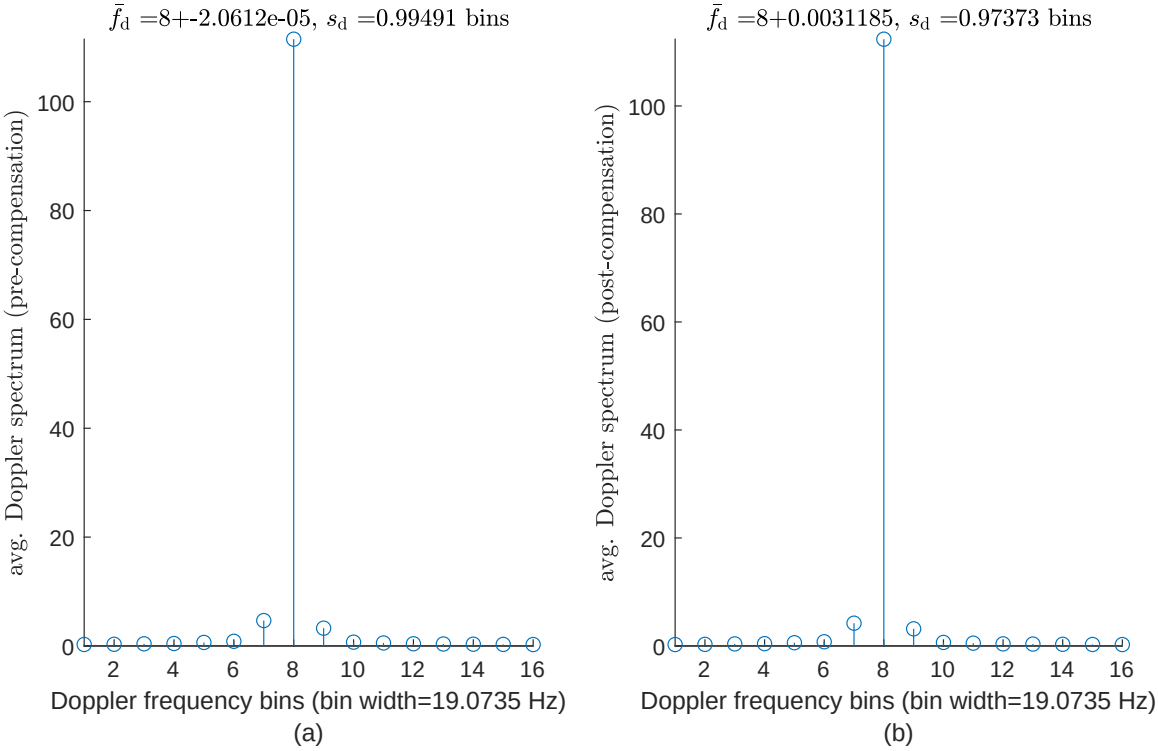

Figure B-23.4: Average Doppler power spectrum comparison (a) before and (b) after compensation for the entire channel ($W = 9.766$ kHz, $d = 1$ km, power level 3). The average is computed over channel delays. The spectrum is shifted so that the Doppler frequency of 0 corresponds to bin 8. Doppler spread is small. The centroid of the spectrum is close to bin 8 before and after compensation.

Appendix C

Chapter 2 Supplement: Fourier Transform and DFT Properties

The Fourier transform $X(f)$ of the function $x(t)$ is defined by the Fourier integral

$$X(f) = \mathcal{F}\{x(t)\} = \int_{-\infty}^{\infty} x(t)e^{-j2\pi ft}dt \tag{C.1}$$

with the inverse given by

$$x(t) = \mathcal{F}^{-1}\{X(f)\} = \int_{-\infty}^{\infty} X(f)e^{j2\pi ft}df. \tag{C.2}$$

The N-point DFT $X[k]$ of the sequence $x[n]$ is defined by the Fourier sum

$$X[k] = DFT\{x[n]\} = \frac{1}{\sqrt{N}}\sum_{n=0}^{N-1} x[n]e^{-j2\pi kn/N} \tag{C.3}$$

with the inverse (IDFT) given by

$$x[n] = IDFT\{X[k]\} = \frac{1}{\sqrt{N}}\sum_{k=0}^{N-1} X[k]e^{j2\pi kn/N}. \tag{C.4}$$

The following Fourier transform and DFT properties are used in Chapter 3.

Circular Shift Properties of the DFT

The circular shift property in time states that, for a given discrete-time shift n_0,

$$DFT\{x[n-n_0]\} = X[k]e^{-j2\pi kn/N}. \tag{C.5}$$

By the duality of the DFT, it also holds true that, for a given discrete-frequency shift k_0,

$$IDFT\{X[k-k_0]\} = x[n]e^{j2\pi kn/N}. \tag{C.6}$$

The time and frequency shifts are modulo N. For example, if $X[k] = \delta[k]$, then

$$DFT\{\delta[k-k_0]\} = e^{j2\pi kn/N}. \tag{C.7}$$

Circular Cross-Correlation Theorem for the DFT

The circular cross-correlation theorem relates the circular cross-correlation of the two sequences $x[n]$ and $y[n]$ with their DFT counterparts $X[k]$ and $Y[k]$. It states that

$$DFT\{x[n] \star y[n]\} = X^*[k]Y[k]. \tag{C.8}$$

Circular Convolution Theorem for the DFT

The DFT of the circular convolution of $x[n]$ and $y[n]$ (modulo N) is given by

$$DFT\{x[n] \circledast y[n]\} = X[k]Y[k]. \tag{C.9}$$

Shift Properties of the Fourier Transform

The shift property in time states that, for a given time shift t_0,

$$\mathcal{F}\{x(t-t_0)\} = e^{-j2\pi f t_0} X(f). \tag{C.10}$$

By the duality of the Fourier transform, it also holds true that, for a given frequency shift f_0,

$$\mathcal{F}^{-1}\{X(f-f_0)\} = e^{j2\pi f_0 t} x(t). \tag{C.11}$$

Scaling Property of the Fourier Transform

For a given scaling factor w,

$$\mathcal{F}\{x(wt)\} = \frac{1}{|w|} X\left(\frac{f}{w}\right). \tag{C.12}$$

Convolution Theorem for the Fourier Transform

The Fourier transform of the convolution of $x(t)$ and $y(t)$ is given by

$$\mathcal{F}\{x(t) * y(t)\} = X(f)Y(f) \tag{C.13}$$

where $Y(f) = \mathcal{F}\{y(t)\}$.

Differentiation Property of the Fourier Transform

The q^{th} derivative of $x(t)$ has the Fourier transform property

$$\mathcal{F}\left\{\frac{d^q}{dt^q}x(t)\right\} = (j2\pi f)^q X(f) \tag{C.14}$$

Bibliography

[1] C. Schlegel and M. Jar, "Embedded Pilot and Multi-Size OFDM Processing for Jointly Time and Frequency Selective Channels," in *ISITA2016*, Monterey, CA, Oct. 30–Nov. 2, 2016.

[2] S. Coleri, M. Ergen, A. Puri, and A. Bahai, "Channel Estimation Techniques Based on Pilot Arrangement in OFDM Systems," in *IEEE TRANSACTIONS ON BROADCASTING*, 48(3), Nov. 2002.

[3] W. Yonggang "Underwater Acoustic Channel Estimation for Pilot Based OFDM," in *2011 IEEE International Conference on Signal Processing, Communications and Computing (ICSPCC)*, Xi'an, China, Sept. 14–16, 2011.

[4] F. Zhou, G. Qiao and N. Li, "Performance Analysis of Different Pilot-symbol Patterns in Underwater Acoustic OFDM System," in *2008 4th International Conference on Wireless Communications, Networking and Mobile Computing*, Dalian, China, Oct. 12–14, 2008.

[5] M. A. Ainslie and J. G. McColm, "A Simplified Formula for Viscous and Chemical Absorption in Sea Water," in *Journal of the Acoustical Society of America*, 103(3), pp. 1671-1672, 1998.

[6] F. H. Fisher and V. P. Simmons, "Sound Absorption in Seawater," in *Journal of the Acoustical Society of America*, 62, pp. 558-564, 1977.

[7] R. E. Francois and G. R. Garrison, "Sound Absorption Based on Ocean Measurements: Part I: Pure Water and Magnesium Sulfate Contributions," in *Journal of the Acoustical Society of America*, 72(3), pp. 896-907, 1982.

[8] R. E. Francois and G. R. Garrison, "Sound Absorption Based on Ocean Measurements: Part II: Boric Acid Contribution and Equation for Total Absorption," in *Journal of the Acoustical Society of America*, 72(6), pp. 879-1890, 1982.

[9] S. Stein, "Differential Delay/Doppler ML Estimation with Unknown Signals ," in IEEE Trainsactions on Signal Processing, 41(8), Aug. 1993.

[10] M. Johnson, L. Freitag and M. Stojanovic, "Improved Doppler Tracking and Correction for Underwater Acoustic Communications," in *1997 IEEE International Conference on Acoustics, Speech, and Signal Processing*, Munich, Germany, April 21–24, 1997.

[11] D. Eiwen, G. Taubock, F. Hlawatsch, and F.G. Feichtinger, "Compressive Tracking of Doubly Selective Channels in Multicarrier Systems Based on Sequential Delay-Doppler Sparsity," in *2011 IEEE International Conference on Acoustics, Speech and Signal Processing (ICASSP)*, Prague, Czech Republic, May 22–27,2011.

[12] J. Trubuil and T. Chonavel, "Accurate Doppler Estimation for Underwater Acoustic Communications ," in *2012 Oceans - Yeosu*, Yeosu, South Korea, May 21–24, 2012.

[13] Y. Li, Y. Wang, and X. Guan, "Joint Synchronization and Doppler Scale Estimation using Zadoff-Chu Sequences for Underwater Acoustic Communications," in *OCEANS 2017 - Anchorage*, Anchorage, AK, USA, Sep. 18–21, 2017.

[14] J. Trubuil, T. Le Gall, and T. Chonavel, "Synchronization, Doppler and Channel estimation for OFDM Underwater Acoustic Communications." in *OCEANS 2014 - TAIPEI*, Taipei, Taiwan, April 7–10, 2014.

[15] L. Liu, Y. Zhang, P. Zhang, L. Zhou, J. Li, J. Jin, J. Zhang, and Z. Lv, "PN Sequence Based Doppler and Channel Estimation for Underwater Acoustic OFDM Communication," in *2016 IEEE International Conference on Signal Processing, Communications and Computing (ICSPCC)*, Hong Kong, China, Aug. 5–8, 2016.

[16] A.Y. Kibangou, C. Siclet, and L. Ros, "Joint Channel and Doppler Estimation for Multicarrier Underwater Communications," in *Proceedings of the IEEE International Conference on Acoustics, Speech, and Signal Processing, ICASSP 2010*, Dallas, Texas, March 14–19, 2010.

[17] L. Wan, Z. Wang, S. Zhou, T.C. Yang, and Z. Shi, "Performance Comparison of Doppler Scale Estimation Methods for Underwater Acoustic OFDM," in *Journal of Electrical and Computer Engineering*, 2012, Jan. 2012.

[18] B. Zhang, Y. Wang, H. Wang, L. Zheng, Z. Zhuang, and K. Xu, "Cyclic-Feature Based Doppler Scale Estimation for Orthogonal Frequency-Division Multiplexing (OFDM) Signals Over Doubly Selective Underwater Acoustic Channels," in *Proceedings of Meetings on Acoustics*, 30(1), Oct. 2017.

[19] C. Hwang, K. Kim, S. Chun, and S. Lee, "Doppler Estimation Based on Frequency Average and Remodulation for Underwater Acoustic Communication," in *International Journal of Distributed Sensor Networks*, 2015(2), Nov. 2015.

[20] Y. Zhao, H. Yu, G. Wei, F. Ji, F. Chen, J. Zhang, "FRFT-Based Parameter Estimation of Time-Varying Wideband Underwater Acoustic Multipath Channels," in *WUWNET '15: Proceedings of the 10th International Conference on Underwater Networks & Systems*, 9, Oct. 2015.

[21] J. Xu, D. Wang, X. Hu, and Y. Xie, "Doppler Effect Mitigation Over Mobile Underwater Acoustic OFDM System," in *WUWNet '18: Proceedings of the Thirteenth ACM International Conference on Underwater Networks & Systems*, 2, Dec. 2018.

[22] Y. Zakharov, A. Morozov, and J. Preisig, "Doppler Effect Compensation for Cyclic-Prefix-Free OFDM Signals in Fast-Varying Underwater Acoustic Channel," in *Proceedings of Meetings on Acoustics*, 17(1), Dec. 2012.

[23] X. Jiang, W. Zeng, and X. Li, "Time Delay and Doppler Estimation for Wideband Acoustic Signals in Multipath Environments," in *The Journal of the Acoustical Society of America*, 130(2), pp.850-857, Aug. 2011.

[24] N.F. Josso, C. Ioana, J.I. Mars, and C. Gervaise, "Source Motion Detection, Estimation, and Compensation for Underwater Acoustics Inversion by Wideband Ambiguity Lag-Doppler Filtering," in *The Journal of the Acoustical Society of America*, 128(6), pp. 3416-3425, Dec. 2010.

[25] G. Yu, T.C. Yang, and S. Piao, "Estimating the Delay-Doppler of Target Echo in a High Clutter Underwater Environment Using Wideband Linear Chirp Signals: Evaluation of Performance with Experimental Data," in *The Journal of the Acoustical Society of America*, 142(4), pp. 2047–2057, Oct. 2017.

[26] W. Zeng and W. Xu, "Fast Estimation of Sparse Doubly Spread Acoustic Channels," in *The Journal of the Acoustical Society of America*, 131(1), pp. 303–317, Jan. 2012.

[27] B.S. Sharif, J. Neasham, O.R. Hinton, and A.E. Adams, "A Computationally Efficient Doppler Compensation System for Underwater Acoustic Communications," in *IEEE Journal of Oceanic Engineering*, 25(1), pp. 52–61, Jan. 2000.

[28] A. B. Carlson and P. B. Crilly, *Communication Systems: An Introduction to Signals and Noise in Electrical Communication*, New York: The McGraw-Hill Companies, Inc., 2010.

[29] J. E Williams, "Hydrodynamic Noise," in *Annual Review of Fluid Mechanics*, vol.1, pp. 197–222, Jan. 1969.

[30] G.M. Wenz, "Acoustic Ambient Noise in the Ocean: Spectra and Sources," in *The Journal of the Acoustical Society in America*, 34(12), pp. 1936–1956, Dec. 1962.

[31] J. G. Proakis and M. Salehi, *Digital Communications*, New York: The McGraw-Hill Companies, Inc., 2008.

[32] H. Schulz and C. Lüders, *Theory and Applications of OFDM and CDMA: Wideband Wireless Communications*, Chichester: John Wiley & Sons, Ltd, 2005.

[33] M. Stojanovic, "Underwater acoustic communications: design considerations on the physical layer," in *Fifth Annual Conference on Wireless on Demand Network Systems and Services*, Jan. 23–25, 2008.

[34] M. Stojanovic, "On the relationship between capacity and distance in an underwater acoustic channel," in *Proc. First ACM International Workshop on Underwater Networks (WuwNet/MobiCom)*, Los Angeles, CA, Sept. 2006.

[35] P. Qarabaqi, "Statistical characterization of a class of underwater acoustic communication channels," Electrical Engineering Dissertations, paper 106, Jan. 2014, Retrieved from `http://hdl.handle.net/2047/d20005071`

[36] Ultra Maritime Digital Communications Centre, *UMDCC Regular Report, December 2014*, 2015, Halifax: Dalhousie University.

[37] P. A. van Walree, T. Jenserud, and R. Otnes, "Stretched-exponential Doppler spectra in underwater acoustic communication channels," in *J. Acoust. Soc. Am.*, vol. 128, no. 5, Nov. 2010.

[38] S. Zhou and Z. Wang, *OFDM for Underwater Acoustic Communications*, Chichester: John Wiley & Sons, Ltd, 2014.

[39] H. Kobayashi, B.L. Mark and W. Turin, *Probability, Random Processes, and Statistical Analysis*, New York: Cambridge University Press, 2012.

[40] M. Stojanovic, "Low complexity OFDM detector for underwater acoustic channels," in *Proc. of MTS/IEEE OCEANS Conference*, Boston, MA, Sept. 18–21, 2006

[41] B. Li, S. Zhou, M. Stojanovic, L. Freitag, and P. Willett, "Multicarrier underwater acoustic communications over fast-varying channels," in *IEEE Journal of Oceanic Engineering*, vol. 33, No.2, pp.198–209, April 2008.

[42] K. Kouassi, G. Andrieux, and JF. Diouris, "PAPR Distribution for Single Carrier M-QAM Modulations," in *Wireless Pers. Commun.*, vol. 104, pp. 727–738, 2019.

[43] X. Cheng, L. Yang, and X. Cheng, *Cooperative OFDM Underwater Acoustic Communications*, Switzerland: Springer International Publishing, 2016.

[44] X. Geng and A. Zielinski, "An eigenpath underwater acoustic communication channel model," 'Challenges of Our Changing Global Environment.' Conference Proceedings. OCEANS '95 MTS/IEEE, San Diego, California, USA, 1995, pp. 1189-1196 vol.2, doi: 10.1109/OCEANS.1995.528591.

[45] L. Zhang, M. Li, G. Li, an R. Wang, "Symbol Estimation Algorithm for MIMO Underwater Acoustic Communication System Based on Multiplicative Noise Model," in *Mathematical Problems in Engineering*, vol. 2015, 2015, Retrieved from `https://doi.org/10.1155/2015/719025`.